Development of Discontinuous Fibre Preforming Processes

Critesh Patel, MEng. (Hons.)

Thesis submitted to the University of Nottingham
for the degree of Doctor of Philosophy

December 2013

Abstract

Discontinuous fibre composites are under increasing investigation for structural and semi-structural components as they are easily automated, making it possible to remove costly hand labour based steps typically associated with advanced fibre reinforced composites. Directed fibre preforming (DFP) is one possible process which has several advantages when compared with competing techniques. Low material and process costs coupled with short cycle times means the process is suited to medium volume production (typically <10,000 ppa). Predicting mechanical performance remains a major obstacle to industrial adoption however, due to the stochastic nature of fibre distribution. This is of particular importance for structural applications where minimum property requirements and a greater certainty of performance must be achieved.

This thesis employs a stochastic macroscale modelling approach to predict fibre locations during the reinforcement deposition stage. This is achieved through process characterisation studying the effects of key microstructural and process-specific parameters on fibre distribution and orientation. The proposed DFP simulation software can generate realistic fibre networks for complex three-dimensional component geometries providing feedback on preform quality. This information is used to optimise the preform structure via process input parameters such as robot trajectory and material properties with validation tests conducted to assess model accuracy.

An interface between the simulation software and commercial finite element code facilitates mechanical property analysis for full-scale components using realistic load cases. The complete software package is intended to streamline the route to manufacture for DFP processes from a conceptual design stage.

Contents

Acknowledgements

I would like to thank my academic supervisors Thomas Turner and Nicholas Warrior for their guidance and support during the course of this project. Project support from Aston Martin Lagonda and the Technology Strategy Board was also greatly appreciated. Many thanks go to Roger Smith and Geoff Tomlinson for their technical assistance and to my project colleagues Dharan Kirupanantham and Tristan Nicholls.

I would also like to thank my friends and colleagues for the entertainment that they've provided me during my PhD studies and the many memorable get-togethers. Finally, I thank my family for their love and support during my time at Nottingham.

Abbreviations

CFD	Computational Fluid Dynamics
CFRP	Carbon Fibre Reinforced Polymer
CoFRM	Continuous Filament Random Mat
CLT	Classical Laminate Theory
CV	Coefficient of Variation
DCFP	Discontinuous Carbon Fibre Preforming
DFP	Directed Fibre Preforming
DIC	Digital Image Correlation
FEA	Finite Element Analysis
FPR	Fibre Projected Ray
FRP	Fibre Reinforced Polymer
GFRP	Glass Fibre Reinforced Polymer
GUI	Graphical User Interface
LCM	Liquid Composite Moulding
P4	Programmable Powder Preforming Process
PLC	Programmable Logic Controller
PTCP	Projected Tool Centre Point
ROM	Rule of Mixtures
RTM	Resin Transfer Moulding
RVE	Representative Volume Element
TCP	Tool Centre Point
UD	Unidirectional
VaRTM	Vacuum assisted Resin Transfer Moulding

Chapter 1. Introduction

Fibre reinforced composite materials are continuing to find new applications in the transportation industry due to potential weight savings over traditional materials whilst maintaining mechanical performance requirements. Composite materials offer high stiffness and strength to weight ratios which are particularly attractive qualities to vehicle manufacturers where energy efficiency is of primary concern. Short fibre composites manufactured via injection moulding and compression moulding techniques have long been established for non-structural applications due to their short manufacturing cycle times and cost effectiveness. High performance structural composites are considerably more expensive to manufacture however, using expensive base materials and requiring longer production cycle times. Whilst continuous fibre materials currently dominate the high performance composite market there is increasing interest in using discontinuous fibre architectures for structural applications. These materials offer high levels of automation removing costly labour intensive steps typically associated with advanced fibre reinforced composites and are under increasing investigation for high volume production. The work presented in this thesis is primarily concerned with affordable technologies for high performance applications using discontinuous fibre composites.

1.1. Composites in the transportation industry

1.1.1. Market forces

UK targets for the reduction in greenhouse gases (GHG) are split between the domestic Climate Change Act and the international Kyoto Protocol. By 2050 the UK is committed to reduce GHG emissions, of which carbon dioxide is the main constituent, by 80% from base year (1990) levels [1]. The transportation sector is currently the second largest contributor (~26%) with marginal year on year improvements compared with other sectors [2]. This means that emissions from the transportation sector are increasing in proportion to total domestic levels. Within the

sector, road transport accounted for 68% of GHG emissions in 2009 with a dramatic increase experienced in international aviation contributing to 20% - twice the base year emissions levels [3].

Current UK trends in transport emissions are representative across most industrialised countries where similarly ambitious emissions targets exist. A concerted effort is being made to curtail environmental impact in transport; particularly with emerging markets such as China and India fuelling further demand for increased mobility. It is estimated that by 2050 the number of vehicles on roads worldwide could increase by 300% to 3.5 billion [4]. A rapid increase in air travel is also anticipated with the International Civil Aviation Organisation (ICAO) projecting an increase in emissions of 70% by 2020; even after factoring in improvements in fuel efficiencies of 2% year on year [5]. Clearly the transportation industry will play a vital role in whether global emissions targets are achieved. Rising fuel costs is another important factor with consumers pressurising manufacturers to improve fuel economy. Using lightweight materials such as polymer composites to replace traditional metals has become a significant area of interest across all transport sectors for this reason. Reducing vehicle weight by 10% translates into an increase in fuel economy of ~6% providing a sustainable solution in reducing GHG emissions [6].

1.1.2. Current status

With a greater understanding and steady technological advancement in processing techniques, advanced composite materials are growing in popularity for a wide range of applications. The role of composites has grown rapidly over the last two decades led by heavy investment in the aerospace industry. Large proportions (>50% by weight) of flagship commercial aircraft, such as the Boeing Dreamliner, now consist of advanced composite materials. The automotive industry is playing catch up with strong interest from high volume manufacturers exploring uses for composites in structural applications which can offer large weight savings of up to 60% over equivalent metallic parts [7, 8]. Polymer composites can take many forms with a myriad of processing techniques available offering flexibility in design and manufacture making them suitable for the majority of applications in the

transportation industry. Many of the obstacles restricting the usage of composites to niche high performance applications are gradually being alleviated.

Mid to high volume car manufacturers are at a particularly interesting juncture whereby technological advances in reducing fleet emissions are offset by increases in vehicle numbers globally [9]. To satisfy long term efficiency goals, major investment is required in adopting alternative propulsion technologies and lightweight designs. The use of composites not only fulfils weight requirements but also increases the viability of using smaller, less powerful engines and fledgling technologies such as electric powertrains; offsetting the increased component weight. For many years lightweight glass fibre reinforced polymer composites (GFRP) have found uses in non-structural applications using well-established high volume manufacturing processes. Carbon fibre reinforced polymer composites (CFRP) offer even higher specific properties suitable for structural applications where metals still dominate; therefore presenting an opportunity for large weight savings. Traditional carbon composite manufacture is labour intensive and costly however, due to the commercially available base material forms. This has restricted its usage to low volume industries such as motorsport, high end luxury cars and aerospace where performance takes precedence over costs and production throughput. Unless a commercially viable manufacturing process for CFRPs is found, the route to mass production in the transportation industry remains unclear.

1.1.3. Production rates

Part production rates are highly dependent on application and industry. The automotive sector represents the largest spread in production volumes ranging from high performance niche vehicles (<1000 units pa) to mass market vehicles (>200,000 units pa). Aerospace and marine industries are generally considered low to mid volume with series production numbers less than 5000 units pa. Required production rates generally dictate the choice of manufacturing process – finding a compromise between cycle times, capital costs, material costs and part performance. The following is a brief overview of commonly deployed processes for different production scales.

For low volume production (<1000 ppa) traditional techniques such as open mould wet lay-up are still used, requiring low initial investment in tooling and affording

flexibility for limited runs. Pre-impregnated (prepregs) fabrics and unidirectional (UD) materials offer a convenient alternative leading to less material wastage and lower variation in mechanical performance between parts. Prepregs typically require the use of an autoclave to achieve the necessary compaction pressures to produce high quality, high fibre volume fraction (~60% V_f) components. Autoclave curing adds considerable capital investment and operational cost however. To overcome this, out-of-autoclave (OoA) prepregs have been developed which can be cured at atmospheric pressure under vacuum bag thus reducing process costs but with the added caveat that a longer curing stage is generally required to remove interlaminar voids.

Liquid composite moulding (LCM) processes are well suited to mid volume production (1000 – 30,000 ppa) with the benefit of short cycle times and the ability to mould near net-shape complex 3D components with good dimensional control. Resin transfer moulding (RTM) is a popular closed mould process requiring low resin injection pressures (<1 MPa) minimising tooling and plant costs. The fibrous reinforcement, called a preform, is pre-shaped to the final part geometry and placed into the mould prior to resin injection. Common material forms used for preforms include woven, random mat, stitched, knitted, braided and unidirectional materials. High fibre content is possible (>50% V_f) making the process suitable for structural and semi-structural components. Faster cycle times can be achieved using structural reaction injection moulding (SRIM) where injection rates are increased using higher pressures (10 - 20 MPa) and low viscosity resin systems [10]. This process is suited to mid to high volume production where the higher plant and tooling costs can be amortized over increased part production.

Compression moulding techniques become attractive when production rates approach high volume (>30,000 ppa) and mechanical performance requirements are less demanding. Sheet moulding compounds (SMC) are popular due to their processability through the use of discontinuous glass fibres (~25 mm) finding applications for large single piece mouldings such as body panels and interior fixtures. Advanced SMCs (A-SMC) replace glass with carbon fibre reinforcement offering improved mechanical properties suitable for semi-structural applications typically seen in the automotive industry. Tooling and plant costs for SMCs are much greater than for LCM processes due to the requirement of heavy duty presses (>500 tonnes), however, shorter cycle times permits production volumes of up to 250,000 ppa.

For cosmetic and non-structural parts, thermoplastic injection moulding processes are capable of producing millions of parts per year with typical cycle times of less than 1 minute. Short fibres (<5 mm) along with heated thermoplastic resin is injected at high pressure into a closed mould and cooled before de-moulding. Thermoset alternatives are also available with the requirement of a heated mould for the curing phase.

1.1.4. Current applications

1.1.4.1. Automotive

The high costs and lengthy manufacturing cycle times associated with CFRPs have typically restricted their use to the high performance market. High specific mechanical properties are of primary importance for structural applications where materials with high reinforcement loadings are typically used (>50% V_f). It is now common for high performance cars to consist of large percentages of carbon fibre composites where low volumes and high price tags still make hand lay-up of prepreg materials cost-effective and sufficiently versatile for short production runs. McLaren sought higher production rates using RTM technology to series produce carbon fibre components for the Mercedes SLR creating up to 700 ppa. Similarly, BMW manufacture CFRP roofs for their M3 and M6 models as well as bumper supports for the M6 using preformed nonwoven fabrics and RTM achieving series production [11]. Further process development has facilitated the extensive use of carbon composites for the high strength passenger cell in the future BMW i-Car series.

High volume manufacturers found non-structural uses for GFRP materials in body panels and interior fixtures due to their low cost, high processability and short cycle times. SMC has predominantly been used for skin panels, side and tail doors and in some cases, modular front ends with usage growing over the last couple of decades [10]. It is reported that the number of body panels on Ford vehicles using SMC grew from 250,000 in the 1990s to 2.5 million in 2002 [12]. Ford investigated the suitability of SMC for semi-structural applications on the Ford Explorer Sport Trac deeming the material suitable to replace steel. The SMC pickup box inner panel provided weight reductions, corrosion resistance, increased durability and a reduction in assembly parts [13]. GM explored applications for SMC to reduce the weight of a structural

transmission cross-member by increasing the materials glass composition to 50% wt. Mechanical design performance was met through modifying the geometric shape of the cross-member and a total weight saving of 56% was realised over a steel counterpart [14]. The 2003 Dodge Viper saw the first application of SMC using carbon fibre as reinforcement (A-SMC) in a body structure. With cure times between 1-3 minutes the process produces high performance structural components with the potential to exceed production volumes of 100,000 ppa [15].

The main competition for the use of CFRPs in high volume applications comes from high strength steel and aluminium; both of which benefit from established processes and lower material costs. Deployment of advanced composites requires a change in design philosophy but at the same time offers an opportunity to optimise existing structures. For example the design and manufacture of complex componentry with increased integration leads to part consolidation – reducing part count and assembly times over metallic alternatives. It is suggested that optimally designed, continuous carbon fibre composites can result in parts as much as 75% lighter than steel [16], 40% lighter than aluminium and 60% lighter than SMC equivalents [17]. In terms of raw material costs, for CFRPs to become viable for mass production in the automotive market, the price of carbon fibre needs to fall substantially from current levels (~$20 /lb). Significant research into alternative precursor material is taking place to reduce the manufacturing costs of industrial grade carbon fibre towards $5 - 10 /lb [6].

Toray Industries, a leading supplier of advanced composites, regards entering the high volume automotive industry a top priority. Development of a proprietary RTM based solution for CFRP components has reduced moulding cycle times from >80 minutes to 10 minutes [18]. Their partnership with Mercedes-Benz targets series production figures of between 20,000 and 40,000 ppa [19]. Recently the prospect of increasing the use of advanced composites in high volume markets has seen many mainstream manufacturers follow suit engaging in partnerships with composite material suppliers [20]. Current initiatives such as the HIVOCOMP project brings together a consortium of companies from different facets of the automotive industry with the unified goal of producing cost effective CFRP components. Both thermoset and thermoplastic based materials are being developed to cater for different performance and process requirements [21]. The development of a commercial automated production process

for low-cost carbon fibre components remains a high priority and an essential barrier to mass market.

1.1.4.2. Aerospace

Full composite airplanes first appeared during the 1970s in the form of small recreational planes recognising the high specific properties exhibited by FRPs and the ability to produce efficient aerodynamic designs [22]. Uptake in commercial aircraft was slow however, due to the knowledge gap for material failure modes and impact damage response [23]. Rising fuel prices and pressure from airline operators motivated manufacturers to begin replacing metallic secondary structures in large civilian craft with advanced composites by the 1980's; namely the Boeing 737 and Airbus A-320. The next decade gave rise to applications in primary structures including the empennage and main floor beams in the Boeing 777, and the centre wing-box and pressure bulkhead in the A-380.

Significant investment was poured into advancing composite manufacturing technology with the development of automated tape layup (ATL) and automated fibre placement (AFP) providing high levels of automation and repeatability. This led to an abandoning of traditional prepreg fabrics in favour of unidirectional tapes/tows - around 70% of structural composite components in modern aircraft use UD materials [24]. Other structural applications include the use of HexMC, a commercially available high performance carbon fibre SMC, for the first composite window frame installed in a commercial craft resulting in significant weight saving and superior damage tolerance compared to existing aluminium frames [25]. A major step in terms of aircraft design was taken with the current Boeing 787 Dreamliner utilising composites for ~50% of the total weight of the structure; aluminium and titanium accounting for the rest. The previous 777 aircraft consisted of only 10 - 12% of composite materials with aluminium structures dominating [26]. Airbus is to follow suit with the A-350 XWB where the fuselage and wing assemblies are manufactured entirely using composite materials.

Away from airframe componentry, advanced composites are increasingly finding applications within aero engines. Progress in manufacturing techniques means that engine fan blades can be made as aerodynamically efficient as titanium blades whilst

providing weight benefits [27]. For less demanding roles glass fibre composites are still used for a wide variety of applications such as radomes, body panels, flooring, engine cowlings and cabin interiors [23].

1.1.4.3. Marine

GFRP composites are used extensively in recreational, utility and commercial craft. Large scale structures and low volume production rates means that open mould wet lay-up is still common with little of the technological advancement seen in aerospace and automotive industries filtering through. Carbon fibre composites have found use in high end competition and military craft but are not generally used in commercial or leisure boats [28].

Even though the industry lags the automotive and aerospace in terms of composite technology, adoption of moulding techniques to streamline operations and reduce manufacturing costs is growing. For example, by switching to closed moulding processes the infusion of matrix for a 80 ft hull can be completed within an hour with the additional benefit of a significant reduction in consumables [29]. Economic pressures have also led to boat manufacturers reassessing their choice of base materials with examples of carbon fibre composite sandwich being used for primary structures in passenger ferries; replacing traditional glass fibre materials [30].

As was the case with aerospace and automotive industries, the niche and high performance part of the sector was the first to adopt CFRP, demanding high specific properties without the cost restraints that impair the transition to commercial applications. However, production boat builders such as Sunseeker are now using carbon fibre prepregs for primary structures observing 75% weight savings over GFRP versions through efficient design [31]. Fire safety regulations have so far restricted use of advanced composites in large boat and ship construction but advances in fire resistant epoxy resin systems are tackling this issue. There remains a large scope for adopting such materials for larger vessels in the future where fuel economy is an ever increasing concern for operators.

1.2. Automating production of composite parts

1.2.1. Driving forces

The benefits of automating manufacturing processes are clear; reduced manual labour, reduced intra-part and inter-part variability and the potential to significantly increase production rates. The aerospace industry has been instrumental in applying automation to advanced composite fabrication with commercial ATL machines being made available in the 1980s. This mature technology offers 70 - 85% reduction in personnel hours over hand lay-up and high deposition rates for large structures (over 1000 kg per week) [32]. The automotive sector still uses labour intensive manufacturing techniques however, particularly for advanced composites, where automation is essential for these materials to break into the mass market. Robotic systems can be used for the fabrication of tool plugs and composite parts, finishing duties and quality control whilst providing scalability and process flexibility [33]. Advances in software control and the ability to perform off-line programming also increases productivity and reduces production down time [34, 35].

1.2.2. Established processes

ATL and AFP technologies are used extensively in the aerospace industry for fabricating load bearing structures using UD prepreg materials. ATL is the more mature process best suited to relatively flat planar surfaces, such as wing skins and empennages, with difficulties arising from double curvature surfaces causing gap, over-lap and buckling issues weakening the laminate [32, 36]. UD tape (75 - 300 mm wide) is laid up as plies oriented to maximise material properties in the loaded direction with compaction and tape slitting operations controlled on-board the tape head enabling near net-shape panels to be formed. Once the charge is formed the composite panel is then cured in a separate process.

To process more complex 3D geometries AFP machines were developed using narrow prepreg tows which can be steered over sharply curved surfaces without buckling. When used with a rotating tool or mandrel, AFP more closely resembles filament winding, though the use of tows tends to make it a faster process with significantly

less waste [37]. Current advanced AFP machines can lay up to 32 tows simultaneously via programmable 7-axis robotic systems. Applications include wing sections for the military F-35 joint strike fighter and monolithic fuselage sections for the Boeing 787 [38]. Tow laying speeds have increased substantially over the last decade with current manufacturers advertising speeds of up to 2000 inches/min. The increased deposition rates have necessitated integration with process modelling techniques to drive high-precision machine programming using products such as FibreSIM®. 'Contact' processes such as ATL and AFP involve complex robot kinematic path planning to ensure the pressure provided by the compaction roller always acts normal to the tooling surface. It has been shown that a non-linear relationship exists between part quality and compaction force requiring careful planning to stay within a 'sweet' spot [39]. High capital investments in equipment, including autoclave curing, and their applicability to relatively large simple component designs mean that these processes are confined to aerospace however.

The potential for high speed, high performance composite manufacture necessary for the automotive market comes in the form of either Advanced SMCs or LCM processes using advanced preforming techniques. Cure times for A-SMCs are very low (1 - 3 minutes) but require large expensive presses and some form of automation for placing the charge, extraction and final trimming. The compression flow process also inherently suffers mechanical performance knockdowns compared to using preforms and LCM.

Automated methods of preforming are generally achieved through directed fibre preforming (DFP). Programmable Powder Preforming Process (P4) is an early example of automated DFP using glass reinforcement; later derivatives adapted the process for use with carbon fibres. P4 utilises low cost raw material in the form of glass fibre rovings/tows (bundled filaments) providing a 40% reduction in raw material costs over preforms constructed with continuous strand mat (CSM) [40]. Rovings are chopped to length through an applicator head and sprayed onto a perforated tool along with a polymeric binder. The chopped segments are held in place under vacuum created by evacuating air from underneath the tool. Once the spray stage is complete the tool is placed into an oven to dry and activate the binder. Preforming can take 4 minutes for a full scale automotive structure and a further 4 minutes for resin infusion using SRIM; opening up the possibility of production rates

close to 50,000 ppa [41]. Demonstrations investigating the potential of automated DFP processes reported 48% cost savings over a prepreg baseline [42]. A P4 derivative, F3P, provides offline robotic programming and advanced chopper gun technology along with other machine and process improvements such as a robotic track adding a 7th axis. High deposition rates (4 kg/min) with scrap rates of less than 1% are reported [43, 44].

A thermoplastic variant using commingled glass yarns, P4-TP, was demonstrated to compete with processes such as GMT and D-LFT [8, 45] where high deposition rates of around 12-15 kg/min were achieved using multiple tows and upgrading the processing speed of the deposition device. To achieve even higher mechanical properties suitable for structural applications in the automotive and aerospace industries, the P4 process was adapted to utilise carbon fibre reinforcements. Further details of discontinuous carbon fibre preforming (DCFP) and the current University of Nottingham DCFP facility is found in Section 1.3.

Another carbon fibre preforming technology 3-DEP is aimed at high volume manufacture (~60,000 ppa) using vacuum extraction to retain fibres within a slurry (carbon fibre / water) [46]. Despite offering high levels of repeatability in terms of part-to-part mass variation, fibre volume fractions of only 17% are achievable making it unsuitable for structural components.

1.2.3. Moulding developments

Most of the recent technological advances in composite moulding have been concerned with reducing costs and cycle times. For low to mid volume production there has been significant development for OoA curing. Plasan has introduced a hybrid OoA process reducing the curing cycle time down to 10 minutes with an ultimate target of 2 minutes through the development of an advanced fast-curing resin matrix enabling production of CFRP parts in volumes of 30,000 – 50,000 ppa [47]. For higher volume production rates; compression and injection moulding processes dominate for non-structural components offering very short cycle times (<3 minutes) at the cost of mechanical performance. Flow orientation and skin-core reinforcement orientation distributions significantly affect mechanical properties, especially when substructures (ribs, bosses, fittings etc.) are present [7].

For these reasons liquid moulding processes such as RTM, VaRTM and SRIM are commonly used for structural applications where a greater control of the reinforcement material in terms of orientation and mass distribution is necessary. Despite the popularity of using prepregs for demanding applications, liquid processes such as these are increasingly being investigated as an alternative [36]; particularly in the automotive sector. The lack of a high speed low-cost preforming process has generally inhibited their usage in high volume markets but advances towards net-shape highly automated preforming means that they are being reconsidered [48]. SRIM commonly uses a polyurethane resin system offering fast cure times (1 - 3 minutes) whereas epoxies are typically used for RTM providing higher mechanical properties with longer infusion times due to higher matrix viscosities [49]. A combination of P4/SRIM is already employed for fabricating pickup truck boxes at a rate of one every 4 minutes [50].

Other liquid moulding developments geared towards mass market automated manufacturing include Compression RTM and High Pressure RTM. In the former process, resin is introduced into a partially closed tool flowing over the preform before being compressed at high pressure to achieve through thickness impregnation [51]. The latter process, which has been adopted by BMW for the upcoming i3 electric vehicles, upgrades the conventional RTM equipment with high pressure mixing (>120 bar) and dosing apparatus. The use of low viscosity resin systems can further reduce fill times. Both processes have produced high volume fraction (>45% V_f) laminates using non-crimp carbon fibre fabrics with total injection and cure times of ~5 minutes [52]. With current development towards low cycle time moulding techniques, the need for a high speed preforming process (such as DCFP) becomes ever more important to reduce overall cycle times for high volume manufacturing.

1.3. Discontinuous carbon fibre preforming

The DCFP process offers a solution for mid to high volume production of high performance structural composites parts. The process is an advanced automated preforming technology used in conjunction with LCM techniques such as RTM and SRIM. Chopping of carbon tows into short bundles of fibre (typically between 3 mm to 200 mm in length) facilitates various means of automation of the costly manual

layup stage typically required in advanced composite manufacture. Figure 1-1 shows the main stages of preform manufacture for DFP processes consisting of reinforcement deposition, preform consolidation, stabilisation and extraction to the moulding station. The work presented in this thesis is based around the development, characterisation and process modelling of the University of Nottingham DCFP facility.

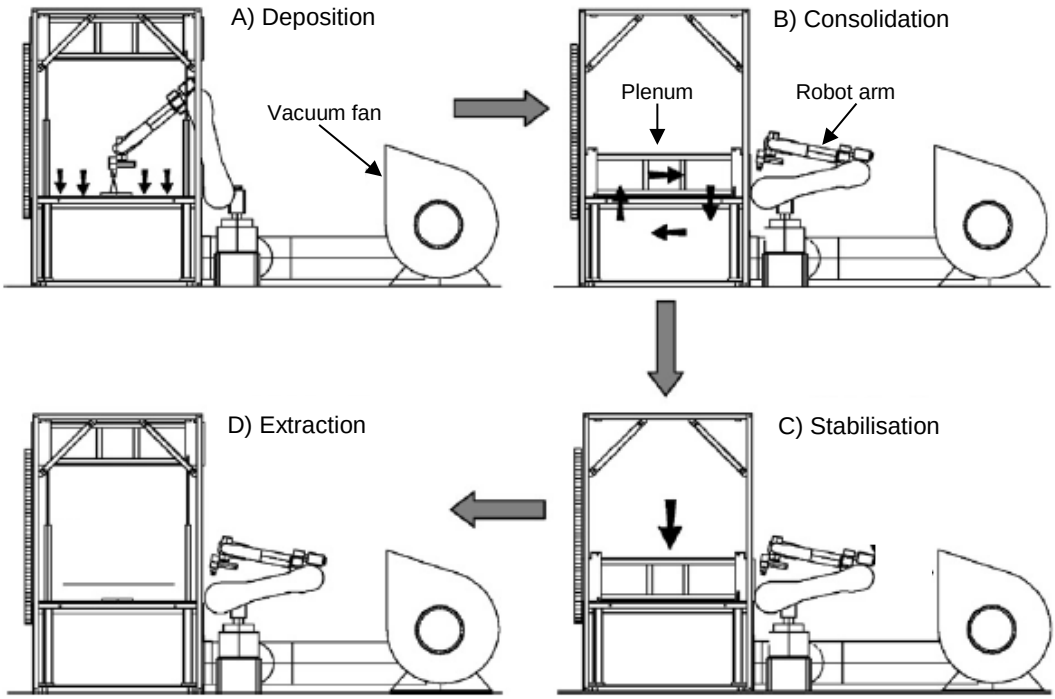

Figure 1-1: A schematic diagram showing the four main stages in directed fibre preforming. Image is taken from [53]. (A) Deposition stage involves applying reinforcing fibre with powdered binder to the preform screen whilst under vacuum. (B) The plenum is lowered applying pressure to the fibre stack with heated air cycled through the stack thickness to activate the binder. (C) Once the binder has cured, cool air is passed through the preform to stabilise prior to extraction (D).

1.3.1. Summary of previous work

Previous DCFP process development identified the need for an improved chopping device specifically designed for carbon tow forms instead of a modified apparatus used in glass fibre preforming (P4/F3P). Inter-preform variability was deemed excessively high (~15%) and additional features such as a tow filamentisation chamber (filamentisation is discussed in detail in Section 2.1.6) and a fibre alignment device were required to conduct a thorough investigation into the influence of microstructural process parameters on the mechanical properties of DCFP composites [53-55].

1.3.1.1. Factors influencing mechanical properties

The following microstructural parameters were investigated: laminate thickness, tow filamentisation, fibre length and fibre orientation. Additionally, the effects of spray path design, chopping device standoff distance and linear robot speed were also examined.

For random fibre architectures, laminate thickness (target areal density) was found to be the most significant variable with a dramatic improvement in mechanical properties as laminate thickness increased. High levels of tow filamentisation and short fibre lengths provided low areal density variation across preforms improving laminate performance; further aided by using slow robot speeds and high chopping apparatus standoff distances. A detailed review of the process and material parameters is provided in Chapter 2.

1.3.2. Machine modifications

1.3.2.1. Previous limitations

Whilst the previous iteration of the DCFP deposition head overcame many of the issues experienced with processing carbon fibre, a number of limitations existed which were addressed in the current design developed for the work presented in this thesis.

A process optimisation study concluded that a slow robot speed (~200 mm/s) and a high standoff distance (300 mm) were required for satisfactory fibre coverage. Preform areal density variation was also improved by up to 30% when processing a single tow of 24K fibre over two robot path layers rather than two tows over a single layer. These findings severely affected deposition rates (<0.5 kg/min). Whilst the UoN facility is a research-scale installation it is still desirable to achieve representative deposition rates (≥2 kg/min) which are scalable for commercial implementation.

The previous deposition head passed chopped fibres through an airmover and diffuser (Figure 1-2) which gave rise to inherent filamentisation of tow segments which was seen to be beneficial for fibre coverage but detrimental in terms of preform loft and permeability [55]. Preform loft is the thickness of the unconsolidated preform where

increasing levels of loft require higher compaction pressures during the consolidation phase, potentially affecting press selection and process costs. Preform permeability, which determines the resin impregnation process, was also seen to noticeably decrease as tow segment diameter decreased (increase in filamentisation) which has a significant impact on moulding cycle times and repeatability. If automated DFP processes are to emerge in higher volume markets for structural component manufacture then increasing moulding cycle times must be avoided.

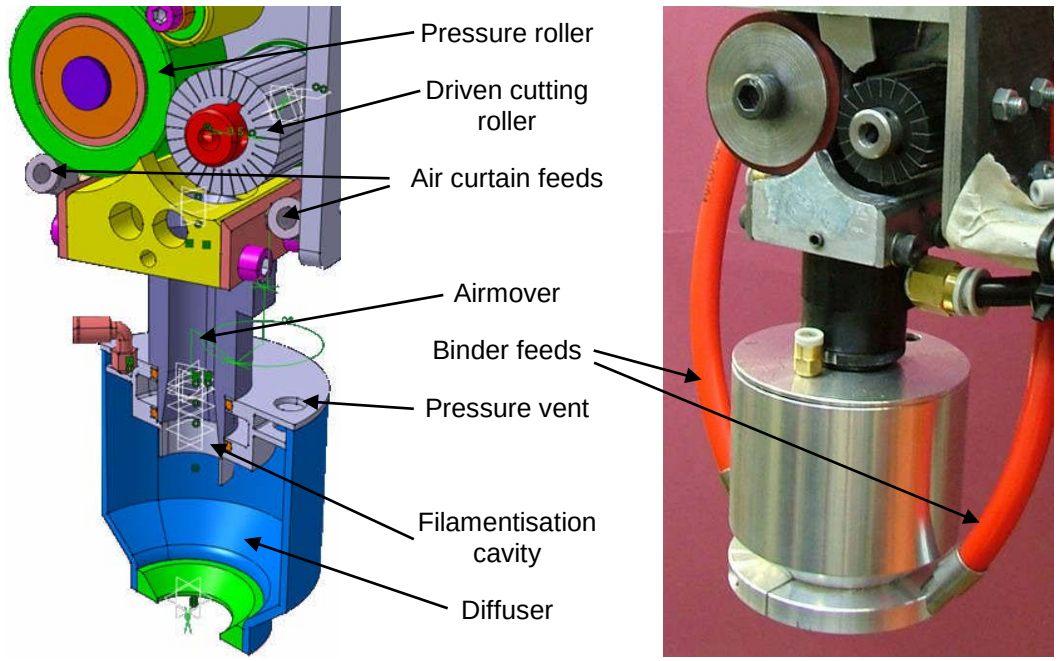

Figure 1-2: CAD diagram and photograph of previous iteration of the UoN DCFP deposition head. Image taken from [56].

A method for aligning chopped segments was also developed to extend the mechanical performance envelope for DCFP [54]. An alignment concentrator was fitted below a revised air-curtain attachment with a narrow slot to align the ejected segments with the deposition head orientation (Figure 1-3). A significant increase in tensile properties was achieved but at the cost of deposition rate and cycle time. Tows passing through the deposition head prior to the airmover attachment have high levels of induced alignment which are then diminished by passing into an unconstrained region at the top of the concentrator before being later re-aligned at the rectangular exit slot. Allowing the fibres to rotate before reaching the bottom of the concentrator contributed to excessive fibre blockage, particularly at high fibre speeds. Because fibre speed is proportional to robot speed (to encourage homogenous fibre coverage)

only very slow robot speeds could be used (~100 mm/s) restricting the maximum deposition rate to 0.12 kg/min for reliable operation.

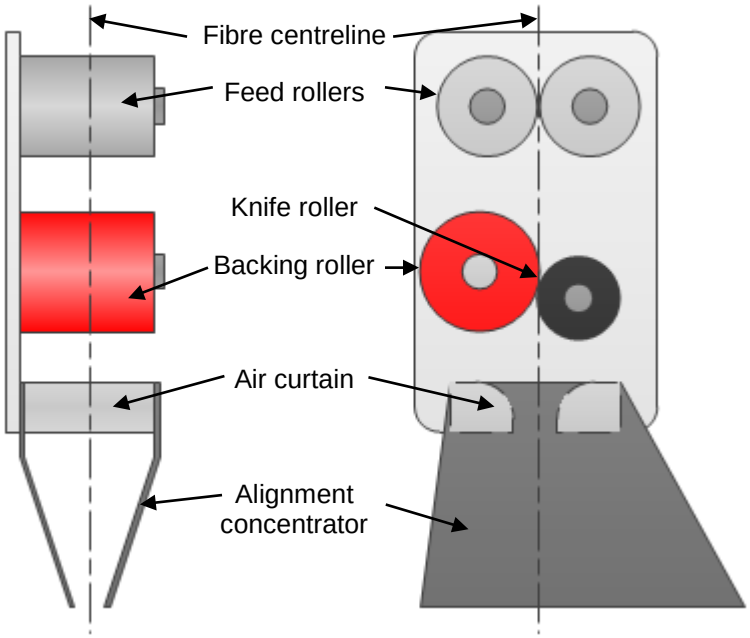

Figure 1-3: Schematic diagram of the alignment concentrator design used in previous studies.

1.3.2.2. Current DCFP deposition head

The current deposition head developed during the course of this thesis is shown in Figure 1-4 with the principle design goals of increasing deposition rate for both random and aligned preforming whilst maintaining segment integrity. The following outlines the current deposition head features:

- Ability to process 4 x 24 K tows individually.
- Breaker bar introduced between feed rollers and chop rollers to constrain the motion of carbon tows prior to chopping.
- Improved alignment concentrator constraining segments immediately after being chopped.
- An increased chop roller diameter of 180 mm expanding the range of possible fibre lengths to 12 (previously 7).
- Tool centre point (TCP) is located further away from robot wrist offering greater 3D spraying flexibility.

- Larger deposition device body to accommodate additional apparatus such as a veil chopper or an experimental resin spray system.
- Self-constraining feed pressure roller to ensure positive clamping forces irrespective of how many tows are being simultaneously processed.

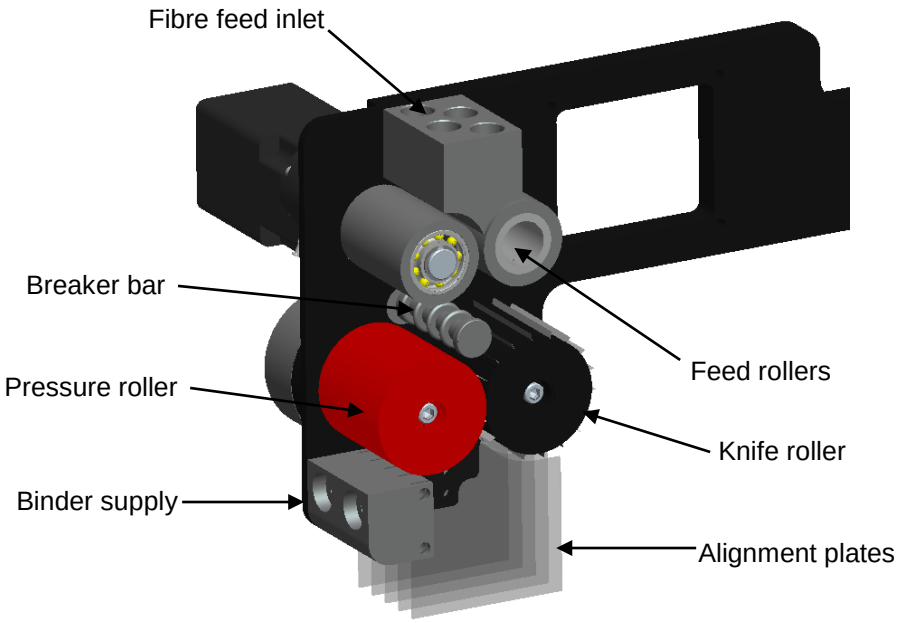

Figure 1-4: CAD diagram of the current UoN DCFP deposition head with fibre alignment concentrator attached.

The increased tow processing capacity ensures that a deposition rate of over 2 kg/min is achievable at fibre speeds of 5 m/s with an effective spray path width of ~50 mm. The alignment concentrator attachment constrains each fibre stream separately therefore reducing the risk of blockage and achieving deposition rates comparable with random spray (>600% improvement in deposition rate over the previous alignment method). The head is still required to pass over the tool surface as close as possible however to minimise the distance and therefore opportunity for tow segments to become misaligned for oriented fibre deposition.

1.3.2.3. Preform heating

The graphical user interface (GUI) and underlying programmable logic controller (PLC) code was redesigned to increase the functionality of the DCFP cell. One of the main improvements was the automation of the preform consolidation phase. An oven was installed to supply and circulate heated air within a closed system once the

plenum is lowered to compact the deposited fibre stack. The lowering of the plenum and initiation of the preform consolidation stage is automatically triggered once the spray routine is complete. Gates in the heated air circuit open and hot air is circulated by fan through the compacted preform. Thermocouples located close to the preform monitor the air temperature feeding data to a time-temperature dependant function which ascertains whether the binder has cured. The time-temperature function is based on the curing characteristics of the powdered binder (Reichhold PRETEX 110) and optimised through experimental trials. Oven temperature is monitored using thermocouples located on the heater fins and close to the oven outlet and controlled to supply a constant temperature across the preform. Once the binder has activated, the consolidation phase is completed by closing the heated air circuit and using the vacuum fan to force ambient air through the preform to cool before transferring to the moulding station.

1.4. Theme of work

The flow of work presented in this thesis reflects the development of a realistic fibre network model which simulates key DCFP process operations. The intention of developing the proposed model is to facilitate the uptake in processes such as DCFP for mid-high volume applications. By simulating 3D fibre preforms and predicting the potential part performance; the model would fulfil the role as a design tool to optimise composite structures using DFP processes.

Chapter 2 consists of a literature review exploring two key areas of research; the performance of DFP composites and current process modelling techniques. The wide array of process and material input parameters available in DFP processes offers manufacturing versatility with a compromise usually required between costs (material, initial capital), composite performance, production volume and component complexity. A detailed understanding of the effects of key parameters on processability and final composite performance is therefore essential. The current techniques for modelling random discontinuous fibre architectures are also addressed. A shift towards numerical based analysis away from traditional analytical methods means that true stochastic fibre networks created using DFP processes can be modelled to capture mesoscale interactions and macroscale variability.

Details of the base materials used to manufacture DCFP tensile specimens for experimental testing, specifically the carbon fibre tow specifications and resin system, are outlined in Chapter 3. Experimental methodology for preform manufacture and mechanical testing is also provided.

Characterisation results from studies focussing on fibre spray are presented in Chapter 4 along with a modelling methodology. The influence of the current UoN DCFP deposition head is examined along with key process parameters within typical operating ranges used for preforming. Fibre segment distribution and orientation relative to the deposition device is of particular interest. A further study aims to model fibre flight motion using a semi-empirical kinematic model.

Preforming technologies typically hold material in place by means of vacuum retention until consolidated into the shape of the final part. However, little knowledge exists on the sizing of the vacuum installation and subsequent retention performance of preformed structures. The retention characteristics of DFP type materials are investigated in Chapter 5 along with other common preforming materials including woven and non-woven mats.

Chapter 6 presents the proposed modelling approach to simulate DFP processes in order to recreate realistic macroscale fibre networks for three-dimensional component geometry. The process software draws upon characterisation data acquired in Chapter 4 to accompany a robot kinematic model to simulate fibre spray based on the same input parameters required for the UoN DCFP facility. An example of the proposed iterative optimisation procedure is provided based on the quality of macroscale preform mass variation. A finite element analysis interface is also presented for mechanical property prediction of the final composite part.

Validation of various model subsystems is performed in Chapter 7 using empirical data obtained via the UoN DCFP facility. The current alignment concentrator detailed in Section 1.3.2.2 is also characterised by mechanically testing manufactured specimens in order to assess the material properties resulting from high speed aligned deposition. The mechanical testing data is subsequently compared to FEA output for simulated aligned preforms created using the process model software.

Chapter 2. Literature review

In this chapter, existing publications relating to discontinuous fibre composites and directed fibre preforming are discussed. The review is divided into two sections; a discussion of microstructural parameters affecting composite performance, and an overview of current modelling strategies concerning DFP processes in particular. Characterising discontinuous fibre composites is challenging due to complex interactions between material and process parameters, therefore a clear understanding of their effects on laminate performance and manufacturing processability is essential.

2.1. Performance of DFP composites

2.1.1. Effect of fibre length

A considerable amount of research has been conducted into modelling the effects of fibre length in discontinuous fibre composites [57-61]; particularly for short fibres (<6 mm) often used in flow moulding processes. Analytical models using shear-lag analysis and micro-mechanical based approaches have been adapted to account for varying fibre lengths in an attempt to accurately predict mechanical properties. To maximise tensile performance, fibre lengths are required to exceed a critical length (a function of fibre diameter) to achieve full stress transfer from matrix to reinforcement preventing interfacial shear failure. For a perfectly aligned discontinuous fibre laminate, 90% strength retention of a continuous fibre laminate can be achieved by utilising a fibre length 5 times greater than the critical length [62]. Calculating the critical length for fibre architectures created using DFP processes is non-trivial however due to the reinforcement taking the form of bundled filaments giving rise to a mesostructure within the laminate. Although chopped segments behave as large diameter single fibres, their cross-sections are usually non-circular meaning that bundle dimensions should be considered in determining critical lengths [63-65]. Harper et al. [66] experimentally observed critical length effects for 3 mm fibres using 24 K carbon fibre tows which resides at the lower end of the DCFP operating range.

This correlated well with critical length values derived using slip-theory and through consideration of intrinsic segment fragmentation which occurs at short fibre lengths reducing bundle size.

The strength of discontinuous fibre composites is strongly correlated to reinforcement length where a trade-off exists between fibre length and the number of fibre ends present in the laminate. Individual filament strength is dependent on the existence of fatal flaws along its length and can be described using a Weibull distribution where tensile fibre strength reduces with length [59]. This is due to the higher probability of containing a critical flaw as length increases. Attempting to negate this effect by utilising shorter fibres presents other problems however. For a constant global fibre volume fraction; decreasing fibre length results in a greater amount of fibres and fibre ends present in the laminate. This increases the number of stress concentrations and areas prone to matrix micro-cracking which can lead to the onset of component failure [67]. Wetherhold [68] developed a probabilistic strength model using the idea of a critical fracture zone where the composite strength is governed by the strength of fibre bundles bridging this failure zone; composite strength in this case increases asymptotically with fibre length.

Masoumy et al. [67] isolated the effects of fibre length, expressed as bundle aspect ratio, on mechanical properties for highly aligned glass fibre specimens at 50% V_f. By increasing the bundle aspect ratio from 50 to 557, stiffness retention improved from 82% to 99% of a UD continuous laminate. Tensile strength was found to be significantly lower than the continuous case however; retention increasing from 26% to 59%. Typically the strength of a discontinuous fibre composite reaches a plateau as the aspect ratio becomes sufficiently large. This has been observed both experimentally and through the use of analytical models [68-71].

Feraboli et al. [25] investigated the effects of fibre length on a random discontinuous composite comprising of unidirectional carbon fibre prepreg tape cut into ‘chips’. Although only limited testing data was attained, significant gains in composite strength was achieved by increasing fibre length from 12.8 mm to 76.2 mm. Tensile strength increased linearly with chip aspect ratio - defined as chip length divided by chip width. No plateau in strength occurred over the dimensions tested suggesting that the critical chip length had not yet been reached. This was further supported after

examining micrographs of failed specimens showing chip pull-out rather than filament fracture. Tensile modulus appeared to be insensitive to aspect ratio but in close agreement with calculated quasi-isotropic values suggesting that a critical fibre length for modulus exists below the tested range. Similar results were observed by Harper et al. [66] where tensile modulus was independent of fibre length through the range of 3 mm to 115 mm. Segment fragmentation meant that fibre length effects could not be studied in true isolation however.

An important consideration for liquid moulding processes such as RTM is preform permeability, which is entirely dependent on fibre architecture. Umer et al. [72] found that in-plane permeability consistently improved through the use of longer fibre lengths in chopped yarn preforms. Increasing lengths from 15 mm to 50 mm resulted in improvements in permeability of between 21% and 25% for different yarn diameters at 40% V_f. Dockum and Schell [73] suggested using a minimum length of 50.8 mm for preforms consisting of low filament count glass tows to aid resin flow using the SRIM process. A limit does exist however, with large fibres (>90 mm) leading to undesirable effects such as folding and distortion during the preforming stage. Fibre distortion both in and out-of-plane is also more likely to occur for longer fibre lengths during resin transfer. This is particularly detrimental to compressive strength with a dramatic reduction in mechanical properties observed for excessive fibre waviness [74]. For processes such as P4-TP, which targets rapid cycle times using compression moulding, shorter fibre lengths are found to be beneficial in enhancing compression flow characteristics [75]. This could be desirable for instances where difficult-to-preform features (ribs, lips etc.) are required but only achievable by allowing reinforcement to flow during the moulding stage. Furthermore, process repeatability can be negatively affected using longer fibre lengths with increased part-to-part coefficient of variation (CV) in mechanical performance observed using the 3-DEP slurry process [46].

Fibre length is also a prominent variable for random fibre structures investigated for crash applications. Jacob et al. [76] looked at the effect of three microstructural parameters (tow size, fibre length and volume fraction) on specific crash absorption. Although the effects of tow size and volume fraction were inconclusive (due to dependencies on the other process variables) a clear trend presented itself where shorter fibre lengths improved crash worthiness. The findings are supported by other

studies showing a similar trend for specific energy absorption performance over a broader range of fibre lengths (30 mm to 90 mm) [45, 77]. Varying fibre length can be a useful mechanism for increasing composite toughness through the use of sub-critical lengths to encourage fibre pull-out.

It is clear that fibre length or aspect ratio should be chosen based upon design objectives with the challenge of optimising between preform processability and permeability, mechanical performance and crash worthiness.

2.1.2. Effect of tow size

Previous studies have focussed on utilising low cost, high filament count carbon fibre tows (12 K – 48 K) to increase the attractiveness of preforming technologies for structural applications [65, 78, 79]. In reality the cost of carbon fibre is highly sensitive to market forces making it difficult to distinguish the true long-term cost savings over the use of smaller tow sizes. It is believed that a significant financial benefit does still exist however. Commercial-grade large tow carbon fibres (48 K – 320 K) are being made available which can be produced more cheaply than smaller form aerospace-grade tows – taking advantage of cost efficiencies during the manufacturing process [80]. Typical tow sizes used for carbon DFP processes reside within the smaller form range (0.5 K – 48 K) with the larger tow sizes carrying a distinct advantage for increasing potential fibre deposition rates – an attractive prospect for a technology aimed at high volume production. Unfortunately, larger tow forms are found to negatively impact composite performance [65, 81-83].

Early attempts to understand input parameters which influence the mechanical performance of discontinuous fibre composites have shown that processing lower filament count tows is beneficial. Schell and DiMario [81] attribute a ~20% increase in tensile strength to halving the glass roving filament count providing greater reinforcement surface area for matrix bonding. Preliminary adoption of carbon fibres for the P4 process used bundle sizes of 3 K and 6 K (several times larger than typical glass rovings) resulting in large variations in material distribution throughout the preform when compared to the equivalent glass fibre process. By analysing the light transmission characteristics of preforms at different areal densities it was found that the effect of reducing tow size improved fibre coverage and hence preform quality

[82]. A more comprehensive subsequent study using tow sizes ranging from 0.5 K to 12 K concluded that low filament count bundles provided significant gains in both mechanical and thermal performance with an average increase in tensile strength of almost 200% [83, 84]. CV for tensile properties reduced by at least a factor of 3 indicating improved preform homogeneity.

Rondeau and Reeve [65] reasoned that the reduction in mechanical properties for architectures using larger tow forms is due to the increased occurrence of synchronised filament ends giving rise to greater stress concentrations. This significantly impacts tensile strength and is particularly apparent for directionally biased depositions where the probability of synchronised segment ends amplify stress concentrations even further. The study also reinforced concepts previously suggesting that a critical tow segment length exists as bundled fibres behave as large diameter single fibres. This phenomena can be observed where different failure modes existed depending on varying bundle size within the same coupon where larger bundles were prone to matrix pull-out [85].

Efforts have been made to mitigate the apparent drawbacks of using larger tow forms whilst still retaining their cost-effectiveness. Dahl et al. [86] used tow splitting apparatus to reduce large tows (80 K) to multiple instances of low filament count tows (1.5 K, 2.5 K & 3 K) specifically for the P4 process. Using mechanical splitters and fibre sizing operations on an intermediary production line, sufficient amounts of fibre was converted for preforming and subsequent mechanical property analysis. Despite the smaller tow forms the mechanical performances for all three tow sizes were marginally inferior to a commercially available 3 K control roving. Whilst the findings were contradictory to popular consensus it was speculated that the sizing operation was sub-optimal and required further development. It is also not clear how the inclusion of this intermediary production phase would impact the cost-effectiveness initially sought by using the 80 K tow.

Harper et al. [55] presented a solution to reducing bundle size by pneumatically disrupting chopped segments prior to exiting the deposition head, known as fibre (or tow) filamentisation (the effects of which are further discussed in Section 2.1.6). Clear improvements in mechanical performance were realised but with undesirable effects such as increased preform loft (affecting achievable fibre volume fractions) and

reduced preform permeability. The latter is an important consideration for LCM processes affecting overall production cycle times. Permeability is determined via inter-tow and intra-tow porosities and despite the shortcomings of using larger tows they have been observed to be beneficial when moulding large structures [87]. Preforms using higher filament count bundles produce a more porous and open structure aiding resin impregnation.

2.1.3. Fibre volume fraction

The mechanical properties of a composite laminate are heavily influenced by the level of reinforcement content present. Random discontinuous fibre laminate stiffness has been experimentally proven to obey a linear relationship with fibre volume fraction up to values of 50% V_f which can be accurately predicted using simple statistical ROM models [56, 88, 89]. Tensile strength generally exhibits a similar relationship [56, 90, 91], however micromechanical failure mechanisms can result in a more complex non-linear relationship [88]. It is suggested that an upper limit of 40% - 50% V_f exists for random discontinuous fibre architectures and 55% - 60% V_f for highly aligned architectures (matching typical high performance continuous fibre composites) before processing difficulties begin to impair mechanical performance gains [65, 92, 93].

Increases in fibre content significantly impact preform permeability requiring elevated injection pressures for moulding processes which can have detrimental effects on final composite performance. For higher injection pressures fibres are susceptible to movement within the mould cavity causing variations in volume fraction and increasing the risk of inducing fibre waviness. A higher binder content could be used to maintain preform integrity but Dockum and Schell [73] found that this can negatively impact laminate performance. There is also an elevated risk of failing to achieve full preform wet-out leaving dry areas of reinforcement and increased void content; compromising the performance and repeatability of the moulded part.

Dahl et al. [43] studied the compaction characteristics of random glass fibre preforms manufactured using the F3P process over a wide range of fibre volume fractions (15% - 45% V_f). Compaction pressure increased exponentially with fibre content for two distinct preform architectures. For structural preforms, a 900% increase in pressure was observed when increasing fibre volume fraction from 32% to 44% to achieve the

required 3 mm preform thickness. Harper [56] reported similar findings for DCFP manufactured preforms using a power law model to describe preform compaction characteristics.

2.1.4. Preform homogeneity

Arguably the most important characteristic influencing the mechanical performance of a discontinuous fibre composite is the degree of preform homogeneity [53, 65, 94-96]. By reducing intra-part mass variability, confidence in characterising and predicting the mechanical response of such fibre architectures increases. For DFP processes, preform homogeneity is governed by several process variables adding to the challenge of designing and manufacturing high quality parts. It is well documented that microstructural parameters such as tow size and fibre length have significant effects on areal mass variation [55, 66, 97]. By reducing tow size and fibre length an increase in fibre segment count is required to achieve a target volume fraction. The introduction of a greater amount of fibre segments encourages improved fibre distribution resulting in a lower intra-preform CV for reinforcement mass. The inclusion of more segments could also be beneficial to failure response from crack propagation. Han and Seigmund [98] presented simulation results using a discontinuous crack growth model to show an improvement in composite failure response for random fibre material. Interestingly, the macroscopic preform permeability is seen to be independent of filament count and bundle length for DCFP preforms [99]. These two material parameters do affect flow characteristics however with larger tow sizes and fibre lengths leading to increased flow unevenness.

Individual segment location within the preform is dictated by the spray process, spray path trajectory, effectiveness of fibre retention and tool geometry. Previous DCFP simulation models have suggested significant improvements in mass distribution across the preform can be attained using orthogonal spray patterns as opposed to a parallel offset pattern [66]. A simulated reduction of 30% in mass variability for a 2D plaque shows the potential benefit of using such process models; particularly for 3D geometries where achieving homogenous coverage is challenging. Initial P4 design specifications set intra-part areal density variations of ±12% as limiting bounds for the

preforming process [40, 97], however, a tighter tolerance is desirable for high performance structural applications where high fibre volume fractions are required.

The intrinsic heterogeneity in discontinuous fibre architectures is highlighted by Feraboli et al. [25] where on average a 50% increase in tensile modulus and strength was achieved through increasing specimen thickness from 2 mm to 6 mm. The significant rise in mechanical performance is highly likely to be a result of improved fibre mass distribution. Thin laminates tend to exhibit inferior mechanical properties due to unreinforced resin rich areas as a consequence of poor fibre coverage.

2.1.5. Fibre alignment

A great deal of work has been conducted to identify fibre orientation distributions in discontinuous fibre architectures to incorporate into analytical models in an effort to improve mechanical property prediction [63, 100-102]. Significant gains in laminate performance are possible by aligning fibre reinforcement in the direction of applied load. For DFP processes the opportunity to tailor laminate performance through fibre alignment paves the way for adoption in semi-structural and structural applications. Aligning fibres is also conducive towards achieving higher fibre volume fractions due to increased packing efficiency compared with random fibre networks [42, 103].

Pneumatic methods adopted in glass mat-reinforced thermoplastics (GMT) used alignment plates to deflect glass strands from a delivery tube during preforming [104]. A relatively wide fibre orientation distribution was experienced however when compared with the much slower hydrodynamic method, once used for prepreg materials. A similar deflection technique along with various fibre orientation devices were developed for the P4-A process where 90% stiffness retention and 50% strength retention was achieved compared to an equivalent continuous fibre composite (normalised to 55% V_f) [42, 105]. Longer cycle times were required compared to random fibre deposition but specific design and performance details for the alignment device were not presented by Reeve [105]. The alignment technology was demonstrated by incorporating aligned fibres into a preform over a three-dimensional complex C-Channel tool. Maintaining levels of alignment proved to be challenging however, particularly on vertical surfaces and subsequently abandoned.

Previous DCFP machine developments for aligned deposition involved mechanically aligning chopped fibres through a concentrator (see Section 1.3.2.1). Harper et al. [54] achieved high levels of alignment particularly for long fibre lengths and high filament count tows (115 mm, 24 K) where 94% of the fibres were aligned within ±10º to the intended direction. The increased segment weight is thought to supress the likelihood for segments to become misaligned as they fall from the concentrator. Specimens containing 24 K reinforcement also showed the largest gain in mechanical properties over the equivalent random fibre benchmark, with increases of 206% and 234% for tensile stiffness and strength respectively. The highest attainable properties were achieved using 115 mm, 6 K tows with absolute tensile stiffness and strength values of 71 GPa and 444 MPa respectively. This represented an increase of 10% and 40% over the 24 K specimens. A major drawback of this method was a substantial increase in cycle time to ensure high levels of alignment. The linear fibre speed was reduced to match the robot travel velocity limiting the deposition rate to 0.15 kg/min for two 24 K tows compared with >1 kg/min for random deposition.

2.1.6. Fibre filamentisation

Filamentisation of fibres, the segregation of fibre bundles into smaller bundle sizes, can occur naturally through the mechanical chopping action in DFP processes. It is particularly likely to occur for high filament count rovings (≥12 K) where bundle integrity diminishes once chopped to length leading to a distribution of bundle sizes [55]. The variation in bundle size within a composite mesostructure further complicates established property modelling techniques making prediction of final laminate performance challenging. Filamentisation can also be deliberately induced via additional processing techniques such as pneumatic interference [87] and mechanical separation via breaker bars or rollers [106].

The benefits of using small filament count tows have already been discussed in Section 2.1.2 which includes improved reinforcement mass distribution and lower intensity stress concentrations arising from synchronised filament ends. Harper et al. [55] investigated the feasibility of reducing large filament tows to smaller bundle sizes using a pneumatic device as a means of improving composite performance whilst retaining the cost-effectiveness associated with large tow sizes. Significant

improvements in mechanical properties for 24 K fibres was realised with gains of 13% and 55% in tensile stiffness and strength respectively. This was achieved using the maximum filamentisation processing available and supported findings from other studies [107].

An undesirable consequence of filamentising chopped fibres is the increase in preform loft. The presence of more single filaments and small fibre bundles results in thicker preforms which in some extreme cases lead to unacceptable levels of loft post-compaction. Preforms made from highly fragmented 24 K segments also exhibited significant reductions in preform permeability for resin injection processes, increasing mould fill time [99] and leading to longer preforming cycle times [66]. This is particularly important for a technology aimed at mid-to-high volume production where low cycle times are necessary for both preforming and moulding stages. A compromise is clearly required between preform processability and the potential for improving mass variability.

Highly filamentised fibres are also used in veil type mats to produce a ‘class A’ surface finish by encouraging a resin rich layer [44, 87]. There is evidence to suggest that the introduction of a surface veil in a non-filamentised preform decreases permeability and increases required compaction pressure [43] which correlates with experimental results for filamentised preforms.

2.2. DFP process modelling

Rapid cycle times and near-net shape preforming are attractive qualities of DFP processes yet adoption in industry remains subdued. There is still very little published work investigating the physical process of fibre deposition and the effects of process parameters on the multiscale preform structure. These have been identified as clear areas of research in developing a process model for DFP technologies [108].

2.2.1. Fibre spray

Automated DFP processes employ a robot-mounted fibre chopping system which ejects tow segments towards a perforated screen. Process parameters such as robot

path trajectory, reinforcement properties and deposition rate have significant influence during the spray process which in turn affects fibre distribution over the entire preforming domain. Areal mass heterogeneity leads to inconsistent local volume fractions resulting in variable mechanical properties. Clearly, a robust method for predicting fibre bundle locations and the resulting fibre distribution is required to reliably predict preform properties for DFP materials.

Previous attempts to model DFP processes have generally been restricted to simulating simple 2D single layer architectures greatly limiting applicability to the physical process. The creation of process simulation software was part of the outcome for the Affordable Lightweight BOdy Structures (ALBOS) project alongside development of DCFP technology. Harper et al. [53] used kinematic mapping to evaluate the stochastic effects of key process parameters on areal density variation across 2D preforms. Fibre deposition was modelled to conform to a virtual spray cone which remained symmetrical irrespective of input parameters with the projected cone diameter dependant on deposition head height relative to the target plane (Figure 2-1). A simple robot program with parallel path offsets was divided into discrete deposition points defining the cone apex location as the program iterated along each fibre release point. Segment location relative to the cone base centre was generated randomly using values returned form a normal distribution where the standard deviation was determined experimentally using a 24 K tow. Segment orientation was also generated randomly using either a uniform distribution or according to a user-defined distribution for directionally biased deposition.

Experimental tensile testing of specimens cut from the 0º and 90º directions (to robot direction) have shown that there is intrinsic directional bias applied for ‘random’ spray which needs to be accounted for to accurately model laminate mechanical response [66]. Figure 2-2 demonstrates the potential of process modelling software with simulated mass distribution correlating well with experimental results.

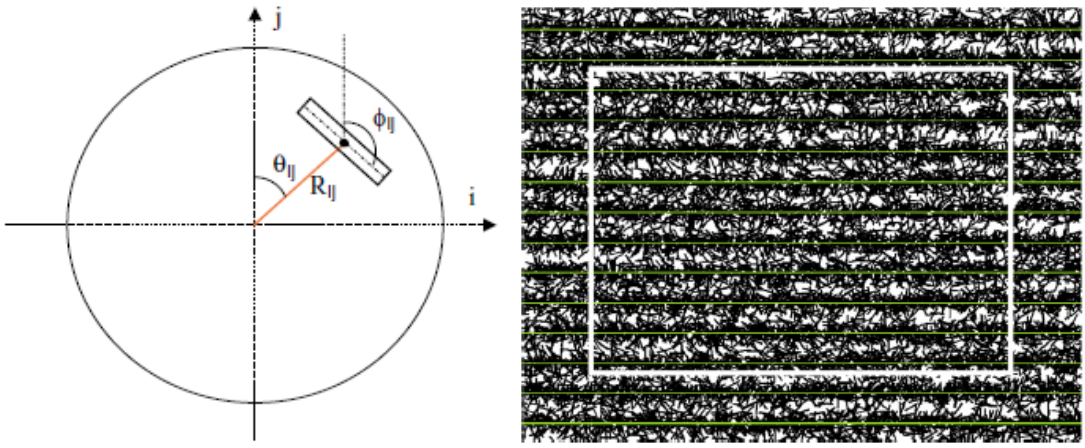

Figure 2-1: (Left) Virtual circular spray cone base used for DFP process simulation where R_{ij}, θ_{ij} and ϕ_{ij} define the location of the segment centre of mass and orientation. (Right) A simulated low areal density preform (0.5 kg/m^2) with the horizontal lines representing spray paths. Images taken from [53].

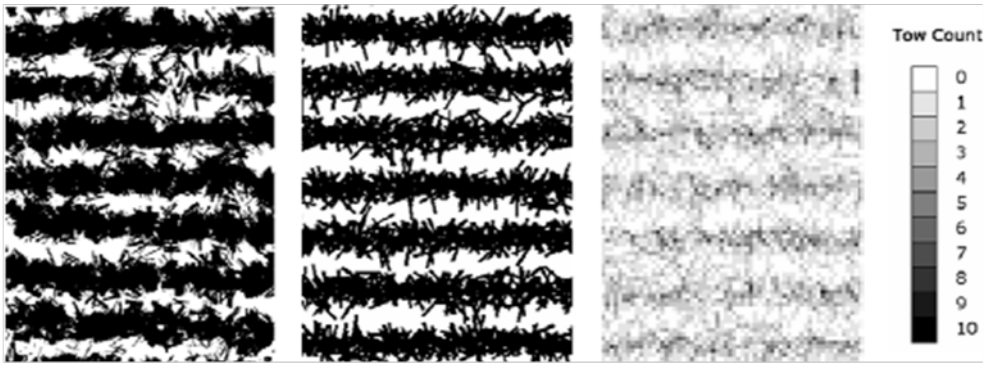

Figure 2-2: (Left) Black and white photo of deposited fibres. (Centre) Simulated deposition using the DFP process model. (Right) 'X-ray' of the deposited fibres showing the amount of tows present in the third dimension. Images taken from [53].

Liakus et al. [109] adopted a similar modelling approach to simulate fibre spray. A discretised robot path was generated relative to a deposition plane where a projected spray radius was created for each fibre release site. The spray radius was a function of chopper head height, chopper nozzle geometry and fibre feedrate with random number generators used to locate the deposited segments within the projected spray domain and determine the in-plane orientation. It is unclear whether the random numbers were generated based upon a probability density function however. Spray processes often bias deposition to the centre of a virtual spray cone rather than uniformly distributing material within the prescribed outer spray boundary [110]. Determining final segment placement was further complicated due to the presence of a circular mould wall and the requirement to include tow-tow interactions. Protruding segments with their centre of gravity outside of the mould perimeter were reflected back inside the boundary and rotated until the full segment was completely contained within the mould. These

boundary interactions resulted in fibre alignment around the mould perimeter similar to experimental observations (Figure 2-3). Tow-mould and tow-tow interactions were considered under the assumptions that the tow segments are circular in cross section and abide to rigid body mechanics.

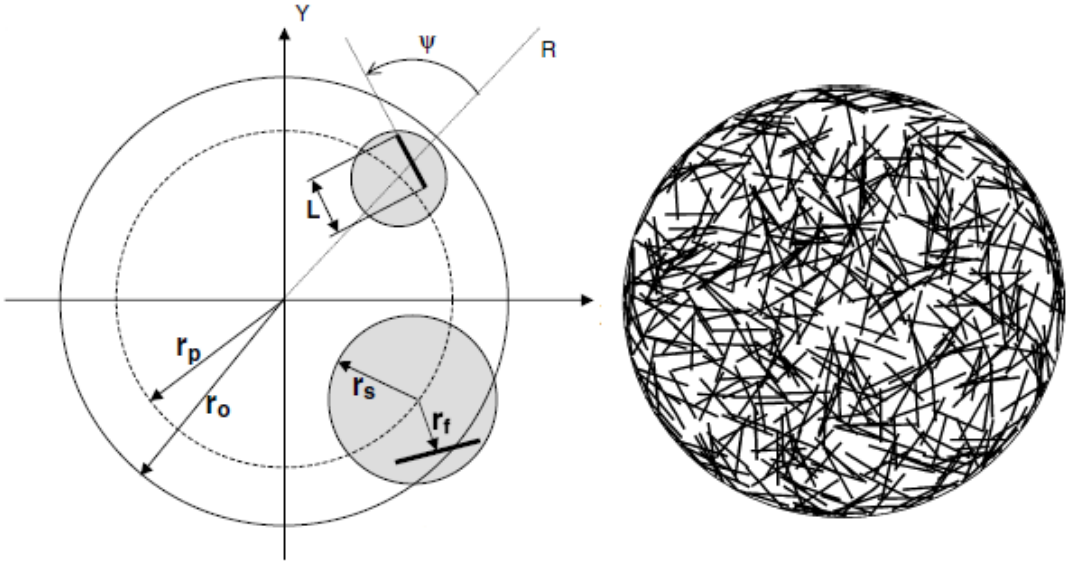

Figure 2-3: (Left) A schematic for the geometry used in the deposition process simulation by Liakus et al. [109] showing the outer mould boundary radius r_o and the virtual spray path radius r_p. (Right) Simulation of the reinforcement deposition with fibres aligned with the mould boundary. Images taken from [109].

Gunnerson et al. [111] proposed an alternative solution to simulating mass distribution for spray processes. Instead of explicitly accounting for each fibre segment location, a similar procedure as used in paint spraying process models was adopted. The deposited fibre mass was represented statistically from empirical observations which in turn feeds a path-planning simulation tool. Computational intensity was given as a primary reason for choosing not to model each segment explicitly; however there is little evidence to support this view with the processing power available with modern computer hardware.

The experimental apparatus used in the study delivers fibres in discrete packets held in a cartridge assembly and released through a focussing nozzle. The shape, size and height of the nozzle affect the segment distribution; all of which remained constant to characterise the fibre deposition. Characterisation was carried out by dropping a sparse amount of segments and using proprietary image analysis software [112] to extract segment location and orientation (Figure 2-4). The analysis software is

unsuitable for dense fibre stacks due to errors arising from overlapping fibres, therefore restricting its applicability for characterising high throughput processes such as DCFP. The experimentally determined mass distribution is compiled from repeated depositions using a Gaussian distribution function to replicate experimental observations.

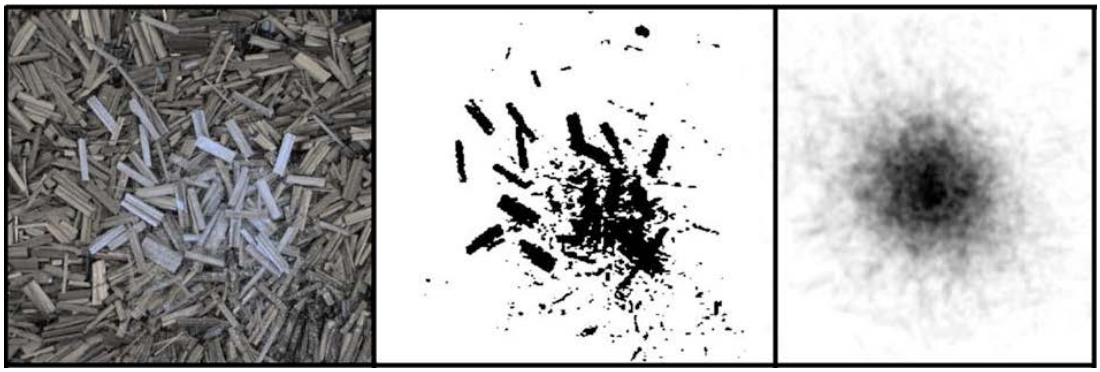

Figure 2-4: (Left) Picture of a discrete fibre deposition (coloured fibres) onto a surface already covered fibres. (Centre) A Digital image of the deposited fibres and (Right) the representative mass distribution after 20 sparse depositions. Images taken from [111].

The physical spray process used discrete sites to release material rather than the common approach of a continuous robot trajectory. A pattern of robot points were evenly distributed using a Coulomb law repulsion algorithm to attempt to achieve a homogenous fibre distribution inspired from similar applications by Drocco et al. [113]. Each point was assigned a constant charge with the algorithm resolving repulsion forces so that the system of charged points transition from a high energy state to a lower stable energy state (Figure 2-5). Whilst this method of distributing deposition sites is unsuitable for a continuous delivery process such as DCFP, it does offer an interesting solution to optimising the distribution of robot path offset points if the points are prescribed a charge proportional to spray cone geometry.

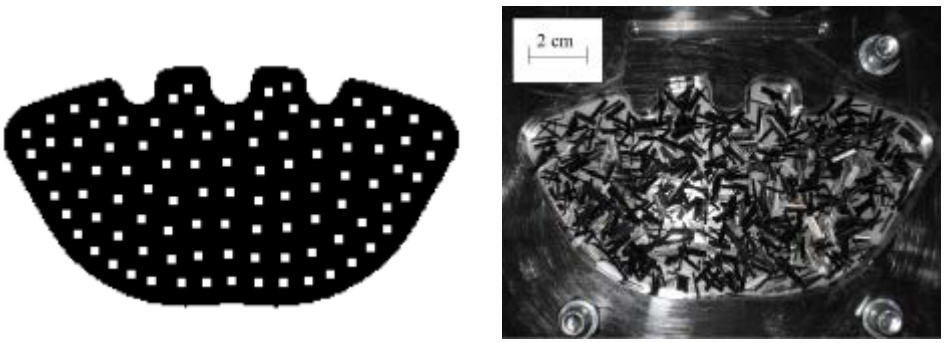

Figure 2-5: (Left) Optimised deposition sites within a mould boundary for brake pad geometries. (Right) Picture of the mould populated with fibres using the optimised deposition sites. Images taken from [111].

Similar processes such as automotive paint spraying, again requiring uniform material distribution, has received considerable attention from several authors to develop reliable process simulation software [35, 110, 114-117]. Paint spray is also modelled to conform to a spray cone within which the paint mass flux distribution is non-uniform resulting in heterogeneous coating thicknesses [114]. Gaussian [116], Beta [114] and parabolic [110, 115] distributions have been used to statistically represent the non-uniform surface distribution based upon empirical thickness measurements. The majority of paint spray models use circular cone geometries as in Figure 2-6, similar to the discontinuous fibre spray models, with Chen et al. [110, 118, 119] adapting their paint spray model to simulate a glass fibre spray forming process based upon the same principles.

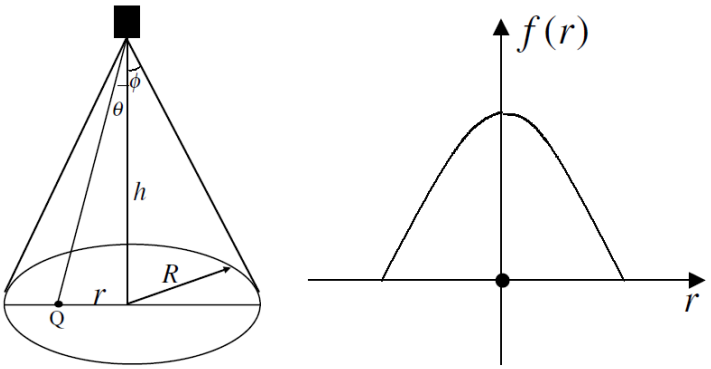

Figure 2-6: (Left) A typical paint gun model used in paint spray process models showing a virtual spray cone. (Right) A paint deposition rate profile with the axis origin representing the centre of the spray cone. Images taken from [120].

A significant proportion of published work with reference to paint spray modelling is predominantly interested in automating robot path planning to achieve macroscopic homogeneous material distribution, whilst also highlighting the necessity to accurately characterise the deposition process.

2.2.2. Robot path planning

The process models developed by Harper et al. [53] and Liakus et al. [109] prescribes the geometric robot path in a method analogous to programming an industrial robot using a teach-pendant. Optimisation of the deposition strategy occurs through trial-and-error, usually by adjusting path offset distance after evaluating the subsequent mass variation. Paint spraying process models briefly mentioned in Section 2.2.1 have

been developed to automate robot path planning by considering the material distribution within the spray cone domain and minimising thickness variations between parallel passes where deposited material overlaps. Paint spraying processes have almost identical input parameters and requirements to DFP processes: part surface geometry, deposition/applicator head configuration, path trajectory and process outputs such as material distribution quality, cycle time, wastage etc. A great deal of work has been conducted in the area of path planning for robotic systems to achieve uniform coverage [121, 122] with some of the methods discussed in this section.

Chen et al. [123] recognised that manual path planning is complex, time consuming and highly dependent on operator skill which is why there is significant interest in optimising and automating path planning duties. Heping et al. [118] simulated glass fibre deposition for a simple 2D rectangular shape showing the potential for off-line simulation techniques producing reasonable correlation between simulated and experimental mass variation results across the preform area. Path offset was based upon an optimised overlap distance using a golden section method [124], however, the applicator head was required to project in a direction normal to the target surface at all times in order to simulate a realistic mass distribution which can become unfeasible for complex 3D geometry. This could lead to complex robot programs and lengthen overall cycle time.

Chen et al. [120] presented a patch forming technique in an effort to minimise the deviation angle between applicator and a target surface consisting of triangular mesh elements. This was achieved by creating a projection plane based on averaged surface element normal vectors contained within a given spray domain. If the deviation angle falls outside of a prescribed threshold then an additional patch is formed. The model generates realistic path lines for simple part geometries using this technique but produces high thickness deviations of up to 35% from the mean material thickness. Commercial software ROBCAD [125] was used to simulate the paint spray process for the generated robot trajectory.

Subsequent development of the path generation software considered the effects of material distribution between multiple patches showing that an optimal trajectory pattern is achievable to minimise mass variation, but becomes increasingly complex

when multiple patches are required to discretise a free-form surface [126]. Again, only simple surface geometries were used questioning the applicability to a complex 3D component. It is anticipated that considerable difficulties would arise if features such as holes and irregular profiles are introduced and whether the optimisation routine would find a suitable solution at all. The authors claim that the developed software decreased robot trajectory generation times from more than 8 weeks using traditional techniques to 4-5 days [119]. The car part shape used to test the algorithm with the resulting disjointed path profile is presented in Figure 2-7.

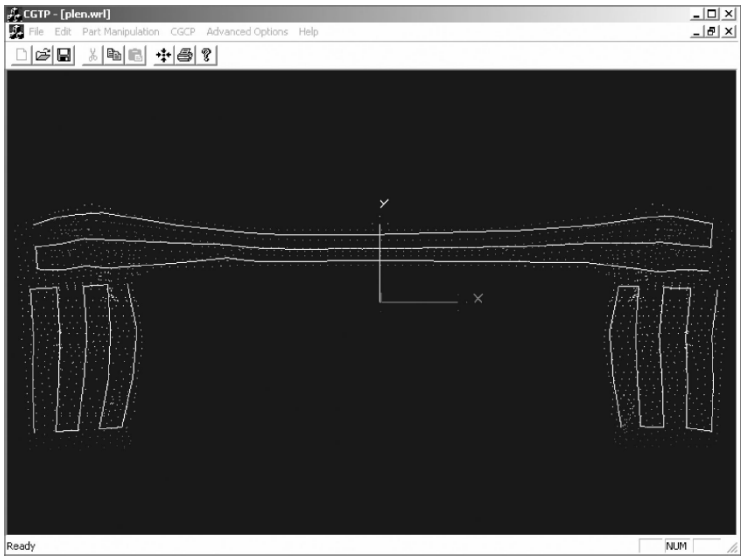

Figure 2-7: Robot trajectory generated using a patch forming technique for an automotive part. Robot path lines are disjointed using this approach despite the relatively simple part geometry. Image taken from [119].

Weihua et al. [127] advanced the process of decomposing surface geometry into patches to eradicate holes and achieve regular topology for each patch. Part of the initial criteria was to minimise cycle time by reducing the amount of deviations the applicator is required to make along a path. The resulting spray pattern for an automotive bonnet does not represent the most efficient path however (Figure 2-8). In reality a much simpler blanket path could be utilised with judicious use of gun operation instructions to achieve much lower cycle times in comparison. Other methods involving path generation include similar decomposition methods to create regular polygon subsets before using genetic [128] or ant colony optimisation algorithms [129] to generate a large number of possible trajectories. Each solution is evaluated against performance criteria to find a trajectory with optimal attributes such as path length and cycle time. Partitioning becomes even more excessive when part complexity increases [127] leading to increasingly disjointed robot programs.

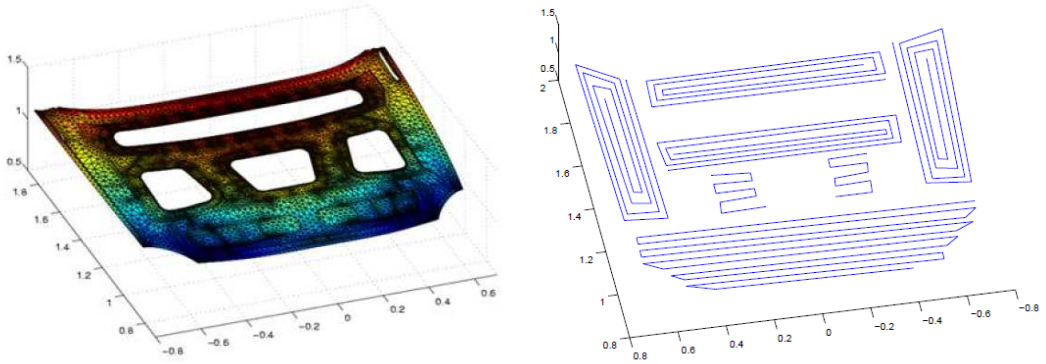

Figure 2-8: (Left) The automotive bonnet geometry used for automated robot path planning in [127]. (Right) the generated robot trajectory after partitioning the bonnet into multiple spray domains.

Arikan and Balkan [114] simulate robot motion by discretising robot path lines to determine spray locations. At each location, paint is sprayed for a time period which is a function of required paint flow rate and the level of path discretisation; effectively simulating a continuous spray motion. After seeding the initial path line, two adjacent paint distribution curves are superimposed to calculate the range of paint thickness within the overlap region. For two equal parabolic distribution curves the optimised offset distance, minimising thickness variation, is the spray area diameter multiplied by 0.608. Paint thickness deviations between simulated and experimental results over a simple part profile are as high as 20% suggesting that further process characterisation is required.

To reduce material waste associated with over-spray, process variables should also be modified to alter spray cone geometry enabling efficient robot path design. Atkar et al. [130] emphasises the importance of intelligent path line seeding which plays a crucial role in achieving this, as well as minimising cycle times. Optimising robot speed relative to spray flow rate improved paint uniformity by as much as 25% in some cases compared with constant speed trajectories.

Even after achieving an optimised robot path using these types of simulation tools, the trajectory has to be physically possible for an industrial robot. Most published trajectory planning techniques take place in Cartesian space whereas industrial robots typically operate in joint space [131]. Transformation from Cartesian to joint space requires the use of inverse kinematics which is non-trivial and can theoretically

produce an almost infinite amount of solutions to the same problem. Conversely, using forward kinematics to translate joint motion to applicator position is usually closed-form and relatively simple. Ideally a commercially available robot simulation software package should be utilised to aid trajectory planning techniques.

2.2.3. Fibre retention and material permeability

Traditional directed fibre preforming methods use a vacuum assisted tool to evacuate air from behind the tool surface thus providing fibre retention on the tooling surface. The challenges in designing effective preform tooling is highlighted in a study to improve preform quality of automotive vehicle B-pillars [86]. Initial preforms suffered from large areal density variations with areas over 100% above target volume fraction levels (40% V_f); mainly attributed to inconsistent airflow through the tool. Efforts to reduce flow variation were performed by baffling sections of the tool after accumulating air flow field data via measurements using an anemometer. Improvements were reported but ultimately insufficient to satisfy preform quality requirements even after modifying other process variables such as fibre length, fibre feedrate, TCP location and air speed. This suggests that air flow and therefore, fibre retention capability is highly sensitive to tooling geometry. Despite the commonplace application of such fibre retention techniques for DFP processes, very little work has been conducted in characterising the retention capabilities for such materials.

There is substantial literature available for examining air permeability through porous media however. The media typically tested comprises of a granular bed using liquid as the permeating fluid with the resistance caused by a granular bed often quoted as obeying Darcy's law where a linear relationship exists between the medium's pressure gradient and the superficial fluid velocity [132]. The Kozeny-Carmen channel model is widely used for relating physical constants to packed beds of particles during laminar flow [133] but has limited use for fibrous materials and highly porous media [134]. Forchheimer and Brinkman [135] observed that Darcy's law only held true for low superficial velocities ("seepage" velocity) catering solely for viscous drag effects where inertial effects are negligible and with frictional losses being attributed entirely to viscous drag from the permeating fluid. Scheidegger [136] surmised that in order to characterise the seepage velocity domain in which Darcy's law holds true, a Reynolds

number could be introduced. Scheidegger noted that numerous investigations focussed on finding a universal critical Reynolds number, above which Darcy's law is no longer valid, ultimately failed due to large discrepancies between the different fluids and media examined.

Deviating from channel theory, Forchheimer [135] proposed the inclusion of a second order term to define inertial drag in addition to viscous forces for higher flow rates. This permits modelling for pressure drops across porous media where flow conditions exist in the turbulent phase at higher fluid velocities. Notably, Forchheimer further suggested the use of higher order terms to provide a closer fit to experimental data. Further extensions were applied by Ergun [137] and Comiti-Renaud [138] to adapt Forchheimers principles to physical properties including porosity, specific surface area and tortuosity for packed particle beds. Belkacemi and Broadbent [139] further developed Kyan's pore model, suited to air flow through fibrous and woven fabrics experiencing high pressure drops, showing good agreement between experimental data and model predictions. An alternative model for woven textiles was developed by Goodings [140] acknowledging the influence of structural parameters such as the weave pattern and warp and weft linear densities. For all of these models several structural properties were required for each material involving experimental characterisation.

Preforming processes use a perforated screen to support the material whilst under vacuum retention which therefore contributes towards the total air flow resistance in the system. Zierep et al. [141] using manufacturer's data for plate porosity failed to describe aerodynamic performance by relating pressure drop across the plate to the superficial velocity. It was suggested that the porosity value should be inferred from aerodynamic performance using a D/B transpiration law. A revision of the D/B constants gave a relationship where the pressure drop was proportional to mass flow squared. For increasing pressure drop the squared function resulted in an adequate fit with experimental data. Haque et al. [142] investigated the influence of perforated plates within electrostatic precipitators to characterise the plate performance for a CFD model. By modelling the plate as thin porous media the pressure drop can be calculated using a combination of viscous and inertial terms emulating Forchheimers equation. Changes in gas viscosity was predicted to have negligible effects on

pressure drop over a wide range of superficial velocities, thereby nullifying the viscous term in turbulent flow conditions.

The bulk of work performed in this area has been concerned with highly homogeneous fabrics at low superficial velocities and typically for single layers. It is not clear from the published literature how the developed models can be applied to the fibre architectures of interest. Work presented in Chapter 5 compares the characteristics of various types of fabrics, fibrous mats and unconsolidated DCFP fibre stacks with respect to a wide range of air velocities to attempt to build upon existing knowledge.

2.2.4. Mesoscale modelling

Material characterisation and accurate mechanical property prediction for discontinuous fibre composites are essential for the development of material models which integrate into existing design procedures. Several analytical modelling methodologies such as classical laminate theory, ROM based and statistical averaging are used to homogenise constituent materials within a given domain. For mechanical stiffness prediction these modelling approaches offer a convenient solution both in terms of speed and accuracy because stiffness is essentially a volume averaged quantity [143]. Strength predictions are less accurate however, with large over-predictions due to the inability to account for complex fibre/matrix, fibre/fibre interactions and localised volume fraction variation within the mesostructure of the composite. Stress concentrations arising from fibre bundle ends and resin rich areas are particularly susceptible to failure initiation and damage evolution; therefore more exhaustive methods of property modelling are required. Numerical modelling combining the generation of random fibre networks with finite element method (FEM) can reproduce the stochastic characteristics of random fibre composites and offers a promising solution to capture localised stress and strain fields required for damage analysis.

Finite Element Analysis (FEA) is commonly used to model the mechanical behaviour of a wide range of fibre reinforced composite materials. The random heterogeneous nature of discontinuous fibre composites means that a repeating unit cell approach used for textile and UD materials is non-applicable however. Hill [144] states that a

representative volume element (RVE) should be used instead which can be defined as a macroscopic statistical representation of the constitutive materials. This means that a sufficiently large sampling of all the microstructural heterogeneities present in the composite is required. An alternative view adopted by Drugan and Willis [145] states that the RVE should be the smallest material volume element which accurately represents the mean constitutive response. Harper et al. [146] provide a useful review of current approaches in generating RVEs for random fibre architectures. It is apparent that accurately recreating mesoscale architectures remains challenging due to complex fibre networks and the wide range of inclusion geometric forms typically used in discontinuous fibre composites.

Numerical generation of RVEs can be categorised by the following methods; Random sequential adsorption (RSA), Monte Carlo (MC) procedures, image reconstruction techniques [147] and process-driven simulation. RSA and MC methods are the most widely adopted; randomly generating fibre centroid positions and orientations which can be tailored to experimental observation by using statistical distributions. For three-dimensional RVE generation, issues relating to ‘jamming’ occur where the constraint preventing fibre intersections is no longer valid prior to reaching the desired fibre volume fraction [146, 147]. This is usually a consequence of modelling high aspect ratio fibres as rigid cylinders. Efforts to increase ultimate volume fraction in RVE generation allow out-of-plane curvature for improved fibre packing efficiency.

A model using a modified RSA technique is presented by Pan et al. [147] for in-plane fibre networks. Fibres are permitted to locally bend to avoid intersecting neighbouring fibres achieving fibre volume fractions of 35% - 40%, approaching levels suitable for structural applications. This is achieved by dividing the RVE into sub-layers to allow fibres to occupy adjacent layers thereby avoiding intersections. Fibre bundles are approximated using a series of polyhedra with elliptical cross sections but still fails to capture realistic out-of-plane curvature (Figure 2-9 – A).

Higher volume fractions were achieved using a random walk force-biased packing approach [148]. Each fibre was modelled as a chain of spheres, limiting its applicability for elliptical carbon tow segments, but does offer control over fibre tortuosity and out-of-plane orientation (Figure 2-9 – B). For a 24 K tow segment with an effective tow diameter of 1.4 mm [146], the maximum fibre volume fraction

permissible is 65% V_f (7.5 mm fibre length) decreasing inversely with aspect ratio to ~50% V_f (46 mm fibre length) [148]. A similar force-biased approach was proposed [149] for mixed dimension modelling targeting >50% V_f. The model can output either 1D truss or 2D shell fibre meshes constrained in 3D continuum elements with no limitations on fibre bundle aspect ratio, producing realistic fibre networks applicable for DFP processes (Figure 2-9 – D). Commercially available software such as DIGIMAT can also provide RVE generation duties with direct portability to ABAQUS/standard but covers a generalised approach rather than process specific, and can only achieve relatively low fibre volume fractions for the architectures of interest.

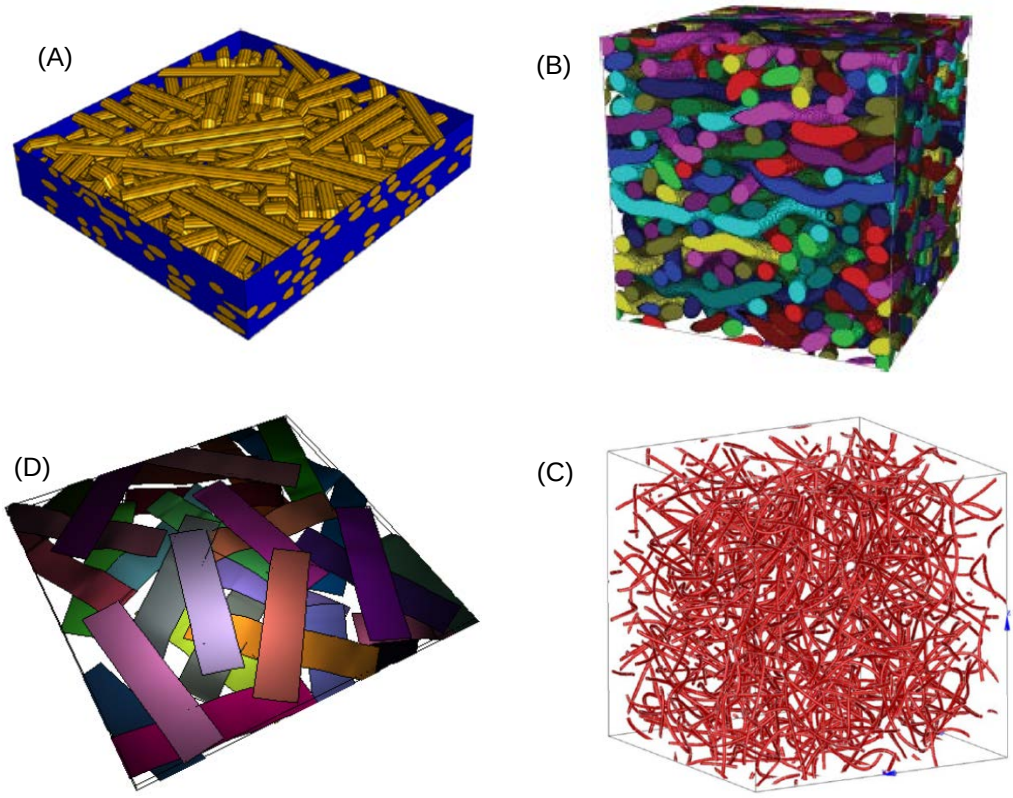

Figure 2-9: (A) RVE of a random chopped fibre composite with curved fibre bundles generated using a model developed by Pan et al. [147]. (B) An RVE generated using a random walk based stochastic model proposed by Altendorf et al. [148]. (C) RVE of a polymer matrix reinforced with carbon nanotubes created using Digimat software [150]. (D) A compressed RVE with shell fibre architectures producing realistic DFP fibre architectures [149].

To remove the fibre volume fraction jamming limit, several researchers have used 1D beam elements permitting fibre intersections [143, 146, 151, 152]. Obviously this simplification to the 2D domain negates complex 3D phenomena resulting from fibre/fibre contact and the effects of out-of-plane curvature on mechanical properties [149]. A stochastic fibre network model developed by Harper et al. [143] was used to

simulate DCFP fibre architectures at the mesoscopic level using 1D beam elements (in ABAQUS/standard) to represent tows which are tied to 2D solid continuum elements using the embedded element technique. Using beam elements is computationally inexpensive and permits the analysis of larger volume models approaching macroscale modelling that replicate process specific fibre networks. For large fibre lengths or high aspect ratios this can alleviate the occurrence of boundary-to-boundary bridging fibres which can exist when constrained to small scale RVE dimensions – a result of using computationally expensive 3D continuum elements.

2.2.5. Macroscale modelling

The process driven models discussed in Section 2.2.1 are capable of spraying virtual macroscale preforms in an effort to simulate the physical preforming process and reproduce accurate mass distributions. The discrete deposition model developed by Gunnerson et al. [111] was used to optimise fibre release locations to manufacture net-shape preforms for an automotive brake pad. A Coulomb law repulsion algorithm was used to distribute deposition locations until the system achieved a low-energy equilibrium providing an optimised deposition pattern. The simulated preforming area was discretised to graphically represent preform height, in the form of a contour map, based on the underlying statistical mass distribution functions. The deposition strategy was replicated for experimental preforming with a 3D scanner used to determine the height of the fibre bed and subsequently compared with simulated results (Figure 2-10). The difference in height between predicted and experimental results was found to be within ±10% across the preform for the specific combination of material parameters presented (8.5 mm, 10 K carbon fibre tow). The simulation software appears to be solely developed for optimising deposition location in order to obtain a uniform material distribution with no further application to predict mechanical properties.

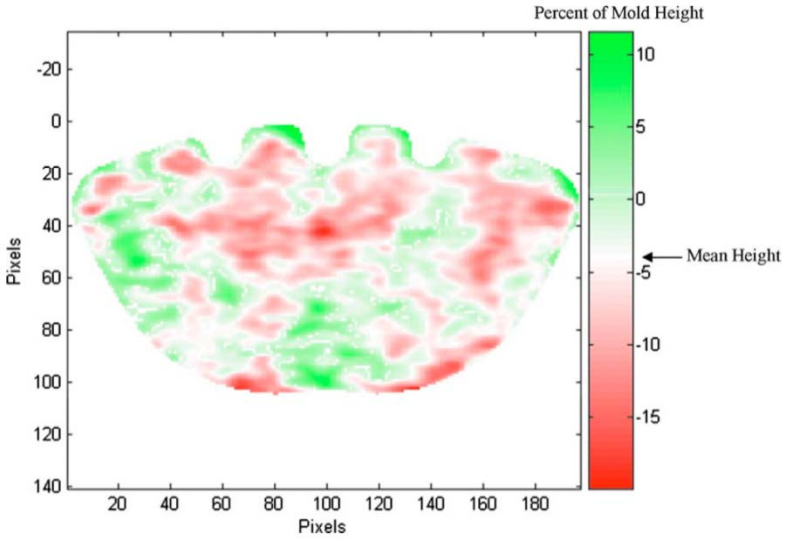

Figure 2-10: A deposition contour map showing the difference between actual fibre mass distribution and model predictions using identical deposition sites. Image taken from [111].

Rather than modelling each deposition as a statistical distribution Liakus et al. [109] explicitly located each fibre in the deposition plane to build up a three-dimensional preform. Tow segments were modelled as rigid bodies with significant out-of-plane orientations resulting from high aspect ratio fibres coupled with the inclusion of a mould wall. As fibre lengths increased from 12.7 mm to 76.2 mm the use of rigid body mechanics led to increasing overestimations of true out-of-plane orientations due to entanglement when faced with certain tow-tow interactions. This would lead to lower in-plane mechanical properties when compared to experimental results. In-plane and out-of-plane fibre orientations were of interest during the study due to the preform thickness being of the same order of magnitude as the preform diameter – resulting in a three-dimensional preform.

A three-level micromechanical modelling approach was applied to predict the elastic constants using the Mori-Tanaka method [153] and to evaluate the dependence of process parameters on elastic and thermal properties. No experimental validation was presented however for the rigid body deposition model or for final composite performance.

Harper et al. [53] used a 2D simulation model to investigate the effect of several process parameters on preform mass variation. Fibre length and global areal density was found to significantly influence the local density variation requiring an optimisation of the deposition strategy to improve variability. Areal mass variation

was reduced when simulating the deposition of shorter fibres (25 mm instead of 75 mm) consequently leading to increases in mechanical properties from experimental testing.

To capture observed non-uniform strain distributions for tested tensile specimens, Feraboli et al. [154] proposed generating multiple random RVEs (RRVE) over a discretised specimen representing the heterogeneous nature of discontinuous fibre composites. By examining distinct strain regions from experimental digital image correlation (DIC) specimen results a characteristic length scale was determined from which defined the RRVE area; in this case 161 mm^2. To put the RRVE area in perspective; the area of a single intact fibre used in study was 426 mm^2. The mechanical properties of each RRVE were generated independently of neighbouring elements based upon classical laminate theory (CLT) and solved simultaneously using FEA (Figure 2-11). The strain distributions generated proved to be similar to experimental DIC plots replicating the heterogeneous reinforcement distribution. Employing CLT based RRVEs is therefore a promising solution to capture the generalised response of discontinuous fibre composites.

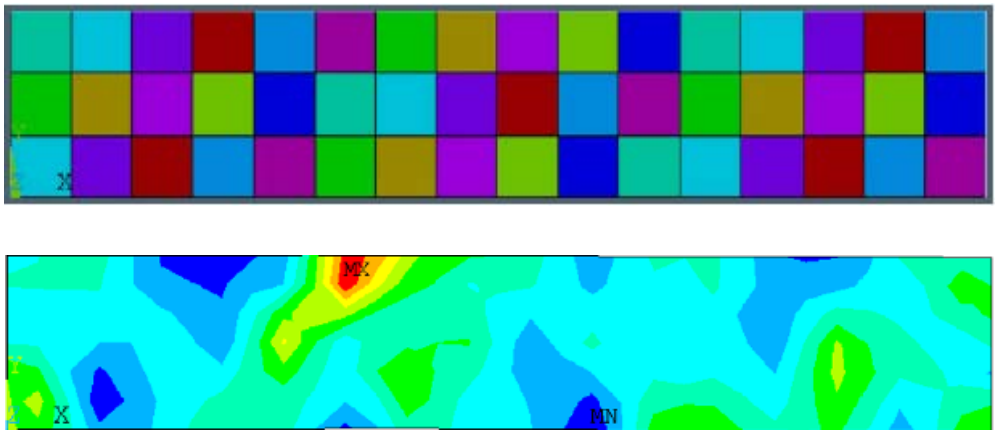

Figure 2-11: (Top) Tensile specimen divided into 48 regions described as RRVEs with independently generated material properties. (Bottom) FE output showing the strain distribution contour plot over the specimen length. Images taken from [154].

2.3. Chapter conclusions

A review of the key microstructural parameters affecting composite fabrication and final laminate performance for DFP materials was conducted. The mesoscale architecture arising from the use of bundled reinforcement makes the optimisation of these parameters challenging. A compromise is often required between material

processability and mechanical part performance. Increasing reinforcement length was proven to be beneficial in terms of increasing laminate properties but can suffer knockdown effects during preforming and resin transfer stages if fibre lengths are excessively long. The cost-effectiveness of using larger carbon tow forms (≥24 K) was found to negatively affect mechanical properties of the composite compared to the use of smaller filament count tows. Both fibre length and tow size dictate preform homogeneity – smaller fibre lengths and bundle sizes increase preform segment count for a given target areal density. The increase in segment count has the net effect of increasing preform homogeneity through improved reinforcement distribution. This is highly desirable to lower intra-preform and inter-preform mass variability thus increasing the repeatability of the process.

Several researchers have attempted to accurately reproduce the material mesostructure to facilitate mechanical property prediction. Numerical modelling approaches have focussed on developing a representative volume element to capture the complex fibre/fibre and fibre/matrix interactions which can lead to failure initiation sites defining the materials mechanical response. Although this method offers the opportunity to characterise the material on the micro and mesoscale a RVE is not necessarily a suitable representation of the macroscale stochastic fibre network, particularly for complex 3D part geometries. Current macroscale process-driven models attempt to recreate mass variation but are limited to simple 2D depositions failing to capture the versatility offered through directed fibre preforming.

Analogous processes such as paint spray deposition have had strong interest in developing macroscale modelling techniques to replicate the physical process and offer a solution to optimise material coverage. The importance of effective deposition characterisation for such models was highlighted. Optimisation of the material distribution was proposed using automated robot path planning based upon the target geometry. Although the potential for such techniques could significantly reduce experimental trials for robot trajectory generation, the examples given often suffered from disjointed path profiles even for simple planar part geometries. The path planning optimisation tools outlined appear to be suited to planar surfaces with little evidence for application to genuine 3D geometries. Suggested robot trajectories become unnecessarily complex particularly with the inclusion of geometric features and irregular part boundaries. Rather than developing autonomous solutions to

effective path planning a more appropriate technique would be to take a heuristic approach allowing the operator to define a simple path program and intuitively optimise process parameters based on performance criteria.

Chapter 3. Experimental techniques

3.1. Preforming materials

Carbon fibres of various types obtained from Toho Tenax Europe GmbH are used as the reinforcement material for all experimental preforming operations and process characterisation throughout this thesis. Four tow sizes were available for investigation with larger tow sizes (higher filament counts) providing a cost advantage due to manufacturing efficiencies. All four derivatives and their properties are summarised in Table 3-1.

Reichhold PRETEX 110, a powdered epoxy with a heat activated curing agent, is used as the preform binder. The binder has an observed melting temperature of ~60 ºC with onset of exothermic reaction at ~75 ºC peaking at ~115 ºC [155].

Table 3-1: Specification of carbon fibre reinforcement used for preforming operations. Values taken from manufacturer's data sheets.

Designation	Fibre modulus (GPa)	Fibre strength (MPa)	Filament diameter (µm)	Density (g/cm^3)	Elongation at break (%)	Linear density (Tex)	Sizing level (%)
3K E HTA40 E13	238	3950	7	1.76	1.7	200	1.3
6K E HTA 5131	238	3950	7	1.76	1.7	400	1.3
12K E HTS40 F13	240	4300	7	1.77	1.8	800	1.0
24K E STS 5631	240	4300	7	1.77	1.8	1600	1.0

3.2. Preform manufacture

The latest iteration of the UoN DCFP deposition head is mounted on a Fanuc RJ3iB six-axis industrial robot with direct fibre feed from bobbins located in close proximity. Chopped fibre segments are directed towards a vacuum plenum, held in place on a perforated screen using a constant vacuum fan speed of 1000 rpm. Powdered binder is stored in a robot-mounted fluidised bed chamber where the atomising and carriage air

streams are calibrated to deliver ~6% wt (of total preform weight) of binder to the deposition head. A Daniels down-stroke press was used for preform consolidation with a 5 minute cure cycle at 120 °C.

To characterise the performance of the updated alignment concentrator (Section 1.3.2.2) several preforms were manufactured to areal densities of 1.611 kg/m^2 (30% V_f) and 2.865 kg/m^2 (50% V_f) for a 3mm mould cavity. Preforms were sprayed to 500 mm by 400 mm dimensions in order to die-cut a final preform area of 400 mm by 300 mm for resin infusion. Due to efficient fibre packing achieved through aligning the chopped segments, preform consolidation was performed without additional compaction pressure using only the weight of the top platen (3148 kg) to ensure the mould cavity was filled. Compaction pressure was therefore ~154 kPa for a preform area of 0.2 m^2.

Prior to manufacturing aligned plaques for mechanical testing, two spray patterns were considered and compared in order to maximise mechanical properties. During an initial trial a typical north-south robot trajectory was programmed with the robot head continually pointing in the northwards direction (Figure 3-1). On southward passes a small proportion of fibres (for fibre lengths ≥60 mm) would stand on end before falling leading to visibly misaligned segments. This was due to a bias applied by the chopping mechanism discussed in Chapter 4. An alternative trajectory was trialled which only sprayed fibres whilst the robot travelled northwards to alleviate this issue, taking advantage of the robot direction to ‘lay down’ chopped segments (Figure 3-1). The robot travelled to the start point of each subsequent offset path using fast joint motion to minimise the impact on cycle time. By monitoring the robot motion signal (as described in Chapter 7) the cycle time was found to be 23% greater when compared with the north-south program. Two plaques were manufactured (6 K, 60 mm, 30% V_f) to assess the difference in mechanical properties with the north-north program offering superior performance for tensile strength. A 21% increase in tensile strength was experienced with less variability between the 10 specimens tested for each plaque. Tensile stiffness was found to be near identical in terms of average stiffness and variability. The north-north strategy was therefore adopted for the rest of the alignment study in Chapter 7.

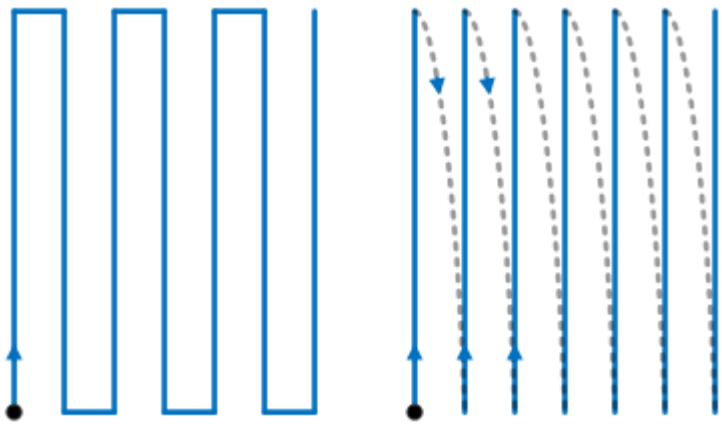

Figure 3-1: (Left) A north-south robot trajectory typically used for single layer coverage for random deposition. (Right) The alternative program used for manufacturing aligned preforms consisting entirely of north passes.

Additional preforms were manufactured specifically for process model validation tests with preform specifications outlined in Chapter 7. The north-south pattern in Figure 3-1 and an orthogonal spray pattern were used for random oriented deposition using the same consolidation conditions as for aligned preforms. The validation tests studied the mass variation across a 400 mm x 300 mm area by die cutting the preform into 25 mm x 25 mm coupons (Figure 3-2). Each coupon was weighed individually to an accuracy of ±0.001 g.

Figure 3-2: Picture of a die cut preform used for process model validation. The preform is cut into 192 coupons of 25 mm x 25 mm dimensions.

3.3. Resin transfer moulding

RTM was employed for all moulding activities using a steel 400 mm x 300 mm tool with a 3 mm cavity. All preforms were trimmed and weighed prior to transfer to the mould station in order to provide a good fit and to ascertain the final plaque fibre volume fraction. A tight fit was required within the mould cavity to prevent compaction issues and race-tracking. The tool was placed into a Daniels down-stroke press with both platens heated to 60 ºC and a pressure of ~2.7 MPa applied to prevent leakage during injection.

The Gurit PRIME™ 20LV epoxy infusion system along with a slow acting hardener was stored, preheated, mixed and injected using a CIject One™ resin injection machine. According to manufacturer's data using the recommended curing cycle, the cured resin system has a tensile modulus of 3.5 GPa and a tensile strength of 73 MPa. The resin system was preheated to ~70 ºC to reduce viscosity and aid preform wet-out to avoid disturbing fibre segments within the preform which can potentially degrade laminate mechanical properties.

A vacuum was applied to expel air from the cavity via the mould tool outlet before and during injection similar to the vacuum-assisted RTM (VaRTM) process used in industry. Initial trials indicated that only low injection pressures (≤1 bar) should be used for aligned fibre preforms to prevent the resin front from advancing too quickly – resin flow coincides with the direction of reinforcement. If a flow path to the outlet develops prior to full preform wet-out there is a high risk of incurring dry regions of reinforcement in the final plaque. To encourage full impregnation, the outlet of the mould tool was briefly closed once resin had reached it with resin still being injected. Once injection was completed the temperature of the platens was raised to 120 ºC and left to cure for an hour before cooling to below 40 ºC for demoulding.

3.4. Mechanical testing

Mechanical property data presented in this thesis is derived from tensile testing to establish basic design information on the strength and stiffness of aligned discontinuous carbon fibre composites. Results can be directly compared to existing

tensile test data pertaining to DCFP architectures as well as random fibre architecture results gathered as part of the overall ASP project.

Each plaque produced 10 specimens cut to 220 mm x 25 mm dimensions in the 0º direction with average thickness and width values, gathered from 5 measurements for each dimension, taken along the gauge area using vernier calipers. Tensile testing was conducted on an Instron 5581 50 kN machine at an extension rate of 1 mm/min in accordance with BS EN ISO 527-4: 1997. Applied load was recorded from the crosshead load cell and strain was measured using an extensometer over a 50 mm gauge length. Young's modulus was measured using the gradient of the linear portion of the stress-strain curve between strains of 0.0005 and 0.0025.

Chapter 4. Process characterisation

4.1. Introduction

Although the high performance composites market is currently dominated by continuous fibre architectures, there is increasing interest in utilising discontinuous fibres for structural applications; mainly in the form of mesoscale advanced sheet moulding compounds (A-SMC) [156]. These materials consist of chopped carbon fibre bundles with resin systems optimised for compression moulding (typically at 80 – 140 bar). Critically, chopping of the carbon fibres into short bundles facilitates various means of automation of the costly layup step in the composite manufacturing process [45, 157] and underlines the potential for directed fibre processes such as DCFP. These processes are generally designed to operate in conjunction with low-cost liquid moulding technologies; although developments towards one-shot deposition strategies to produce similar materials to A-SMCs do exist [158].

The heterogeneous fibre architectures resulting from DFP processes make material property prediction challenging and difficult to implement into established industrial design practices. For demanding structural applications requiring high mechanical properties, a detailed knowledge of the fibre architecture is required. Attempts at explicitly modelling such architectures thus far have either focussed on the mesoscale [143, 147-149] or are only applicable to simple two-dimensional component geometries [53, 109, 111]. A realistic process-driven model suitable for complex three-dimensional geometries is currently lacking restricting the uptake for DFP processes and is the main focus of study throughout this thesis. In order to develop a macroscale process model, detailed process characterisation is required to identify the dominant parameters affecting reinforcement distribution.

In the present work a methodology to characterise and model the UoN DCFP deposition head is outlined. The chopping device dictates fibre location and orientation with fibre spray being a function of material parameters (fibre length, tow size) and process parameters (head position and orientation, fibre feedrate, induced

fibre directionality). A further study attempts to characterise chopped segment flight kinematics as a precursor to generating a fibre flight model.

4.2. Deposition head characteristics

4.2.1. Methodology

Fibre spray can be assumed to conform to a spray cone emanating from the deposition device creating a projection area on the tool surface [53, 109, 119]. The shape of the projected area on the deposition plane is dictated by the spread of fibres released from the tool centre point (TCP) which coincides with the pinch point between the chop rollers (Figure 4-1). The spread of the fibres is accounted for in orthogonal directions; in-line with the device orientation *x'* and the perpendicular direction *y'*. This is due to observations that in some cases the fibre spread assumes an elliptical distribution rather than a symmetrically circular distribution.

A preform screen was placed in the deposition plane with a marked grid split into 100 mm by 100 mm squares. The grid was used as orthogonal datum lines to position the deposition head and to later calibrate measurement scales when processing data in CAD software. The TCP was aligned with the centre intersection of 4 adjacent grid cells as in Figure 4-2 and the TCP height determined by measuring the distance between the pinch point of the chop rollers and the preform screen.

Each deposition consisted of passing 1.8 m of carbon tow (~10 times greater than the chop roller circumference) at a predetermined feedrate whilst the robot was stationary. Photographs of each deposition were taken using a high resolution digital camera (tripod mounted for consistency) and subsequently imported into AutoCAD 2005 where the preform screen gridlines were used to scale the image. Once calibrated, vector lines were manually drawn in the position of each fibre segment in the image. In the case of overlapping fibres – as long as a fibre end was visible an accurate estimation for fibre orientation was feasible. Position and orientation data for each vector line is relative to the projected TCP (PTCP) and the positive *x'* axis respectively (Figure 4-2). Data for each line is then exported to a spreadsheet for further processing.

The cone base centre point was located by averaging the midpoints of each vector line, essentially calculating the centre of mass for the deposited fibre stack. The degree of spread from the mean midpoint location was attained statistically, dictating the projected cone boundary and fully defining the spray cone domain relative to the TCP. Segment orientations were sorted into a discrete frequency distribution in the range of ±90º about the positive *x'* axis using 18 classes (each frequency bin equating to 10°).

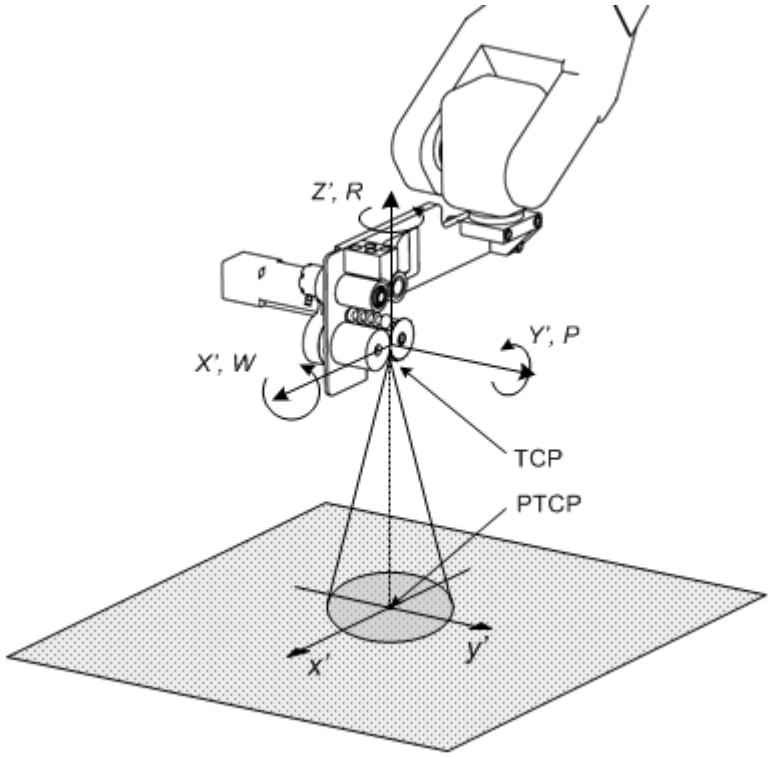

Figure 4-1: Coordinate system convention used for process modelling.

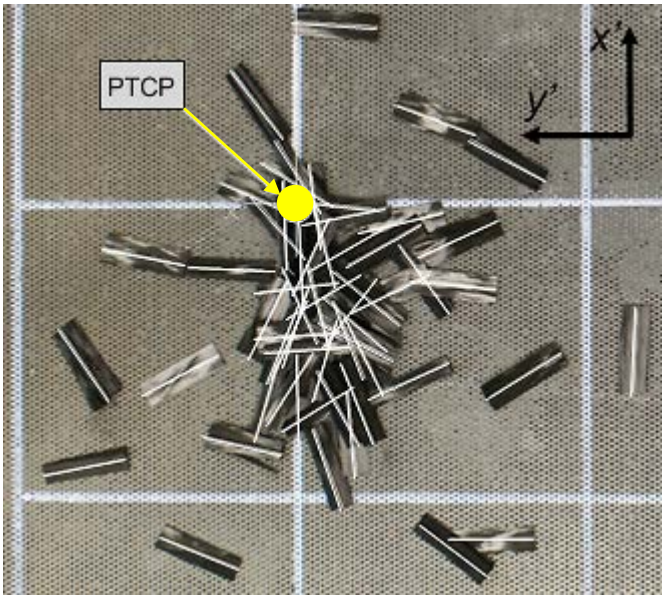

Figure 4-2: Photograph of a static deposition of fibres illustrating the spread of fibre segments around the PTCP. White lines are drawn on each segment in AutoCAD to obtain orientation and position data.

A method for automating the detection of fibre location and orientation is presented by Mather et al. [112] using an image analysis technique in MATLAB. Although the software showed potential; processing images of high throughput depositions, as is the case here, is limited due to poor segment edge definition and multiple instances of overlapping segments. Manual detection was preferred to allow for more sophisticated interpretation and informed decision making in determining segment location and orientation.

4.2.2. Design of experiments

An experimental feasibility study was conducted to determine the process parameters which affect spray cone geometry with four variables identified: tow size, fibre length, fibre speed and TCP height. Range bounding and intermediary values for each variable were chosen to represent typical DCFP operating conditions, summarised in Table 4-1. The range of tow sizes tested includes the entire range of reinforcement material forms available during the project listed in Table 3-1. A fibre length of 10 mm was chosen as a lower bound value because smaller fibre lengths suffered from excessive fragmentation where the integrity of the fibre bundle diminishes, making it difficult to accurately determine segment count and location. For the upper bound value, the knife roller installed in the deposition head can cut segments up to 180 mm in length. However, during the feasibility study segments of this length had an

undesirable tendency to fold leading to excessive in-plane distortion. This would severely impact mechanical performance due to inefficient stress transfer between fibre and matrix and was therefore omitted from the study with the next size down (90 mm) selected as the limiting value. The maximum fibre speed for this experiment (3 m/s) was chosen based upon achieving reliable and repeatable deposition across all fibre length and tow size combinations. Slower feedrate values of 1 m/s and 2 m/s were included to assess the effect on the location of the cone centre point. For TCP height, 300 mm is a typical value used in preform manufacture to encourage even fibre coverage [56]. For instances where this is unfeasible due to three-dimensional part profiles, geometric features or robot reach, a lower value of 100 mm was also studied.

Table 4-1: Process parameters and corresponding values investigated for random spray characterisation.

Process parameters	Units	Values investigated
Tow size	-	3 K, 6 K, 12 K, 24 K
Fibre length	mm	10, 30, 90
Fibre speed	m/s	1, 2, 3
TCP height	mm	100, 300

A full factorial experimental design for the factors and levels outlined in Table 4-1 was conducted resulting in 72 unique depositions, providing a thorough investigation into the random spray process. Each unique deposition was repeated a further two times for additional data and to assess repeatability.

The experiment was replicated for aligned depositions where an alignment concentrator was fitted to the deposition head to mechanically induce directional bias to chopped segments. The distance between the bottom of the concentrator and the preform screen was fixed at 50 mm (equating to a TCP height of 110 mm) after manufacturing trial preforms. Alternative distances were investigated with fibre blockage and fibre bed disruption culminating from distances too close to the screen. Conversely, noticeable degradation in alignment levels was experienced as the distance increased negating the benefits of using the alignment concentrator. A 110 mm TCP height produced reliable highly aligned depositions and was subsequently used for preform manufacture as in Chapter 3. During the feasibility study it was visually apparent that the concentrator was ineffective in orienting 10 mm fibre lengths due to the fixed concentrator plates being set 11 mm apart to accommodate the

width of 24 K tows. Chopped segments were able to rotate between the plates leading to low levels of alignment; therefore an intermediate fibre length of 60 mm was investigated instead. The complete list of factor levels used in the alignment characterisation study is presented in Table 4-2.

Table 4-2: Process parameters and corresponding values investigated for aligned spray characterisation.

Process parameters	Units	Values investigated
Tow size	-	3 K, 6 K, 12 K, 24 K
Fibre length	mm	30, 60, 90
Fibre speed	m/s	1, 2, 3
TCP height	mm	110

4.2.3. Results and discussion

4.2.3.1. Random deposition

The most significant observation for the random spray characterisation experiment is that in each case the spray cone centre point (fibre stack centre of mass) was located rearwards (-*x'*) of the PTCP. This is due to a bias applied by the chopping mechanism where the knife roller is situated behind the pressure roller in terms of position along the local head *X'* axis. Figure 4-3 illustrates the effect of the chopping bias with the spray cone centre point moving away from the PTCP as TCP height increases.

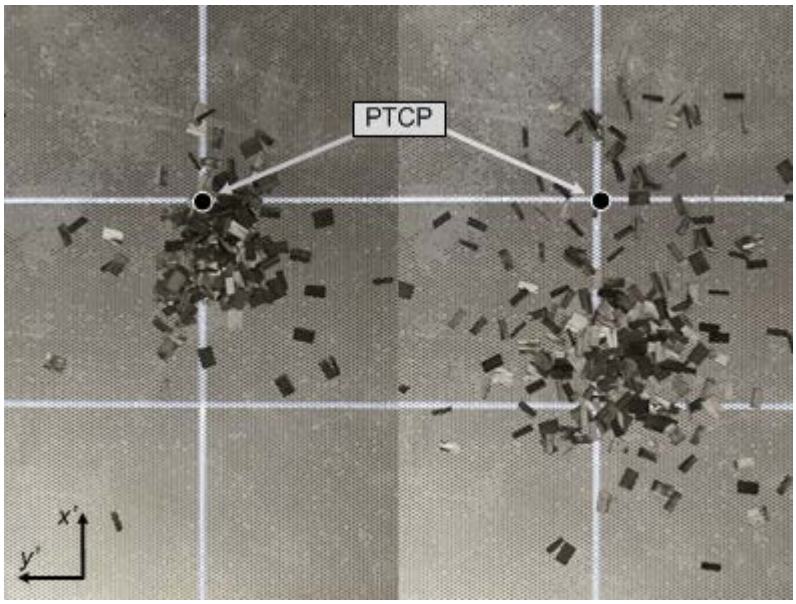

Figure 4-3: The effect on fibre distribution when increasing TCP height in isolation (12k, 10mm, 2m/s).

Minitab v.16 was used to analyse the effect of each factor in the full factorial experiment by performing a general linear analysis of variance (ANOVA). Mean fibre distance from the PTCP and fibre distribution to one standard deviation in the *x'* and *y'* directions were investigated separately. Figure 4-4 shows the mean fibre midpoint distance from the PTCP along the *y* axis. The main effects plot shows that fibre speed is relatively insignificant compared to the other three factors with tows size and TCP height having the greatest effect on location. The variation in mean fibre locations from the overall mean (-8.5 mm) is small however when the scale of a typical preform is taken into consideration. Boundary mean values (-5 mm and -12 mm) and the overall mean clearly indicates that a bias is applied by the deposition head resulting in fibres being sprayed off centre.

A two-way interaction plot is presented in Figure 4-5 where it is clear that many interactions exist between the four variables investigated. Increasing any one variable with respect to another does not provide a predictable response in mean fibre location. For example the mean response for the three fibre lengths tested between speeds of 1 m/s and 2 m/s show that 30 mm and 90 mm fibre lengths behave in a very similar manner approaching the PTCP as speed is increased. 10 mm fibre length depositions oppose this trend with the mean fibre location moving further away from the PTCP. Increasing the speed from 2 m/s to 3 m/s now shows depositions using 10 mm and 90 mm fibre lengths responding similarly and opposite to the behaviour observed for 60 mm fibre lengths. These types of interactions make it very difficult to have any confidence when trying to predict the response of mean fibre location when using intermediary values or values outside the scope of this designed experiment.

Figure 4-6 shows the main effects plot for mean midpoint distance along the *x'* axis from the PTCP. The factor which is responsible for the largest deviation from the PTCP is the TCP height. A further significant effect is also observed when increasing tow size from 12 K to 24 K. The mean distance from the PTCP for 24 K depositions was 11 mm – at least a factor of 3 lower than results for other tow sizes. When considering individual segment properties; heavier segments and segments with a larger geometric form would be expected to fall closer to the PTCP. This is not apparent when comparing 6 K and 12 K tows however. The spray bias applied by the chopping mechanism appears to be accentuated when increasing feedrate above 1 m/s

with a plateau between 2 m/s and 3m/s indicating that further increases in feedrate may not have any further influence on mean fibre locations.

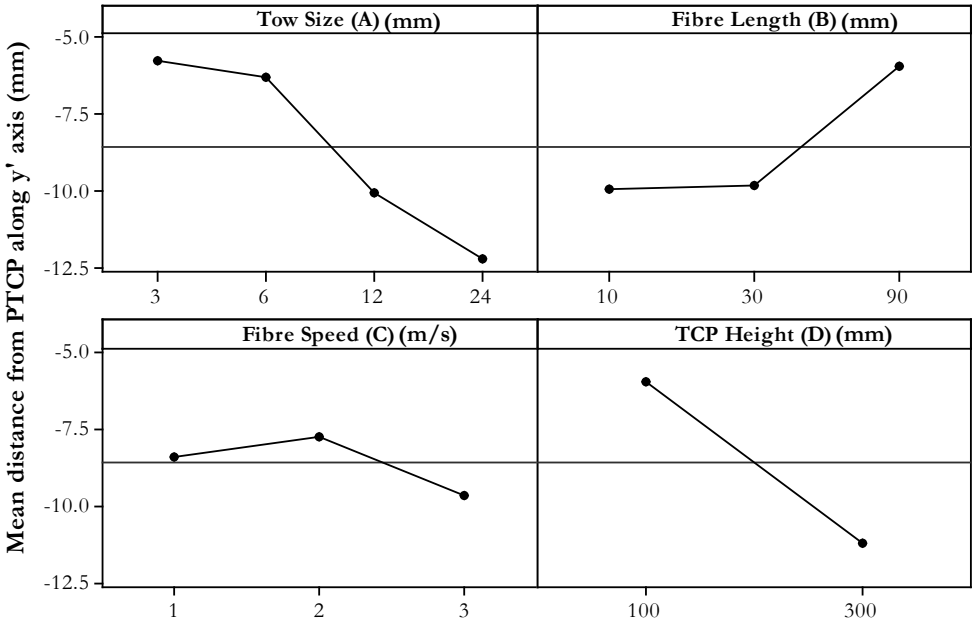

Figure 4-4: Main effects plot for mean segment midpoint location along the *y'* axis.

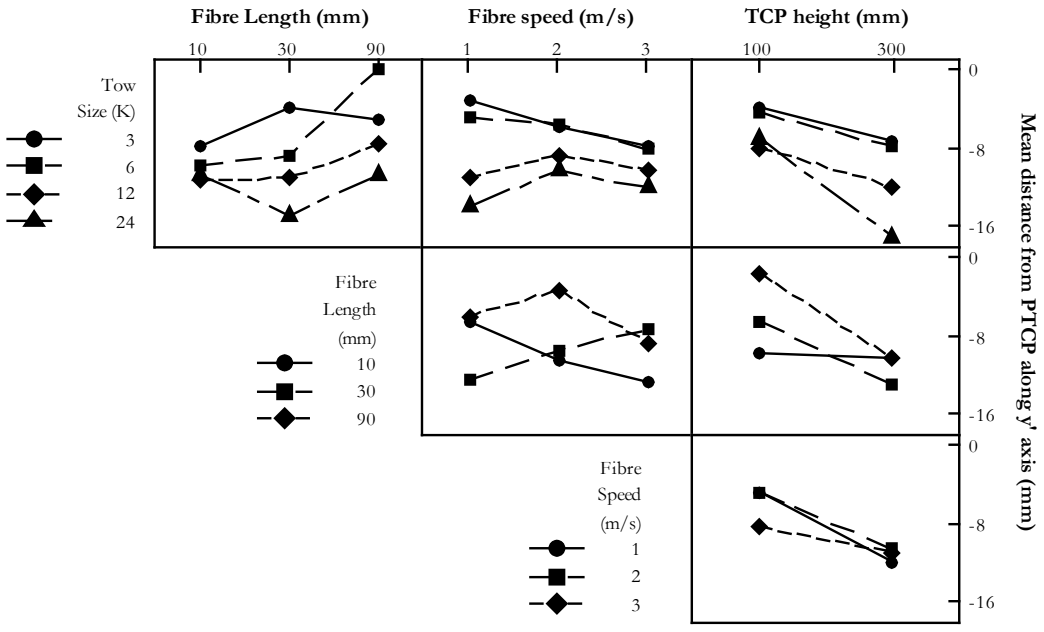

Figure 4-5: Two-way interaction plot for mean segment midpoint location along the *y'* axis.

Secondary interactions are shown in Figure 4-7. Although the main effects plot suggests that TCP height is the dominant factor with regards to mean fibre location, it is also apparent from the interactions plot that 24 K tows are affected less than other

tow sizes when changing the other factors investigated. The interactions plot confirms the complex relationships that exist between each factor as experienced for mean fibre location along the *y'* axis.

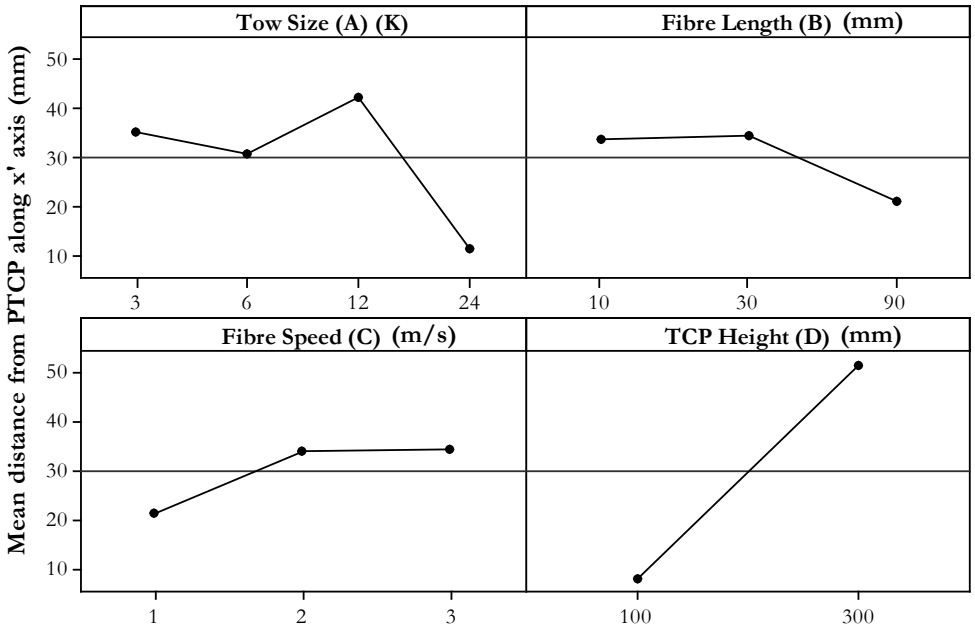

Figure 4-6: Main effects plot for mean segment midpoint location along the –*x'* axis

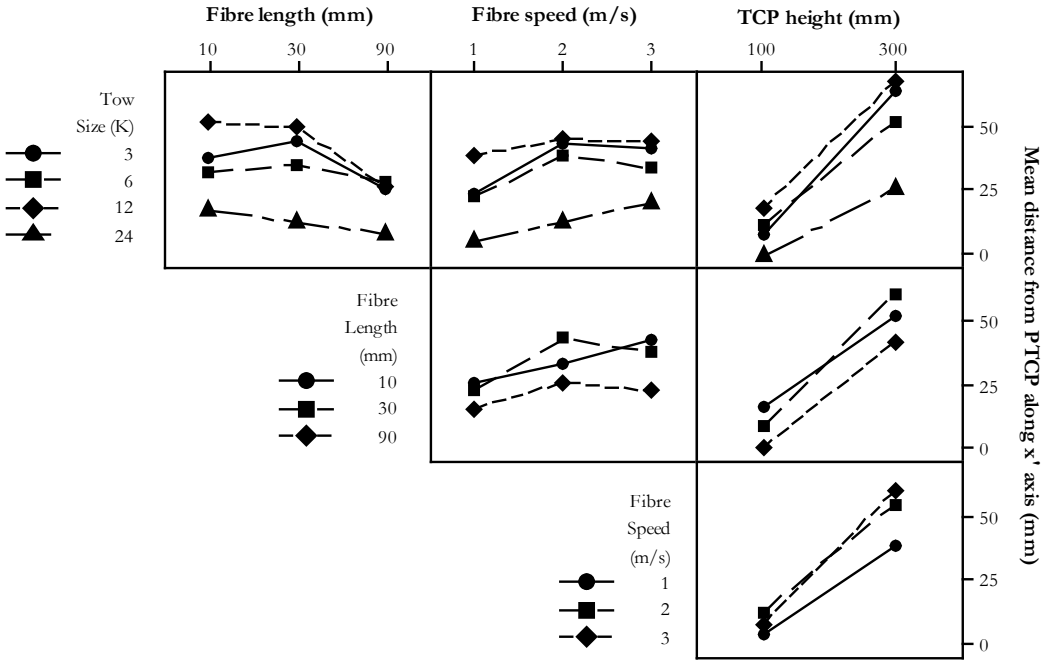

Figure 4-7: Two-way interaction plot for mean segment midpoint location along the –*x'* axis

As expected the distribution of fibres from the mean midpoint location was seen to increase in both the *x'* and *y'* directions with increasing TCP height in almost all

cases. This infers that as the deposition head moves away from the deposition plane the projected spray cone area increases. Figure 4-8 and Figure 4-9 present the main effects plots for dispersion from the mean to one standard deviation in the *y'* and *x'* directions respectively. TCP height is the dominant factor for fibre spread along the *y'* axis and also has a significant effect along the *x* axis; however, increasing fibre length between 30 mm and 90 mm sees the largest variation in dispersion from the mean. Fibre spread increases linearly with fibre speed in both cases whereas tow size appears to have very little effect. The mean dispersion for all the treatments highlight that a greater spread of fibres exists along the *x'* axis ($\sigma_{x'}$ = 36 mm) than the *y'* axis ($\sigma_{y'}$ = 24 mm). This suggests that the typical spray cone shape using the current deposition head design is elliptical rather than circular. Therefore, the generalised approach of using a circular spray cone shape utilised in other spray process models [53, 118, 159] is unsuitable.

Further analysis of each recorded deposition concluded that a normal distribution provides a satisfactory fit to describe the dispersion of segments from the mean in both the *x'* and *y'* directions. An example of the statistical fit is provided in Figure 4-10. Table 4-3 presents collated data for 3 K depositions which is used to define the geometric properties of the spray cone. The entire array of experimental data from the full factorial experiment is provided in Appendix B.

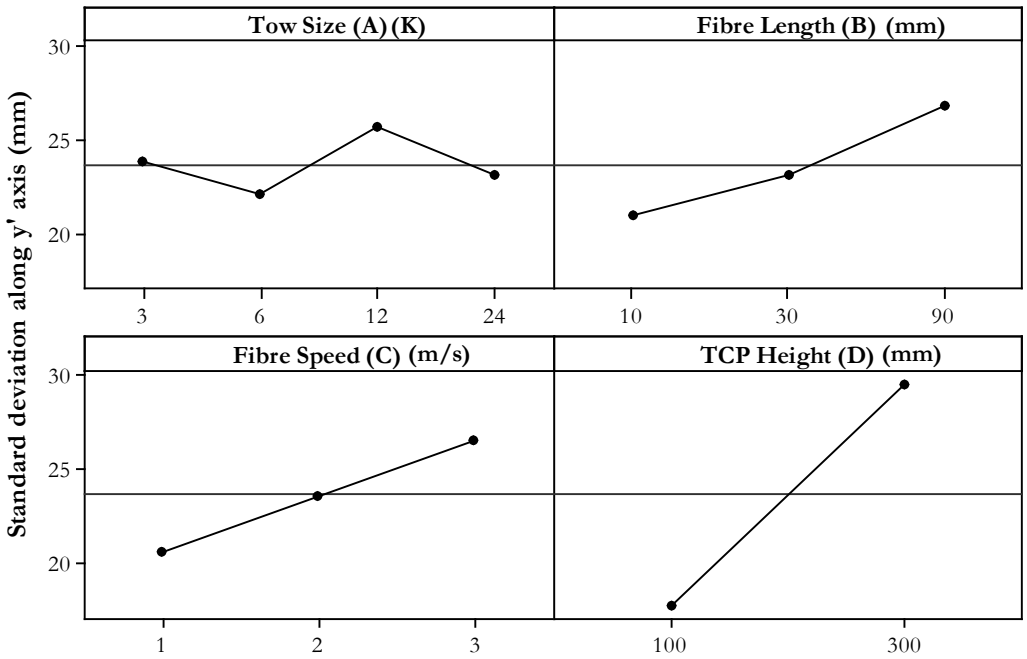

Figure 4-8: Main effects plot for segment midpoint spread to one standard deviation from mean midpoint locations (*y'* axis)

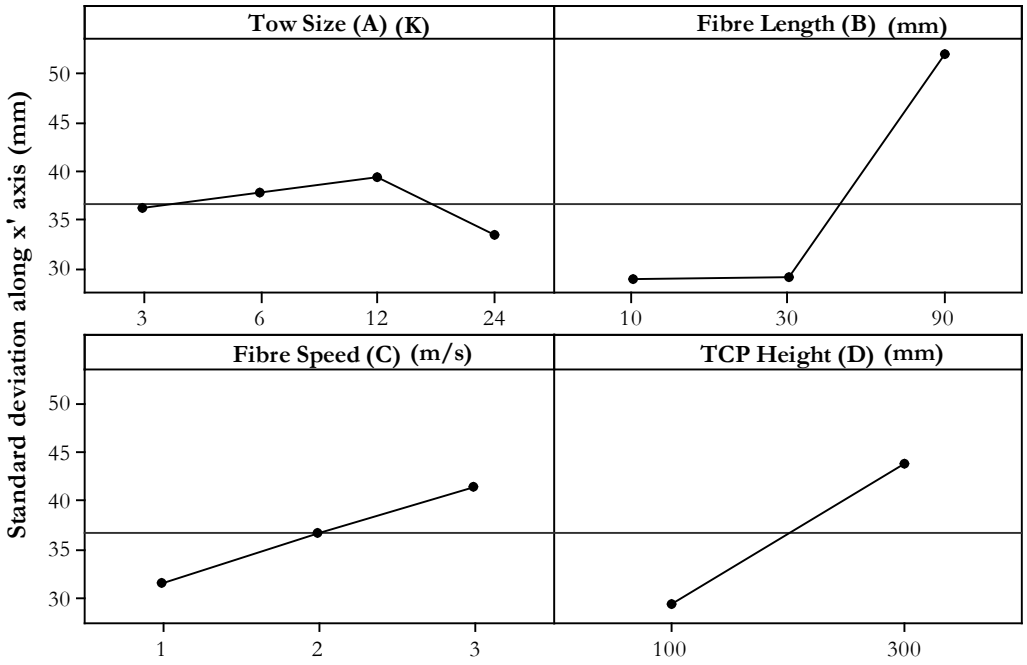

Figure 4-9: Main effects plot for segment midpoint spread to 1 standard deviation from mean midpoint locations (*x'* axis).

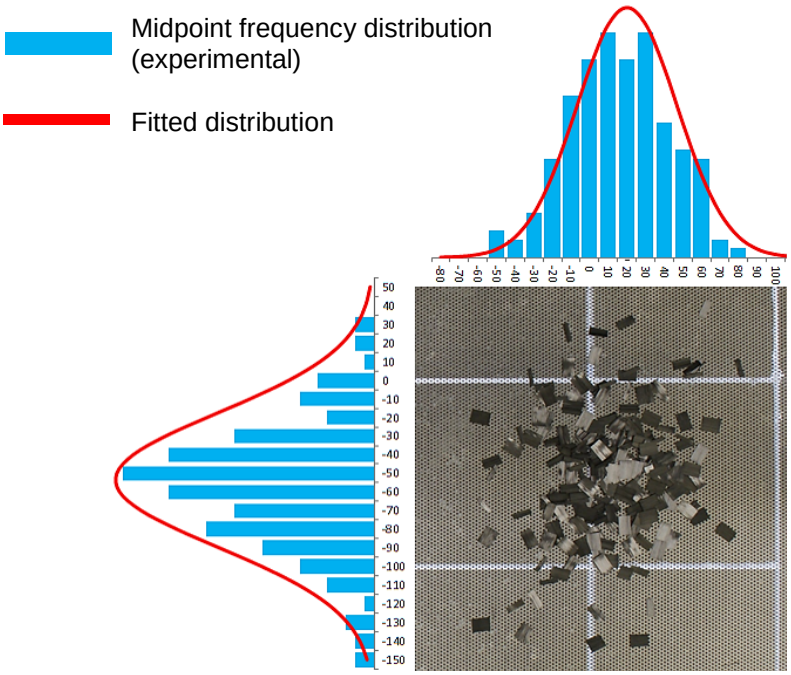

Figure 4-10: Fibre distribution from the mean midpoint location for a 12 K deposition (100 mm TCP height, 10 mm fibre length).

Table 4-3: Spray cone characteristics for 3 K tow segments. (* Projection angle values are explained in Section 4.2.4.2). Characteristics for 6, 12 & 24 K tow segments can be found in Appendix B.

Fibre length (mm)	Fibre Speed (m/s)	TCP height (mm)	Mean fibre location (mm)		Standard deviation (mm)		Projection angle* (degrees)	
			x'	*y'*	*x'*	*y'*	*x'*	*y'*
10	1	100	9.69	-7.69	12.40	12.90	1.06	5.82
		300	30.74	-3.59	30.47	29.67		
	2	100	21.28	-9.56	14.92	13.21	2.12	10.57
		300	55.13	-9.12	26.33	23.17		
	3	100	22.92	-10.55	17.37	14.36	1.92	15.07
		300	82.13	-7.64	34.02	27.96		
30	1	100	7.71	3.91	25.33	19.31	0.26	12.07
		300	68.69	-2.80	39.04	33.57		
	2	100	19.67	-7.61	19.80	10.43	1.31	15.74
		300	87.38	-5.09	26.98	21.56		
	3	100	-1.99	-11.40	36.35	14.83	0.86	13.70
		300	81.91	-1.18	36.98	35.58		
90	1	100	-7.36	2.34	51.04	21.63	2.40	3.95
		300	25.45	-12.00	54.12	26.27		
	2	100	11.44	2.75	44.52	23.47	0.63	10.85
		300	60.09	-6.81	63.88	29.74		
	3	100	-21.67	2.24	40.76	26.30	1.60	12.38
		300	80.36	-19.11	78.45	44.94		

The final procedure to characterise fibre spray was to determine the distribution of segment orientations between ±90° about the positive *x'* axis. It was observed that two types of distribution were common throughout the results; normal and uniform. For each treatment both distributions were fitted to a frequency density plot with the Kolmogorov Smirnov test employed to determine goodness of fit. A low significance level value ($\alpha = 0.01$) was used to compare with the test statistic to determine which hypothesized distribution was in closest agreement with the experimental distribution.

All depositions using 10 mm fibre lengths could be adequately approximated to a uniform distribution. Treatments with 90 mm fibres followed a normal distribution with increasing levels of alignment experienced as TCP height was reduced to 100 mm. For 30 mm fibre lengths, 24 K tows were uniformly distributed between ±90° for all fibre speed and TCP height combinations. For the other tow sizes a uniform distribution was only suitable for a fibre speed of 1 m/s. Faster rates of fibre ejection produced normally distributed fibre orientations. Orientation results for 3 K segments are presented in Table 4-4 with a complete set of results for each tow size in Appendix B.

Table 4-4: Fibre orientation distribution for depositions utilising 3 K tow.

Fibre length (mm)	Speed (m/s)	TCP height (mm)	Uniform distribution	Normal distribution	Mean (degrees)	Standard deviation (degrees)
10	1	100	•	-	-	-
		300	•	-	-	-
	2	100	•	-	-	-
		300	•	-	-	-
	3	100	•	-	-	-
		300	•	-	-	-
30	1	100	•	-	-	-
		300	•	-	-	-
	2	100	-	•	5.17	36.65
		300	-	•	0.61	43.63
	3	100	-	•	-2.29	40.96
		300	-	•	0.61	43.63
90	1	100	-	•	5.79	37.37
		300	-	•	8.33	39.38
	2	100	-	•	6.95	38.96
		300	-	•	3.06	42.09
	3	100	-	•	-3.21	41.00
		300	-	•	-4.77	39.15

The dominant factor affecting fibre orientation distribution was fibre length, the effects of which are clearly depicted in Figure 4-11 for a 24 K deposition. Longer fibre lengths have less time to rotate once released meaning that the inherent aligned state attained whilst processing the carbon tows through the deposition device is retained to some degree. As TCP height was raised to 300 mm the variance in segment orientation also increased for permutations following a normal distribution and remained uniform for all other treatments. Changes in fibre speed only appeared to noticeably influence the orientation distribution for treatments with 30 mm fibre length.

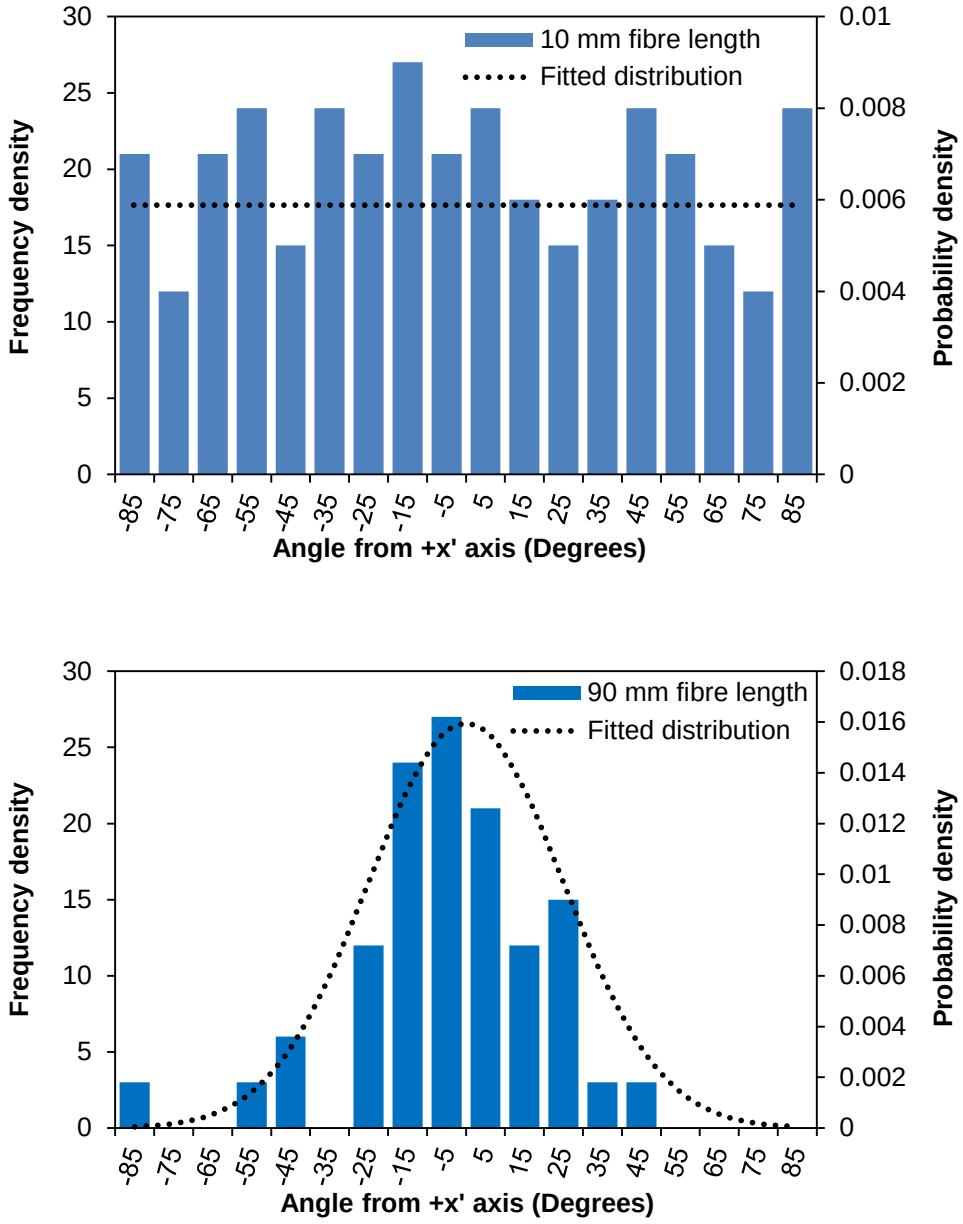

Figure 4-11: Frequency density plots for segment orientation with corresponding fitted distributions. Effects of increasing fibre length is clear, all other variables are kept constant (24 K, 100 mm TCP height, 1 m/s fibre speed).

4.2.3.2. Aligned deposition

Due to the close proximity of the alignment concentrator to the preform screen (50 mm) fibre speed had very little influence on the mean fibre location relative to the PTCP. Alignment plates restricted the motion of chopped segments along the *y'* axis with mean fibre locations within ±5 mm from the PTCP for all but one of the permutations (24 K, 90 mm). The mean fibre location along the *x'* axis was found to be fibre length dependant with fibre ends contacting the preform screen behind the

PTCP before falling forwards. This resulted in the mean fibre location moving closer to the PTCP as fibre length increased.

A large disparity exists between segment dispersion from the mean in the *x'*-*y'* plane due to the 12 mm channel between alignment plates constraining fibre motion in the *y'* direction. After averaging all the treatment results, $\bar{\sigma}_{x'}$ is found to be a factor of four greater than $\bar{\sigma}_{y'}$. This means that a slender elliptical spray cone is generated for aligned depositions at a TCP height of 110 mm.

In previous studies, levels of alignment were found to increase with tow filament count and fibre length [54]. This trend was observed for fibre length; however, alignment performance was less sensitive to tow size for long fibre lengths (90 mm) and was found to deteriorate using shorter fibres (30 mm) due to tow filamentisation (Figure 4-12). Peak levels of alignment were achieved processing 24 K, 90 mm fibres with 90% of fibres oriented within ±10º of the desired direction.

A Laplace distribution (double exponential distribution) was used to approximate fibre orientation with a normal distribution fit proving inadequate, agreeing with previous work conducted by Harper et al. [54]. For each treatment, segment orientations were reduced to angles between 0º and 90º and then mirrored about 0º resulting in a symmetrical distribution between ±90º. This increased the number of data points available to fit a Laplacian function as in Figure 4-12 using the following probability density function:

$$f(\theta) = \alpha\left(\frac{exp[-(|\theta| - \mu/\beta)]}{2\beta}\right) \quad \textbf{(4-1)}$$

where μ is the location parameter, β is the shape parameter, α is the normalisation constant and θ is the fibre orientation in radians between –π/2 and π/2. Curve parameters and percentage of fibres between ±10º for each aligned deposition (averaged over the fibre speeds investigated) is presented in Table 4-5.

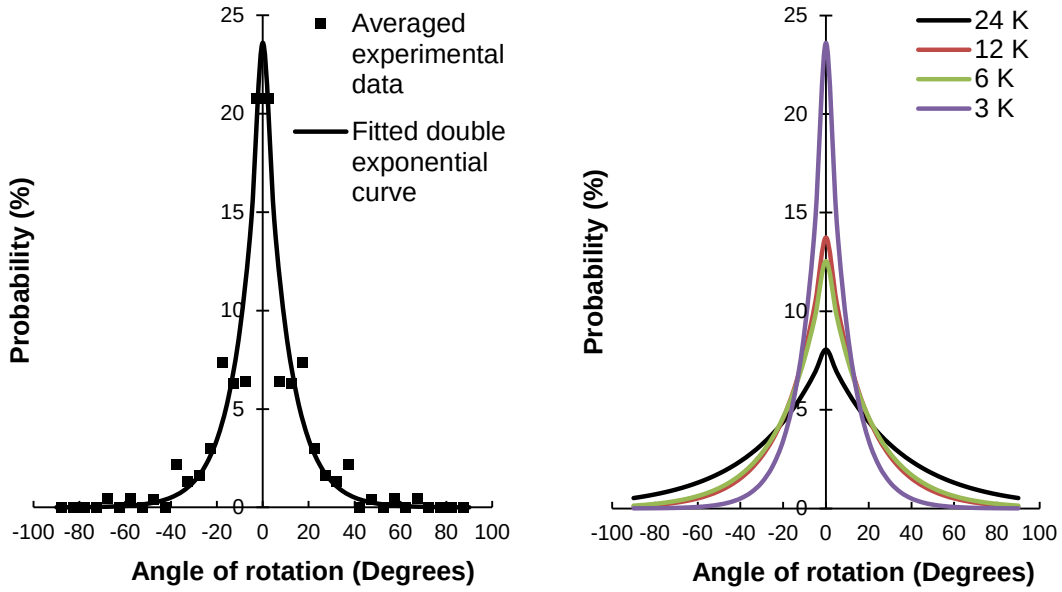

Figure 4-12: (Left) A typical aligned fibre distribution plot with fitted Laplacian curve. (Right) Fitted orientation distribution curves for 30 mm fibre lengths.

Table 4-5: Orientation distribution parameters for all tow size and fibre length permutations considered for alignment characterisation.

Tow size (K)	Fibre length (mm)	Normalization constant (α)	Location parameter (μ)	Shape parameter (β)	Fibres between ±10° (%)
3	30	1.20377	-0.4513	0.1814	60.2
3	60	1.03247	-0.3238	0.1387	51.7
3	90	1.03579	-0.3184	0.1362	88.3
6	30	1.23382	-0.4181	0.1664	55.3
6	60	1.09016	-0.3483	0.1458	81.3
6	90	1.05147	-0.2541	0.1080	89.7
12	30	1.11827	-0.7643	0.3175	47.3
12	60	1.10112	-0.3807	0.1587	75.0
12	90	1.08280	-0.3173	0.1332	75.1
24	30	1.09635	-1.3386	0.5752	31.1
24	60	1.05475	-0.4325	0.1345	82.4
24	90	1.09003	-0.1364	0.0571	90.0

4.2.4. Spray cone modelling

4.2.4.1. Modelling schema

Due to the complex interactions that exist between the four factors investigated, most likely arising from stochastic spray behaviour, it is unfeasible to produce a predictive model which can define spray cone geometric parameters with any confidence. Therefore a database containing spray cone characteristics was formed using the averaged results obtained from repetitions for each permutation. The database is

populated with information from both full factorial experiments for random and aligned depositions.

Prior to preform manufacture, the material parameters tow size and fibre length are fixed according to preform requirements. This leaves fibre speed and TCP height as the only variables which can change during the spray process. Fibre speed is dependent on both preform property requirements and robot trajectory whereas TCP height is entirely governed by robot trajectory and tool geometry. The database structure is therefore designed around this parameter order so that the process model can extract spray characteristics efficiently by performing a closest-match routine to each variable.

Tow size was seen to have a greater influence on the spray cone base centre point than fibre length (Figure 4-4 & Figure 4-6), consequently, the characterisation data is initially grouped by tow size and then by fibre length. The data can then be grouped further by fibre speed as this variable is less likely to change as frequently as TCP height for three-dimensional geometries. This leaves the spray cone characterisation data for each tow size, fibre length and fibre speed permutation stored as a function of TCP height. The database order is depicted in Figure 4-13 with the closest-match routine assessing each variable in turn to generate the appropriate spray characteristics.

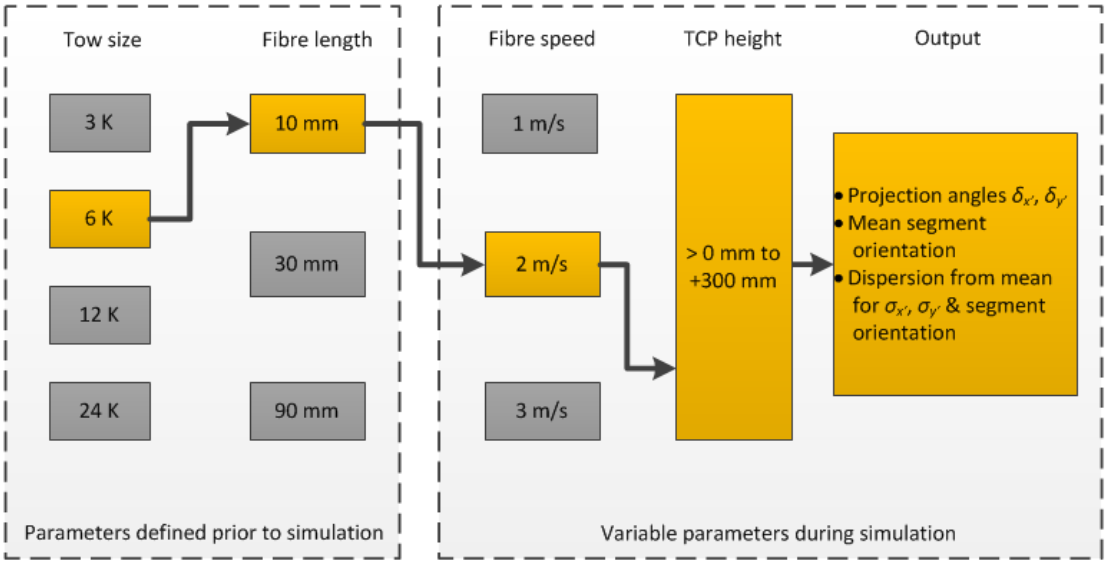

Figure 4-13: A diagram showing the execution order of the closest-match routine to extract spray cone geometry and segment orientation based upon tow size, fibre length, fibre speed and TCP height.

4.2.4.2. Determining spray cone characteristics

Figure 4-14 illustrates the response of mean fibre location as TCP height is increased for three separate variable permutations. Tow size and fibre length are held constant in this case (12 K, 10 mm) with the three data series representing different fibre speeds. A linear fit appears to provide a good approximation to the mean response in both directions and is tied through the origin. Figure 4-14 is representative for all tow size and fibre length combinations. The linear approximations in effect represent the spray cone centrelines in the *x* and *y* directions – finding the inverse tangent of the linear gradients provides the spray cone angles ($\delta_{x'}$, $\delta_{y'}$) used for process modelling in Chapter 6. Table 4-3 lists the spray cone angles for 3 K depositions and in Appendix B for other tow sizes.

For segment distribution from the mean, a linear approximation between the two data points (TCP heights of 100 mm and 300 mm) for each series is used (Figure 4-15). A third data point (the origin) cannot be applied in this case as in Figure 4-14. The same approach is used to describe the distribution of segment orientations about the mean orientation for random spray. For aligned depositions the TCP height is always assumed to be 110 mm and therefore the aligned spray cone characteristics are not stored as a function of TCP height.

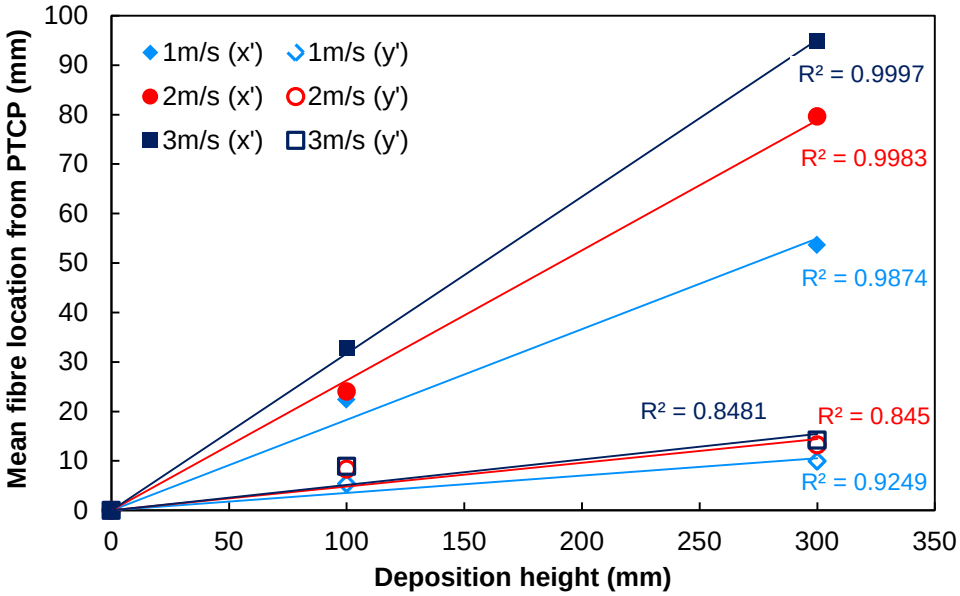

Figure 4-14: The effect of increasing TCP height on mean midpoint location. Different fibre speeds are shown for 12 K 10 mm fibres. A linear fit provides a good approximation to the spray cone centre point along both *-x'* and *y'* axes.

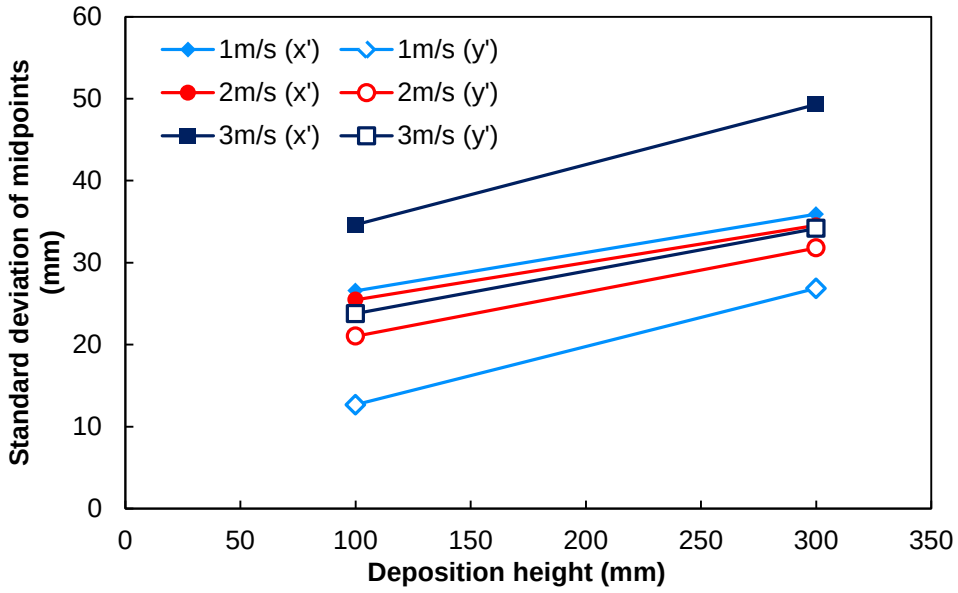

Figure 4-15: The effect of increasing TCP height on spread of segment midpoints from the midpoint mean. Different fibre speeds are shown for 12 K 10 mm fibres.

For every combination of tow size, fibre length and fibre speed there are six spray cone characteristics stored in the database: spray angles ($\delta_{x'}$, $\delta_{y'}$), distribution of fibres from the mean ($\sigma_{x'}$, $\sigma_{y'}$), orientation distribution σ_θ (if the orientation distribution is not uniform) from the mean orientation θ.

The process of simulating the randomised position and orientation of a fibre segment using the proposed database is described in Chapter 6. In summary, the spray angles are combined to generate a single spray cone centreline. The TCP height is then used to find the position of the spray cone centre point relative to the PTCP. Two random numbers are then generated to locate the segment midpoint in the deposition plane using the standard deviation values $\sigma_{x'}$ and $\sigma_{y'}$. A Box-Muller transformation is employed to transform a two-dimensional set of uniformly distributed random numbers to a bivariate normal distribution (Equations (4-2) and (4-3)). The simulated location for each fibre within the spray cone can then be found by scaling the normally distributed numbers by the fibre spread (to one standard deviation) depending on TCP height.

$$Z_{x\prime} = \sqrt{-2lnU_1}\cos(2\pi U_2) \quad \textbf{(4-2)}$$

$$Z_{y\prime} = \sqrt{-2lnU_1}\sin(2\pi U_2) \quad \textbf{(4-3)}$$

$$s_{x\prime} = \sigma_x Z_x \quad \textbf{(4-4)}$$

$$s_{y\prime} = \sigma_y Z_y \quad \textbf{(4-5)}$$

where $Z_{x',y'}$ is the standardised score, $U_{1,2}$ are uniformly distributed random numbers and $s_{x',y'}$ is the segment location from the mean in the in the *x'*-*y'* plane. The segment orientation is either uniformly random or calls once more on the Box-Muller transformation to randomly generate an orientation using the mean θ and standard deviation σ_θ. An example of a fitted segment midpoint distribution is presented in Figure 4-16 for both *x'* and *y'* directions.

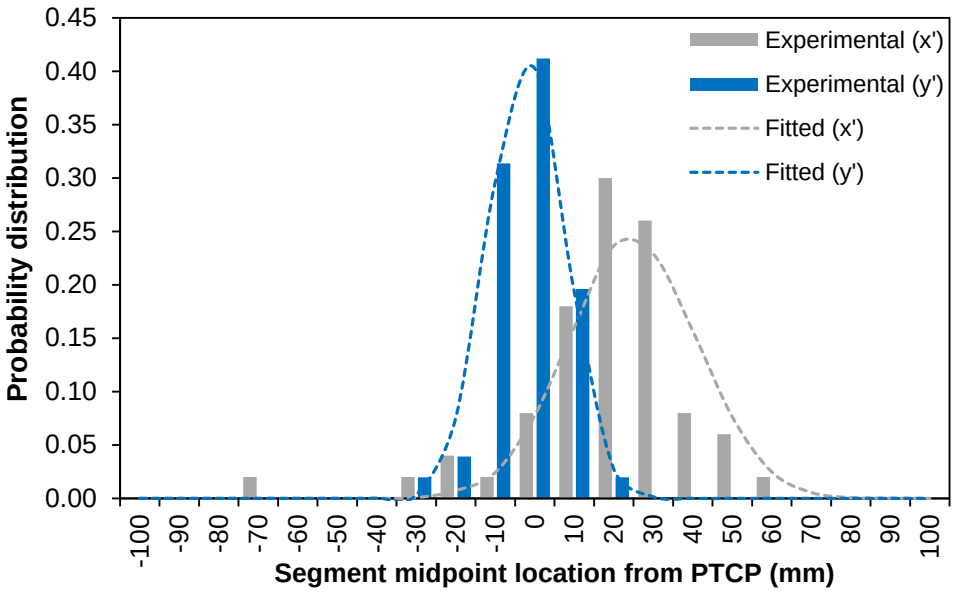

Figure 4-16: Experimental segment distribution versus a fitted distribution using the Box-Muller transformation for 6 K, 30 mm fibres at 2 m/s and a TCP height of 100 mm.

4.2.5. Conclusions

Four variables were identified as the principle factors governing fibre location distribution and orientation during preforming; fibre length, fibre speed, tow size and TCP height. Full factorial experiments for random and aligned depositions were performed over a range of values for each factor representing typical DCFP operating conditions. TCP height was determined as the dominant factor in defining spray cone geometry for random fibre spray. Increasing height accentuated a bias applied by the chopping mechanism which resulted in almost all depositions accumulating behind

the PTCP (along the local negative *x'* axis). Fibre distributions about the segment midpoint mean also increased in both the *x'* and *y'* directions with height thereby increasing the size of the virtual spray cone.

An important observation was made with regard to segment orientation for random fibre spray. Processing fibre lengths of ≥30 mm gave rise to a directional bias meaning that a quasi-random deposition can no longer be achieved without orienting the gun on subsequent passes to alleviate this effect. This is an important consideration when designing spray strategies to achieving desired laminate mechanical performance. The directional bias can also be diminished by increasing TCP height and reducing fibre speed.

Tight control over spray cone geometry was achieved using the alignment concentrator due to the constraints placed on ejected fibres. As a result of the slender spray cone profiles, accurate robot trajectory planning is required to produce homogeneous preforms. An optimised distance of 50 mm (110 mm TCP height) between the concentrator and the fibre bed was established through trial preforming operations where high levels of orientation could be achieved without disturbing deposited fibres. Orientation analysis showed that very high levels of alignment (>90% between ±10°) can be achieved whilst maintaining deposition rates comparable with typical random spray preforming.

A modelling schema was also presented which structures the entire array of characterisation data into a database with the intention of using a closest match routine to find representative empirically derived data to suit simulation conditions. The data is structured in order by tow size, fibre length and fibre speed. Spray cone geometry is retrievable as a function of TCP height which is the variable most likely to change during 3D preforming. This approach was adopted due to the complex interactions existing between the four parameters investigated meaning that a predictive model was unfeasible. Whilst this method of characterising the deposition device requires an investment in terms of time, it is clear that a reduced DOE may have missed some of the parameter interactions and possibly led to incorrect trends being identified.

4.3. Fibre flight kinematics

The deposition head characterisation study outlined a procedure to replicate fibre spray onto planar surfaces with knowledge of key process variables during simulation. To recreate fibre distribution for complex three-dimensional preforming other factors such as gravity and aerodynamic effects need to be considered. The initial trajectory of the fibre, from being released from the head, is determined by the head orientation and the four variables discussed in Section 4.2.2. The motion of the fibre is then dictated by aerodynamic drag and gravity which will ultimately determine final fibre locations on the tool surface; this section of work attempts to quantify these effects to develop a fibre flight model.

4.3.1. Methodology

This study comprised of two separate experiments. The first was a simple vertical fibre drop test to calculate drag terms for different tow and fibre length permutations. The second experiment involved processing the fibres through the deposition head positioned horizontally and recording the distance between the point of release and the landing site. The results from the second experiment were used to validate the drag coefficients derived from the drop test via a numerical fibre flight model.

Test specimens were selected to represent typical DCFP process parameters using four tow sizes; 3 K, 6 K, 12 K and 24 K cut to four lengths; 30 mm, 60 mm, 90 mm and 180 mm. The tow segments were released from a height of 4.34 m in a stable environment with the descent time recorded. The average descent velocity was calculated to find the resulting quadratic drag term. The quadratic drag equation was employed due to observed turbulence and relatively high speeds (>2 m/s) encountered when fibres are ejected from the deposition head.

$$F_D = -\frac{1}{2}\rho v^2 C_D A \tag{4-6}$$

where F_D is the drag force, ρ is the density of air, v is the fibre velocity, C_D is the drag coefficient and A is the reference area. The drag force can be determined assuming the fibre segment is in steady state where:

$$mg - F_D = 0 \tag{4-7}$$

During the experiment it was observed that fibres tend to fall in either a tumbling motion with angular momentum (bluff body) or close to vertical along the fibre axis (streamlined) (Figure 4-17). This adds significant complexity in trying to establish a consistent value for the reference area *A* therefore a value for the combined drag-area term C_DA was calculated – knowledge of the independent drag coefficient is unnecessary in context to creating a fibre flight model.

$$C_DA = \frac{2mg}{\rho v^2} \tag{4-8}$$

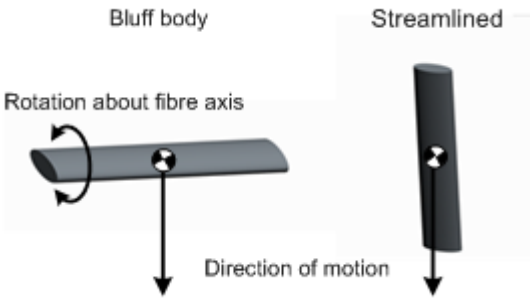

Figure 4-17: A diagram of bluff body and streamlined orientations which define segment descent behaviour.

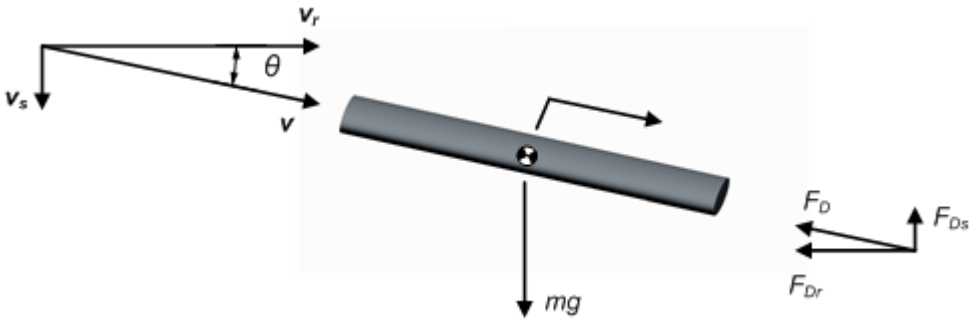

Figure 4-18: Free body diagram of the forces and velocity components acting on a tow segment during flight in the plane of motion.

A numerical model was developed to simulate projectile motion derived from the free body diagram in Figure 4-18. The fibre trajectory, after being released from the deposition head, was determined by considering motion in the horizontal *r* and

vertical *s* directions individually. The quadratic drag force in Equation (4-6) resolves along both axes as follows:

$$F_r = F_D cos\theta, \quad cos\theta \approx \frac{v_r}{v} \text{ so } F_r = F_D\left(\frac{v_r}{v}\right) \tag{4-9}$$

$$F_s = F_D sin\theta, \quad sin\theta \approx \frac{v_s}{v} \text{ so } F_s = F_D\left(\frac{v_s}{v}\right) \tag{4-10}$$

Substituting $b = \frac{1}{2}\rho C_D A$ so that $F_D = -bv^2$:

$$F_r = -bv^2\left(\frac{v_r}{v}\right) = -bvv_r \tag{4-11}$$

$$F_s = -bv^2\left(\frac{v_s}{v}\right) = -bvv_s \tag{4-12}$$

Resolving the forces along *r* and *s* gives:

$$ma_r = -bvv_r \tag{4-13}$$

$$ma_s = -bvv_s - mg \tag{4-14}$$

Substituting $v = \sqrt{v_r^2 + v_s^2}$ and rearranging gives the following closed form expressions for the segment acceleration along *r* and *s*:

$$\frac{d^2r}{dt^2} = \frac{-bv_r\sqrt{v_r^2 + v_s^2}}{m} \tag{4-15}$$

$$\frac{d^2s}{dt^2} = \frac{-bv_s\sqrt{v_r^2 + v_s^2} - mg}{m} \tag{4-16}$$

The solutions for v_r and v_s and position along *r* and *s* were solved numerically using the Euler method with a 0.001 s time step. The adopted Euler method was written in the C# programming language specifically for this task.

The second experiment involved positioning the deposition head so that segments are ejected parallel to the datum surface at an initial height of 0.4 m (Figure 4-19). The same tow size and fibre length permutations were processed from 1.8 m lengths of carbon tow at an initial fibre speed of 2 m/s. A grid of 20 x 20 mm cells was

positioned on the datum surface to accurately locate the deposited tow segments using the same image analysis outlined in Section 4.2.1 to find the mean segment midpoint location and the distribution from the mean to one standard deviation. The results from the second experiment were compared with predicted fibre locations output from the numerical model using C_DA values calculated from the first part of the study.

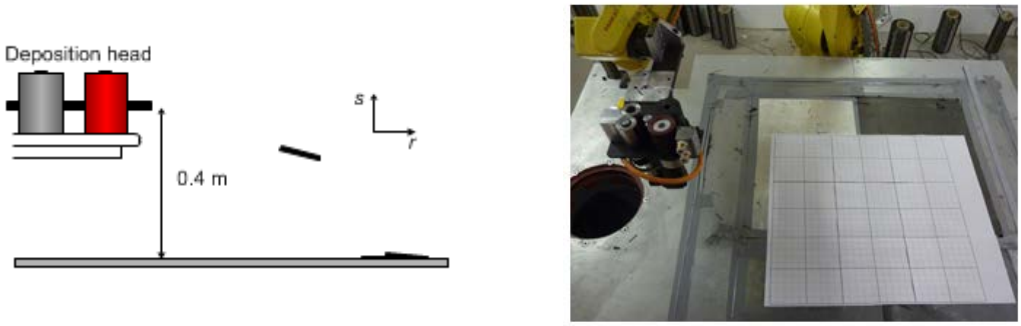

Figure 4-19: (Left) Schematic of the experimental setup (Right) with the 20 mm by 20 mm grid in place to accurately locate each deposited segment using image analysis techniques outlined in Section 4.2.1.

4.3.2. Results and discussion

Table 4-6 presents the C_DA terms calculated from the drop test using Equation (4-8). As anticipated C_DA values for the 12 K and 24 K segments are significantly larger than for 3 K and 6 K segments due to larger cross sectional areas in each of the segments principle axes. The predicted landing positions along with experimental data obtained from the second experiment are presented in Figure 4-20. The error bars for the experimental data series represent the dispersion of fibres from the mean location to one standard deviation.

The quadratic drag model significantly underestimates the distance travelled by each segment. Predicted values are ~50% of the observed mean midpoint locations for all tow size and fibre length permutations. However, the relationship between predicted distances for each permutation correlates well with experimental results which share similar trends.

Table 4-6: C_DA terms derived experimentally for each tow size and fibre length permutations. * denotes the two-component C_DA terms obtained to increase the accuracy of the numerical model. This is explained later in the text.

Tow size	Fibre length (mm)	Segment mass (kg) ($x10^{-5}$)	C_dA (m^2) (values from initial drop test, $x10^{-4}$)	C_dA_1* (m^2) ($x10^{-4}$)	C_dA_2* (m^2) ($x10^{-4}$)
3 K	30	0.6	0.64	0.72	0.32
	60	1.2	1.01	1.54	0.45
	90	1.8	1.74	2.04	0.50
	180	3.6	2.60	3.10	0.71
6 K	30	1.2	0.79	0.96	0.39
	60	2.4	1.33	1.79	0.51
	90	3.6	1.93	2.81	0.66
	180	7.2	2.52	3.78	0.91
12 K	30	2.4	1.86	2.48	0.86
	60	4.8	4.06	5.27	1.70
	90	7.2	4.88	6.27	2.11
	180	14.4	6.66	8.92	2.92
24 K	30	4.8	2.01	2.71	0.65
	60	9.6	4.44	5.44	1.23
	90	14.4	6.56	8.34	1.60
	180	28.8	8.54	12.70	2.01

By observing the flight of the fibre segment once ejected from the deposition head, it is clear that C_DA values are too high for the horizontal component of drag force. The segment initially exits the head aligned horizontally and therefore has a very low frontal reference area. In the vertical direction the entire length of fibre is contributing to the reference area and will therefore provide a greater resistance to motion. To account for this the model was modified so that separate C_DA terms were used along the longitudinal axis of the fibre, C_DA_1 and in the corresponding perpendicular direction accounting for the full length of fibre, C_DA_2. As previously discussed, two different mechanisms exist when describing tow segment descent during the vertical drop test. The longitudinal fibre axis was either aligned with the direction of travel or parallel to the ground revolving about this axis with angular momentum. The vertical drop test was extended to include 15 measurements for both characteristics separately, thereby achieving representative C_DA values rather than the combined values gathered previously. The two-component drag-area terms are included in Table 4-6. Figure 4-21 shows a vast improvement for model prediction by considering the orientation of the segment and the appropriate $C_DA_{1,2}$ terms in the r and s directions. Predicted values fall within experimental uncertainty for each tow size and fibre length permutation.

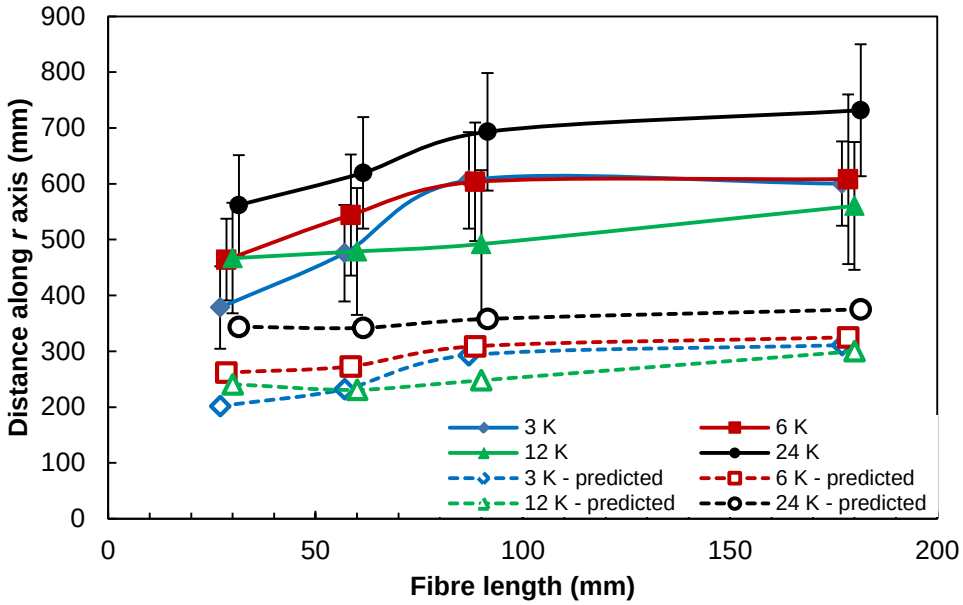

Figure 4-20: Comparison of experimental and predicted values for the distance along the *r* axis versus fibre length for each tow size. Predicted values using the numerical fibre flight model consistently under predict the final segment location by ~50 %.

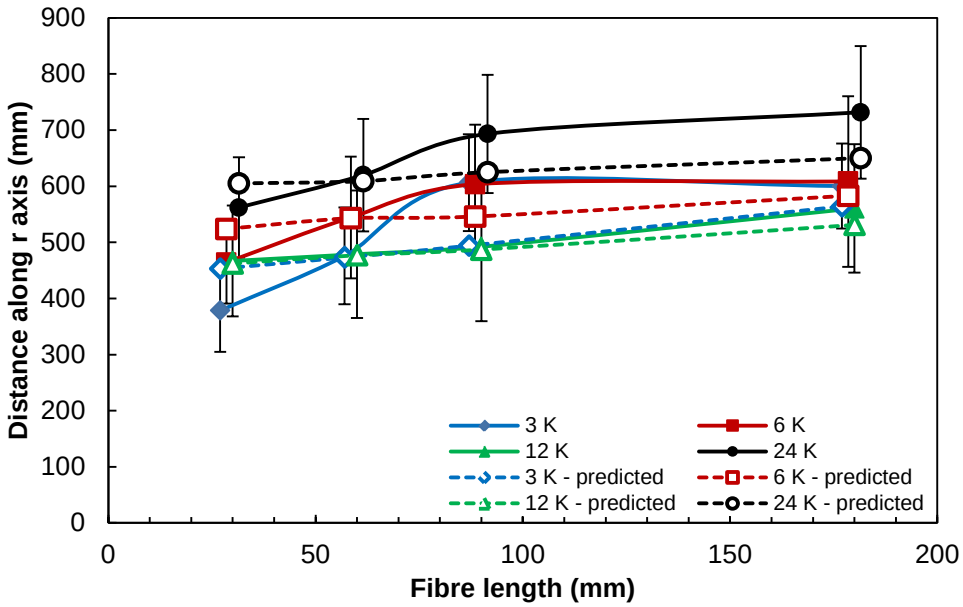

Figure 4-21: Comparison of experimental and predicted values for the distance along the *r* axis versus fibre length for each tow size. Predicted values are obtained using the two-component drag term producing simulated values within the error margins of the experimental results.

Plotting C_DA_1 and C_DA_2 terms against fibre length for each tow size investigated highlights a distinct relationship. Similar C_DA values exist for 3 K and 6 K tows and likewise for 12 K and 24 K tows (Figure 4-22 and Figure 4-23). This is due to the similarity in segment aspect ratios within the two groups where 12 K and 24 K segments are at least twice the width of the 3 K and 6 K variants. Quadratic curves are fitted to each tow size data series to approximate C_DA terms over the full range of

fibre lengths that can be processed using the UoN DCFP equipment. Table 4-7 presents the quadratic equation coefficients for each tow size.

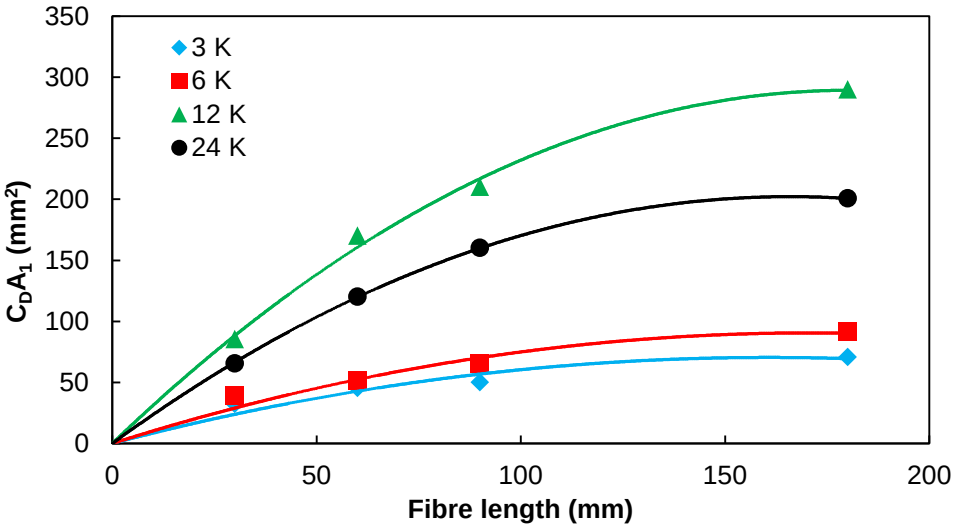

Figure 4-22: Streamlined drag term C_DA_1 versus fibre length for each tow size approximated by quadratic polynomial curves.

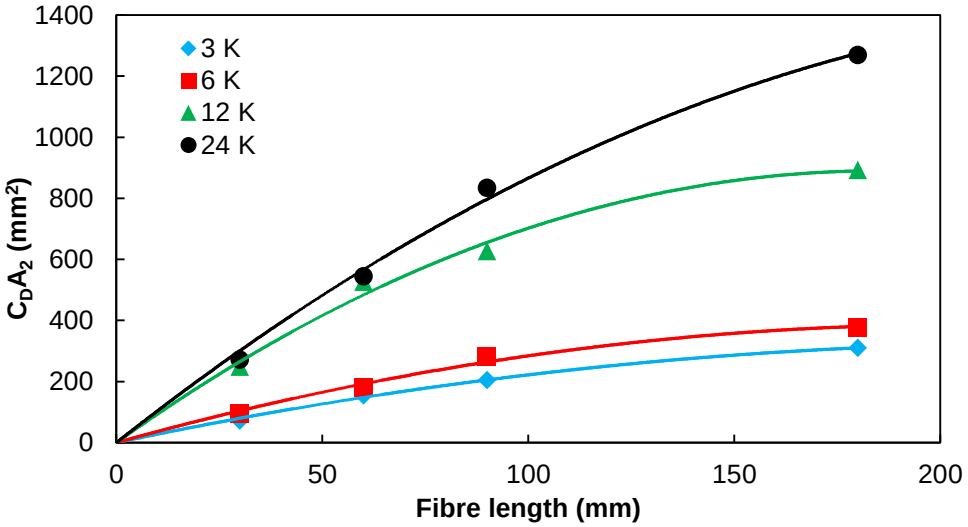

Figure 4-23: Bluff body drag term CDA2 versus fibre length for each tow size approximated with quadratic polynomial curves.

Table 4-7: Coefficients for the quadratic polynomial curves used to approximate the relationship between drag-area terms and fibre length in Figure 4-22 and Figure 4-23.

Tow size (k)	Quadratic coefficients					
	C_dA_1			C_dA_2		
	x^2	x	R^2	x^2	x	R^2
3	-0.0027	0.8772	0.84	-0.0062	2.8417	0.99
6	-0.0031	1.0590	0.91	-0.0091	3.7535	0.98
12	-0.0073	2.4380	0.99	-0.026	9.6250	0.99
24	-0.0089	3.2128	0.99	-0.0197	10.635	0.99

Figure 4-24 illustrates the effect of assuming zero drag or using a linear drag term compared with the adopted quadratic drag model for the predicted flight trajectory. For this particular case the zero and linear drag models overestimate the landing site by 20.1% and 14.4% respectively.

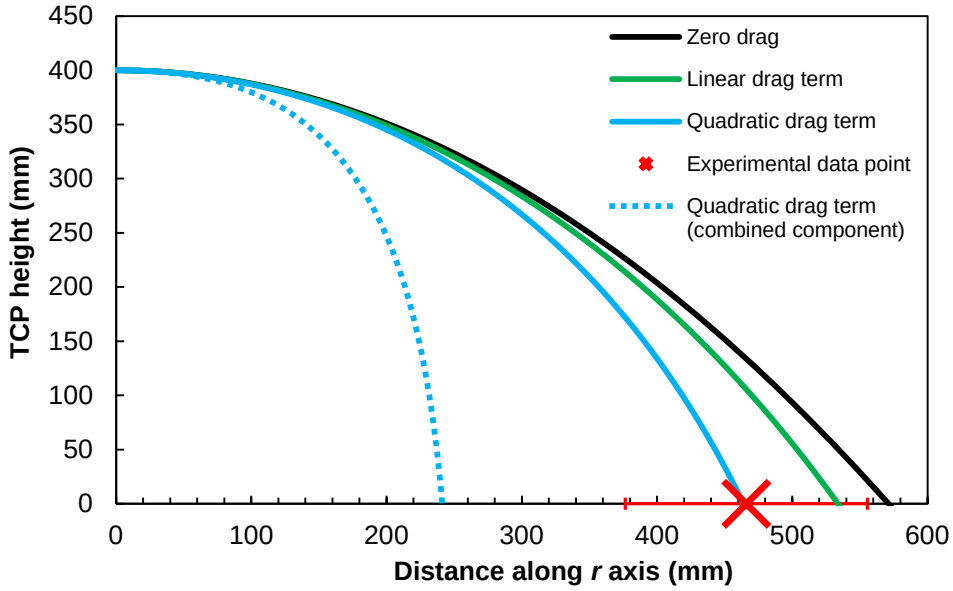

Figure 4-24: TCP height versus distance along *r* axis (horizontal distance) for simulated 12 K, 30 mm segment trajectories using different drag terms. An experimental data point with error bars (one standard deviation) is provided.

Further modifications are required to Equations (4-15) and (4-16) to account for variable deposition head orientations. It is assumed that the fibre segment is always aligned with the initial release trajectory for simplicity so that the two-component C_DA terms can be resolved along the horizontal and vertical directions in the plane of motion. The limiting bounds for the two C_DA values have been identified as the streamlined and bluff body orientations:

$$b_{1,2} = \frac{1}{2}\rho C_d A_{1,2} \quad \textbf{(4-17)}$$

However, to consider head orientations that are not coincident with the orthogonal directions *r* and *s*, new C_DA values must be obtained. This is achieved by determining the orientation of the deposition head relative to the vertical axis within the plane of motion and then scaling the C_DA values proportionately. For example, if the deposition head ejects segments vertically down to the tool surface the drag term along the *s* axis will be C_DA_1 due to the streamlined orientation. C_DA_2 would be used to resolve the segment velocity along the *r* axis. Turning the head through 90º so that the segments are now ejected along the *r* axis will switch the C_DA values accordingly. Any orientations in between will be proportionally scaled to lie between these two bounding conditions as follows:

$$ma_r = -\left[\left(1 - \frac{\theta}{90}\right)(b_2 - b_1) + b_1\right] v_r v \quad \textbf{(4-18)}$$

$$ma_s = -\left[\left(\frac{\theta}{90}\right)(b_2 - b_1) + b_1\right] v_s v - mg \quad \textbf{(4-19)}$$

$$\frac{d^2r}{dt^2} = -\frac{1}{m}\left[\left(1 - \frac{\theta}{90}\right)(b_2 - b_1) + b_1\right] v_r \sqrt{v_r^2 + v_s^2} \quad \textbf{(4-20)}$$

$$\frac{d^2s}{dt^2} = -\frac{1}{m}\left[\left(\frac{\theta}{90}\right)(b_2 - b_1) + b_1\right] v_s \sqrt{v_r^2 + v_s^2} - g \quad \textbf{(4-21)}$$

4.3.3. Conclusions

A study into the flight characteristics of typical tow size and fibre length combinations used in DCFP has highlighted the need for an appropriate model for 3D preforming simulation. Two modes of flight have been identified; streamlined and bluff body, which significantly alter the corresponding drag-area term required for predicting fibre trajectory. Through observation, it was found that chopped segments exit the deposition head in a streamlined orientation with the initial direction of travel. By

using a two-component drag-area term, to account for segment orientation, a numerical model based upon projectile motion was developed providing reasonable approximations for all tow size and fibre length permutations investigated when compared to experimental results. A further modification was made to the governing projectile motion equations to account for variable deposition head orientations. This was achieved by scaling the two-component drag-area terms according to initial segment trajectory in the plane of motion.

4.4. Chapter conclusions

The objective of this chapter was to identify and understand the key process variables which affect fibre distribution during the preforming process. Four variables (tow size, fibre length, fibre speed and TCP height) were varied within typical operating bounds for DFP processes to characterise their influence on fibre location and orientation relative to the deposition device. Fibre spray was modelled to conform to a cone with segment midpoint location data, obtained from discrete depositions, used to define the cone geometry. TCP height was found to have the greatest effect on cone geometry for random spray with the projected spray area increasing as TCP height increased. A chopping bias was also accentuated with TCP height resulting in segments accumulating at varying distances from the target area. The other variables investigated also affected both fibre distribution and orientation, however, data analysis failed to identify consistent interactions between the process parameters required for predictive modelling. Therefore, it was suggested that the acquired characterisation data is stored in a database employing a closest-match routine to extract spray cone geometry and orientation data for process modelling.

Characterisation of aligned fibre deposition showed that very high levels of alignment (>90% between ±10°) is achievable whilst maintaining deposition rates comparable to random spray preforming – a significant improvement over previous alignment methods used in DCFP. Levels of alignment were seen to increase with fibre length leading to slender spray cone profiles making accurate robot path programming essential to achieve homogeneous fibre distribution.

A study into the flight kinematics of ejected tow segments revealed that initial fibre orientation to the direction of motion has a significant bearing on flight trajectory predictions. A semi-empirical fibre flight model was developed with a two-component drag-area term to take into account the initial segment trajectory. Predicted deposition sites fell within experimental bounds of uncertainty for each tow size and fibre length permutation tested.

The modelling procedures discussed in this chapter are used in the development of the DFP process model in Chapter 6.

Chapter 5. Process characterisation – fibre retention

5.1. Introduction

Many preforming processes are reliant upon air suction to provide retention of fibres, fibre bundles or textile broad goods. This method of retention is particularly prevalent in directed fibre preforming and other process derivatives. A large centrifugal fan evacuates air from behind a perforated screen with fibres retained on the screen by atmospheric pressure until a binder is applied and cured. Upon cessation of the air flow the shape of the preform is retained. Sizing of the fans for this type of process tends to be highly empirical and little data is available on the performance of various fibre types and on the factors that dominate performance. Of particular interest is the force available to retain the fibre bundles on the preform screen and thus the maximum thickness or areal density that can be deposited on vertical or complex surfaces. This section of work aims to identify the limiting factors in fan selection and to investigate various fibres and preform types to determine the maximum areal density and determine coefficients that can be used in analytical and computational fluid dynamics models. Furthermore the exact mechanism of fibre retention is not well understood – the relative contribution of atmospheric pressure derived force and aerodynamic bluff body inertial force is not known.

5.2. Methodology

This section provides details on the apparatus used to measure air flow characteristics and on the performance of the installed UoN DCFP vacuum fan.

5.2.1. Air flow measurement

BS EN ISO 5801:2007 provides the recommended apparatus geometry and a method for determining the mass flow rate for air drawn from free space - as is the case for the DCFP facility. Mass flow rate was measured using a conical inlet duct taking pressure

readings with respect to atmosphere at a certain point downstream of the inlet. Figure 5-1 shows the geometry of the airflow measurement duct which was placed in the position normally occupied by the preform screen (Figure 5-2). To initially characterise the entire system (vacuum fan with upstream ducting including the plenum section) the differential pressure was measured with a FC0510 digital micromanometer and logged with respect to fan speed. The materials tested in this study were placed on a perforated screen located in the middle of the duct with a second micromanometer attached to the apparatus to measure pressure differential readings across the plate and fibre stack in order to generate mass flow/pressure drop curves. The mass flow rate was determined according to Equation (5-1).

$$q_m = \alpha\varepsilon\pi\frac{d^2}{4}\sqrt{2\rho_u}\Delta p \quad \textbf{(5-1)}$$

q_m, mass flow rate (kg/s)

d, throat diameter (m)

ρ_u, upstream density (kg/m^3)

Δp, pressure difference (Pa)

α, flow coefficient

ε, expansibility factor

where d = 0.2 m (Figure 5-1), $\alpha\varepsilon$ = 0.94 in accordance with BS EN ISO 5801:2007 and ρ_u = 1.1839 kg/m^3 at an ambient temperature of 25ºC.

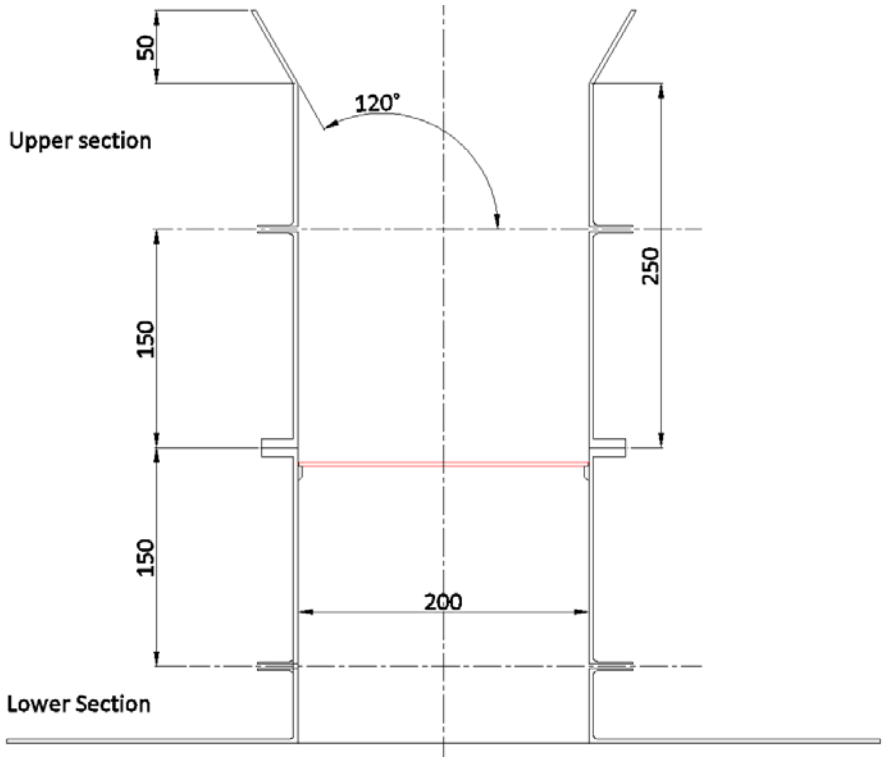

Figure 5-1: Schematic cross section of the conical test duct used to measure mass flow rate. A perforated plate is placed near the middle of the duct which holds the material specimens.

Figure 5-2: Experimental setup with the test duct positioned in place of the perforated screen.

5.2.2. Fan performance

A Halifax Fan Ltd Chinook No. 27 backward inclined centrifugal fan is used to provide a vacuum for fibre retention in the current UoN DCFP facility. The initial sizing of the fan was based on discussion with DFP system users which suggested that a fan of 10,000 m^3/hr volume flow rate and 800 mmWG fan pressure would be

sufficient for a 1 m^2 preform area. The fan speed is controlled by a 37 kW WEG CFW09 inverter. A filter system is used between the fan and the preform bed which comprises of 3 large F9 grade particulate bag filters with efforts being made to seal the entire system from air leakage. Figure 5-3 shows the pressure versus mass flow rate characteristics of the fan at various speeds using data supplied by the fan manufacturer. Figure 5-4 shows the absorbed power for both a fully open condition (no preform screen) and the fully blocked condition. The final operating power is determined by the extent of preform coverage and the size of the installed preform screen and thus lies somewhere in the region bounded by the two curves. Maximum suction level for a fan speed of 2500 rpm was measured at 5492 Pa which agrees well with the manufacturers' scaled performance data reproduced in Figure 5-3 and suggests that some leakage in the system upstream of the test apparatus allows the generation of slightly higher static pressures at zero measured mass flow.

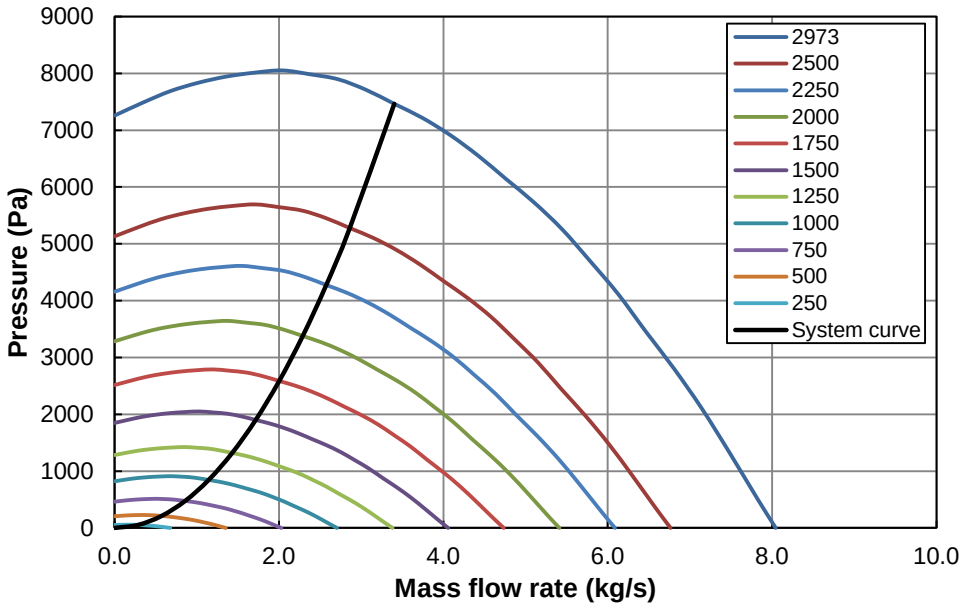

Figure 5-3: Performance characteristics of the installed DCFP fan for various fan speeds given in rpm.

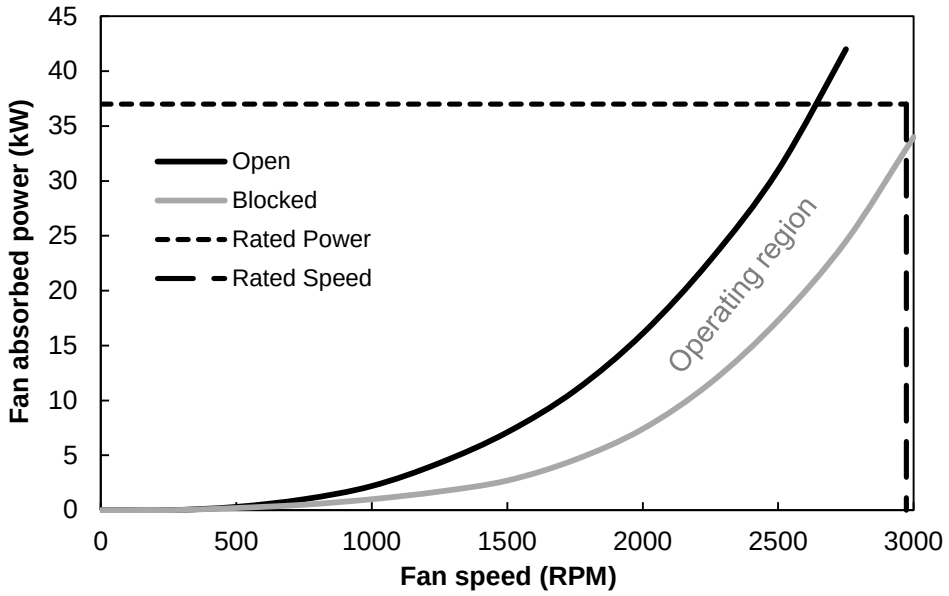

Figure 5-4: Absorbed power characteristics of the installed DCFP suction fan

Table 5-1 summarises the wide variety of materials tested to provide an extensive cross section of fibrous architectures and mediums available for preforming. It was of particular interest to determine the effect of tow size i.e. the difference between a highly lofted low filament count random material and a 24 K unidirectional material with large stitches. It was also desirable to establish whether DCFP architecture is analogous to a fabric material as deposited areal mass increases.

Specimens for the apparatus were prepared using a circular die cutter of 200 mm diameter to place over the top of the perforated plate in the experimental duct. Glass and carbon fibre rovings were chopped directly into the duct using the DCFP deposition device with an Archimedean spiral robot trajectory programmed to provide a uniform distribution.

Pressure differential measurements for each material type across the range of areal mass values supplied in Table 5-1 were logged for fan speed increments of 250 rpm between 0 rpm and 2250 rpm.

Table 5-1: Details of the coupon materials and their corresponding lay-up configurations. * denotes supplier areal density data.

Material type	Supplier	Designation	Areal density*	Tow size	Tested orientations	Tested areal density (gsm)
Non-woven carbon fibre mat	Technical fibre products	TP-10	10 gsm	Single filament CF	0°	10,20…120, 200, 300, 500
UD Non-crimp fabric	Sigmatex	PC333	450 gsm	24 K Toho Tenax STS 5631 CF	0°	450,900,1350…3600
UD Non-crimp fabric	Sigmatex	PC251	300 gsm	12 K Toray T700 50C	0º, 0/90º, 0/90/±45º	300, 600, 900….3600
UD Non-crimp fabric	Sigmatex	PC278	200 gsm	12 K Toray T700 50C	0°	200,400,600...1200
Continuous filament random mat	Vetrotex	U750-375	375 gsm	25/50 tex GF	Random	375, 750, 1125…9000
Chopped strand mat	Owens Corning	M534-450	450 gsm	N/A	Random	450,900,1350…4500
Chopped glass roving (F3P)	PPG	2001-600TEX	-	600 tex	Random	32, 64, 96, 128, 256, 384, 512, 640, 960, 1280
DCFP	Sotira	-	-	-	Random	1267, 2597, 3947
DCFP	UoN	24 K E STS 5631	-	24 K	Random	939, 1951
DCFP	UoN	3 K E HTA40 E13	-	3 K	Random	471, 1009, 1509, 2040

Two perforated preform screens (coarse and fine), manufactured from mild steel, were tested as representative of commonly used screen geometries. The coarse screen has a thickness of 2.5 mm with 4 mm diameter holes on a 6 mm diagonal pitch (40% open area). The fine screen has a thickness of 1 mm with 1 mm diameter holes on a 2 mm diagonal pitch (23% open area).

5.3. Modelling porous media

The computational fluid dynamics code Fluent (Ansys Ltd) was used to model the behaviour of the perforated plates and preform layers. The recommended porous jump boundary condition is a 1D simplification of a porous zone and allows the user to specify coefficients which describe the performance of a perforated plate or a packed bed under various flow conditions. The pressure drop produced by a porous jump is described by Equation (5-2) which is a modified form of Darcy's law including an inertial resistance term.

$$\frac{\Delta p}{\Delta h} = \frac{\mu}{\alpha} U + \frac{1}{2} \rho C_2 U^2 \qquad \textbf{(5-2)}$$

where μ is the laminar fluid viscosity, α is the permeability of the medium, C_2 is the pressure-jump coefficient, U is the air velocity normal to the porous face, and Δh is the thickness of the medium [160].

5.4. Results

5.4.1. Performance of perforated preform screens

Figure 5-5 shows the mass flow versus pressure drop performance across the coarse and fine preform screens. As expected the screen with fine perforations provides significantly higher resistance to air flow than the coarse plate. A polynomial curve was fitted to the experimental data where the behaviour was seen to be entirely dominated by the pressure-jump coefficient C_2 and not the permeability α from Equation (5-2). An excellent quality of fit was obtained up to flow rates of 1 kg/s. For the coarse plate C_2 = 2715 (R^2 = 0.997) and for the fine plate C_2 = 17117 (R^2 = 0.9999) implying that the pressure drop caused by the fine plate is approximately 6 times that of the coarse plate. Table 5-2 summarises the limiting performance of the ducted system at each fan speed set point for a fully open and closed duct.

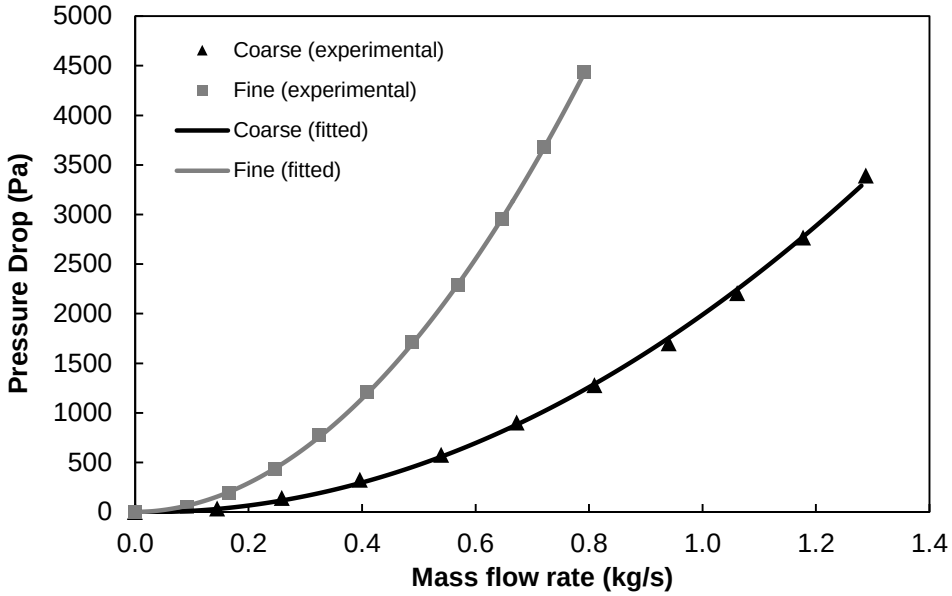

Figure 5-5: Characterisation of perforated plate performance comparing two different geometries.

Table 5-2: Performance limits of the ducted system.

	Open duct (no plate)	Closed duct (sealed)
Fan speed (rpm)	**Mass flow rate (kg/s)**	**Pressure drop (Pa)**
250	0.296	53.9
500	0.647	223.6
750	0.951	513.9
1000	1.305	924.8
1250	1.609	1451.4
1500	1.928	2069.2
1750	2.282	2804.7
2000	2.563	3657.9
2250	-	4560.1

5.4.2. Performance of various fabric preform architectures

The same curve fitting approach was employed for both the fabric and discontinuous fibre preforms using experimental data recorded at fan speeds up to 2250 rpm. For the majority of fabrics the quadratic curve fit (Equation (5-2)) produced a poor fit as areal mass increased. A high quality fit to experimental data was achieved using a quartic polynomial curve. For all materials tested the cubic and linear terms of the polynomial were over 10 orders of magnitude smaller than the quartic and quadratic terms and therefore considered negligible in determining pressure drop. Therefore the fitted curves take the form of a biquadratic expression as follows:

$$\frac{\Delta P}{\Delta h} = aU^4 + bU^2 \quad \textbf{(5-3)}$$

Initial biquadratic expressions combined the effect of both the first layer of fabric and the coarse preform plate. Subsequent layers of fabric contribute to increasing *b* values as air flow reduces towards 0 m/s and material thickness increases. The quartic coefficient *a* does not follow a similar correlation with areal mass across the different materials. Figure 5-6 shows the superficial air velocity versus pressure drop performance of a single layer of fabric restrained by the coarse preform screen for selected materials. It should be noted that maximum pressure drop across the plate is achievable when the duct is completely sealed above the plate resulting in no air flow through the duct. Fitted curve coefficients for each tested fabric over the range of areal masses set out in the design of experiments is presented in Appendix C.

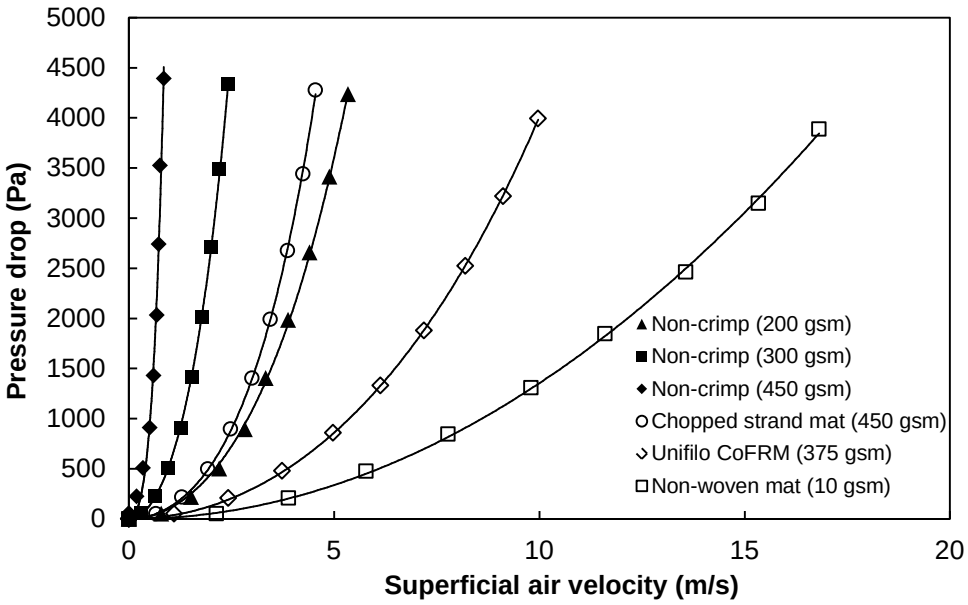

Figure 5-6: Comparison of the resistance characteristics for the first layers of selected woven and non-woven fabrics.

5.4.3. Performance of discontinuous fibre architectures

Discontinuous fibre preforming consists of depositing fibres at a desired rate to achieve a target areal density. This differs to fabrics which build up part thickness through the addition of discrete layers. As fibres are deposited in DFP processes the areal density increases as a function of linear fibre speed. Therefore to efficiently manage the fan speed to provide enough retention pressure throughout the deposition,

a characterisation study was conducted using both 24 K and 3 K fibres. By controlling the speed of the fibres being processed through the deposition head, the number of chopped fibres could be determined and used to calculate the areal mass for each cycle. Figure 5-7 shows the pressure drop and superficial air velocity response as areal mass is increased for a maximum fan speed of 2250 rpm. The random deposition of carbon tow segments shares very similar characteristics with the non-crimp UD fabric, particularly for 3 K tows. To achieve equivalent areal densities, the segment count for 3 K depositions is 8 times greater than when using 24 K tows. The increase in segment count results in improved coverage of the perforated plate – blocking open channels for which air can pass through. This explains the lower superficial velocities recorded up to 600 gsm and the faster rise in pressure drop before reaching a plateau.

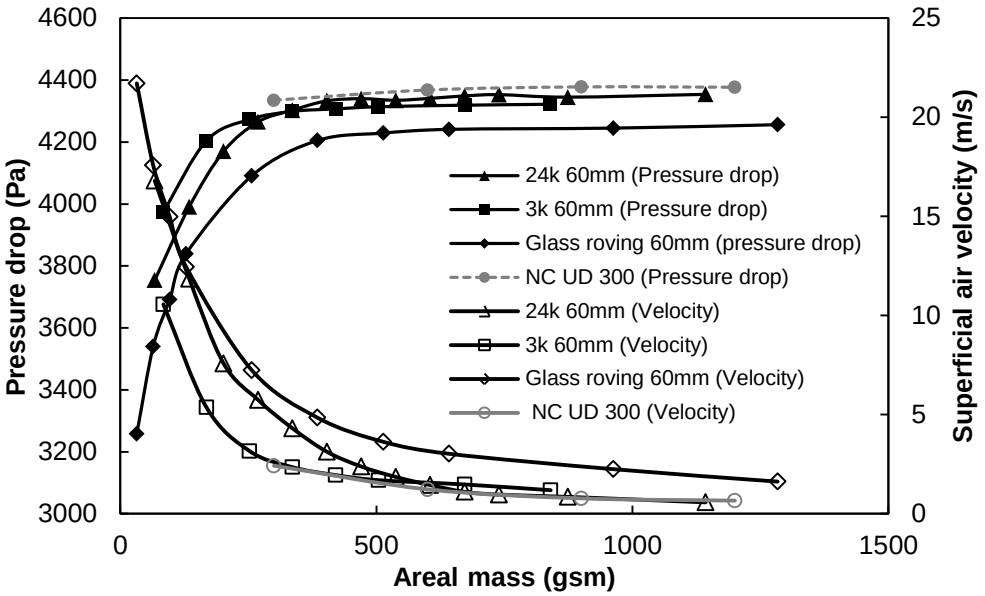

Figure 5-7: Change in pressure drop and superficial air velocity as areal mass is increased for 24 K and 3 K carbon tows and glass rovings. All fibre segments are 60 mm in length and fan speed is held constant at 2250 rpm. The data for NC-300 UD fabric is included for comparison.

5.4.4. Discussion

The purpose of this study was to characterise the chosen materials so that for a given areal density the air velocity is sufficient for full retention on the preform screen. The pressure required to retain the material was calculated from the areal density (kg/m^2) for one layer of fabric by dividing the weight of the fabric by the area of the specimen. A summary of the required pressure values for each fabric is presented in Table 5-3. In theory additional layers can be added until the maximum permissible pressure drop

at that particular fan speed is reached, however this is unrealistic as an undetermined amount of fabric layers is required to achieve a fully sealed state. This is due to the nature of the porous media, such as the materials investigated, allowing air to flow through the thickness preventing complete vacuum. The method of determining if there is enough available head pressure is to add a layer of material and observe the pressure difference between the current and previous layer. If the change in pressure drop between layers is less than the required pressure drop then this means the current fan speed is insufficient to hold the fabric in place. In this case the fan speed needs to be increased until a high enough head pressure is reached within the system limits.

Table 5-3: The retention pressure required for selected fabrics and discontinuous fibre architectures.

Material type / Composition	Areal density (gsm)	Required retention pressure (Pa)
Non-crimp UD 0º	200	1.96
Non-crimp UD 0º	300	2.94
Non-crimp UD 0º	450	4.41
Unifilo CoFRM	392	3.87
Chopped strand	512	5.03
Non-woven mat	10	0.10
24 K DCFP preform	939	9.21
3 K DCFP preform	471	4.62
24 K DCFP segment spray	67	0.66
3 K DCFP segment spray	84	0.82
Glass roving spray	32	0.31

Results suggest that for 300 gsm non-crimp fabric a maximum of 3 layers (900 gsm) can be retained by the fan at 2250 rpm whereas the glass CoFRM mat can be built up to over 9300 gsm. By combining the pressure drop and mass flow data with the fan curve a decision can be made on how many layers can be stacked before being constrained by fan performance.

To calculate the required speed for a given fan specification an iterative model is proposed. Using manufacturer's data for volume flow rate versus head pressure a fan curve can be modelled and scaled accordingly with respect to fan speed. Each ply of material deposited onto the preform screen can be represented by a resistance curve on the fan curve plot. The equations for each resistance curve is fitted as described previously. Initially, there are two resistance curves for the preform screen and the first layer of fabric, and a fan curve for the minimum operating speed. By intersecting the fan curve with both resistance curves two pressure drop values are obtained. If the

difference between the two pressure drop values does not exceed the required pressure drop value (Table 5-3) then the current fan speed is insufficient to achieve retention. The fan speed is then incremented giving a new curve equation with which to evaluate against the two resistance curves continuing until the required pressure drop difference is achieved.

Due to the resistance curves being based on test specimens of relatively small size, up-scaling is required to represent the final preforming scale for a given part.

5.5. Scalability

To achieve a target areal mass that can be fully retained under vacuum the size of the part and fan characteristics need to be considered. For a given areal mass and to maintain a constant superficial velocity across the preform bed, the volume flow rate of air is related to the square of the part area. Therefore if the part area is doubled then the volume flow rate needs to be increased four times to maintain superficial velocity. The limiting value for which can be determined by consulting the maximum speed plot on the fan curve. The fan curve also provides the maximum possible value for head pressure thus giving the limiting areal mass that can be deposited. The pressure drop is independent of area unlike the volume flow rate and therefore consideration of the two variables is important when sizing a fan for these types of applications. This study looked at characterising fabrics and the preforming screen rather than the observing the overall performance of the fan. To be able to relate the fan performance as areal mass is increased, to the manufacturers fan curve; additional manometers are required to measure the pressure and mass flow rates upstream and downstream of the fan according to BS EN ISO 5801:2007. This will also provide information on losses throughout the system.

For this study however the materials tested have been characterised using pressure drop versus superficial air velocity plots which is area independent. The required pressure drop across the material is always constant for a given areal mass. To calculate the fan speed needed to provide sufficient pressure difference for a given part area and areal mass, knowledge of the quartic and quadratic terms discussed

earlier is required for the current layer and subsequent layer (or deposition masses if considering automated discontinuous fibre processes).

5.6. Chapter conclusions

Attempts have been made to characterise the air permeability of various fabrics and preform types to determine the fibre / fabric retention force on a perforated preforming tool. This permits the sizing of fan equipment and intelligent design of both tooling and deposition patterns. Results show that a wide range of air permeability is displayed for common preforming materials with the implication that different limits in areal mass exist for retention purposes. Individual carbon fibre segments were also characterised and shown to behave in a similar way to non-crimp UD fabrics even at low areal masses (300 gsm).

An iterative approach to determining the required fan speed to fully retain material was proposed. By approximating the resistance curve for each layer of material experimentally, the resistance curves can be used in conjunction with fan speed characteristics data to increment fan speed until the required pressure drop is achieved to retain the next layer of material. It is anticipated that a maximum of ~900 gsm of non-crimp UD fabric (and DCFP type architectures) can be fully retained using the current UoN vacuum fan installation. This equates to low volume fraction laminates (~17% V_f for 3 mm part thickness) and highlights the requirement for either upgraded fan specifications or alternative forms of fibre retention. Additional testing is required to validate this theory by developing the experimental rig further in order to record the force required to remove a layer whilst under retention from the fan.

Other forms of forms of retention should also be investigated for discontinuous fibre architectures, especially when targeting structural specification preforms of high areal mass (>2000 gsm). One possible solution could involve spraying the resin system simultaneously with the reinforcement. By selecting an appropriate resin system, such as used for prepreg materials, having undergone a staging cycle (giving a ‘tacky’ characteristic) the potential exists to retain fibres in-situ for 3D profiles.

Chapter 6. Process modelling

6.1. Introduction

Chapter 2 has highlighted the potential to increase manufacturing efficiency for various deposition processes through parameter optimisation using computational modelling techniques. The ability to recreate discontinuous fibre networks for three-dimensional component geometry was lacking however. In this chapter a modelling schema for a versatile software package capable of simulating a typical DFP process is presented with specific details on modelling approaches and software implementation provided throughout. Whilst the modelling methodology is applicable to any DFP process, the software developed in this chapter is based around the UoN DCFP facility drawing upon characterisation data acquired in Chapter 4.

6.1.1. Model requirements

The rationale behind developing a process model is to streamline the route to manufacture for DFP processes from a conceptual design stage. Several requirements were identified in order for the model to succeed in this capacity:

- The design procedure for creating a process model should consider each element or subsystem involved in the physical process to gain an understanding of the potential limitations and difficulties which may exist in formulating modelling strategies.
- The principle mechanism for maximising the performance of parts manufactured using DFP processes is through the optimisation of reinforcement coverage. A meaningful method of assessing the quality of areal mass coverage is therefore required with the ability to modify process parameters to improve preform quality.
- Once optimised, the preform architecture is to be made available for subsequent mechanical property prediction. This is achieved via an interface with commercial Finite Element Analysis software.

- Model validation is a necessity for confidence in simulation output which is achieved through characterisation studies and direct comparisons with empirical data. The majority of the validation work is summarised in Chapter 7.

6.1.2. Previous modelling limitations

Previous attempts at modelling DFP processes have generally focussed on microscale and mesoscale structures. Due to the stochastic nature of the material and the complexity in predicting mechanical properties based on fibre architecture, much of the work has been conducted on producing realistic RVEs. This approach by its definition means that the RVE is representative of the entire preforming area which can cause complications when determining appropriate RVE scales. This approach may offer a suitable solution for simple planar structures but their suitability for capturing the mass variability across genuine three-dimensional part geometry is limited. Through observation, it is significantly more difficult to optimise fibre distribution for three-dimensional preforming than for planar profiles due to various factors including; non-trivial robot trajectory planning, gravitational effects which affect final segment location and the difficulty in assessing preform quality. It is therefore questionable whether a mesoscale RVE is indeed representative over an entire preform structure for real part geometries.

Other modelling attempts have included process-driven approaches such as a previously developed two-dimensional DCFP process model which was primarily concerned with specimen scale analysis [53]. Very basic spray cone characterisation coupled with rudimentary robot path generation has restricted its applicability to the physical preforming process; however, this has demonstrated the potential for replicating macroscale mass variability for complete structures. The work presented in this section builds upon ideas from the existing model [53] to resemble the physical process more faithfully.

6.2. Program development

6.2.1. Basic framework

The complete software package is implemented in C# via Microsoft's Visual Studio – an integrated development environment (IDE). Visual Studio provides an extensive set of libraries and toolkits to aid efficient software development with built-in support for applications requiring a front end Graphical User Interface (GUI) to operate the underlying software engine. Managed DirectX is used for more intensive graphical rendering calling upon Direct3D, one of the APIs contained within DirectX.

An object-oriented programming design philosophy is adopted which is well suited to modelling DFP processes. These types of processes can be decomposed into core functional subsystems which can be programmed as self-sufficient independent modules enabling explicit control of data flow during program execution. This is important for program stability and to permit revisions and expansions in module functionality without compromising overall program execution.

To model the DCFP process each element of the process was examined to ascertain to what extent it can be feasibly modelled. Figure 6-1 illustrates the main subsystems involved for spraying a preform via DCFP with additional subsystems included which are required for computational simulation. The flow diagram serves as a visual representation of the program framework and the interactions that exist between each subsystem. Details for each part of the flow diagram are discussed in the following sections.

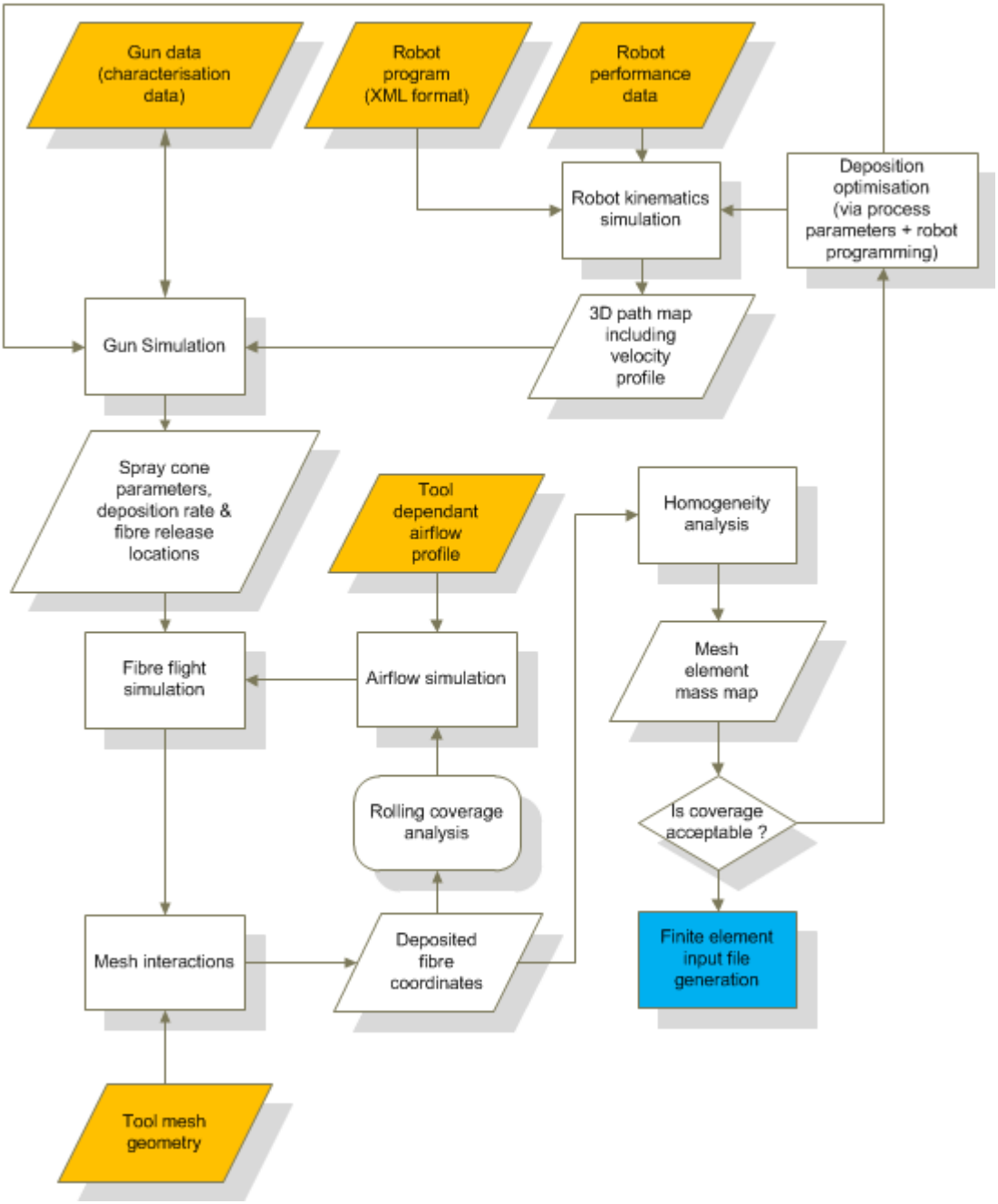

Figure 6-1: Process model flow diagram combining DCFP processes with simulation requirements. Orange blocks represent user-defined input files for the model. The top row of orange blocks signifies the required inputs to initiate execution of the process model. Final output is an input file for finite element analysis (blue block).

6.2.2. Tool meshing and import of surfaces

The typical modern day design approach takes advantage of parametric 3D CAD software to generate component geometry. The vast array of software available means that choosing a file format common across all platforms is important for program accessibility. A parametric model (in file formats such as STEP and IGES) gives a

precise representation of the geometry, however, each surface is independent making overall surface analysis for material coverage unnecessarily complex [123]. Graphics engine requirements mean that component geometry has to be expressed as a three-dimensional surface consisting of triangular facets creating a tessellated model. The file format .STL is ideal in terms of both universal CAD software adoption and its raw geometry definition structure. It was found that in general 3D CAD packages only offer very basic mesh generation options such as the ability to alter chord height which controls element resolution. This is acceptable for simple planar profiles, but for geometries where features such as curves, rounds and holes are present element surface areas tend to vary significantly as in Figure 6-2 (left). Analysing coverage variation using this type of mesh would not only be computationally expensive but also of limited value when attempting to visualise mass distribution across the component surface. Significantly distorted element geometries can also give rise to errors in downstream FEA techniques.

To achieve greater control over mesh generation it is suggested that CAD geometry is imported into meshing software where node seeding, element resolution, distribution and shape can be modified. Tailored seeding of element nodes improves the distribution of elements which is vital for effective coverage analysis described in Section 6.2.6. The mesh import routine was extended to accept the native .INP file format for ABAQUS/CAE which has been chosen in this thesis to generate meshes as well as for fulfilling FEA duties. Figure 6-2 (right) shows the improved mesh after processing the original .STL file in ABAQUS.

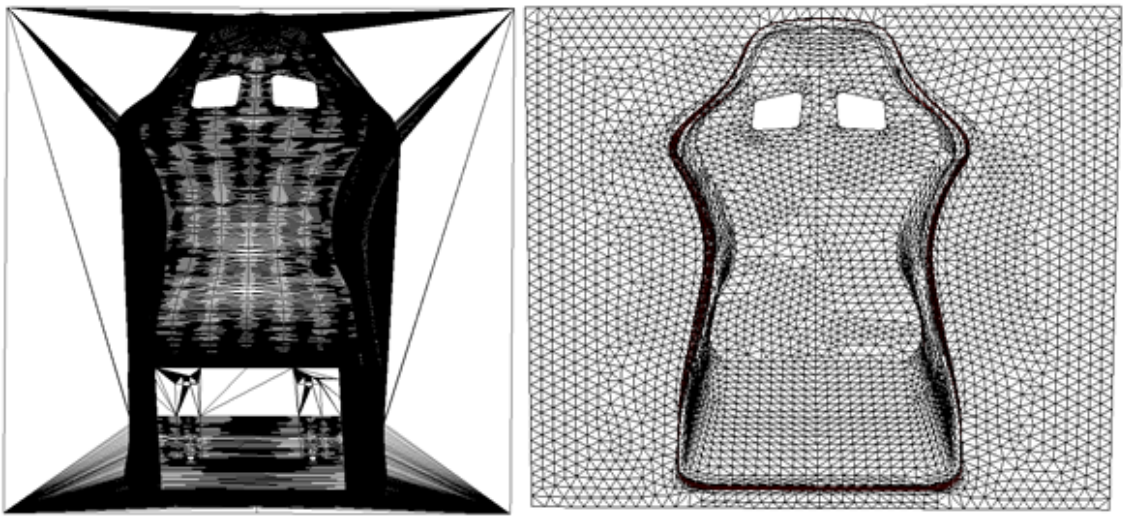

Figure 6-2: Comparison of mesh quality generated from identical surface geometry. The left image is a .STL file output from Pro/Engineer which offers very limited mesh control. Element area is affected by geometric features resulting in significant area variation. Mesh quality is improved using ABAQUS/CAE by controlling element seeding. The images are top down views of a car seat tool.

6.2.3. Modelling robot dynamics and defining preform properties

Modelling of the Fanuc RJ3iB robot used in the UoN DCFP cell is generalised to simulate any industrial 6-axis robot which can differ in the exact nature of their programming methodology but remain kinematically similar. The laboratory robot executes commands based on coordinates for 3D position and spatial rotations, movement control parameters and gun control instructions. Movement control parameters dictate point-to-point robot motion via a smoothing variable. No smoothing means that each path point is reached with the robot sacrificing speed for accuracy whereas increasing levels of smoothing allows the robot to calculate a trajectory to minimise speed variation but at the cost to positional accuracy. For the purposes of this model it is assumed that no smoothing is applied for simplicity.

In this subsystem the intention is not to model the rotations of each robot joint but to store a local copy of the desired point location, tool centre point (TCP), and target velocity information programmed to the robot. The structured data file therefore consists of 3 coordinates (x, y and z in world space), 3 rotations (w, p and r about the local tool centre point axes (X', Y', Z') respectively), target path velocities and deposition head control signals on a line-by-line basis. The data is stored in an XML file allowing for efficient parsing and editing via a custom user interface.

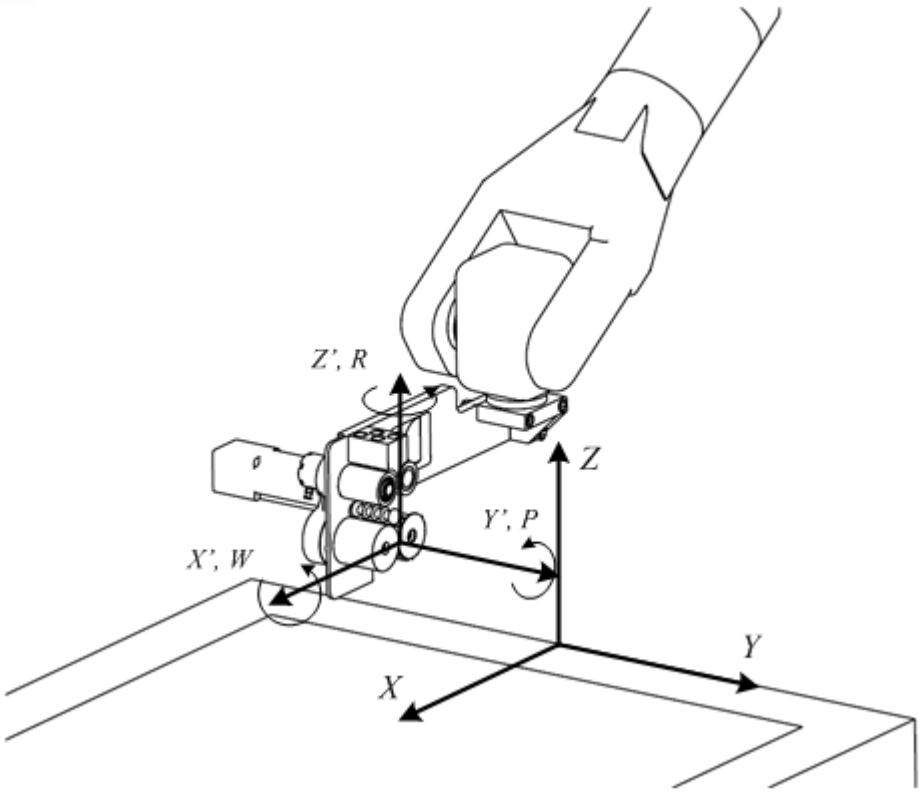

Figure 6-3: Diagram showing the process model coordinate systems. (*X, Y, Z*) is the world axes shown as centre of the virtual platen where *X* projects into the preforming area. The local deposition head coordinate system is also shown with relevant notation to describe head orientations.

The robot program can be further modified by initiating a graphical representation where each program line corresponds to a manipulable spherical node (Figure 6-4). The nodes can be selected and transformed via user interaction with the imported mesh geometry overlaid for visual reference. Figure 6-4 shows an optimised robot path used in later sections to create 3D preforms.

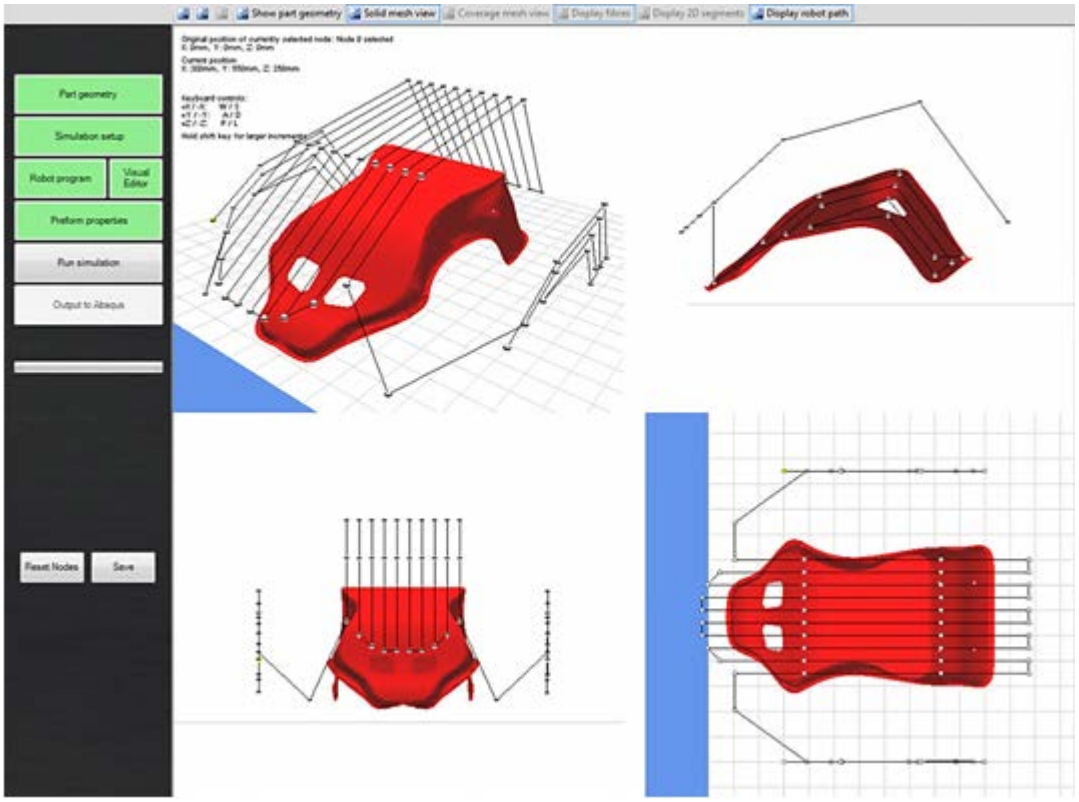

Figure 6-4: Screen shot of the process model GUI for robot trajectory editing. The robot program has been read from an external XML file and converted to a graphical representation with each instruction line taking the form of a spherical node. Orthogonal view planes are rendered to aid accurate node placement.

6.2.3.1. Robot kinematics

Once the robot trajectory is defined, a set of kinematic equations are applied to account for accelerations as the path changes direction. The robot is assumed to be capable of accelerating at $20g$ with a peak velocity of 2 m/s. The distance between two point locations is calculated to obtain the stroke distance s as follows:

$$s_n = \sqrt{\Delta x_{n,n-1}^2 + \Delta y_{n,n-1}^2 + \Delta z_{n,n-1}^2} \quad \textbf{(6-1)}$$

As previously mentioned, motion smoothing is not utilised meaning that the robot accelerates from and to rest. Therefore the time taken to accelerate between points t_a is found using the target velocity v:

$$t_{a_n} = \frac{v_n}{20g} \quad \textbf{(6-2)}$$

where g is gravitational acceleration (~9.81 m/s^2). Total distance taken to accelerate s_a and to travel at peak velocity s_v is expressed as:

$$s_{a_n} = 10gt_{a_n}^2 \quad \textbf{(6-3)}$$

$$s_{v_n} = s_n - 2s_{a_n} \quad \textbf{(6-4)}$$

The elapsed stroke time at constant velocity t_v is given by:

$$t_{v_n} = \frac{s_{v_n}}{v_n} \quad \textbf{(6-5)}$$

Thus giving a total stroke time t_s and total cycle time t_c:

$$t_{s_n} = t_{v_n} + 2t_{a_n} \quad \textbf{(6-6)}$$

$$t_c = \sum_{i=1}^{n} t_{s_i} \quad \textbf{(6-7)}$$

Storing this data for each path stroke means that a velocity profile can be mapped along the path lines with respect to time. At any given distance along the robot path the instantaneous robot speed, required for spray deposition simulation, and accumulated cycle time can be deduced.

6.2.3.2. Preform design

Several material and process parameters are configurable to satisfy preform design requirements prior to simulation (Figure 6-5). Material parameters include; tow size, number of tows, fibre length and target areal density. Other process variables requiring definition include; area of interest (component area), total robot path length and knife roller circumference. The UoN deposition head uses 180 mm circumference knife rollers to accommodate a large range of segment lengths from 7.5 mm to 180 mm. Total path length is determined via the robot kinematics module by summing each path length. Component area A_p is calculated on generation of the part mesh object by summing the area of each element which are defined by three position vectors ($\boldsymbol{v_1}$, $\boldsymbol{v_2}$, $\boldsymbol{v_3}$) so that:

$$\boldsymbol{u}_n = \boldsymbol{v}_{2n} - \boldsymbol{v}_{1n} \tag{6-8}$$

$$\boldsymbol{v}_n = \boldsymbol{v}_{3n} - \boldsymbol{v}_{1n} \tag{6-9}$$

$$A_p = \sum_{i=1}^{n} \frac{1}{2} |\boldsymbol{u}_n \times \boldsymbol{v}_n| \tag{6-10}$$

These parameters are subsequently used to determine the location of where each fibre is likely to be released from the deposition head along the robot path. The calculations used for this stage resemble those used by the DCFP laboratory equipment; essentially simulating the function of a programmable logic controller.

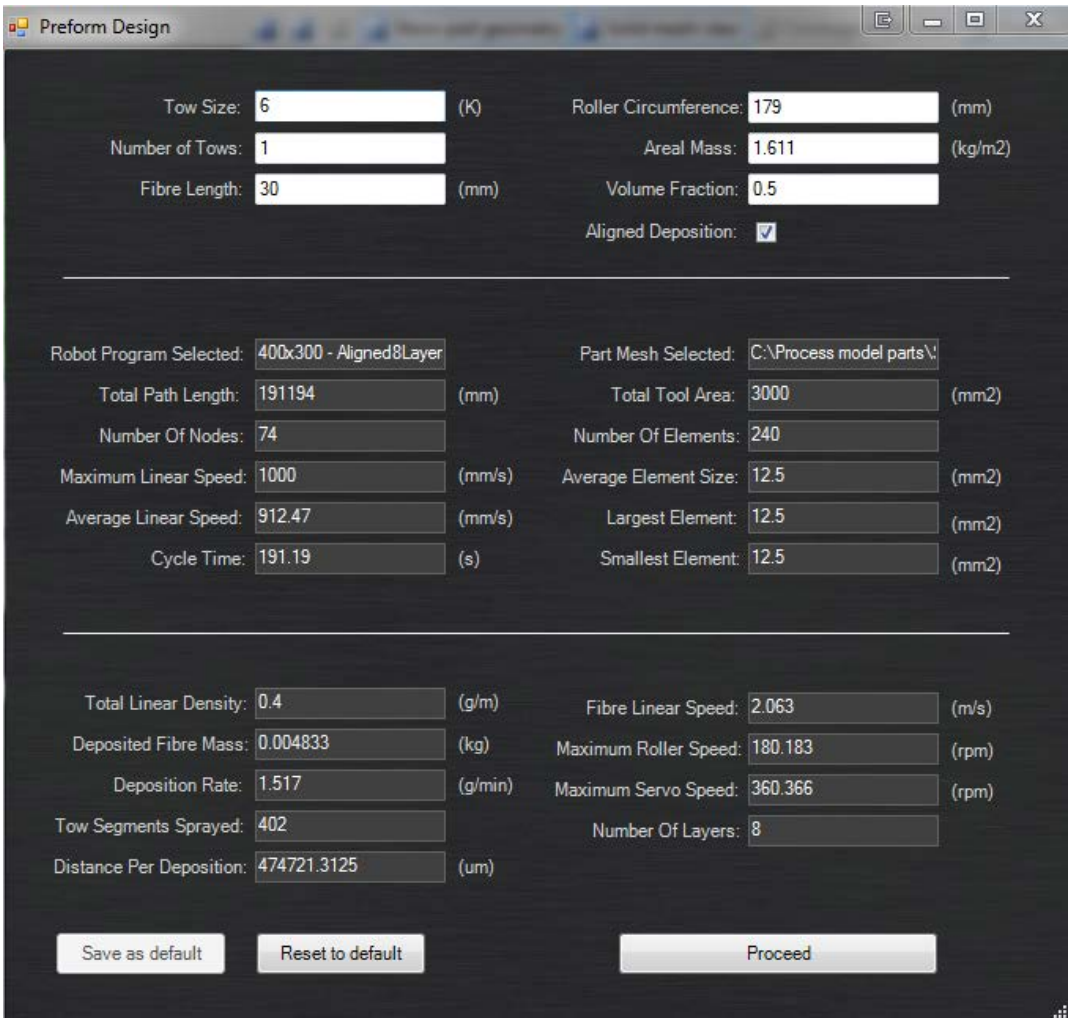

Figure 6-5: Screenshot of the preform design input form. The top section is used to set process variables such as microstructural properties and target areal density. The mid-section displays key attributes from the robot input and component mesh files. The bottom section displays the process outputs based upon calculations using the previous two sections.

To find the distance between deposition locations the calculations can be split into two parts. When designing a preform the key consideration is the desired areal density. This value dictates the required linear density of material for processing through the deposition head based on robot path length. Required linear density is a value for the mass of fibre deposited per millimetre of robot travel.

$$fibre\ mass\ target\ (g) = target\ areal\ mass \times part\ area \tag{6-11}$$

$$required\ linear\ density\ (g/mm) = \frac{fibre\ mass\ target}{total\ path\ length} \tag{6-12}$$

Tow size multiplied by the number of tows processed equates to the available linear density of reinforcement:

$$available\ linear\ density\ (g/mm) = \frac{tow\ size \times number\ of\ tows}{15} \tag{6-13}$$

Dividing the required linear density by the available linear density provides a density ratio:

$$linear\ density\ ratio = \frac{required\ linear\ density}{actual\ linear\ density} \tag{6-14}$$

Finally, dividing the linear density ratio by the chosen fibre length results in a value for the number of segments deposited per millimetre of robot travel. Dividing by a further factor of 1000 and taking the inverse gives a figure for the number of microns travelled per deposition. The reason for converting to microns is for the benefit of iterative routines where positive integers are beneficial compared to fractions of millimetres.

$$distance\ per\ deposition\ (\mu m) = \frac{1000 \times fibre\ length}{linear\ density\ ratio} \tag{6-15}$$

Fibre release locations are mapped out along the robot trajectory by incrementing by the distance found in Equation (6-15) from the initial seed point. This information is

fed back into the robot kinematics module to find the instantaneous robot speed at each release location and subsequently stored for spray simulation.

It should be noted that segment release locations are assumed to be evenly spaced along a given path stroke even though the robot does not maintain a constant speed between points due to acceleration zones. This is because the laboratory setup is configured so that fibre feedrate is controlled proportionally to robot velocity in an effort to provide homogeneous fibre coverage. This means that release locations are independent of robot velocity explaining its absence from Equations (6-11) to (6-15). The instantaneous robot velocity is used in this case to calculate fibre feedrate only.

6.2.4. Modelling fibre spray

The deposition head simulation subsystem deals with the mechanics of fibre spray where the output is a projection path from the head to the tool surface for each released segment. A deposition head characterisation study was conducted in Chapter 4 to gain an understanding of which process variables affect deposition. The results from this study are stored in a structured XML file describing the spray cone geometry via projection angles and bivariate mass distributions. An orientation distribution is also stored to fully define the ejected segment on the tool surface.

With tow size, fibre length, TCP height and fibre speed known at each release point, the program cycles through the characteristics file applying a closest-match routine. The routine begins by matching tow size and fibre length; storing values for projection angles and segment spread as a function of TCP height for all available fibre speeds, as these two process variables change during preforming simulation.

Prior to any fibre segment being released, the local orientation of the deposition head has to be accounted for. Figure 6-3 shows the local head coordinate system in relation to the world coordinate system. An initial fibre projection ray (FPR) projects down the local -*Z'* axis of the chopping device as in Figure 6-6 (left). This projection ray is the idealised path a segment would take if there was no bias applied via the chopping mechanism. However, results from Chapter 4 indicate that a bias does exist. Depending on the values for the four process variables investigated in the characterisation study, two rotations are applied about the local *X'* and *Y'* axes

respectively to transform the FPR. This represents the cone centre line projecting from the deposition head TCP.

Using the height-dependant segment distribution values, a virtual spray cone is created where a further two rotations are applied generating a randomised FPR as in Figure 6-6 (right). Several rotations are required for each segment released in order to fully define the FPR exiting from the deposition head. Because of this, a decision was made to utilise quaternions which are found to be computationally efficient in size and speed when compared with equivalent matrix representations for three-dimensional spatial rotations.

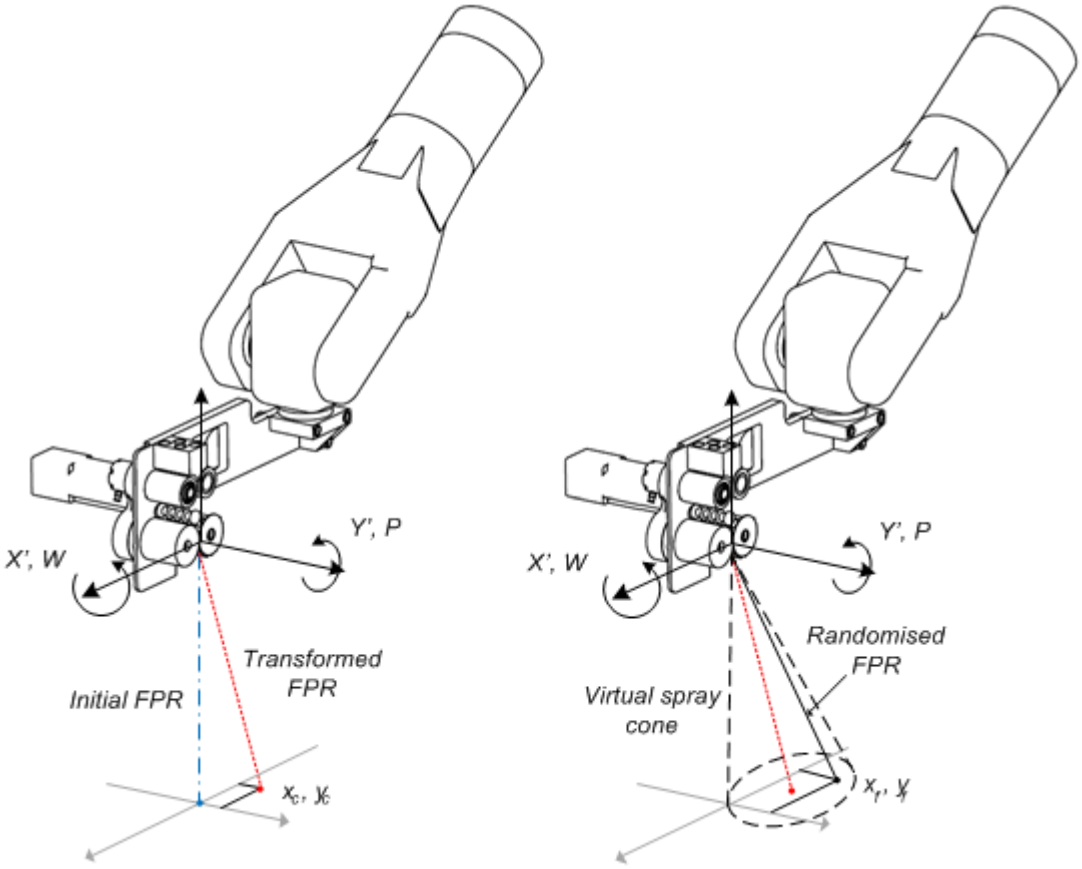

Figure 6-6: Schematic diagram showing the rotations applied to the fibre projection ray (FPR). The left image has two rotations applied to the FPR which defines the cone centre line (red line). The right image shows a further two rotations producing a randomised FPR conforming to process parameter dependent spray cone characteristics.

The q_1, q_2 and q_3 component of a quaternion describes the axis about which a rotation will occur. The q_0 component is the magnitude of the rotation about this axis.

$$Q = q_0 + q_1 i + q_2 j + q_3 k = q_0 + (q_1 i, q_2 j, q_3 k) \quad \textbf{(6-16)}$$

where q_0, q_1, q_2 and q_3 are real numbers and:

$$i^2 = j^2 = k^2 = ijk = -1 \quad \textbf{(6-17)}$$

It is convenient to think of the component q_0 as a scalar and the imaginary part ($q_1 i$, $q_2 j$, $q_3 k$) as a vector $\boldsymbol{v}$ which means the quaternion takes the form of a scalar plus a vector:

$$Q = w + \boldsymbol{v} \quad \textbf{(6-18)}$$

A pure rotation about the unit vector $\hat{\boldsymbol{v}}$ by an angle θ can be represented as:

$$Q = cos\frac{\theta}{2} + \hat{\boldsymbol{v}} sin\frac{\theta}{2} \quad \textbf{(6-19)}$$

The deposition head orientation is permitted to change during preforming with all rotations described in the robot program file. Initially the head orientation is described using an identity quaternion:

$$Q_i = 1 + (0i + 0j + 0k) \quad \textbf{(6-20)}$$

Rotations are applied in the same order as the laboratory robot with rotations about the *Y*' axis first, the *X*' axis second and finally the *Z*' axis through angles *p*, *w* and *r* respectively. Therefore the first rotation can be expressed using Equation (6-19) as:

$$Q_y = cos\frac{p}{2} + (0i + 1j + 0k) sin\frac{p}{2} \quad \textbf{(6-21)}$$

$$Q_y = cos\frac{p}{2} + j.sin\frac{p}{2} \quad \textbf{(6-22)}$$

Expressing rotations about the *X'* and *Z'* axes in the same manner results in a further two quaternions. To add rotations, quaternions are simply multiplied together in order – quaternions are noncommutative so care must be taken in multiplying them in the correct order. At each release location the head rotation Q_h is therefore calculated as follows:

$$Q_h = Q_i Q_y Q_x Q_z \tag{6-23}$$

The next stage is to express the FPR as a quaternion. There are two rotations about the local *X'* and *Y'* axes which describes the cone centre line direction such that:

$$Q_c = Q_{Ry} Q_{Rx} \tag{6-24}$$

A final quaternion is required to apply the additional rotation to the FPR to produce the randomised fibre trajectory according to the normal segment distribution. Using the Box-Muller method a uniform set of random numbers in the interval (0, 1] are transformed into two independent normally distributed values. These values are then scaled by the height dependent distribution variables to generate a location point in the *X'*-*Y'* plane (offset by TCP height). This gives a random fibre location (x', y', z_{TCP}) relative to the TCP. To find the axis and angle by which to transform a projection ray from the cone centre line to the randomised fibre location some vector algebra is required. An initial vector $\boldsymbol{v_o}$ is created:

$$\boldsymbol{v_o} = (0, 0, -1) \tag{6-25}$$

The fibre location derived from the distribution values is expressed as a position vector $\boldsymbol{v_f}$:

$$\boldsymbol{v_f} = (x', y', z_{TCP}) \tag{6-26}$$

Vector $\boldsymbol{v_f}$ is normalised so that the axis of rotation can be found using the cross product rule as follows:

$$\boldsymbol{a} = \boldsymbol{v_o} \times \hat{\boldsymbol{v}}_f \tag{6-27}$$

The angle of rotation about axis vector $\boldsymbol{a}$ is calculated using the dot product rule:

$$\theta = cos^{-1}(\boldsymbol{v}_c \cdot \hat{\boldsymbol{v}}_f) \tag{6-28}$$

Finally, this can be converted to quaternion notation as before:

$$Q_f = cos\frac{\theta}{2} + \boldsymbol{a}sin\frac{\theta}{2} \tag{6-29}$$

All the information to construct the final randomised FPR is now available. The quaternion containing rotations for the head, cone centre line, and randomised fibre location within the cone is given by:

$$Q_{FPR} = Q_h Q_c Q_f \tag{6-30}$$

The FPR itself is a vector defined by an origin and a direction in 3D space. The origin is always the TCP location (x, y, z) and the ray direction $\boldsymbol{v}_{FPR}$ is found by transforming $\boldsymbol{v}_o$ as follows:

$$\boldsymbol{v}_{FPR} = Q_{FPR}\boldsymbol{v}_o Q_{FPR}^{-1} \tag{6-31}$$

Quaternions Q_h and Q_c can remain constant depending if the input parameters remain consistent as the fibre release location is incremented from point to point. The quaternion Q_f is recalculated at each step however, providing the randomised fibre path within the spray cone.

Two pieces of information now exist for each released segment; initial exit velocity and trajectory. Program execution is passed to the fibre flight model which further manipulates the FPR based on the factors and equations presented in Chapter 4. A small time step (0.01 s) is used to resolve the segment velocity and location in 3D space as it falls from the deposition head to the tool surface. At each time step the FPR is passed to a mesh intersection algorithm to ascertain whether the segment has

collided with the mesh surface. The fibre flight routine increments until a collision is detected with the resulting intersection point stored as the segment midpoint.

6.2.5. Modelling airflow

One of the features of the DCFP process is the use of a vacuum fan to expel air from underneath the perforated tool providing a means of fibre retention. The air from the surrounding environment is forced through the tool area by a centrifugal fan creating an airflow profile above the tool. Fibres being dropped from a height above the tool will be influenced by this air flow in addition to the gravitational effects taken into consideration via the fibre flight model.

To take into account the flow of surrounding air through the porous tool, the DCFP cell can be conveniently modelled using a Computational Fluid Dynamics (CFD) software package. To develop the full field airflow the DCFP environment is imported into CFD software along with the tool geometry and permeability properties. This is described in greater detail in Chapter 5 for small coupon-scale characterisation.

Once the system is solved for a particular set of boundary conditions the resulting air velocity profile can be exported as a three dimensional vector field covering the entire spatial envelope above the tool. As a segment is released from the deposition head there is a set of 8 vector nodes surrounding the segment centroid. By averaging and weighting the effect of the 8 vectors, dependent on node proximity, a resultant force can be included in the fibre flight free body diagram (Figure 6-7).

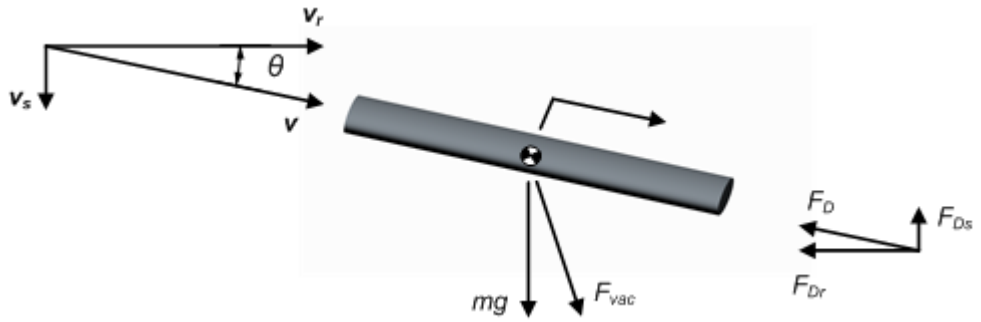

Figure 6-7: Fibre flight free body diagram with the addition of a force provided by the resultant external airflow.

For the purposes of this thesis, this stage is omitted from the model due to high computational expense and inefficiencies that arise from implementing the airflow

model. The methodology of interpolating surrounding vectors to find the resultant airflow induced force is applicable, but a more efficient method of locating neighbouring vector nodes on each time step is required. An additional reason for the omission of the airflow model is that a full characterisation study would need to be conducted to ensure that a reliable and robust method of modelling air extraction through different tool profiles is possible. Other challenging aspects include being able to accurately model the effects on airflow of partial fibre coverage during deposition as layers are built up. Chapter 5 demonstrated that tool perforations can be covered at low areal density levels significantly affecting the total pressure drop through the fibrous stack and tool thickness, therefore impacting retention capacity.

6.2.6. Coverage routine and preform analysis

So far the fibre spray subsystem has simulated segment descent and intersected the mesh creating a segment midpoint on the tool surface. Code execution now passes to a routine which assembles the segment to the required fibre length. The orientation of the fibre segment, relative to the local deposition head coordinate system, is randomly generated using the parameter dependent distributions derived from the characterisation study in Chapter 4. It was demonstrated that for random deposition the orientation distribution was found to be adequately approximated by using either a normal or uniform distribution depending on process parameters. For normally distributed orientations the Box-Muller transform method is used with mean and standard deviation values applied to scale the distribution accordingly. For aligned deposition the Laplace distribution was found to provide a close fit to experimental data in Chapter 4. To generate samples from this distribution a general purpose Acceptance-Rejection algorithm is used. Bounding values for the distribution are determined and tested against using uniformly independent random numbers within the range [-90°, 90º] to see if they fall within the probability function. The three orientation distribution curves employed by the model are presented as generic functions for illustrative purposes in Figure 6-8.

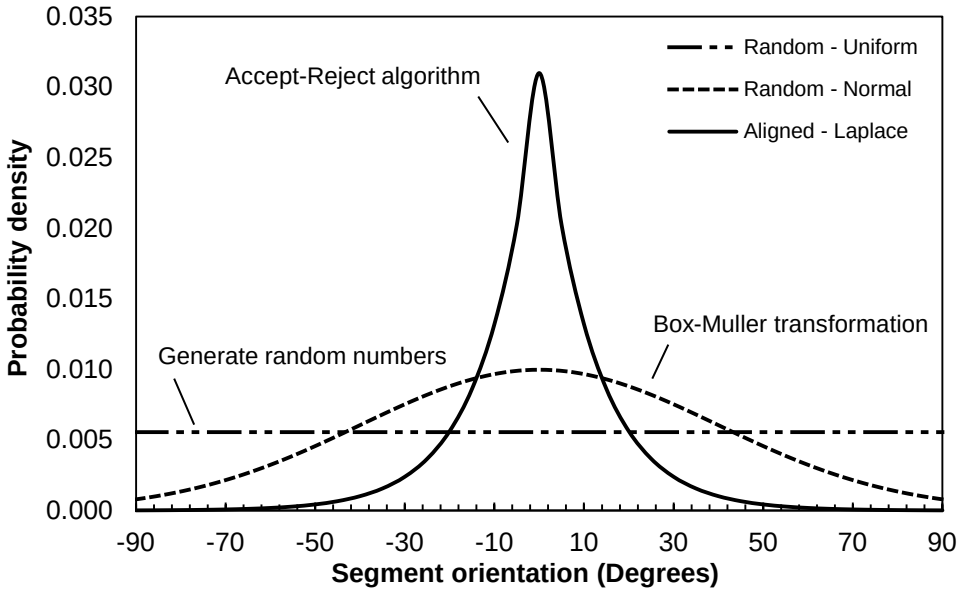

Figure 6-8: Generic orientation distributions used for random and aligned deposition. Values from a random number generator are scaled for depositions that can be approximated as a uniform distribution. A normal distribution is used for random spray where levels of alignment bias are expected – the Box-Muller transform is used to generate fitted values. The Laplace distribution is approximated for aligned deposition using an Acceptance-Rejection algorithm.

6.2.6.1. Fibre segment assembly algorithm

The coverage routine begins by projecting the segment (fibre bundle) midpoint vertically up (+*Z* axis) onto a two-dimensional *X*-*Y* reference plane above the mesh surface and incremented 1 mm in the direction of orientation. From this incremental step, an intersection ray is constructed to project vertically down (-*Z* axis) to intersect the mesh again. The new surface point represents the first portion of the fibre segment. This process is repeated by incrementing in the reference plane and projecting down to generate intersection points until half of the fibre length is reached; this is illustrated in Figure 6-9. The segment is then incremented in the opposite direction from the midpoint. Total segment length is found by summing the distance between each mesh intersection point with the entire process repeated for each subsequent fibre deposited. Figure 6-10 shows the difference between random and oriented spray modes on a 2D surface with intersections points visible along the segment lengths.

A value for mass is assigned to each intersection point taking into account that the number of intersections will be one greater than the fibre length:

$$mass\ per\ intersection\ (g) = \frac{tow\ size}{15{,}000} \cdot \frac{fibre\ length}{fibre\ length+1} \tag{6-32}$$

For each intersection point the element identification number is retrieved from the mesh object and the intersection mass value is incremented to the element mass attribute. Once the spray simulation is complete, the total mass for each element will be proportional to the number of times it has been intersected.

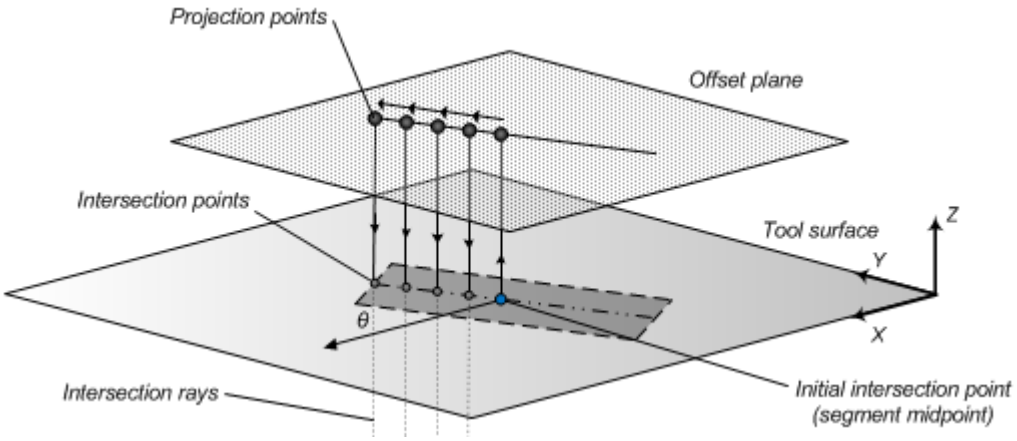

Figure 6-9: Schematic of how the intersection algorithm builds up a virtual tow segment. Half of the segment has been assembled on the tool surface.

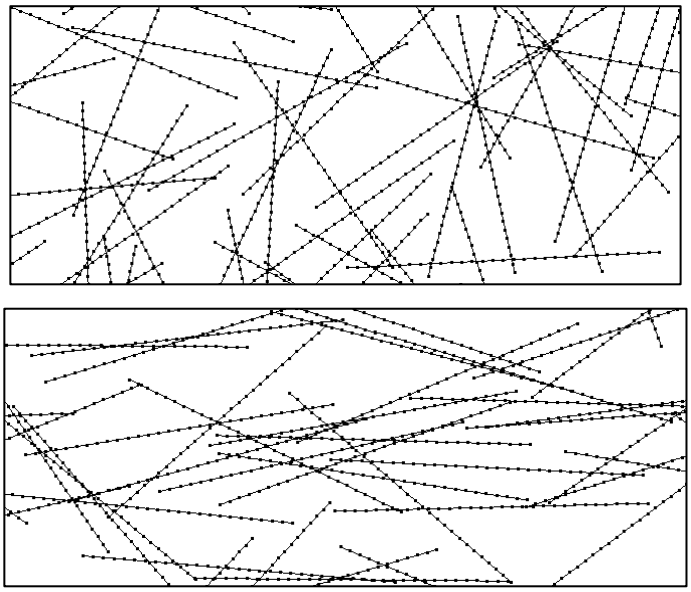

Figure 6-10: Close-up screenshots of sparse segment depositions using random (top) and aligned (bottom) orientation distributions. Segments of 30 mm length are used with the intersection points visible along the segment lengths.

This method for assigning segment mass distribution across the mesh is satisfactory for 2D preforming simulation; providing a fast route to evaluating macroscale fibre homogeneity. Problems occur on significantly contoured tool geometries however. Accuracy for each incremental intersection location diminishes for surfaces that deviate away from the *X*-*Y* plane. This can result in the iterative assembly routine completing prematurely due to the target fibre length condition being satisfied even though the number of intersection points indicates that the segment is underweight. This is demonstrated in Figure 6-11 where the target length is achieved in the top diagram (2D surface) but ill-defined in the bottom diagram (3D surface). The accuracy of segment mass distribution is lost due to the surface gradient resulting in the fibre assembly routine completing after only 7 intersections compared with 11 for the 2D case. Trial 3D part geometries were used during subsystem development with deposited mass approaching levels 20% lower than target mass values in extreme cases. Since the process model is primarily concerned with evaluating preform properties by examining areal mass variation, it was imperative to improve the method of fibre assembly for 3D surfaces.

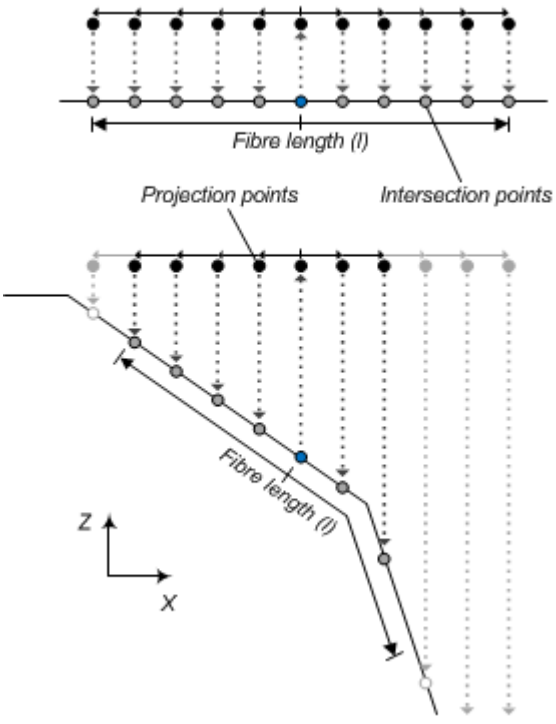

Figure 6-11: A diagram showing the potential problems with using the incremental intersection routine for heavily profiled 3D surfaces. The segment is built up to the correct fibre length in the top image on a 2D surface. The segment is poorly defined in the bottom image with fewer intersection points due to steep surface gradients deviating away from the *X*-*Y* plane.

The revised segment assembly method retrieves mesh element properties after the initial intersection. 4 position vectors (3 element vertices and the intersection point) are translated to global axes origin by subtracting the last element vertex from each point. The element normal vector is calculated along with the axis and angle of rotation to the *X*-*Y* plane – found using the same methodology set out in Equations (6-25) to (6-29). The resulting pure rotation quaternion is used to transform all 4 points into 2D space. The same method is also applied to transform the rotations of the deposition head to 2D space thereby determining the positive *x* direction relative to the element so that the orientation of the fibre segment can be correctly assigned. The orientation determines the direction in which to incrementally assemble the fibre as was previously accomplished.

Once incremented, a barycentric technique is employed to check whether the new intersection point remains within the element boundaries and then transforms the point back into 3D space. If the point was found to remain within the element boundaries then the 3D coordinate is stored as the next segment intersection point. If not then the point is offset relative to the element plane. This is achieved by multiplying the element normal by a nominal value to ensure that the point is far enough away from the mesh. An intersection ray is sent back to the mesh via the inverse element normal. If the ray encounters another element in the mesh, the new intersection point is stored as the next segment point. The properties of the currently intersected element are stored and used to transform to 2D space as before. This process is repeated until the target fibre length is achieved. Execution of the routine is illustrated in Figure 6-12 where the intersection points appear to traverse the element surface to accurately assemble the segment. This provides a robust method of distributing segment mass on contoured tool geometries with errors of <1.5% between target mass and simulated values.

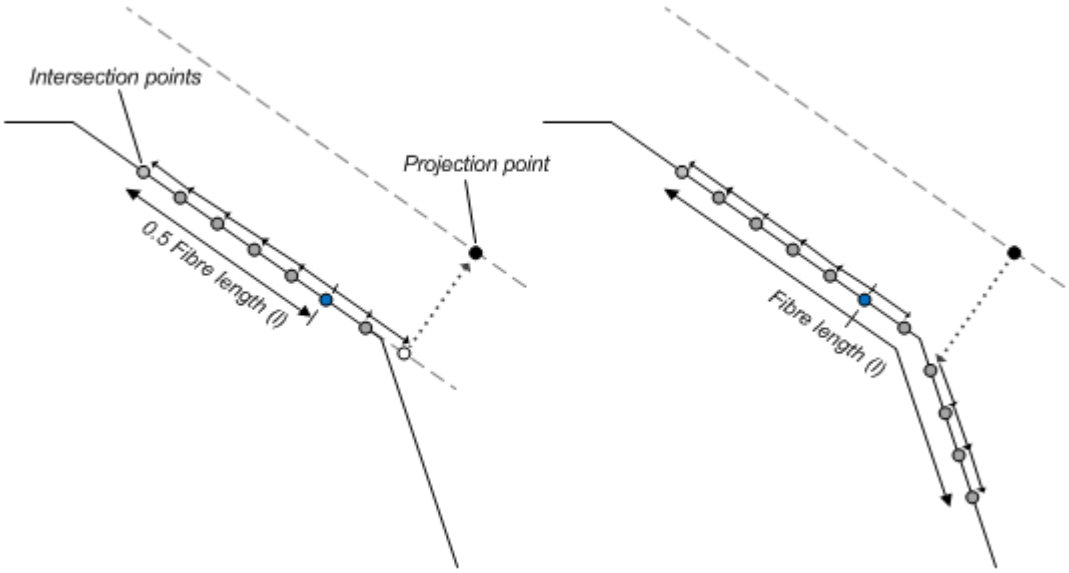

Figure 6-12: An example of segment construction using the improved 3D intersection routine. The segment is assembled by traversing the element surface from the midpoint until it crosses the element boundary (left). A projection point is established by transforming the 'overshoot' point into a parallel offset plane and then projecting back to the mesh to locate the next element (right). The process is repeated until target fibre length is achieved.

Once preforming simulation completes, the next phase is to meaningfully quantify levels of fibre coverage. Fibre mass per element and the corresponding areal mass are determined by:

$$element\ mass\,(g) = number\ of\ intersections \times mass\ per\ intersection \quad \textbf{(6-33)}$$

$$element\ areal\ mass\,(gsm) = \frac{element\ mass}{area\ of\ element} \quad \textbf{(6-34)}$$

During preform design (Section 6.2.3.2) a value for target areal mass was required to calculate the fibre deposition rate. The areal mass for each element is evaluated against this global target areal mass value to determine the relative error per element. This leads to the creation of an error map which is scaled via user-defined limits to a colour palette. This allows visual feedback of areal density variation over the entire tool area. By visualising preform variability the user can modify robot path points and other process parameters accordingly to produce higher quality depositions. Additionally, fibre distribution is quantified by finding the coefficient of variation (CV) of reinforcement mass over the entire population of mesh elements.

Thus far, a key assumption for coverage analysis is that using mass-weighted intersection points provides a suitable approximation to modelling the full fibre

segment on the mesh surface. The primary reason for adopting this method is that for 3D meshes it is a relatively inexpensive procedure to simulate fibre deposition. A more realistic but complex assessment of coverage is achieved by assigning each segment an areal mass value (dependent on tow properties) and finding the true segment area within each element. Figure 6-13 is an example of how the mass distribution can differ. The 'idealised' method of using segment area encounters over twice as many elements than the intersection method in this case. Element mass is proportional to segment area whereas element mass is proportional to the number of intersection points for the adopted method.

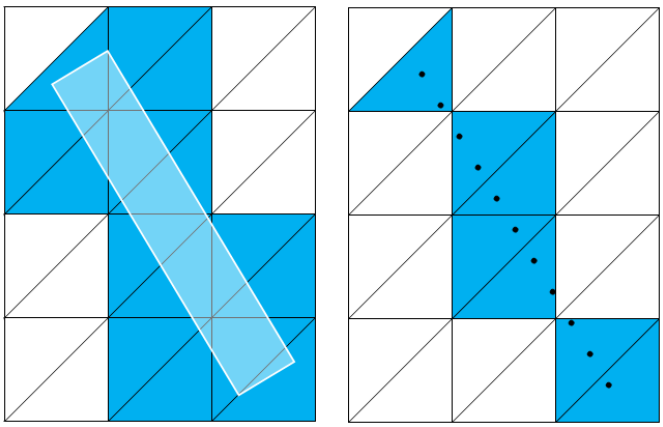

Figure 6-13: An illustration of the number of elements encountered using the polygon coverage method (left) and the intersection method (right). In this particular case the polygon coverage method interacts with over twice the number of elements.

Clearly the mass-weighted approximation performance will be sensitive to mesh resolution, with divergence expected as element size decreases. Therefore, a validation study was conducted to understand the limitations of the adopted method and to attempt to formulate a suggested range for average element area through the use of planar meshes. This required developing a polygon clipping algorithm to evaluate the 'idealised' method (referred to as the polygon coverage method) in Figure 6-13 (left).

6.2.6.2. Polygon coverage algorithm

The routine uses the same segment midpoint and orientation values as the mass-weighted method to allow for direct comparisons with identical fibre architectures. Using simple trigonometry the four corner points of each segment are calculated forming rectangles known as subject polygons. All mesh elements are stored as

triangles which are called clipping polygons. The aim is to determine whether subject polygons exist within any given clipping polygon and calculate the corresponding area occupied. By summing the subject areas the total mass within each element can be established. To achieve this, a modified Sutherland-Hodgman algorithm adapted from [161] is utilised to clip each subject polygon to each element boundary in turn.

Elements are dealt with sequentially by cycling through all subject polygons and checking whether the segment vertices (subject polygon corner points) exist inside the clip line.

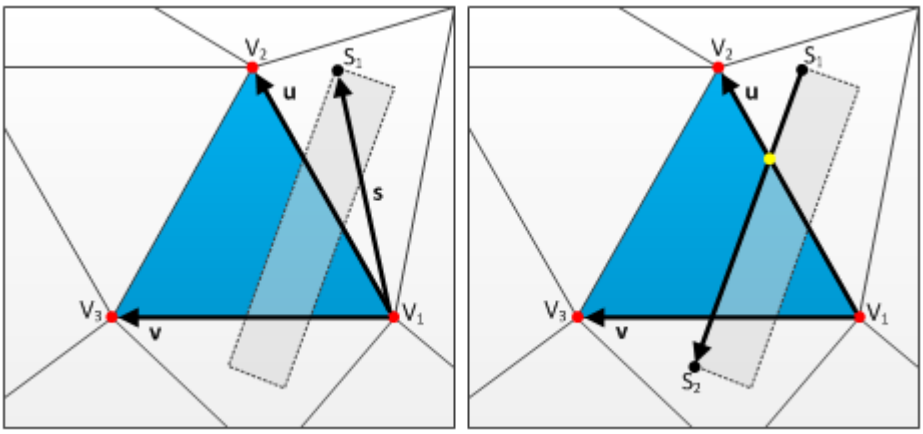

Figure 6-14: Vector and vertex definitions used for the Sutherland-Hodgman polygon clipping algorithm. In the left image the first subject vertex is checked against the element clipping edge (vector *u*). S_1 is immediately rejected and a line intersection test is conducted between S_1 and S_2 and the clipping edge (right).

This is accomplished by creating three vectors; ***v***, ***u*** and ***s*** as in Figure 6-14. Element edge vectors ***v*** and ***u*** are used to find the normal vector ***Q*** for the clipping polygon. Vector ***u*** is also the clipping edge. Subject vector ***s*** changes depending on which vertex is being tested. To determine if a subject vertex lies inside the element boundary, normal vectors of both sets of vectors are calculated using the cross product rule:

$$\mathbf{P} = \mathbf{u} \times \mathbf{s} \tag{6-35}$$

$$\mathbf{Q} = \mathbf{u} \times \mathbf{v} \tag{6-36}$$

If the subject vertex lies inside the clipping edge then both normal vectors (***P***, ***Q***) will be of the same sign. The model checks this by taking the dot product of both vectors; if the result is positive then the subject vertex exists within the clipping edge. In the case of Figure 6-14 the dot product would return negative which means that the vertex

is rejected by the algorithm and would move onto the next subject vertex. The algorithm executes by testing each vertex against each clipping face whilst also testing for any intersections between subject vertices and the clipping edge (Figure 6-14 – right).

After testing against a clipping edge has completed, a fresh set of 'clipped' vertices are stored and passed to the next clipping edge for testing and repeated until the algorithm has traversed around the element boundary. This is visualised in Figure 6-15 (top left) where s_1 and s_4 have been rejected by the first clipping edge. Two intersections have been detected with 4 vertices stored for the next clipping edge. If all of the segment vertices were to exist outside of the clip edge, the segment is immediately rejected and the algorithm advances to the next segment.

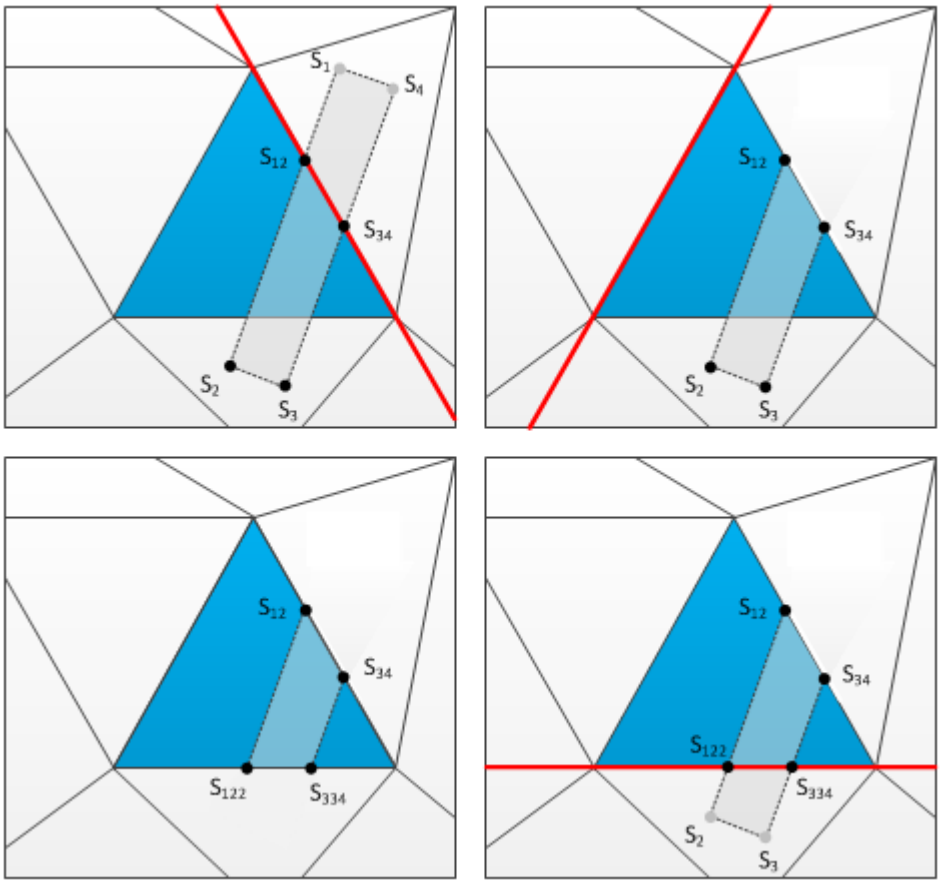

Figure 6-15: A schematic showing the progressive clipping of a segment polygon to the element boundary (clockwise from top left). All subject vertices are tested against each clip edge in turn resulting in the shaded portion in the bottom left image.

All the clipped polygons are further subdivided into triangles for graphical representation and to determine polygon areas by summing the area of each triangle. This method gives a rigorous evaluation of segment distribution across a 2D area.

In reality the tow segment footprint is affected by the processing route through the chopping device and is not necessarily a consistently uniform area. The widths of the subject polygons are based on empirically derived values for tow segment widths taken from an average of 30 processed samples for each of the four tow sizes investigated (3 K, 6 K, 12 K, and 24 K). Even though the polygon coverage method provides a close approximation to true areal coverage, mass distribution across a tow segment width is non-uniform and therefore segment mass is not spread evenly over the segment footprint. The cross section of a tow is generally elliptical with the greatest concentration of filaments towards the mid-plane of the segment. For the purposes of this study the mass distribution at filament-scale is neglected as the effect is insignificant when considering the scale of analysis.

6.2.6.3. Mesh sensitivity study

The majority of published work on FEA modelling for mechanical property response in discontinuous fibre composites has concentrated on the microscale and mesoscale. Fibre/matrix and fibre/fibre interactions have been the principle area of interest which typically requires elements of between 0.02 mm and 0.5 mm depending on desired RVE scale. However, topological tool areas suitable for DFP processes could range from experimental plaque scale (~0.1 m^2) to several square metres depending on application. Using a 0.5 mm element would result in approximately 8 million elements for a tool surface area of 2 m^2. Clearly this is impractical for FEA and for the current process modelling technique where issues surface within Direct3D; the upper limit for a single mesh object is ~65,500 facets. Tool meshes can be discretised and imported into the model but at a significant cost to computation time due to the spray simulation routine calling on a mesh intersection algorithm, testing each mesh object in turn. Therefore a compromise must be met between average element area and model accuracy; both in terms of geometrical representation in the process model and for subsequent FEA.

Each intersection in the adopted method takes the form of a mass-weighted node representing a discretised portion of tow segment. It was anticipated that the variation in simulated areal mass over a meshed area will diverge between the polygon coverage and intersection coverage routines as element area decreases. If meshes are too fine then there is a risk of obtaining anomalous values for element mass due to the inability to replicate mass distribution over segment widths.

To establish the lower bound for element area a mesh sensitivity study was performed. Two tow sizes (3 K and 24 K) have been investigated due to the vast difference in aspect ratios and their similarities in geometric form to 6 K and 12 K tow sizes respectively. A preform area of 400 mm x 300 mm was sprayed targeting 3 different areal densities (100, 200 and 300 gsm). Identical fibre distributions were used to allow direct comparisons between the two methods with 5 repetitions performed for each permutation of variables.

The performance of the mass-weighted routine was assessed by comparing element mass found using this routine against the ‘idealised’ polygon coverage values which gives a mass error value. In all cases the mean error for the entire mesh area is a small percentage (<2%) of the target areal density. This is as expected; even though variation exists on an element-to-element basis, the two methods will average out to give very similar global mass totals. The standard deviation of error values across the mesh provides a clearer picture of the relative performance of the intersection routine.

In Figure 6-16 standard deviation is expressed as a percentage of target areal density to allow direct comparison between all experimental permutations. In each case the variation from element-to-element shows that mass distribution is highly sensitive to element area, particularly for the larger tow size. Small element areas coupled with increasing tow density leads to localised mass concentrations compared with results using the polygon routine. The effect is seen to reduce as target areal density is increased in both cases with variation between the two methods reducing by as much as 50% for 24 K segments. A tolerance level of 10% (depicted by the horizontal line, Figure 6-16) was chosen as a compromise between mesh detail and mass distribution accuracy which suggests an element area of 200 mm^2 is acceptable for 24 K tows as long as the target areal densities exceeds 300 gsm. For 3 K segments a much finer mesh is permissible down to 20 mm^2 for the equivalent areal density.

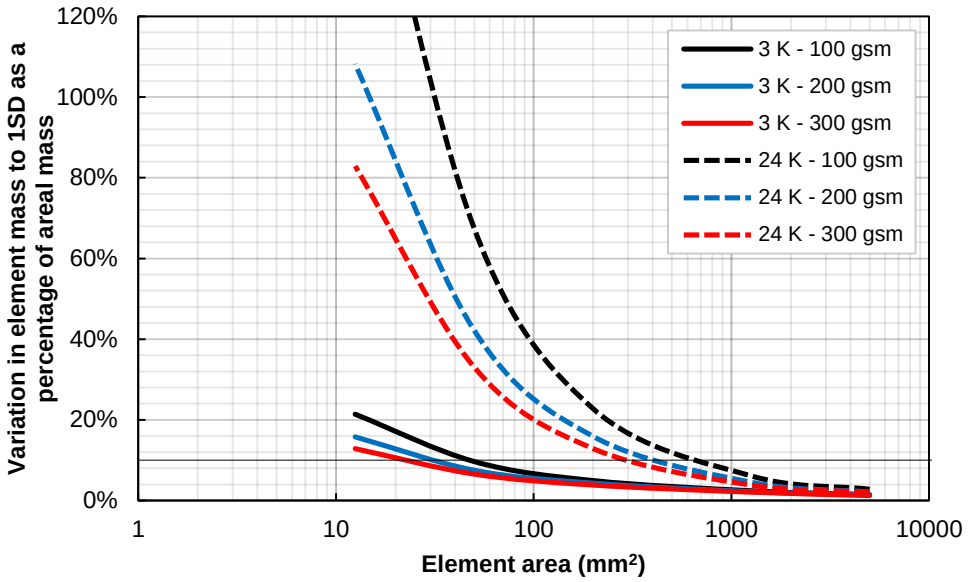

Figure 6-16: Element mass variation between the two coverage algorithms versus average element area. Mass variation is expressed as a percentage of target areal density for 3 K and 24 K depositions with a 10% threshold line used to determine element size limits. Mass distribution accuracy for the intersection algorithm is highly sensitive to element size for higher filament count segments.

Figure 6-17 shows the number of elements encountered by the intersection routine normalised to the polygon method. For 3 K, 100 gsm preforms 96% of the same elements are occupied using 20 mm^2 element areas. A mesh consisting of 200 mm^2 elements results in around 98% of the same elements encountered for depositions using 24 K segments at 300 gsm.

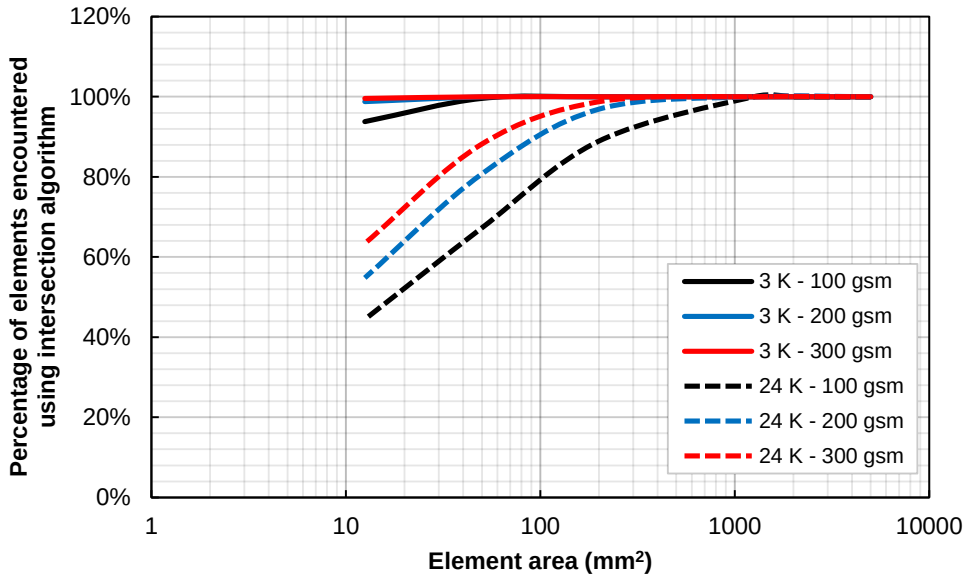

Figure 6-17: Percentage of elements occupied using the intersection routine normalised to the number encountered by the polygon routine across different mesh densities.

For a reliable representation of mass distribution across the tool surface the conclusions from this study is that for slender aspect ratio segments (3 K and 6 K) a minimum mesh element size of 20 mm^2 is recommended. For 12 K and 24 K tows a mesh element area of 270 mm^2 should be used. In both cases at least 300 gsm should be deposited ensuring that the segment count is sufficiently high to reduce the effect of localised mass concentrations. In reality, final preform areal densities are not going to be as low as 300 gsm; this would equate to a fibre volume fraction of ~6% for a 3 mm thick moulded laminate. This value is far more likely to represent a single layer during the spray process where it may be desirable to analyse the coverage performance of the layer in isolation.

Whilst the Sutherland-Hodgman polygon clipping algorithm can be extended to process 3D contoured meshes, it is computationally more expensive than the intersection routine in its un-optimised state. Rather than commit significant time to extending, optimising and testing the routine, the intersection method is preferred providing an acceptable approximation to macroscale mass distribution.

6.2.7. Preform areal mass variability

The stochastic nature of spray processes result in inherently variable areal coverage. Previous work has investigated the effects of three microstructural parameters (tow size, fibre length and laminate thickness) on simulated areal density variation and experimental mechanical performance [53]. Simulated depositions showed that areal density variation was strongly correlated with laminate thickness and tow size. Increasing the target areal density from 0.75 kg/m^2 to 2.25 kg/m^2 resulted in an average decrease of 31% in areal density variability. A decrease in tow size from 24 K to 6 K saw an average decrease of 50%. The mean effect of increasing fibre length was found to be significant at the lower areal density bound but generally less of a factor than the other two parameters. These correlations translated to clear trends in mechanical performance highlighting the need to understand and limit areal variation.

Due to the change in modelling design philosophy and experimental set up for this thesis, it was important to perform a similar investigation into the likely effects on areal mass variation across virtual preforms. The same three parameters were studied with the experimental design shown in Table 6-1.

Table 6-1: The three factors investigated in the simulated areal mass variability study with their corresponding factor level values.

Tow size (K)	Fibre length (mm)	Target areal density (gsm)
3, 6, 12, 24	10, 30, 90	200, 400, 800, 1200, 1600, 2000, 4000

The deposition head height was fixed at 300 mm from the mesh and an orthogonal robot path used to promote even fibre coverage. The spray area was oversized in relation to the tool mesh to remove any large mass variations that arise at spray boundaries. Each robot pass targeted a deposition of 200 gsm so for higher areal densities multiple passes were required.

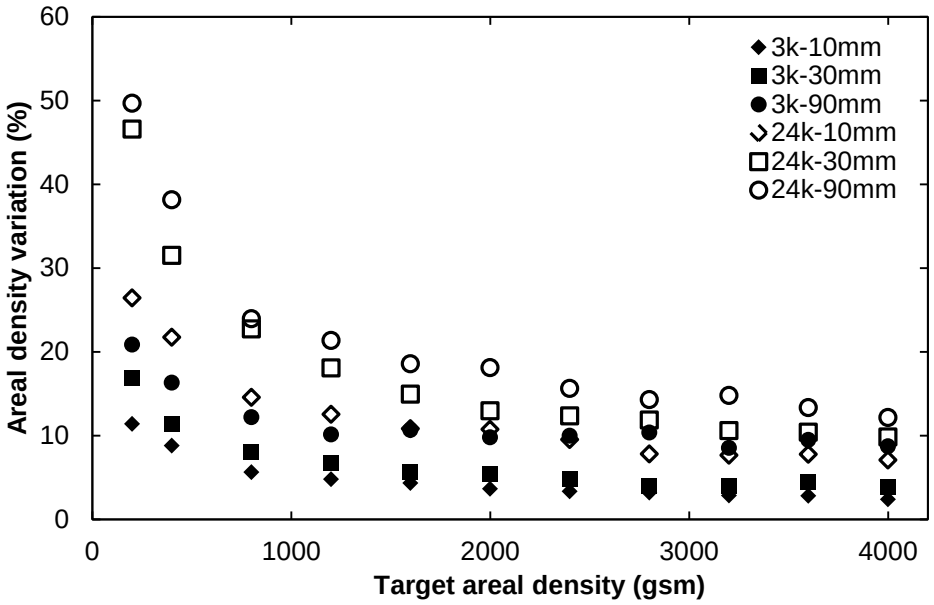

Figure 6-18: Areal density variation across the simulated preform versus target areal density for 3 K and 24 K fibre architectures. An inverse power law relationship is observed in each case.

The simulated results for the relationship between target areal density and mass variation follows a decaying power law in each case. As previously observed, increasing bundle filament count results in increases in mass variation for any given target areal density. This is due to fewer segments being sprayed on each robot pass. Figure 6-18 illustrates the potential increase in variation when switching from a 3 K tow to a 24 K tow whilst keeping all other process variables constant. For a preform designed for 30% V_f at 3 mm laminate thickness (~1600 gsm) the areal mass variation can be expected to rise by an average of ~130% for the three fibre lengths investigated.

Preforms consisting of 3 K tow will result in segment counts eight times greater than for the equivalent 24 K tow preform. The actual segment count can be estimated in the model by dividing robot path length by Equation (6-15):

$$number\ of\ segments\ deposited = \frac{robot\ path\ length}{distance\ per\ deposition} \tag{6-37}$$

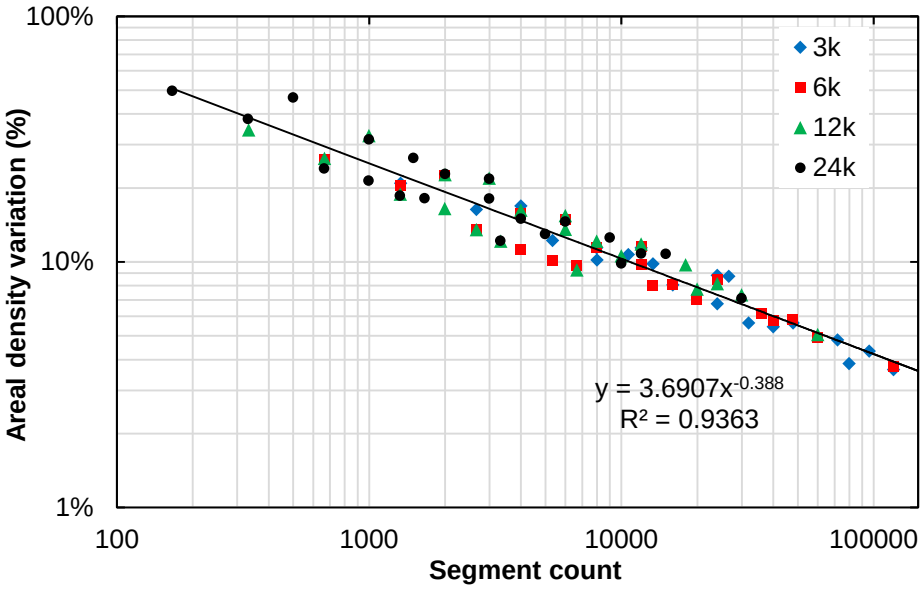

Figure 6-19: Areal density variation versus segment count for all tow size and fibre length permutations investigated. An inverse power law is observed giving a linear relationship using log-log axes. Simulations suggest that areal variation is strongly dependent on the number of segments deposited.

Expressing preform areal density variation for all tow sizes and fibre length permutations with respect to segment count results in Figure 6-19. Model simulations suggest that areal density variation is strongly dependent on segment count and not on the specific microstructural parameters investigated. The literature review in Chapter 2 highlighted the improvements in intra-preform CV for discontinuous fibre laminates when tow size and fibre length are reduced and laminate thickness is increased (keeping global fibre volume fraction constant). The net effect is an increase in the number of segments present in the composite thereby reducing the occurrence of unreinforced resin rich areas prone to failure initiation. The relationship in Figure 6-19 further supports these observations.

For this particular robot path strategy, attempting to limit the areal mass variation to 5% across the 400 mm x 300 mm preform area would require ~65,000 segments. If a fibre length of 10 mm is selected, using 3 K tows would require an areal density of

least 1090 gsm (~20% V_f for a 3 mm thick plaque). This is comfortably within the operating range for both physical preforming and moulding operations. Increasing the tow size to 24 K means that the lowest global areal density value is eight times greater, due to the difference in tow linear density, which is unfeasible for a 3 mm cavity (this laminate thickness is used to create mechanical testing specimens in Section 7.4.2). Therefore preform quality would have to be sacrificed to accommodate larger filament counts unless the part thickness was substantially increased.

If the use of larger tow sizes is desirable for reasons such as material cost and potential deposition rates, then the fibre length should be reduced to approach critical length to increase segment count. Other modifications to the spray process should also be considered to further improve coverage such as programming more complex robot paths by offsetting sequential orthogonal passes. Fibre filamentisation procedures have also been effective in decreasing intra-preform CV by splitting fibre bundles into lower filament-count forms [55, 87, 106]. Filamentisation can occur naturally during fibre spray (as a result of low levels of sizing or short fibre lengths) or induced mechanically; however, undesirable effects such as increasing preform loft and reducing permeability can negatively impact manufacturing cycle times and preform processability. The current iteration of the UoN DCFP deposition head tends to retain tow integrity during fibre spray, therefore low levels of inherent filamentisation is experienced.

6.2.8. Iterative solution based on homogeneity

The visualisation of fibre distribution and preform variability offers a useful mechanism of feedback to optimise process parameters based upon initial design criteria. As described in previous sections; three-dimensional fibre networks are graphically represented using fibre centrelines constructed from intersection points spanning the tool mesh. Intra-preform variability is illustrated in the form of a coverage map based on the difference in areal density between the local element domain and the average preform areal density. Areas which deviate excessively from the preform mean are identified according to a user-defined colour scale. Process parameters can then be modified to improve material distribution until preform mass CV requirements or other design criteria are met. In Chapter 2, work investigating the

optimisation of material distribution for paint spray process showed potential for automated techniques; however, severe limitations existed for complex 3D geometries such as unrealistic robot programs and large disparities between simulated and experimental data. The conclusion was that a heuristic approach would be viable if process simulations can be performed rapidly to simulate informed changes to process parameters. The current simulation software adopts this approach demonstrated by the following example.

Figure 6-20 shows an iterative process to transform a simple planar robot trajectory, suitable for spraying flat plaques, into a 3D trajectory to spray the complex seat tool geometry. Deposition head orientations were also modified (not shown) to ensure the deposition head is always oriented towards the target mesh in an effort to reduce wastage (<6% for the final simulated preform). Figure 6-21 and Figure 6-22 show the resulting coverage maps and preform structures for the basic 2D robot program and the optimised program respectively using 6 K tows, 30 mm fibre length and targeting an areal density of 300 gsm. The initial simulation produced an inconsistent preform with unoccupied areas of reinforcement on the lateral bolster sections of the seat (Figure 6-21) leading to a preform mass CV of ~36%. With the revised robot program in Figure 6-22, the lateral bolster sections are successfully sprayed producing a more homogenous preform with a mass CV of ~20%. The return edges are still lean on reinforcement; however, the structural sections of the seat show improved coverage for a low target areal density. Comparisons between different tow sizes and target areal densities is summarised in Table 6-2 with the highest quality preform (14.7% CV) achieved using 3 K tows at 1611 gsm. Preforming simulation and coverage analysis completed in ~79 s for 3 K, 300 gsm depositions and ~415 s for a 1611 gsm preform. The fast simulation times allows for rapid optimisation of process parameters compared with conducting experimental trials.

Table 6-2: Comparison of preform mass CV values and wastage for different tow size, target areal density and robot program permutations.

Tow size (K)	Target areal density (gsm)	Robot program	Average areal density (gsm)	Wastage (%)	CV (%)
3	300	CS04	284.26	5.3	17.7
3	1611	CS04	1537.62	4.6	14.7
6	300	CS01	255.87	14.7	36.3
6	300	CS02	213.68	28.8	34.3
6	300	CS03	249.79	16.7	33.9
6	300	CS04	290.69	3.1	20.0
6	1611	CS04	1511.38	6.2	15.4
12	300	CS04	271.76	9.4	25.7
12	1611	CS04	1522.62	5.5	16.8
24	300	CS04	288.37	3.9	32.7
24	1611	CS04	1543.06	4.2	18.8

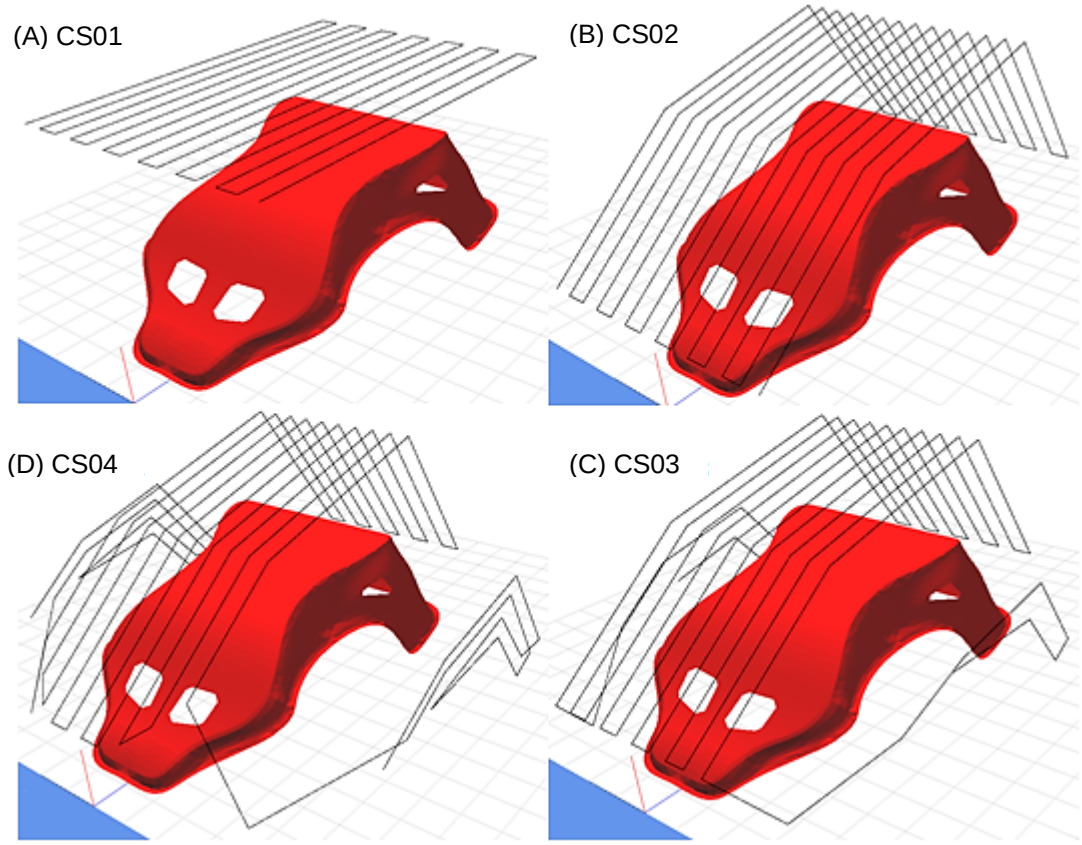

Figure 6-20: Evolution in robot trajectory planning for the car seat geometry. Black lines depict the continuous robot paths used to simulate different preforming strategies. (A) A simple trajectory commonly used for 2D preforming was employed to establish the preform baseline quality. (B & C) The robot trajectory was progressively modified to conform to the tooling geometry with path lines added to spray the lateral bolsters with optimised deposition head orientations. (D) The robot trajectory used to produce the simulated preform in Figure 6-22 which is optimised for fibre coverage and to limit material wastage during preforming.

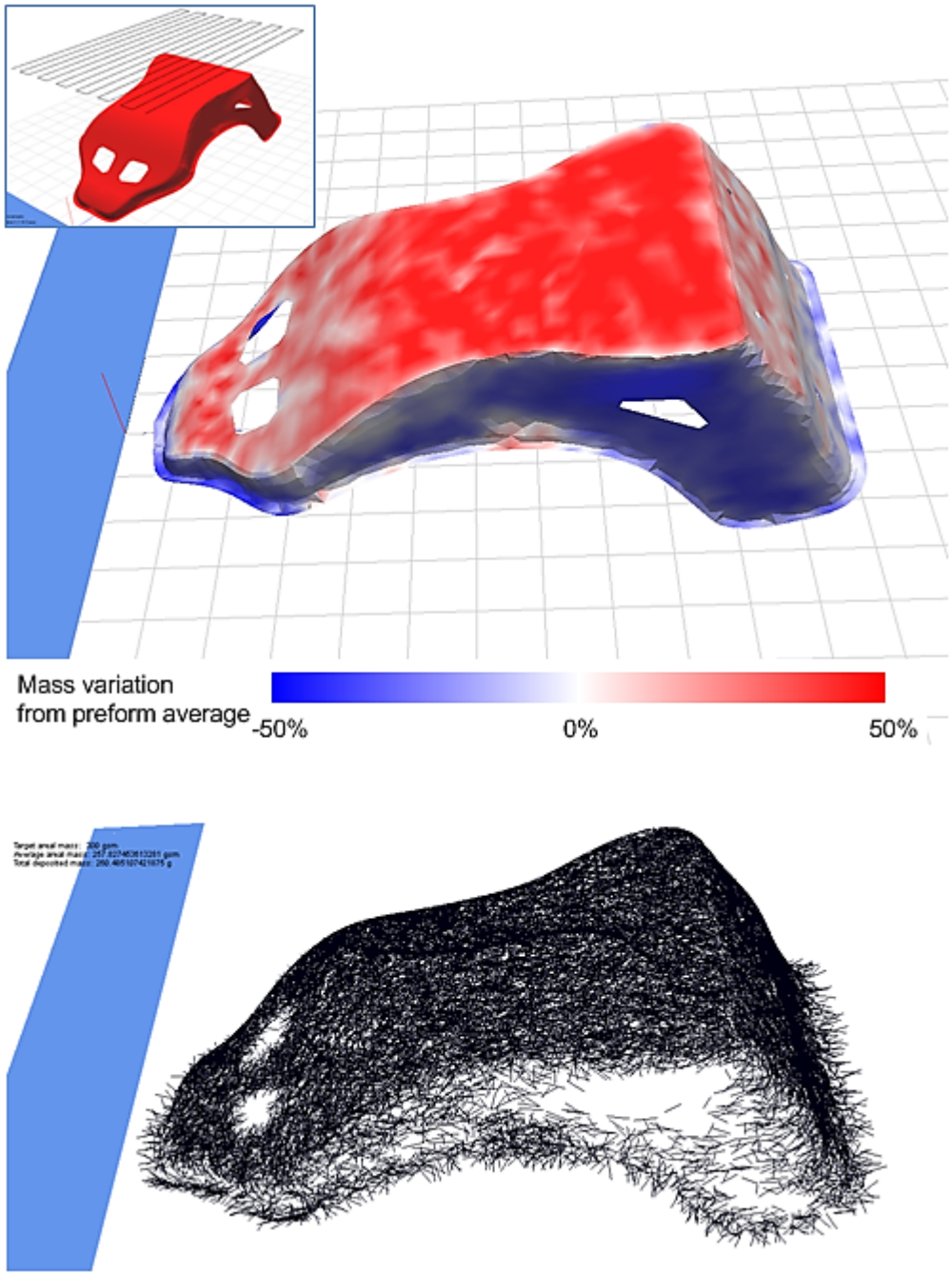

Figure 6-21: Initial preforming effort using a basic robot program, 6 K tows and 30 mm fibre length targeting 300 gsm. (Top inset) Single layer robot trajectory using North-South passes. (Top) Preform mass coverage map showing the variation of areal mass from the preform average. Clearly the deposition is unbalanced with very low levels of reinforcement in the lateral bolster sections. (Bottom) The simulated preform structure with visibly poor coverage. The preform CV of mass is 36.3%.

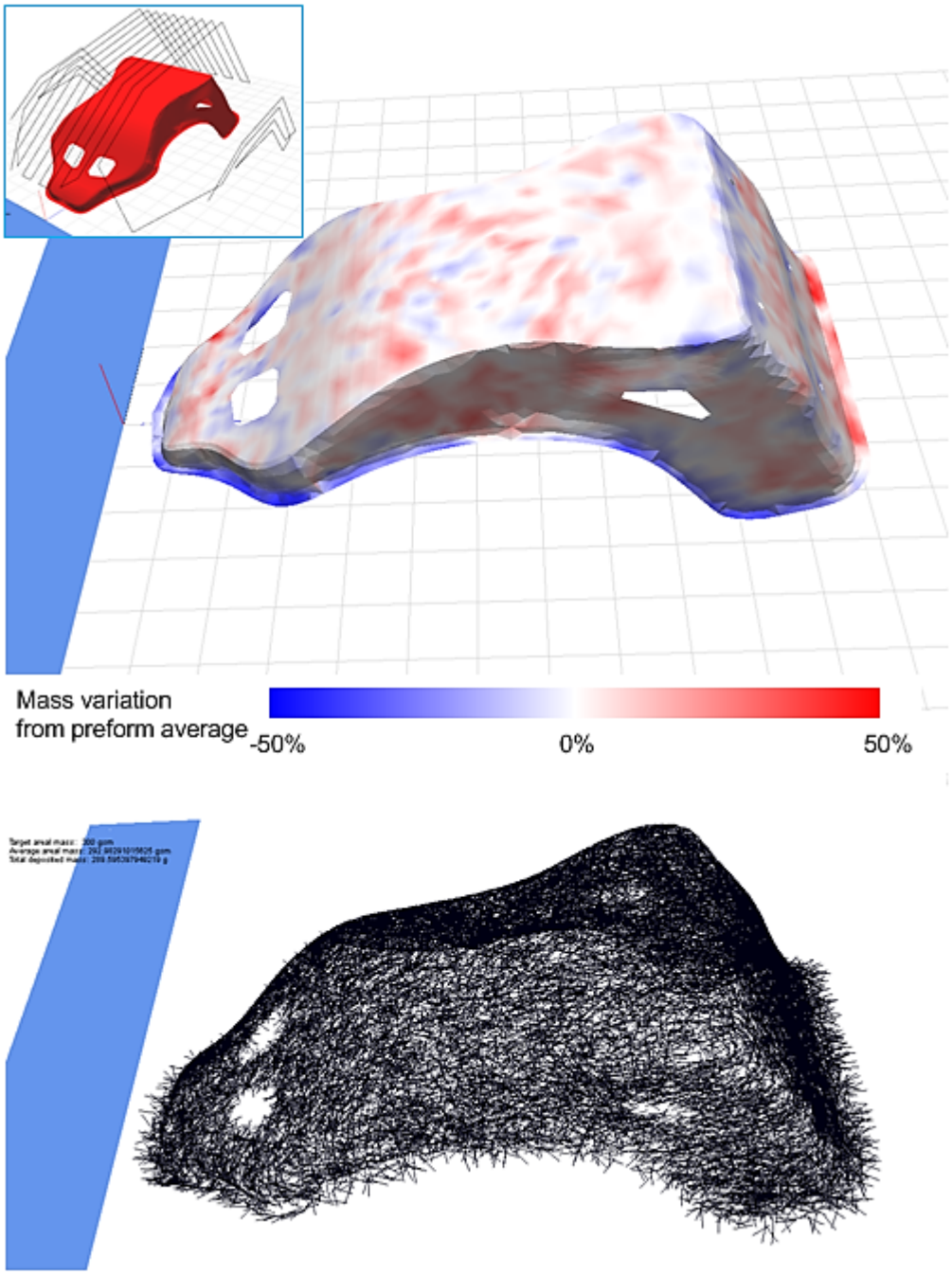

Figure 6-22: Improved deposition strategy using the visual robot trajectory editor with the robot path extended to spray the lateral bolster sections directly (Top inset). The coverage map shows a more uniform distribution of reinforcement with only the return edges lacking fibre content. The process variables remain constant using 6 K tows, chopped to 30 mm fibre length targeting 300 gsm. (Bottom) The simulated 3D fibre network with an intra-preform CV of mass of 20.0%.

6.2.9. Finite Element Analysis output

Further analysis of the simulated fibre network can be completed using FEA to model the mechanical response as a complete composite part. Analysis is performed in the commercial FEA package ABAQUS using an input deck generated from within the process model software. To capture the macroscale heterogeneous response of discontinuous fibre architectures the properties for each element domain is treated separately to neighbouring elements building upon concepts presented by Feraboli with the use of random RVE's [154]. Two modelling approaches are provided; rule of mixtures (ROM) and classical laminate theory (CLT). The ROM approach is a simplistic route to mechanical property analysis calculating the fibre volume fraction within each element and assigning appropriate fibre and matrix properties. Properties within each element domain are assumed to be isotropic with fibre orientations disregarded. A more complex analysis is performed by applying CLT which takes into account individual fibre orientations. Each fibre is modelled as a unidirectional (UD) tape with the addition of a resin ply to achieve target laminate thickness. The input file supplies ABAQUS with model geometry, material definitions and history input data leaving boundary and loading conditions to be defined within ABAQUS prior to processing finite element data.

6.2.9.1. Rule of mixtures

The ROM approach is applied to each element independently using the element areal mass found using Equation (6-34) to calculate fibre volume fraction:

$$V_{f\,i} = \frac{m_{A\,i}}{\rho_c t_i} \tag{6-38}$$

where ρ_c is the density of carbon fibre, m_A is the areal mass and t is the thickness of the ith element. A linear elastic material model is applied to each element with Young's modulus in the principle direction E_1 and Poisson's ratio v_{12} calculated as follows:

$$E_{1_i} = \left[\eta_\theta V_f E_f + (1 - V_f) E_m\right]_i \tag{6-39}$$

$$v_{12} = \left[V_f v_f + (1 - V_f) v_m\right]_i \tag{6-40}$$

The Krenchel efficiency factor η_θ for predicting the effect of fibre orientation on stiffness is taken as 0.375 for perfectly random orientations [162]. For simplicity the original nodal and element definitions used for geometrical representation in the process model are retained and reproduced as shell section elements (type S3) in ABAQUS. Mesh element resolution is limited by the findings from the mesh sensitivity study where element areas ≥200 mm^2 are recommended for larger tow sizes (≥12 K) to avoid large localised mass concentrations for target global areal densities of ≥300 gsm. For smaller tow sizes (≤6 K) a finer mesh is permissible down to an element area of 20 mm^2 spacing without affecting the accuracy of mass distribution.

To avoid multiple unique material definitions for each element, the range of areal masses across the meshed domain are discretised into equal length bins. An arbitrary value of 20 bins is chosen where each element mass is evaluated and assigned to the closest mid bin value.

To assess the tensile stiffness response using the ROM approach, a specimen scale mesh was generated for the process model (Figure 6-23). An area which covered twice the fibre length from the boundary of the area of interest (AOI) was sprayed. The resulting mass distribution was then imported into ABAQUS/Standard for static tensile testing. The specimen size was in accordance with typical experimental testing standards; width of 25 mm and gauge length of 120 mm, and pinned at one end with the other end loaded via a dummy node. A displacement boundary condition was applied to the dummy node and the resulting force recorded to calculate principle stress and tensile modulus.

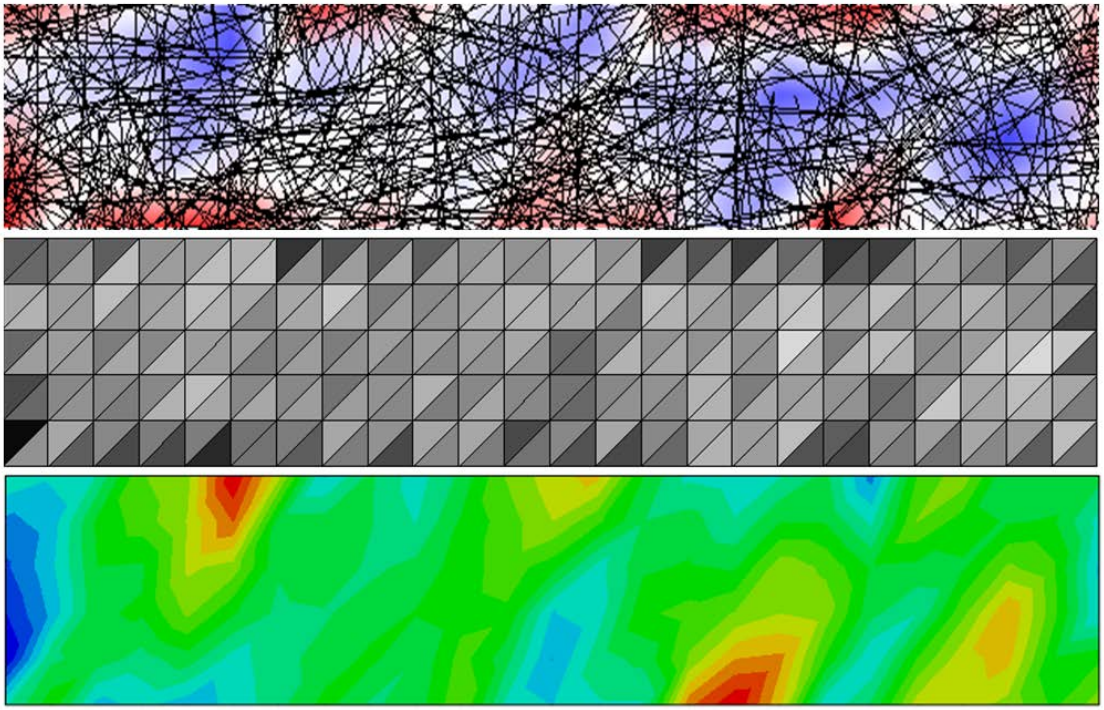

Figure 6-23: (Top) Close-up screenshot of a random deposition with the line segments representing bundle centrelines. The corresponding mass coverage map is visible behind the fibre network highlighting the fibre rich/lean areas. (Centre) The specimen mesh imported into ABAQUS/CAE complete with material property definitions created using ROM. The greyscale depicts fibre volume fraction with darker elements representing areas of high fibre content. (Bottom) A sample result obtained from FE analysis with the specimen subject to a tensile load (applied to the right hand edge). The contoured image shows the strain distribution along the specimen.

6.2.9.2. Classical Laminate Theory

An alternative method to modelling the fibre segments distributed throughout the part is to treat each instance of fibre within each element as a ply of unidirectional material covering the area of the element.

$$\rho_{A_p} = \frac{m_{f_p}}{A_p} \quad , p = 1, 2, \dots, n \tag{6-41}$$

where ρ_A is areal density, A_p is the ply area (equal to the element area) and m_f is the mass of fibre within each ply p. Each unidirectional ply will have the same material properties along its principle axis with the thickness of the ply proportional to the equivalent segment areal mass. The thickness is calculated by assigning a volume fraction to the fully impregnated tow segment. Using a value of 0.6 [146]:

$$V_p = \frac{V_{tow}}{V_{f\,tow}} = \frac{m_{f\,p}}{0.6\rho_f} \quad \textbf{(6-42)}$$

The thickness of the ply t_p can be expressed as:

$$t_p = \frac{V_p}{A_p} \quad \textbf{(6-43)}$$

The ply principle axis orientation equates to the tow segment orientation relative to the global axes. Once all UD plies within an element have been assigned the remaining composite part thickness t_r is assigned as an isotropic resin ply.

$$t_r = t_c - \sum_{i=1}^{n} t_{p_i} \quad \textbf{(6-44)}$$

where t_c is the target composite thickness. The isotropic resin ply t_r is halved and assigned as the surface plies of the composite element as in Figure 6-24. If the total segment ply thickness exceeds the cavity depth then the resin ply thickness is set to zero. This is caused by localised segment agglomeration which results in the local part thickness being greater than the tool depth. This is a concern during manufacture if experienced regularly across the tool surface with implications on pressure required for tool closure suggesting that the preform design volume fraction is too high. If the occurrence is infrequent then it is reasonable to assume that through preform handling and consolidation prior to moulding, the areas of excessive areal mass will go through some distribution phase to surrounding zones with lower areal mass. The process model software provides a percentage value for element ply stacks exceeding tool cavity depth with the addition of the fibre coverage map so that the user can make an informed decision of whether to proceed with property analysis or refine the deposition strategy. A sample FE output is presented in Figure 6-25 showing the strain distribution over the specimen length. High strain areas match low areas of low volume fraction in the top image, particulary at the specimen boundary.

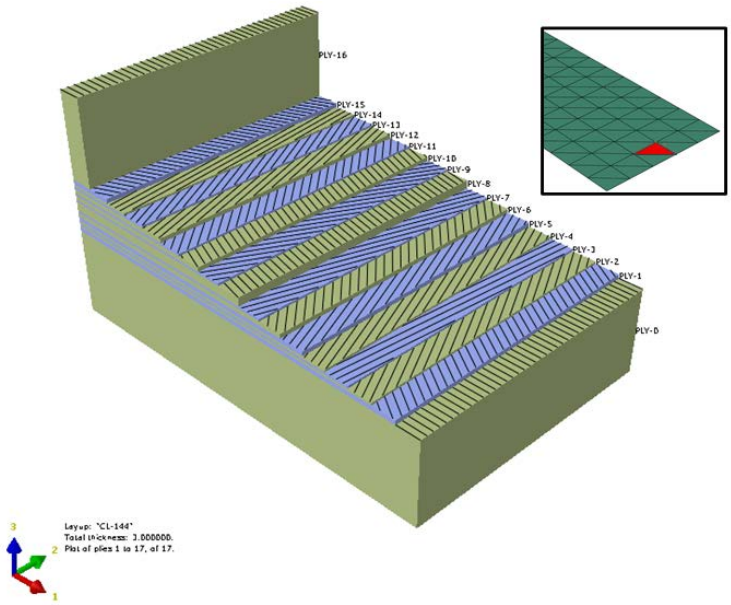

Figure 6-24: A screenshot of a ply stack plot in ABAQUS for the element highlighted in the inset image. The two thick bounding layers represent resin-only regions modelled as an isotropic material. Each UD ply towards the middle of the composite represent individual impregnated tow segments using the laminate analogy. The banded lines on each ply signify the ply orientation.

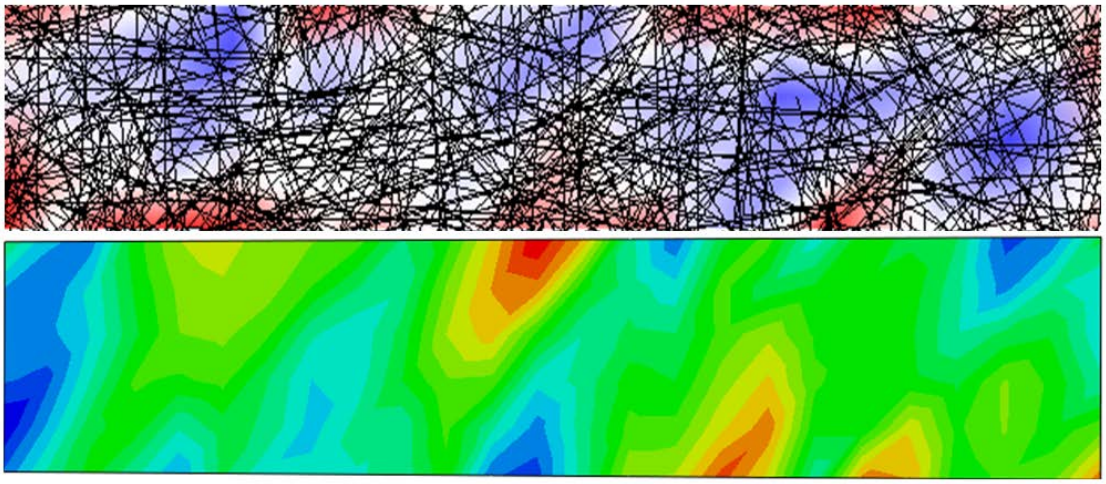

Figure 6-25: (Top) Close-up screenshot of a random deposition with the line segments representing bundle centrelines. The corresponding mass coverage map is visible behind the fibre network highlighting the fibre rich/lean areas. (Bottom) A sample result obtained from FE analysis using CLT based definitions with the specimen subject to a tensile load (applied to the right hand edge). The contoured image shows the strain distribution along the specimen.

6.3. Chapter conclusions

In this chapter a modelling schema to create realistic fibre networks for three-dimensional preforms was presented. The proposed software package can import complex tool geometry along with the flexibility to define various process and material parameters to simulate the physical DFP process. The process model draws

upon deposition head characterisation data and fibre flight kinematic modelling in Chapter 4 to simulate the macroscale deposition process. The resulting preform structure is then analysed to determine the quality of reinforcement distribution in order to facilitate process parameter optimisation.

The method adopted to assemble fibres was demonstrated and compared against a robust fibre coverage method and was observed to be sensitive to part mesh density. An element size of 270 mm^2 for 12 K and 24 K preforms and 20 mm^2 for smaller tow forms is suggested to provide close approximations to chopped segment mass distributions.

A mass variability study was conducted for simulated 2D preform architectures where it was observed that variability is heavily dependent on the number of segments present in the structure. An inverse power law exists between areal density variation and segment count where for a 300 mm x 400 mm area (experimental plaque scale), ~10,000 chopped segments are required to achieve a preform mass CV of ~10%. In terms of input process parameters this points to the usage of small tow sizes and small fibre lengths to improve preform quality and process repeatability. Repeatability and material uniformity is particularly important for design procedures when selecting these types of materials. An example of the proposed iterative preform design process for genuine 3D tool geometry illustrated the improvements in preform mass CV that can be realised through the optimisation of robot trajectory and material parameters.

Two methods for mechanical property analysis were presented as a means of assessing the macroscopic performance of the final moulded component. A ROM based method homogenises each element within the component mesh taking the form of an isotropic material with properties dependent on fibre content. This method provides a fast route to FE analysis suitable for random fibre architectures. A more intensive analysis is available using laminate analogy to take into account fibre segment orientation. This method is adopted in Chapter 7 to predict the tensile modulus of aligned fibre specimens and compared against experimental data.

Chapter 7. Model validation

7.1. Introduction

In this chapter the process model outlined in Chapter 6 is subject to validation tests using empirical data obtained from the UoN DCFP facility. The two core components of the process model are the robot simulation model and the mechanism for simulating fibre deposition. Fibre spray modelling is to some degree validated within the typical operating limits of the current DCFP process by using characterisation data collated in Chapter 4. The robot simulation subsystem is derived entirely from first principles however, using simple kinematic equations which are validated in the following section. Additionally, a fibre alignment study is performed to characterise the mechanical performance of aligned DCFP architectures using the current concentrator. The latest iteration of the concentrator was designed to achieve high deposition rates whilst retaining the properties reported in previous work [54]. This also provided an opportunity for comparison with the classical laminate plate theory method developed for FEA analysis in the previous chapter.

7.2. Cycle time

In Chapter 6 the robot was assumed to accelerate at a constant rate using an arbitrary value to develop the kinematic model. In this section the kinematic model is compared with the laboratory robot to assess model accuracy. The robot performance is considered in isolation with quoted cycle times equating to robot program execution only rather than the cycle time for the complete preforming process.

A simple path profile was chosen which is typically used to deposit a single layer of reinforcement for a 600 mm x 400 mm flat plaque (Figure 7-1). The overall path length is 11.6 m consisting of an east/west pass followed by a north/south pass covering a target area of 0.24 m^2. The overall cycle time for the program was recorded experimentally via data logging software communicating directly with the

programmable logic controller (PLC) which monitors user defined outputs from the robot unit. The simulated cycle time for a target linear robot speed of 1 m/s was 11.84 s which compares with the experimentally recorded cycle time of 21.67 s; resulting in an error of 45.4%. The error remained unacceptably high over a range of target velocities investigated – over 30% lower than experimental results.

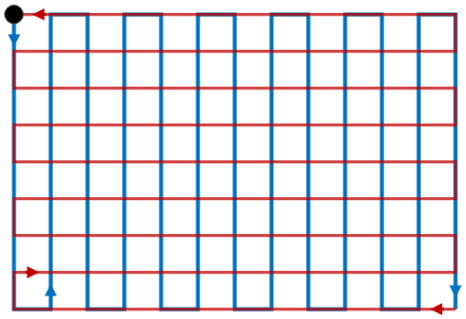

Figure 7-1: Robot path lines for an orthogonal spray pattern typically used for 2D experimental plaque preforming.

In each case the peak velocities were equal for each path line indicating that a large discrepancy exists between true and simulated robot acceleration. Due to the lack of information available for detailed motion control of the laboratory robot, an in-depth study into the acceleration characteristics was conducted. A National Instruments USB-6009 data logger was used to fulfil the requirement for a higher sampling rate (~5000 Hz), than available via the PLC, to record the response during the short acceleration phases. A start-stop single path program was used to analyse both acceleration zones, from rest to target velocity and vice versa, using a calibration constant of 0.4 V/mm^2 to deduce the velocity profile over the single path.

The recorded signal consisted of high levels of noise so a simple recursive filter was employed twice; forwards and backwards through the raw data set, resulting in a zero-phase filtered signal as in Figure 7-2. From this the peak acceleration was calculated from the linear acceleration region of the curve. An average acceleration was also derived by taking into account the S-curve motion profile essentially creating a trapezoidal velocity model, Figure 7-3.

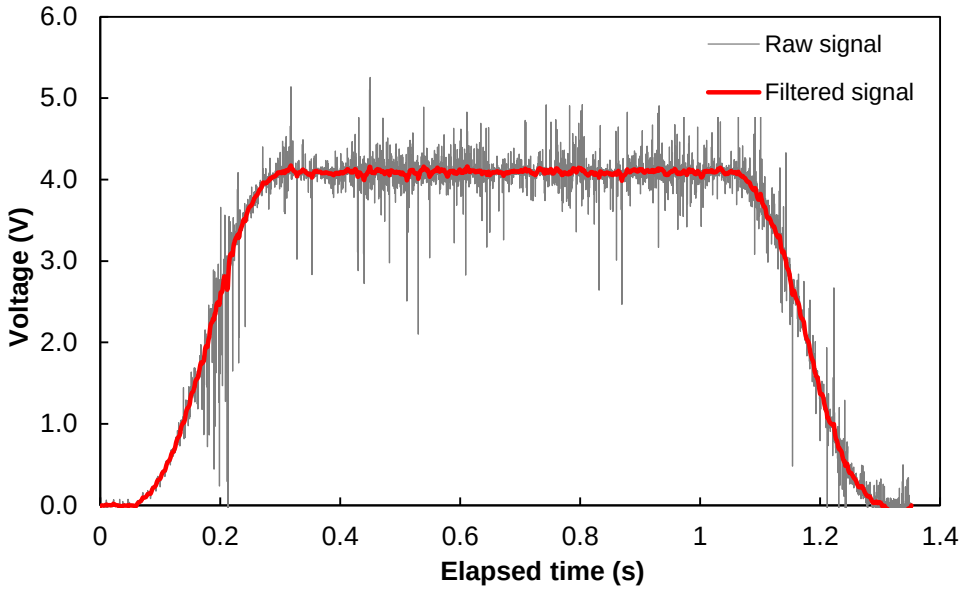

Figure 7-2: Voltage signal from the robot control unit for a single robot path (1000 mm, 1000 mm/s). The signal is proportional to the linear robot velocity. A custom recursive zero-phase filter was used to smooth the raw data set.

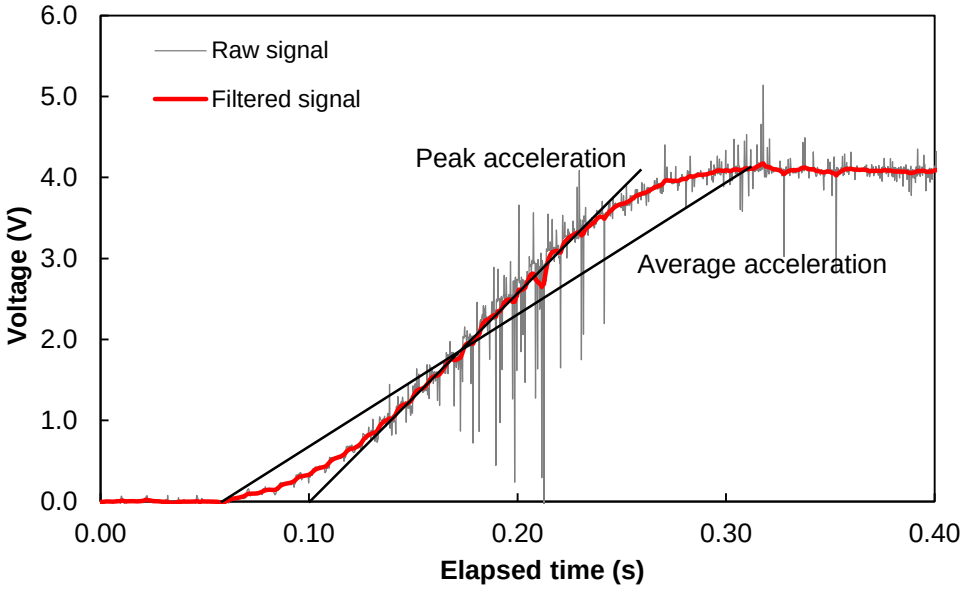

Figure 7-3: Voltage signal response over an acceleration zone starting from rest. The average acceleration zone accounts for the S-curve motion profile.

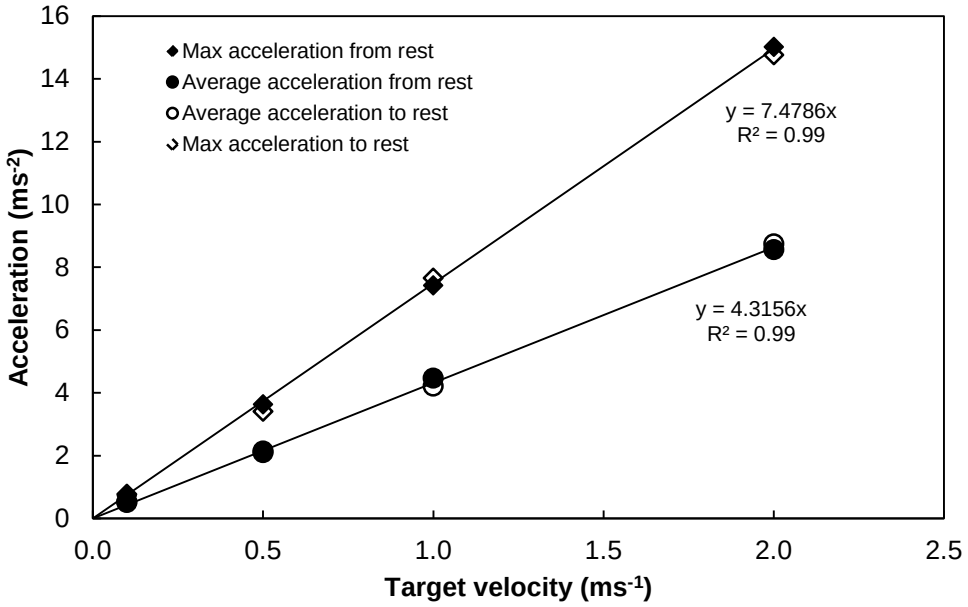

Figure 7-4: Experimentally derived peak and average accelerations versus programmed target velocity.

Four target velocities were investigated; 100, 500, 1000 & 2000 mm/s to examine the response in robot acceleration. Figure 7-4 shows that a linear fit satisfies the relationship between target velocity and acceleration over the tested range and implies that the time taken to accelerate is independent of the programmed target velocity or more specifically; the potential change in velocity. For the Fanuc RJ3iB the constant acceleration (averaged zone) time is ~0.23 s.

Updating the robot model subsystem with the empirically derived values for acceleration time and acceleration constant achieves a close approximation to experimental results for cycle times over a single start-stop path of 1000 mm. The maximum cycle time error is 2 orders of magnitude lower than previously attained (Table 7-1). Applying the revised model to the full-scale preform pattern in Figure 7-1 reduces the maximum recorded error in cycle time to ~1.6% from ~45.4% for a target velocity of 1 m/s. Cycle time comparisons for each target velocity is presented in Table 7-2. The error that exists between the model and observed cycle times is within an acceptable tolerance (>2%) to have confidence that path strategies can be faithfully replicated within the process model. This not only provides realistic projected cycle times but also accurate instantaneous robot velocity data required for deposition modelling.

Table 7-1: Actual cycle times compared with simulated cycle times for various robot linear velocities. Cycle time error is reduced to <1% by using the experimentally derived acceleration constant.

Target velocity (mm/s)	Distance travelled (mm)	Actual cycle time (s)	Simulated cycle time* (s)	Error*	Simulated cycle time** (s)	Error**
100	1000	10.24	10.00	2.34%	10.23	0.08%
500	1000	2.23	2.00	10.16%	2.23	0.12%
1000	1000	1.23	1.00	18.06%	1.23	0.42%
2000	1000	0.73	0.51	30.05%	0.73	0.32%

* Using the original acceleration constant, 20g

** Acceleration constant linear to target velocity, y = 4.3156x

Table 7-2: Actual cycle time versus simulated cycle time for an orthogonal spray program (Figure 7-1) at various robot linear velocities.

Target velocity (mm/s)	Distance travelled (mm)	Actual cycle time (s)	Simulated cycle time (s)	Error
100	11600	126.42	125.73	0.55%
500	11600	32.84	32.93	0.27%
1000	11600	21.67	21.33	1.57%
2000	11600	15.75	15.53	1.40%

7.3. Preform variability

One of the key objectives in developing the process-driven model detailed in Chapter 6 was to accurately recreate preform fibre networks in order to capture the macroscopic mass variability in DFP materials. The predicted preform mass CV values for a broad set of process parameter combinations suggested that segment count was a dominant factor with lower CV values obtained by increasing the number of segments. Segment count is a function of tow size and fibre length with the implication that for a given a target global areal density, preform CV can be reduced by using smaller tow sizes and fibre lengths. An inverse power law relationship was identified between preform mass CV and segment count.

In this section, preform simulations using the process model software are compared to equivalent experimental preforms to assess the model performance. The experimental flat plaque preforms (400 mm x 300 mm) were manufactured as described in Chapter 3 with a die cutter used to divide the preform into 25 mm x 25 mm coupons. Preforms were cut from the centre of the deposition area to avoid edge effects with the orthogonal robot program in Figure 7-1 used to encourage good quality coverage. The weight of each coupon was measured and averaged over the preform area to determine

average coupon weight, total preform weight and to represent each coupon as a percentage of the average as in Figure 7-5. The preform mesh used in simulations was sized to match the die cutter geometry so that direct comparisons were permitted using identical process parameters. Figure 7-5 and Figure 7-6 shows comparative 6 K, 30 mm fibre length preforms with a target areal density of 0.6 kg/m^2 and 1.2 kg/m^2 respectively. In both cases the predicted average coupon mass and overall preform mass is underweight – mainly attributed to the additional binder content (~5% *wt*) necessary for consolidation. The CV values compare favourably for both areal densities investigated with 13.5% versus 14.6% for experimental and predicted depositions respectively targeting 0.6 kg/m^2. The effect of doubling the target areal density results in a decrease of 38% to 8.4% in preform mass CV for the experimental preform and a 34% reduction to 9.7% for the simulated preform. Table 7-3 summarises the results for both preform architectures with the addition of a 24 K, 30 mm fibre length, 1.0 kg/m^2 preform included to validate predicted results for larger tow sizes.

Two further preforms were manufactured to investigate the accuracy of the simulated spray cone domain with tow size, fibre length and target areal density held constant (6 K, 30 mm, 1.2 kg/m^2). To assess the fibre distribution relative to the robot trajectory a simple north-south path was programmed using a regular 50 mm offset and a single 100 mm offset near the centre of the preform area as in Figure 7-7. The preforms were cut 25 mm from the top trajectory boundary in order to capture edge effects arising from increasing the TCP height. A height of 75 mm (Figure 7-8) and 350 mm (Figure 7-9) was programmed to assess the model performance when required to extrapolate outside of the observed characterisation interval defined in Chapter 4. In both cases the process model adequately replicates the experimental results with absolute CV values <1% higher producing similar mass variation plots. In Figure 7-8 the low TCP height produces a clearly defined channel of very low areal mass as a result of the reduction in the projected area dimensions of the spray cone and the 100 mm path offset. Four of the experimental coupons were not measured within this channel due to the loss in preform integrity post preform consolidation. Therefore coupon mass values were unassigned which marginally increases the experimental CV value. Figure 7-9 shows the same preform spray pattern but with the TCP height set at a distance of 350 mm above the deposition plane with a distinct spray boundary present

in both the experimental and simulated preforms. This is a result of the chopping mechanism which ejects fibres with a bias towards the local deposition head -*x'* axis. Raising the TCP height to 350 mm also produces a greater projected spray cone area with evidence of spray overlap into the channel created by the vacant robot path. Preform mass properties for both specifications are summarised in Table 7-3.

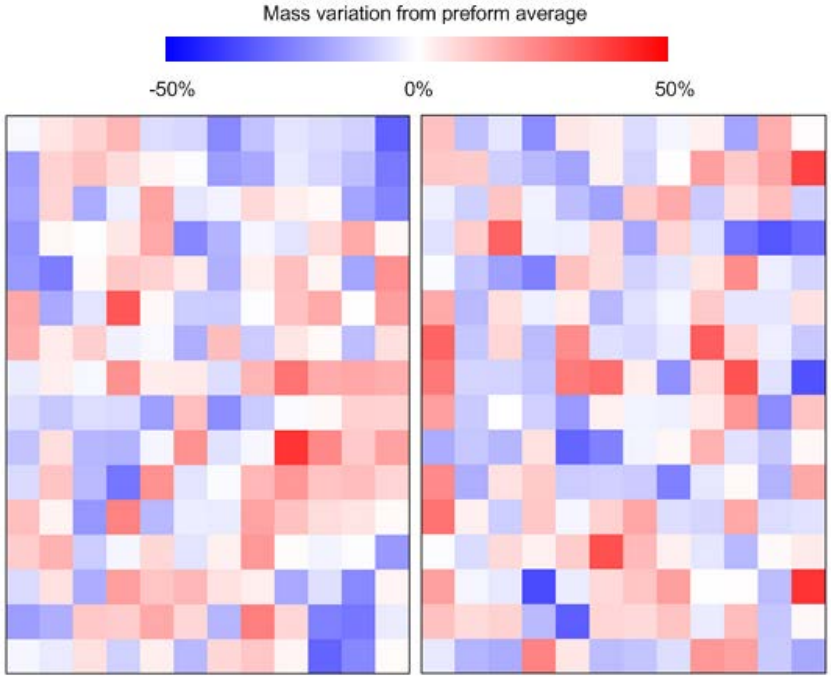

Figure 7-5: Comparison between experimental (left) and predicted (right) mass variability for a preform consisting of 6 K, 30 mm segments with a target areal density of 0.6 kg/m^2. Preforms are flat with dimensions of 400 x 300 mm.

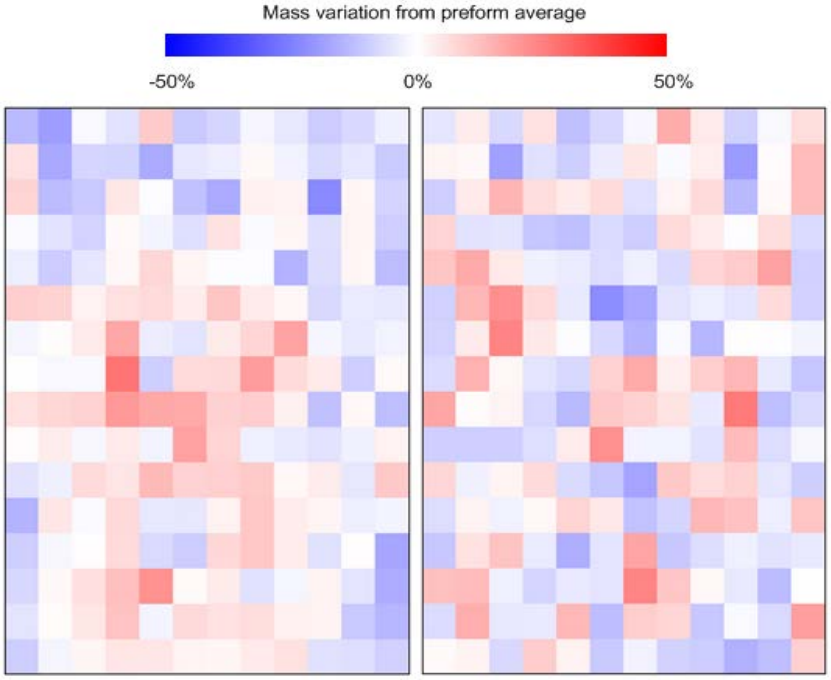

Figure 7-6: Comparison between experimental (left) and predicted (right) mass variability for a preform consisting of 6 K, 30 mm segments with a target areal density of 1.2 kg/m^2. Preforms are flat with dimensions of 400 x 300 mm.

Table 7-3: Mass properties for manufactured preforms obtained from dividing the preform in to 25 mm by 25 mm coupons. Equivalent simulated preform properties use identical process parameters to the experimental setup.

Preform properties		Preform mass (g)	Average coupon mass (g)	Lowest coupon mass (g)	Highest coupon mass (g)	CV (%)
6 K, 30 mm, 0.6 kg/m^2	Experimental	72.95	0.380	0.263	0.531	13.52
	Simulated	71.11	0.370	0.240	0.519	14.55
6 K, 30 mm, 1.2 kg/m^2	Experimental	150.23	0.78	0.604	0.995	8.43
	Simulated	141.42	0.74	0.573	0.930	9.66
24 K, 30 mm, 1.0 kg/m^2	Experimental	115.38	0.601	0.315	0.891	20.59
	Simulated	116.82	0.608	0.326	1.03188	20.26
6 K, 30 mm, 1.2 kg/m^2 – gap (75 mm TCP height)	Experimental	113.79	0.592	0.000	1.048	37.58
	Simulated	108.16	0.563	0.055	0.988	38.43
6 K, 30 mm, 1.2 kg/m^2 – gap (350 mm TCP height)	Experimental	104.81	0.546	0.0813	0.9304	36.63
	Simulated	99.80	0.520	0.061	0.844	37.25

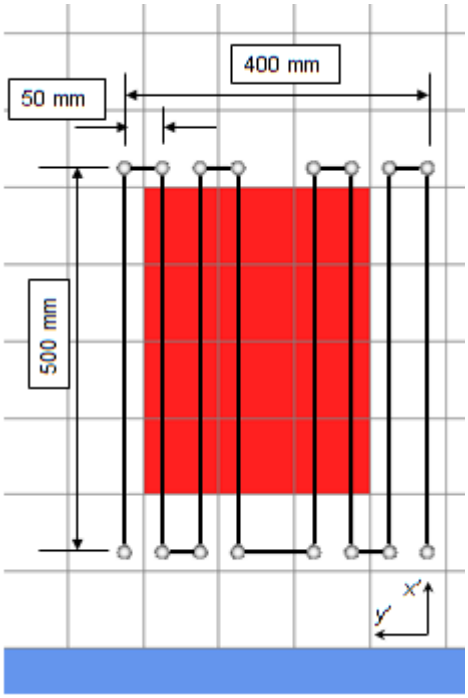

Figure 7-7: Screenshot of a simple north-south robot trajectory programmed for the process model with a path line omitted. The 400 mm by 300 mm preform (red area) was taken 25 mm from left and top trajectory boundaries for mass variability analysis. Experimental preforms were created using the same robot program and process parameters. The preforms were cut close to the top trajectory boundary so that edge effects could be compared between simulated and experimental preforms along with the effect of increasing path offset distance.

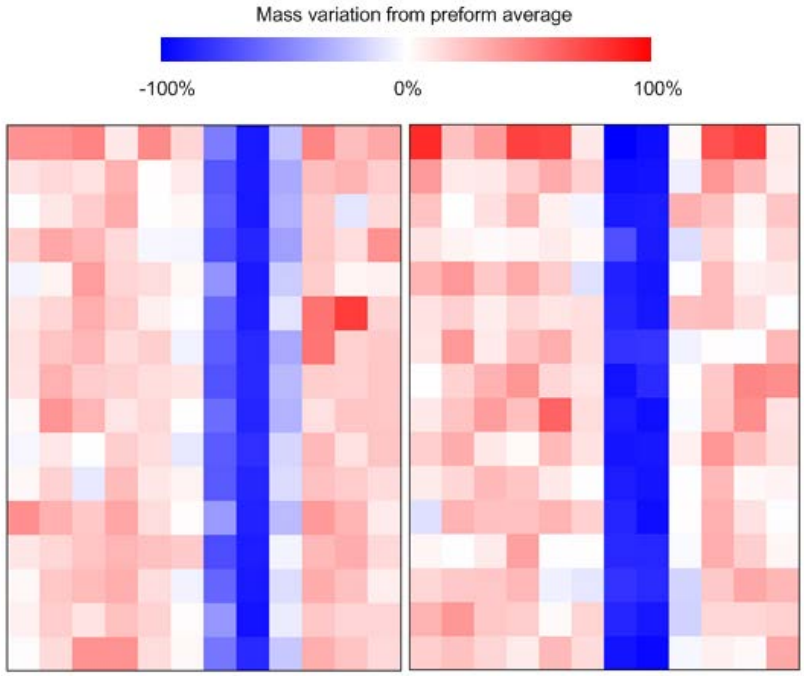

Figure 7-8: Comparison between experimental (left) and predicted (right) mass variability for a preform consisting of 6 K, 30 mm segments with a target areal density of 1.2 kg/m^2 using the robot trajectory in Figure 7-7. TCP height was held constant at 75 mm above the deposition plane resulting in a clear section lean in fibre mass – corresponding to the omitted robot path. The experimental mass plot has a less well defined channel which is highly likely due to a small error in positioning the die cutter relative to the robot trajectory.

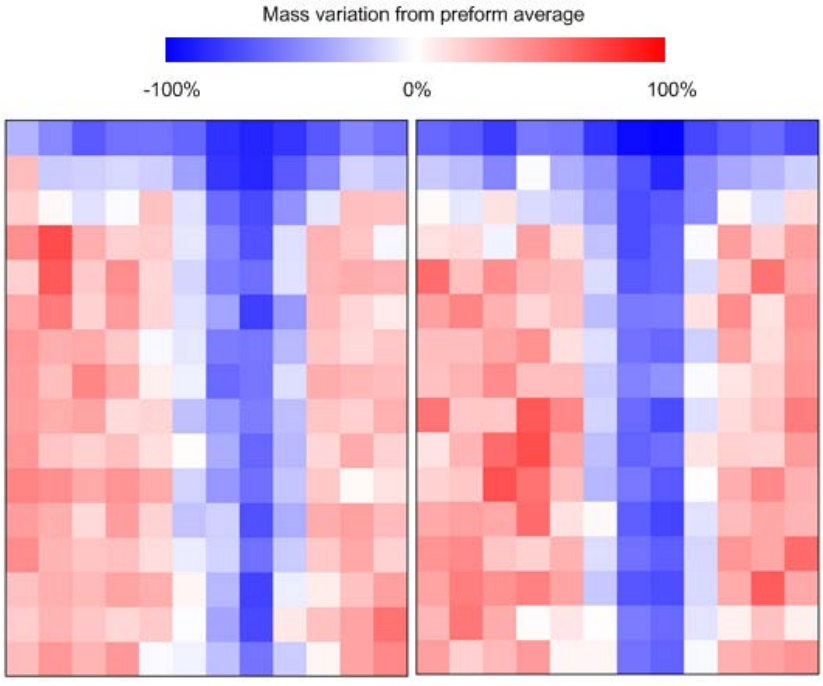

Figure 7-9: Comparison between experimental (left) and predicted (right) mass variability for a preform consisting of 6 K, 30 mm segments with a target areal density of 1.2 kg/m2 using the robot trajectory in Figure 7-7. TCP height was raised to 350 mm above the deposition plane producing a greater spray cone projection area. This is evident with higher fibre content in the region of the vacant robot path line. The effect of spray bias is also demonstrated with the preform boundary visible along the top portion of the preform.

7.4. Fibre alignment

An effective way to maximise mechanical performance for discontinuous fibre composites is through the alignment of reinforcement in the direction of applied load. Previous studies conducted using the UoN DCFP facility used a funnel concentrator to mechanically align chopped segments (Section 1.3.2.1) [54]. High levels of alignment were achieved, particularly for long fibre lengths and high filament count tows (115 mm, 24 K), where ~94% of the deposited segments could be aligned to within ±10° of the robot travel direction. Tensile stiffness and strength gains of 206% and 234% respectively were attained over equivalent random architectures. Deposition rate was considerably affected however with fibre processing issues limiting maximum output to 0.12 kg/min compared with >2 kg/min for random deposition. The proven scope for expanding the DCFP mechanical performance envelope via fibre alignment was enough incentive to develop a new concentrator in order to remove the limitations on deposition rate. The redesigned concentrator is detailed in Section 1.3.2.2 with the following experimental study conducted to assess the performance of the concentrator and key process parameters.

7.4.1. Design of experiments

Table 7-4 summarises the experimental design for investigating the effect of three process variables on mechanical properties; fibre length, tow size and fibre volume fraction. Fibre volume fraction was held constant at 30% V_f to study the effects of fibre length and tow size in isolation and to provide a direct comparison to random fibre architectures consisting of the same target fibre content. Two further preforms were manufactured using 6 K tows with 30 mm and 60 mm fibre lengths at 50% V_f representing a high performance structural specification. Each preform was manufactured, moulded and tested according to the experimental methodology in Chapter 3.

Table 7-4: Design of Experiments for aligned plaques studying the effects of tow size, fibre length and volume fraction. All plaques were moulded to a target thickness of 3mm with 5% wt of Pretex binder.

Tow size (K)	Fibre length (mm)	Target volume fraction (%)
3	30	30
3	60	30
3	90	30
6	30	30
6	30	50
6	60	30
6	60	50
6	90	30
12	30	30
12	60	30
12	90	30
24	30	30
24	60	30
24	90	30

7.4.2. Mechanical tensile testing results

Results from the experimental tensile tests are summarised in Figure 7-10 and Figure 7-11 with the random fibre 6 K, 50% V_f results taken from [163] for comparison.

Tensile properties for all tow sizes at 30% V_f are observed to improve with increasing fibre length. Tensile stiffness values are similar for 6 K, 12 K & 24 K plaques with an average gain of 24% when increasing fibre lengths from 30 mm to 90 mm. 3 K plaques exhibit noticeably superior performance for 30 mm fibre lengths; however the stiffness trend lines for all 30% V_f plaques suggest that a plateau may exist around ~60 GPa. The highest tensile modulus achieved at 30% V_f was observed for the 3 K, 60 mm permutation at 56.5 GPa. Results are omitted for 90 mm 3 K fibres due to processing issues resulting in poor quality preforms. The close proximity of the deposition head to the preform tool coupled with the tow width being of the same scale as the circular perforations in the preform tool meant that chopped segments became lodged in the perforations disrupting fibre spray on subsequent passes. An increase of at least 64% is observed in tensile strength as fibre length is increased from 30 mm to 90 mm (6 - 24 K tows), most likely due to the reduction in segments present in the preform. This effectively reduces the amount of stress raisers emanating from fibre bundle ends resulting in higher strength values.

The effect of filament count is particularly significant to tensile strength performance with UTS values increasing as the tow size is reduced. Strength increases by 53% and 60% for 30 mm and 90 mm fibre length plaques respectively when reducing tow size from 24 K to 6 K at 30% V_f. The substantial increase in strength can be attributed to two important factors. The decrease in bundle filament count results in more segments in the laminate to achieve an equivalent fibre volume fraction – whilst this means that a greater amount of segment ends are present, the smaller filament bundle sizes means that the stress concentrations arising from the bundle ends are less intense. The increased number of segments also improves preform homogeneity and hence quality, as demonstrated in Section 7.3. The 3 K, 60 mm combination once again exhibited the highest properties with an absolute strength value of 510.4 MPa, but with the potential of even higher properties if 90 mm fibre lengths could have been reliably processed. The amount of data points collected over the fibre lengths of interest did not provide conclusive evidence of a plateau being reached for tensile strength typically seen for discontinuous fibre composites.

Increasing the fibre volume fraction to 50% V_f for 6 K, 30 mm and 60 mm fibre length plaques provided significant improvements in modulus as anticipated. Increasing the fibre length from 30 mm to 60 mm produced a 34% gain in tensile stiffness with a highest absolute value of 91.6 GPa. Strength values appeared to be relatively insensitive to lengthening the fibre length by a factor of two, with UTS falling fractionally by 2% with an absolute highest value of 507.5 MPa (6 K, 30 mm). A gain of 68% and 83% was experienced for 30 mm and 60 mm fibres lengths respectively over the 6K 30% V_f case. Improvements of 76% and 29% were observed for ultimate tensile strength. Aligned high performance specification (6 K, 50% V_f) specimens experienced an increase of 49% and 111% in modulus over the equivalent random architecture for 30 mm and 60 mm fibre lengths respectively and UTS improved by 137% and 78%. The properties for the high performance specification equate to maximum retention values of 77% and 40% for stiffness and strength compared to an equivalent continuous UD laminate.

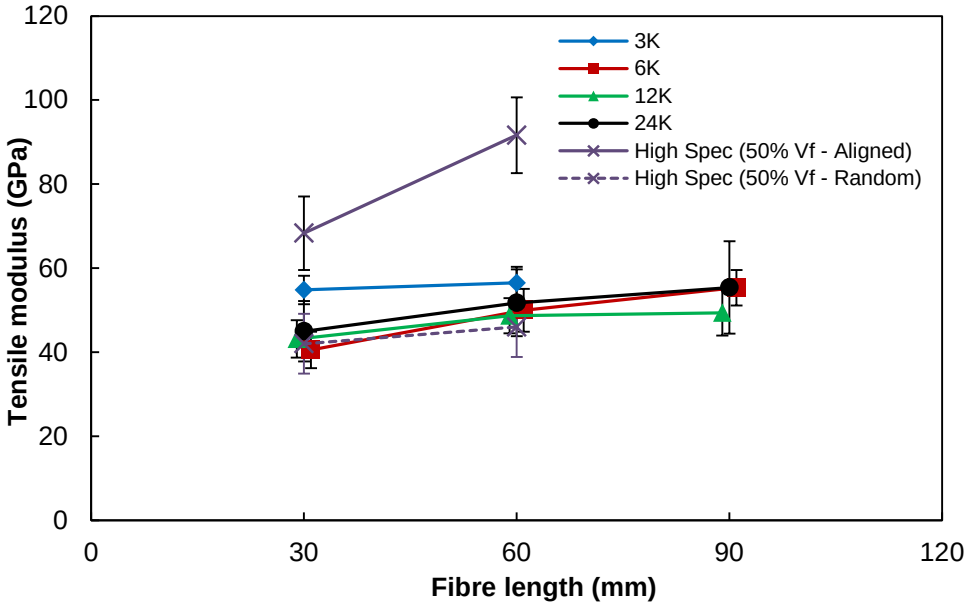

Figure 7-10: Tensile modulus versus fibre length for all 30% and 50% V_f plaques. Data for the high performance specification (50% V_f) random architecture plaques is taken from [163].

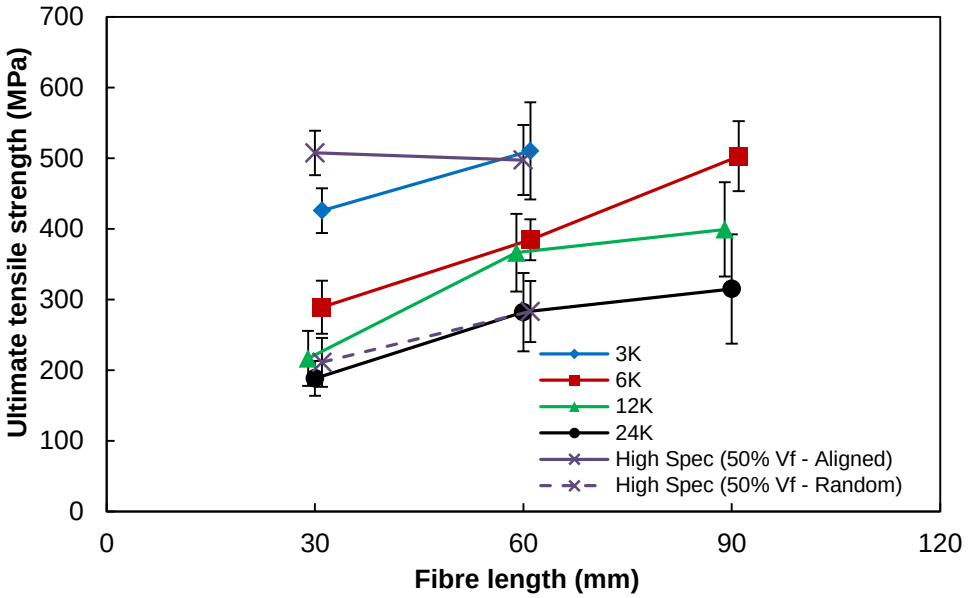

Figure 7-11: Ultimate tensile strength versus fibre length for all 30% and 50% V_f plaques. Data for the high performance specification (50% V_f) random architecture plaques is taken from [163].

Normalised testing data for 30% V_f aligned and random specimens is presented in Figure 7-12 for 30 mm fibre lengths to allow for a direct comparison with available data [163]. The benefit of aligning fibres can be clearly seen for each tow size with considerable performance gains in both tensile stiffness and strength. The highest mechanical properties as well as the largest percentage increase over the random fibre laminate is realised for 3 K tows with a gain of 137% and 148% in modulus and ultimate tensile strength respectively.

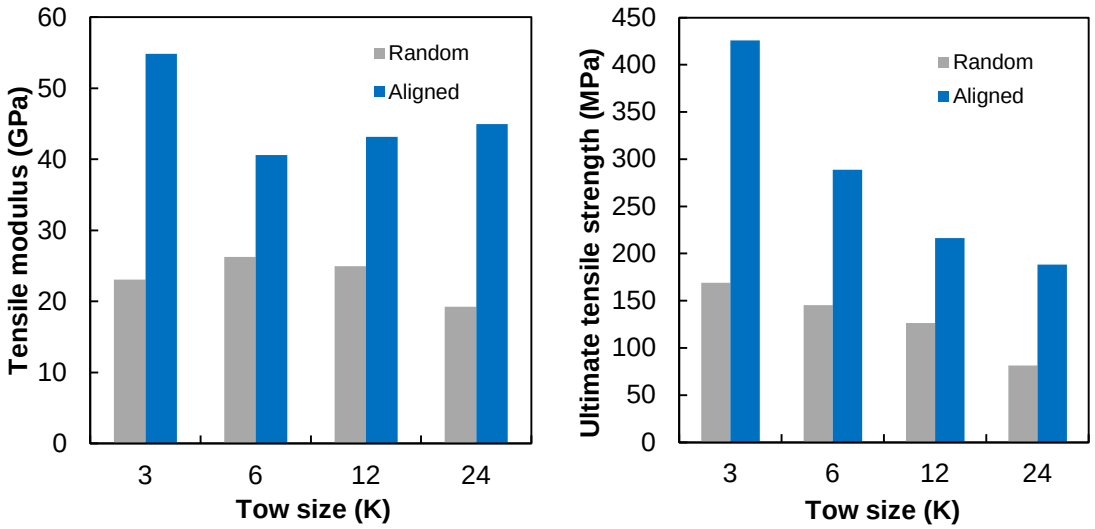

Figure 7-12: Mechanical performance comparison between random and aligned specimens normalised to 30% V_f. Fibre length is held constant at 30 mm with a target laminate thickness of 3 mm.

Normalised results (to 30% V_f) for tensile testing data is summarised in Figure 7-13 comparing mechanical performance of plaques manufactured using the current method for fibre alignment with plaques created using the previous DCFP concentrator (data taken from [54]). Tensile stiffness values for 6 K and 24 K tows are bounded by the previous results with superior properties for 24 K plaques using the current alignment concentrator. The distinction between 6 K and 24 K properties is far less pronounced for the current alignment process however. Whilst direct comparisons cannot be made between both sets of data due to geometric differences in chopping mechanism; significant improvements in ultimate tensile strengths has been realised. Processing 6 K, 90 mm fibre produced the highest absolute strength of 502.9 MPa, 25% higher than the best case from the previous study. Considering that the segment count will be roughly equal between the two alignment methods for 30 mm and 60 mm architectures, the increase in strength experienced using the current alignment device is more than likely a result of improved preform homogeneity. This could be the result of an optimised deposition strategy used for the current work where spray layers were staggered to encourage improved fibre coverage.

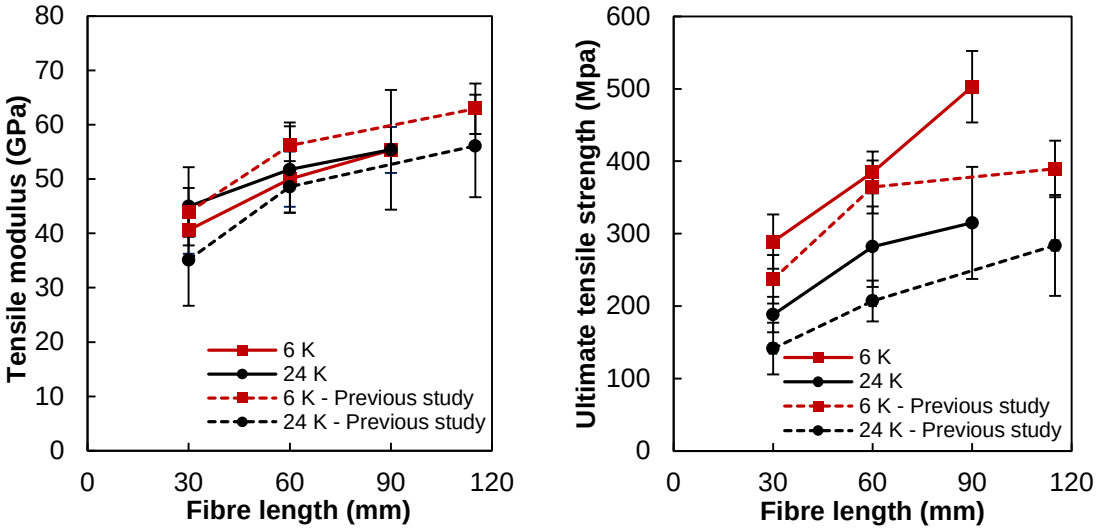

Figure 7-13: Mechanical performance comparison between using the current alignment concentrator and the previous concentrator normalised to 30% V_f.

7.4.3. Mechanical stiffness prediction using FEA

Results from the fibre alignment experimental study were used to validate the FE input deck generated by the process software as described in Section 6.2.9. The CLT approach was chosen to account for aligned fibre distributions which significantly affect final laminate performance. The input deck defines mesh geometry, ply definitions for each mesh element (thickness and orientation) and material properties for a 60% V_f UD ply and neat resin. The material properties are derived from the constituent properties summarised in Chapter 3. Additional simulation setup was completed within ABAQUS/CAE to assign boundary and loading conditions prior to execution using the finite element code ABAQUS/Standard.

Each of the tow size and fibre length permutations for 30% V_f aligned plaques were simulated using identical input parameters including the north-north program discussed in Chapter 3 to provide a fair comparison. A 120 mm x 25 mm specimen mesh was extracted from the centre of the deposition area with one edge assigned a pinned boundary condition and the opposite edge loaded via a dummy node using a fixed displacement (2 mm).

FE results for tensile stiffness are provided in Figure 7-14. For almost all of the permutations tested, predicted mechanical stiffness values exceed experimental values and reside close to the upper experimental uncertainty range. Simulated results over-predict modulus by 6% - 14% (excluding 24 K, 30 mm and 12 K, 90 mm

permutations) but still capture the general trend of tensile stiffness increasing with fibre length for each plaque specification. Despite the comparative difference in tensile modulus between simulations and experimental data, the laminate analogy approach combined with alignment characterisation data accumulated in Chapter 4 demonstrates the applicability for mechanical property analysis for full macroscale geometries.

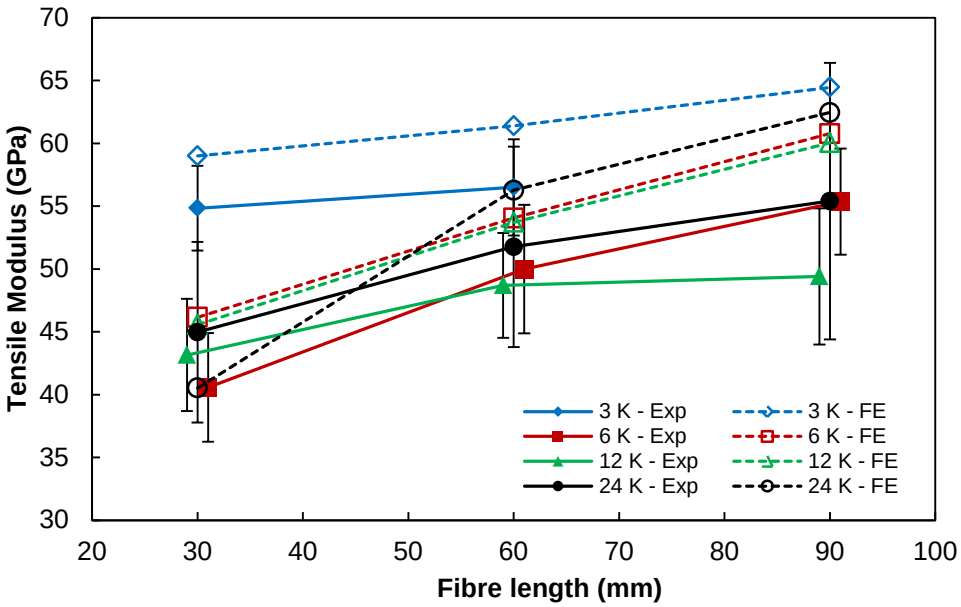

Figure 7-14: Comparison between experimental and FE simulation results for specimen tensile stiffness. Each tow size and fibre length permutation was normalised to 30% V_f.

7.5. Chapter conclusions

The validity of several important subsystems contained within the DFP process simulation software has been tested in this chapter as well as characterising the performance of the current alignment concentrator. Analysis of the velocity profile for the UoN DCFP 6-axis robot has revealed that the time taken to accelerate between programmed changes in velocity is a fixed quantity (~0.23 s). Applying this knowledge to the robot kinematic model developed in Chapter 6 reduces the predicted cycle time error from 45.4% to 1.6% for a typical orthogonal spray pattern used to manufacture experimental preforms. Increasing the accuracy of robot motion simulation allows for a closer approximation to the true fibre release sites during preforming.

Preform mass variability was studied for random 2D fibre architectures in an effort to validate mass coverage results obtained from the model software. Close agreements for preform mass CV between experimental and simulated depositions exist confirming the relationship between mass variation and segment count established in Chapter 6. Further analysis has shown that by modelling fibre deposition conforming to a spray cone and using the characterisation data acquired in Chapter 4; spray area boundaries can be successfully reproduced. This is particularly important for three-dimensional tool profiles where accurate deposition head control is required for net-shape preforming.

The performance envelope and flexibility of the DCFP process has been enhanced through the development of an alignment concentrator designed for high deposition rates. Cycle times are on a par with random fibre preforming achieving satisfactory rates in excess of 2 kg/min when processing four 24 K tows with high levels of fibre alignment. Gains in tensile modulus and strength over random architecture (quasi-isotropic modulus 21.4 GPa and UTS 136.2 MPa) for 30% V_f plaques of 137% and 148% respectively underline the potential of DCFP as a highly automated process for structural applications. Maximum tensile properties attained from 30% V_f laminates were for the 3 K, 60 mm combination with tensile stiffness and strength values of 56.5 GPa and 510.4 MPa respectively. Increasing volume fraction to 50% V_f using 6 K tows produced further gains in tensile modulus with the highest value observed in this study of 91.6 GPa which further confirms the potential for using aligned discontinuous fibres for structural applications as previously investigated by Cordell and Reeve [42, 105]. Both the characterisation study (Chapter 4) and mechanical testing results have demonstrated that high levels of alignment can be maintained, compared to the previous DCFP concentrator, even though a very significant increase in deposition rate (>600%) has been achieved.

Mechanical property prediction for aligned specimens has been provided using a classical laminate theory approach showing reasonable agreement to experimental results. The oriented fibre networks produced by the process software was approximated using UD plies within each element domain and solved simultaneously using commercial finite element code. An increasing modulus with fibre length trend was reproduced over the tow size and fibre length permutations investigated

demonstrating the viability of such methods to predict macroscale behaviour for complete structures.

Chapter 8. Thesis conclusions

The main aim of this thesis was to further the development of discontinuous fibre preforming processes, predominantly via the generation of computational design software. This required a detailed understanding of the process and material parameters available for the manufacture of discontinuous fibre composites to formulate effective modelling strategies.

An extensive characterisation study was performed to identify the key variables affecting fibre distribution during the preforming stage. Tow size, fibre length and fibre speed were all found to affect mean fibre location in the deposition plane, however, tool centre point height had the greatest influence on both mean location and on fibre distribution from the mean. Increasing TCP height results in a larger effective spray area whilst also accentuating a bias applied by the chopping mechanism resulting in fibres being ejected at an angle to the intended direction. The complex interactions which exist between the variables investigated, as a result of the stochastic nature of this type of spray process, meant that predictive modelling of deposition sites was unfeasible. Instead, fibre deposition was modelled to conform to a spray cone domain - the geometry of which can be modified depending on the process input parameters. This approach requires sufficient characterisation data to be acquired over the typical operating range of DFP processes.

A stochastic macroscale model was developed to generate realistic fibre networks for three-dimensional component geometries. Existing macroscale process models concerning discontinuous fibre materials have been restricted to the 2D domain limiting their applicability to the physical process [53, 111]. The versatile software developed during the course of this thesis has extended the scope for simulating DFP processes for use as a preforming design tool. Rapid simulation times facilitate efficient process parameter optimisation with the potential to significantly reduce the reliance on costly experimental trials. The software provides direct feedback on the quality of reinforcement homogeneity which has a strong bearing on final composite

performance. This is a vital step to increasing the attractiveness of DFP processes in industry which has been previously highlighted by Vaidya [108].

Preform simulations suggest that intra-preform mass variability is heavily dependent on the number of fibre segments present in the preform and not on the specific microstructural parameters. Segment count is a function of tow size, fibre length and target areal density however. The accuracy of the model predictions for preform mass variability was validated against experimental data with close agreement for different fibre architectures.

Mechanical property prediction for simulated preform structures was facilitated via an interface with commercial finite element analysis code. Classical laminate plate theory was applied to individual elements over an entire specimen-scale domain taking into account individual segment orientations and showing reasonable agreement with experimental tensile results. This method is applicable to full scale 3D component geometries permitting the prediction of the mechanical behaviour for the finished laminate and offering a distinct advantage over current statistical methods adopted [154].

A physical process development involved expanding the performance envelope for DCFP through the design of an improved deposition head and fibre alignment device. Applying directional bias to fibre reinforcement in the direction of the load path provides a useful mechanism for increasing discontinuous fibre composite properties. The updated deposition device is capable of spraying highly aligned fibres at deposition rates comparable to random fibre preforming achieving ~2 kg/min for a research-scale installation. This potentially opens up the use of highly automated low cost preforming technologies such as DCFP for structural applications where the design criteria are stiffness limited. This is a significant increase in deposition rate for aligned fibre spray over previous attempts [54]. Tensile modulus results obtained for aligned laminates at 50% fibre volume fraction are comparable with aluminium demonstrating the breadth in mechanical properties that can be achieved.

8.1. Recommendations for further work

In this thesis the process modelling techniques presented have attempted to capture the complex mechanisms involved in directed fibre preform manufacture in order to create realistic fibre networks. The main limitations of the proposed software have been highlighted in Chapter 6 which offers the potential for further development work to expand the capabilities of the model.

To increase the accuracy for representing fibre segments across the tool geometry the method for fibre assembly should be improved. Currently the intersection method described in Section 6.2.6.1 is used for 3D tool profiles but a more realistic representation can be achieved by extending the polygon method in Section 6.2.6.2 into the 3D domain. This would allow finer meshes to be used which are particularly beneficial for complex structures with numerous features.

For the purposes of this thesis an airflow model was omitted from the preform simulations performed in Chapter 6 & 7. The airflow model is essentially a vector averaging routine which takes into account surrounding air velocity and manipulates a fibre segment travelling from the deposition head to the preform screen. The surrounding airflow is dependent on the tool geometry, fan system specification and the level of fibre coverage already deposited. Because fibre coverage is increased gradually over the duration of preforming it is a non-trivial task to model airflow through the entire system accurately. It was suggested that CFD (Section 5.3) may provide a convenient means to model airflow which could output the required velocity field on a layer-by-layer basis for example. Developing this side of the model would require significant effort however for an uncertain gain in the accuracy of fibre deposition.

The FE input deck or integration with commercial FEA software requires substantial validation work against experimental data. The work presented in Section 7.4.3 only considered tensile stiffness data for aligned fibre preforms at 30% V_f. A similar study is required for random fibre architectures and over a realistic range of volume fractions (i.e. 15% to 50% V_f). Tensile strength was not considered due to the lack of a realistic macroscale damage model which is applicable to discontinuous architectures. Being able to predict the final part mechanical properties would further enhance the

attractiveness of using the process model in conjunction with design tools such as CAD.

In Chapter 5 the issue of retaining the deposited fibres in place prior to preform consolidation was investigated. Although a great deal of data was obtained relating pressure drop and superficial air velocity through a material layer/stack thickness, the exact nature of retention is still unknown. A theory relating the available pressure drop across the preform screen versus the required retention pressure for the medium was presented which requires validation. This could be achieved via modifications to the testing apparatus where the force to remove a layer or thickness of material under vacuum can be recorded, or the apparatus inverted so that the material is being retained against its own weight. The vacuum fan can then be controlled until a limiting condition is met where the pressure drop is no longer sufficient to hold the material in place. Other forms of retention should also be investigated with the potential to ‘tack’ fibres into place by introducing a resin system during fibre spray. This could open up further possibilities of reducing part manufacture to a one-shot deposition process producing a charge similar to compression moulding processes. Benefits would include a reduction in cycle times, manufacturing stages and number of tools required. An increased tooling and press cost would be incurred however due to the requirement of higher tool closing pressures compared to RTM.

References

1. Department of Energy & Climate Change, UK Government, *Climate Change Act 2008*, 2008
2. Department of Energy & Climate Change, UK Government, *2011 UK greenhouse gas emissions - provisional figures*, 2012
3. Department for Transport, UK Government, *UK transport greenhouse gas emissions factsheet*, 2012
4. Brady M. and Brady P., *The road to lightweight performance*, Reinforced Plastics, 2008, 52(10), pp. 32-36.
5. International Civil Aviation Organization (ICAO), *Environmental Report 2010 - Aviation & Climate Change*, 2010
6. Baker F.S., Gallego N.C., Baker D.A. and Naskar A.K., US Department of Energy, *Lightweighting Materials - Low-Cost Carbon Fiber*, 2007 Progress report, 2007
7. Balaji Thattaiparthasarathy K., Pillay S., Ning H. and Vaidya U.K., *Process simulation, design and manufacturing of a long fiber thermoplastic composite for mass transit application*, Composites Part A: Applied Science and Manufacturing, 2008, 39(9), pp. 1512-1521.
8. Norris R.E., Lomax R.D., Xiong F., Dahl J.S. and Blanchard P.J., *Advanced High Speed Programmable Preforming*, SAMPE 2010, Seattle, WA, USA, 2010
9. Fuglestvedt J., Berntsen T., Myhre G., Rypdal K. and Skeie R.B., *Climate forcing from the transport sectors*, Proceedings of the National Academy of Sciences, 2008, 105(2), pp. 454-458.
10. Hulme A.J., Johnson M.R. and Tucker N., *Manufacturing With Thermoset Composites*, in Tucker N. and Lindsey K., eds., *Introduction to Automotive Composites*, 2002, Shrewsbury, UK, Smithers Rapra, pp. 91-118.
11. Jacob A., *BMW counts on carbon fibre for its Megacity Vehicle*, Reinforced Plastics, 2010, 54(5), pp. 38-41.
12. Brady M. and Brady P., *Automotive composites – the search for efficiency, value and performance*, Reinforced Plastics, 2007, 51(1), pp. 26-29.
13. Houston D., *The Development of a Structural SMC Pickup Box*, Automotive Composites Conference, Troy, MI, USA, 2001
14. Myers A.D., *GM Moves Towards Composite Transmission Cross-Member for Full-Size Trucks*, Automotive Composites Conference, Troy, MI, USA, 2004
15. Bruderick M., *Applications of Carbon Fiber SMC for the 2003 Dodge Viper*, Automotive Composites Conference, Troy, MI, USA, 2002
16. Guillermin O., *Enabling Design Innovation in Automotive Composite Applications*, 6th Automotive Composite Conference, Troy, MI, USA, 2006
17. Brosius D., *Carbon Fiber: The Automotive Material of the Twenty-First Century Starts Fulfilling the Promise*, Automotive Composites Conference, Troy, MI, USA, 2003
18. Stewart R., *Carbon fibre composites poised for dramatic growth*, Reinforced Plastics, 2009, 53(4), pp. 16-21.
19. Anon, *COMPOSITES EUROPE highlights solutions for mass production of automotive composites*, Reinforced Plastics, 2011, 55(4), pp. 45-46.
20. Anon, *Cytec teams up with Jaguar Land Rover*, Reinforced Plastics, 2012, 56(5), pp. 12.
21. Manson J.-A., *HIVOCOMP: large-scale use of carbon composites in the automotive industry*, Reinforced Plastics, 2012, 56(6), pp. 44-46.

22. Kasapoglou C., *Aerospace Series (PEP) - Design and Analysis of Composite Structures : With Applications to Aerospace Structures*, 2010, Hoboken, NJ, USA, Wiley.
23. Baker A.A., Dutton S. and Kelly D.W., *Composite Materials for Aircraft Structures*, 2004, American Institute of Aeronautics and Astronautics.
24. Roberts T., *Rapid growth forecast for carbon fibre market*, Reinforced Plastics, 2007, 51(2), pp. 10-13.
25. Feraboli P., Peitso E., Deleo F., Cleveland T. and Stickler P.B., *Characterization of Prepreg-Based Discontinuous Carbon Fiber/Epoxy Systems*, Journal of Reinforced Plastics and Composites, 2009, 28(10), pp. 1191-1214.
26. Lamb A.M., Daim T.U. and Anderson T.R., *Forecasting airplane technologies*, Foresight, 2010, 12(6), pp. 38-54.
27. Marsh G., *Aero engines lose weight thanks to composites*, Reinforced Plastics, 2012, 56(6), pp. 32-35.
28. Greene E., *Marine Composites*, 1999, Eric Greene Associates.
29. Stewart R., *Better boat building — trend to closed-mould processing continues*, Reinforced Plastics, 2011, 55(6), pp. 30-36.
30. Marsh G., *Marine composites — drawbacks and successes*, Reinforced Plastics, 2010, 54(4), pp. 18-22.
31. Marsh G., *Prepregs boost marine quality*, Reinforced Plastics, 2011, 55(2), pp. 32-35.
32. Grimshaw M.N., *Automated tape laying*, *ASM Handbook, Composites (ASM International)*, 2001.
33. Groppe D., *Robots improve the quality and cost-effectiveness of composite structures*, Industrial Robot: An International Journal, 2000, 27(2), pp. 96-102.
34. Neto P., Pires J.N. and Moreira A.P., *3D CAD-based robot programming for the SME shop-floor*, 20th International Conference on Flexible Automation and Intelligent Manufacturing, FAIM 2010, San Francisco, USA, 2010
35. Penin L.F., Balaguer C., Pastor J.M., Rodriguez F.J., Barrientos A. and Aracil R., *Robotized spraying of prefabricated panels*, Robotics & Automation Magazine, IEEE, 1998, 5(3), pp. 18-29.
36. Mills A., *Development of an automated preforming technology for resin infusion processing of aircraft components*, Proceedings of the Institution of Mechanical Engineers, Part G: Journal of Aerospace Engineering, 2006, 220(5), pp. 499-505.
37. Beckwith S.W., *Filament Winding vs. Fiber Placement Manufacturing Technologies*, SAMPE Journal, 2008, 44(2), pp. 54-55.
38. Marsh G., *Automating aerospace composites production with fibre placement*, Reinforced Plastics, 2011, 55(3), pp. 32-37.
39. Aized T. and Shirinzadeh B., *Robotic fiber placement process analysis and optimization using response surface method*, The International Journal of Advanced Manufacturing Technology, 2011, 55(1-4), pp. 393-404.
40. Chavka N.G. and Dahl J.S., *P4: Glass fiber preforming technology for automotive applications*, 44th International SAMPE Symposium, 1999, Long Beach, CA, USA.
41. Brandt M.R. and Reeve S.R., *Directed fibre preform case studies*, Composites 2001 Convention and Trade Show, 2001, Tampa, FL, USA, Composite Fabricators Association.
42. Cordell T., Tolle T.B. and Rondeau R., *The Programmable Powdered Preform Process for Aerospace: Affordable Performance Through Composites*, SAMPE International Symposium, 2000, SAMPE.
43. Dahl J.S., DeBolt M. and Steenkamer D., *Processing and performance of chopped glass fiber reinforced RTM composites*, 14th International Conference on Composite Materials, 2003, San Diego, CA, USA, ASC.
44. DeVries J.E., Chavka N.G. and Dahl J.S., *Recent advances in glass fiber preforming: Implementation of the Ford Programmable Preform Process (F3P)*, International Conference for Manufacturing of Advanced Composites, 2001, Belfast, N.I.

45. Jespersen S.T., Baudry F., Schmäh D., Wakeman M.D., Michaud V., Blanchard P., Norris R.E. and Månson J.A.E., *Rapid Processing of Net-Shape Thermoplastic Planar-Random Composite Preforms*, Applied Composite Materials, 2009, 16(1), pp. 55-71.
46. Janney M., Geiger E.J. and Baitcher N., *Fabrication of chopped fiber preforms by the 3-DEP process*, COMPOSITES & POLYCON - ACMA, Tampa, FL, USA, 2007
47. Stewart R., *Rebounding automotive industry welcome news for FRP*, Reinforced Plastics, 2011, 55(1), pp. 38-44.
48. Verrey J., Wakeman M.D., Michaud V. and Månson J.A.E., *Manufacturing cost comparison of thermoplastic and thermoset RTM for an automotive floor pan*, Composites Part A: Applied Science and Manufacturing, 2006, 37(1), pp. 9-22.
49. Johnson C.F. and Rudd C.D., *Manufacturing Process Selection for Composite Components*, in Kelly A. and Zweben C., eds., *Comprehensive Composite Materials*, 2000, Oxford, Pergamon, pp. 1049-1072.
50. Das S., *Cost assessment of carbon-reinforced composite automotive part*, 14th International Conference on Composite Materials, 2003, San Diego, CA, USA, ASC.
51. Bhat P., Merotte J., Simacek P. and Advani S.G., *Process analysis of compression resin transfer molding*, Composites Part A: Applied Science and Manufacturing, 2009, 40, pp. 431-441.
52. Chaudhari R., Viebahn F., Karcher M., Elsner P. and Henning F., *Characterization of high-performance composites manufactured by using High-Pressure RTM process variants*, 12th Annual Automotive Composites Conference & Exhibition Troy, MI, USA, 2012
53. Harper L.T., Turner T.A., Warrior N.A. and Rudd C.D., *Characterisation of random carbon fibre composites from a directed fibre preforming process: Analysis of microstructural parameters*, Composites Part A: Applied Science and Manufacturing, 2006, 37(11), pp. 2136-2147.
54. Harper L.T., Turner T.A., Martin J.R.B. and Warrior N.A., *Fiber Alignment in Directed Carbon Fiber Preforms — A Feasibility Study*, Journal of Composite Materials, 2009, 43(1), pp. 57-74.
55. Harper L.T., Turner T.A., Warrior N.A. and Rudd C.D., *Characterisation of random carbon fibre composites from a directed fibre preforming process: The effect of tow filamentisation*, Composites Part A: Applied Science and Manufacturing, 2007, 38(3), pp. 755-770.
56. Harper L.T., *Discontinuous carbon fibre composites for automotive applications*, 2006, University of Nottingham: Nottingham.
57. Fu S.Y. and Lauke B., *Effects of fibre length and fibre orientation distributions on the tensile strength of short-fiber-reinforced polymers*, Composites Science and Technology, 1996, 56, pp. 1179-1190.
58. Kaverov M.E. and Varshavsky V.Y., *Carbon Fibres*, in *Fibre Science and Technology*, 1995
59. van Hattum F.W.J. and Bernado C.A., *A model to predict the strength of short fibre composites*, Polymer Composites, 1999, 20(4), pp. 524-533.
60. Fu S.-Y., Hu X. and Yue C.-Y., *The flexural modulus of misaligned short-fiber-reinforced polymers*, Composites Science and Technology, 1999, 59(10), pp. 1533-1542.
61. Thomason J.L. and Vlug M.A., *Influence of fibre length and concentration on the properties of glass fibre-reinforced polypropylene: 1. Tensile and flexural modulus*, Composites Part A: Applied Science and Manufacturing, 1996, 27(6), pp. 477-484.
62. Campbell F.C., *Structural Composite Materials*, 2010, ASM International.
63. Kacir L., Narkis M. and Ishai O., *Oriented short glass fiber composites. III. Structure and mechanical properties of molded sheets*, Polymer Engineering and Science, 1977, 17(4), pp. 234-241.

64. Mulligan D.R., Ogin S.L., Smith P.A., Wells G.M. and Worrall C.M., *The effect of fibre-bundling on the mechanical properties of a short-fibre composite*, ICCM-11, 1997, Australia.
65. Rondeau R., Reeve S. and Bond G., *Effect of Tows and Filament Groups on the Properties of Discontinuous Fiber Composites*, SAMPE International Symposium, 1999, SAMPE.
66. Harper L.T., Turner T.A., Warrior N.A. and Rudd C.D., *Characterisation of random carbon fibre composites from a directed fibre preforming process: The effect of fibre length*, Composites Part A: Applied Science and Manufacturing, 2006, 37(11), pp. 1863-1878.
67. Masoumy E., Kacir L. and Kardos J.L., *Effect of fiber-aspect ratio and orientation on the stress-strain behavior of aligned, short-fiber-reinforced, ductile epoxy*, Polymer Composites, 1983, 4(1), pp. 64-72.
68. Wetherhold R.C., *Probabilistic aspects of the strength of fiber-dominated short-fiber composites II: Biased fiber distribution*, Materials Science and Engineering, 1987, 91, pp. 13-18.
69. Boylan S. and Castro J.M., *Effect of reinforcement type and length on physical properties, surface quality, and cycle time for sheet molding compound (SMC) compression molded parts*, Journal of Applied Polymer Science, 2003, 90, pp. 2557–2571.
70. Halpin J.C. and Kardos J.L., *Strength of discontinuous reinforced composites: 1. Fiber reinforced composites*, Polymer Engineering and Science, 1978, 18(6), pp. 496-504.
71. van Hattum F.W.J., Nunes J.P. and Bernado C.A., *A theoretical and experimental study of new towpreg-based long fibre thermoplastic composites*, Composites Part A: Applied Science and Manufacturing, 2005, 36(1), pp. 25-32.
72. Umer R., Bickerton S. and Fernyhough A., *The effect of yarn length and diameter on permeability and compaction response of flax fibre mats*, Composites Part A: Applied Science and Manufacturing, 2011, 42(7), pp. 723-732.
73. Dockum J.F. and Schell P.L., *Fiber directed preform reinforcement: Factors that may influence mechanical properties in liquid composite molding*, 6th Annual ASM/ESD Advanced Composites Conference, 1990, Detroit, MI, USA, ASM International.
74. Mandell J.F., Samborsky D.D. and Wang L., *Effects of fibre waviness on composites for wind turbine blades*, 48th International SAMPE symposium, 2003, Long Beach, CA, USA.
75. Jespersen S.T., Baudry F., Wakeman M.D., Michaud V., Blanchard P., Norris R. and Månson J.A.E., *Flow Properties of Tailored Net-Shape Thermoplastic Composite Preforms*, Applied Composite Materials, 2009, 16(6), pp. 331-344.
76. Jacob G.C., Starbuck J.M., Fellers J.F. and Simunovic S., *Effect of fiber volume fraction, fiber length and fiber tow size on the energy absorption of chopped fiber-polymer composites*, Polymer Composites, 2005, 26(3), pp. 293-305.
77. Turner T.A., Harper L.T., Warrior N.A. and Caliskan A., *Energy Absorption Performance of Meso-Scale Discontinuous Carbon Fibre Composites*, Internation Journal of Vehicle Structures & Systems, 2011, 3(2), pp. 80-86.
78. Starbuck J.M. and Cataquiz L.B., *Evaluation of large tow-size carbon fiber for reducing the cost of CNG storage tanks*, Oak Ridge National Laboratory & US Department of Energy, 1998.
79. Mills A., *Automation of carbon fibre preform manufacture for affordable aerospace applications*, Composites Part A: Applied Science and Manufacturing, 2001, 32(7), pp. 955-962.
80. *Fiber reinforcement forms*, 2012, viewed: 01/02/2013, Available from: http://www.compositesworld.com/articles/fiber-reinforcement-forms.
81. Schell P.L. and DiMario J.M., *Fiber Directed Preform Reinforcement: Factors That May Influence Mechanical Properties in Liquid Composite Molding*, 46th Annual

Conference, Composites Institute, The Society of the Plastic Industry Inc., Washington, DC, USA, 1991

82. Dahl J.S. and Hoseck T., *Investigation into the light transmission characteristics of random chopped carbon fiber preforms*, 48th International SAMPE Symposium, 2003, Long Beach, CA, USA.
83. J. S. Dahl, G. L. Smith, J. E. deVries and Houston D.Q., *The Influence of Fiber Tow Size on the Performance of Chopped Carbon Fiber Reinforced Composites*, 37th ISTC Conference, Seattle, WA, USA, 2005
84. Dahl J.S., Warren C.D., Carpenter J.A. and Sklad P.S., U.S. Department of Energy, *Automotive lightweighting materials program annual progress report - Development of manufacturing methods for fiber preforms*, 2004
85. Pimenta S., Pinho S.T., Robinson P., Wong K.H. and Pickering S.J., *Mechanical analysis and toughening mechanisms of a multiphase recycled CFRP*, Composites Science and Technology, 2010, 70(12), pp. 1713-1725.
86. Dahl J.S., Warren C.D. and Carpenter J.A., *Automotive lightweighting materials program annual progress report - Development of manufacturing methods for fiber preforms*, 2005
87. Carley E.P., Dockum J.F. and Schell P.L., *Preforming for Liquid Composite Molding*, Polymer Composites for Structural Automotive Applications, 1990, Detroit, MI, USA.
88. Taha I. and Abdin Y.F., *Modeling of strength and stiffness of short randomly oriented glass-fiber polypropylene composites*, Journal of Composite Materials, 2011.
89. Sk L. and Chakraborty S., *Effective Moduli of Random Short Fiber Composite: A Probabilistic Study*, Journal of Reinforced Plastics and Composites, 2004, 23(7), pp. 751-760.
90. Thomason J.L., *The influence of fibre length, diameter and concentration on the strength and strain to failure of glass fibre-reinforced polyamide 6,6*, Composites Part A: Applied Science and Manufacturing, 2008, 39(10), pp. 1618-1624.
91. Olivero K.A., Hamidi Y.K., Aktas L. and Altan M.C., *Effect of Preform Thickness and Volume Fraction on Injection Pressure and Mechanical Properties of Resin Transfer Molded Composites*, Journal of Composite Materials, 2004, 38(11), pp. 937-957.
92. Campbell F.C., *Manufacturing Processes for Advanced Composites*, 2004, Elsvier Ltd.
93. Lavengood R.E., *Strength of short-fiber reinforced composites*, Polymer Engineering and Science, 1972, 12(1), pp. 48-52.
94. Ericson M.L. and Berglund L.A., *The effect of microstructure on the elastic modulus and strength of performed and commercial GMTs*, Polymer Composites, 1993, 14(1), pp. 35-41.
95. Feraboli P., Peitso E., Cleveland T. and Stickler P.B., *Modulus Measurement for Prepreg-based Discontinuous Carbon Fiber/Epoxy Systems*, Journal of Composite Materials, 2009, 43(19), pp. 1947-1965.
96. Mulligan D.R., Ogin S.L., Smith P.A., Wells G.M. and Worrall C.M., *Fibre-bundling in a short-fibre composite: 1. Review of literature and development of a method for controlling the degree of bundling*, Composites Science and Technology, 2003, 63, pp. 715-725.
97. Dahl J.S., Hoseck T., Warren C.D., Carpenter J.A. and Sklad P.S., U.S. Department of Energy, *Automotive lightweighting materials program annual progress report - Development of manufacturing methods for fiber preforms*, 2003
98. Han J. and Siegmund T., *A combined experimental-numerical investigation of crack growth in a carbon–carbon composite*, Fatigue & Fracture of Engineering Materials & Structures, 2006, 29(8), pp. 632-645.
99. Endruweit A., Harper L.T., Turner T.A., Warrior N.A. and Long A.C., *Random discontinuous carbon fibre preforms: Permeability modelling and resin injection*

simulation, Composites Part A: Applied Science and Manufacturing, 2008, 39(10), pp. 1660-1669.

100. Kacir L., Ishai O. and Narkis M., *Oriented short glass-fiber composites. IV. Dependence of mechanical properties on the distribution of fiber orientations*, Polymer Engineering & Science, 1978, 18(1), pp. 45-52.
101. Kim J.W., Lee J.J. and Lee D.G., *Effect of fiber orientation on the tensile strength in fiber-reinforced polymeric composite materials*, Key Engineering Materials, 2005, 297, pp. 2897-2902.
102. Jules E.J., Tsujikami T., Lomov S.V. and Verpoest I., *Effect of Fibres Length and Fibres Orientation on the Predicted Elastic Properties of Long Fibre Composites*, Macromolecular Symposia, 2004, 17.
103. Toll S., *Packing mechanics of fiber reinforcements*, Polymer Engineering and Science, 1998, 38(8), pp. 1337-1350.
104. Ericson M.L. and Berglund L.A., *Processing and mechanical properties of orientated preformed glass-mat-reinforced thermoplastics*, Composites Science and Technology, 1993, 49(2), pp. 121-130.
105. Reeve S., Rondeau R., Bond G. and Tervet F., *Mechanical Property Translation in Oriented, Discontinuous Carbon Fiber Composites*, SAMPE International Symposium, 2000, SAMPE.
106. Jander M., *Industrial RTM - New developments in molding and preforming technologies*, Advanced Composite Materials: New Developments and Applications, 1991, Detroit, MI, USA.
107. Katayama T., Tanaka K. and Miura Y., *The Evaluation of fibre filamentisation in the LFRTP Moulding*, 8th Japan-US Conference on Composite Materials, 1998.
108. Vaidya U., *Discontinuous Reinforcement-Based Processes for Automotive and Transportation Applications, Composites for Automotive, Truck and Mass Transit: Materials, Design, Manufacturing*, 2010, DEStech Publications, pp. 134-137.
109. Liakus J., Wang B., Cipra R. and Siegmund T., *Processing–microstructure-property predictions for short fiber reinforced composite structures based on a spray deposition process*, Composite Structures, 2003, 61(4), pp. 363-374.
110. Heping C., Ning X., Weihua S., Yifan C. and Dahl J., *Optimal spray gun trajectory planning with variational distribution for forming process*, Robotics and Automation, 2004. Proceedings. ICRA '04. 2004 IEEE International Conference on, 2004.
111. Gunnerson K.A., Cipra R.J. and Siegmund T., *Near-Net-Shape Manufacturing of Short Fiber Composite Parts via Discrete Depositions*, Journal of Manufacturing Science and Engineering, 2008, 130(6), pp. 061002.
112. Mather A., Bodily T., Cipra R. and Siegmund T., *An Image Analysis Technique to Assist in the Determination of Orientation Distributions of the Manufacture of Carbon Fiber Composites*, North American Manufacturing Research Institution SME, 2006.
113. Drocco J.A., Reichhardt C.J.O., Reichhardt C. and Janko B., *Structure and Melting of Two-Species Charged Clusters in a Parabolic Trap*, Physical Review E, 2003, 68(6 Pt. 1).
114. Sahir Arıkan M.A. and Balkan T., *Process modeling, simulation, and paint thickness measurement for robotic spray painting*, Journal of Robotic Systems, 2000, 17(9), pp. 479-494.
115. Li F.-z., Zhao D.-a. and Xie G.-h., *Trajectory Optimization of Spray Painting Robot Based on Adapted Genetic Algorithm*, Proceedings of the 2009 International Conference on Measuring Technology and Mechatronics Automation - Volume 02, 2009
116. Stepanenko D.A., *Modeling of spraying with time-dependent material feed rate*, Applied Mathematical Modelling, 2007, 31(11), pp. 2564-2576.
117. Xia W., Sheng-Rui Y. and Liao X.P., *Paint deposition pattern modeling and estimation for robotic air spray painting on free-form surface using the curvature circle method*, Industrial Robot, 2010, 37(2), pp. 202-213.

118. Heping C., Ning X., Weihua S., Dahl J. and Hongjun C., *Analysis of system performance for robotic spray forming process*, Intelligent Robots and Systems, 2005. (IROS 2005). 2005 IEEE/RSJ International Conference on, 2005.
119. Chen H., Xi N., Masood S.K., Chen Y. and Dahl J., *Development of automated chopper gun trajectory planning for spray forming*, Industrial Robot, 2004, 31(3), pp. 297-307.
120. Chen H., Sheng W., Xi N., Song M. and Chen Y., *CAD-based automated robot trajectory planning for spray painting of free-form surfaces*, Industrial Robot, 2002, 29(5), pp. 426-433.
121. Ren T.R., Kwok N.M., Liu D.K. and Huang S.D., *Path planning for a robotic arm sand-blasting system*, Information and Automation, 2008. ICIA 2008. International Conference on, 2008.
122. Suh S.H., Woo I.K. and Noh S.K., *Development of an automatic trajectory planning system (ATPS) for spray painting robots*, Robotics and Automation, 1991. Proceedings., 1991 IEEE International Conference on, 1991.
123. Chen H., Fuhlbrigge T. and Li X., *A review of CAD-based robot path planning for spray painting*, Industrial Robot: An International Journal, 2009, 36(1), pp. 45-50.
124. Rao S.S., *Optimization: theory and applications*, 1984, Halsted Press.
125. Dahl J.S., Hoseck T., Warren C.D., Carpenter J.A. and Sklad P.S., U.S. Department of Energy, *Automotive lightweighting materials program annual progress report - Development of manufacturing methods for fiber preforms*, 2002
126. Chen H. and Xi N., *Automated tool trajectory planning of industrial robots for painting composite surfaces*, The International Journal of Advanced Manufacturing Technology, 2008, 35(7-8), pp. 680-696.
127. Weihua S., Heping C., Ning X. and Yifan C., *Tool path planning for compound surfaces in spray forming processes*, Automation Science and Engineering, IEEE Transactions on, 2005, 2(3), pp. 240-249.
128. Jimenez P.A., Shirinzadeh B., Nicholson A. and Alici G., *Optimal area covering using genetic algorithms*, Advanced intelligent mechatronics, 2007 IEEE/ASME international conference on, 2007.
129. Tewolde G.S. and Weihua S., *Robot Path Integration in Manufacturing Processes: Genetic Algorithm Versus Ant Colony Optimization*, Systems, Man and Cybernetics, Part A: Systems and Humans, IEEE Transactions on, 2008, 38(2), pp. 278-287.
130. Atkar P.N., Greenfield A., Conner D.C., Choset H. and Rizzi A.A., *Uniform coverage of automotive surface patches*, The international Journal of Robotics Research, 2005, 24(11), pp. 883-898.
131. Balkan T., Ozgoren M.K., Sahir Arikan M.A. and Baykurt H.M., *A method of inverse kinematics solution including singular and multiple configurations for a class of robotic manipulators*, Mechanism and Machine Theory, 2000, 35(9), pp. 1221-1237.
132. Muskat M., *Darcy's Law and the Measurement of the Permeability of Porous Media*, *The Flow of Homogeneous Fluids Through Porous Media*, 1937, McGraw-Hill Book Company.
133. Carman P.C., *Fluid flow through granular beds*, Transactions of the Institution of Chemical Engineers, 1937, 15, pp. 150-166.
134. Chen C.Y., *Filtration of Aerosols By Fibrous Media*, Chemical Reviews, 1955, 55(3), pp. 595-623.
135. Forchheimer P., *Wasserbewgung durch Boden*, Zeit. Ver. Deut. Ing., 1901, 45, pp. 1781-1788.
136. Scheidegger A.E., *Physics of Flow Through Porous Media*, 1957, University of Toronto, Oxford University Press.
137. Ergun S. and Orning A.A., *Fluid Flow through Randomly Packed Columns and Fluidized Beds*, Industrial & Engineering Chemistry, 1949, 41(6), pp. 1179-1184.
138. Comiti J. and Renaud M., *A new model for determining mean structure parameters of fixed beds from pressure drop measurements: application to beds packed with*

parallelepipedal particles, Chemical Engineering Science, 1989, 44(7), pp. 1539-1545.
139. Belkacemi K. and Broadbent A.D., *Air Flow Through Textiles at High Differential Pressures*, Textile Research Journal, 1999, 69(1), pp. 52-58.
140. Goodings A.C., *Air Flow through Textile Fabrics*, Textile Research Journal, 1964, 34(8), pp. 713-724.
141. Zierep J., Bohning R. and Doerffer P., *Experimental and analytical analysis of perforated plate aerodynamics*, Journal of Thermal Science, 2003, 12(3), pp. 193-197.
142. Haque S.M.E., Rasul M.G., Deev A., Khan M.M.K. and Zhou J., *The Influence of Flow Distribution on the Performance Improvement of Electrostatic Precipitator*, The 10th International Conference on Electrostatic Precipitator, 2006, Cairns, Australia.
143. Harper L.T., Turner T.A., Martin J.R.B. and Warrior N.A., *Fiber Alignment in Directed Carbon Fiber Preforms - Mechanical Property Prediction*, Journal of Composite Materials, 2010, 44(8), pp. 931-951.
144. Hill R., *Elastic properties of reinforced solids: Some theoretical principles*, Journal of the Mechanics and Physics of Solids, 1963, 11(5), pp. 357-372.
145. Drugan W.J. and Willis J.R., *A micromechanics-based nonlocal constitutive equation and estimates of representative volume element size for elastic composites*, Journal of the Mechanics and Physics of Solids, 1996, 44(4), pp. 497-524.
146. Harper L.T., Qian C., Turner T.A., Li S. and Warrior N.A., *Representative volume elements for discontinuous carbon fibre composites - Part 1: Boundary conditions*, Composites Science and Technology, 2012, 72(2), pp. 225-234.
147. Pan Y., Iorga L. and Pelegri A.A., *Numerical generation of a random chopped fiber composite RVE and its elastic properties*, Composites Science and Technology, 2008, 68(13), pp. 2792-2798.
148. Altendorf H. and Jeulin D., *Random-walk-based stochastic modeling of three-dimensional fiber systems*, Physical Review E, 2011, 83(4), pp. 041804.
149. Luchoo R., Harper L.T., Bond M.D., Dodworth A. and Warrior N.A., *Macro-scale Modelling of Discontinuous Fibre Composites*, 18th International Conference on Composite Materials, Jeju, Korea, 2011
150. Digimat, *DIGIMAT for NANO-COMPOSITES*, in *e-Xstream engineering*2010.
151. Eason T.G. and Ochoa O.O., *Material Behavior of Structural Reaction Injection Molded Composites under Thermomechanical Loading*, Journal of Composite Materials, 2001, 35(5), pp. 411-432.
152. Ionita A. and Weitsman Y.J., *On the mechanical response of randomly reinforced chopped-fibers composites: Data and model*, Composites Science and Technology, 2006, 66(14), pp. 2566-2579.
153. Nadeau J.C. and Ferrari M., *Microstructural optimization of a functionally graded transversely isotropic layer*, Mechanics of Materials, 1999, 31(10), pp. 637-651.
154. Feraboli P., Cleveland T., Stickler P. and Halpin J., *Stochastic laminate analogy for simulating the variability in modulus of discontinuous composite materials*, Composites Part A: Applied Science and Manufacturing, 2010, 41(4), pp. 557-570.
155. Brody J.C. and Gillespie J.W., *Reactive and non-reactive binders in glass/vinyl ester composites*, Polymer Composites, 2005, 26(3), pp. 377-387.
156. Becke J. and Stieg J., *Advanced SMC - Material concepts for lightweight exterior vehicle surfaces*, European Alliance for SMC, Automotive Seminar, 2004.
157. Dawson D., *Rapid Fiber Preforming On A Large Scale*, in *Composites Technology*, 2006
158. Luchoo R., Harper L., Bond M., Warrior N. and Dodworth A., *Net shape spray deposition for compression moulding of discontinuous fibre composites for high performance applications*, Plastics, Rubber and Composites, 2010, 39(3-5), pp. 3-5.
159. Chen W. and Zhao D., *Tool Trajectory Optimization of Robotic Spray Painting*, Intelligent Computation Technology and Automation, 2009.

160. *Porous Jump Boundary Conditions*, 2009, viewed: 05/01/2013, Available from: https://www.sharcnet.ca/Software/Fluent12/html/ug/node256.htm#eq-porous-jump1.
161. Sutherland I.E. and Hodgman G.W., *Reentrant polygon clipping*, Commun. ACM, 1974, 17(1), pp. 32-42.
162. Hull D. and Clyne T.W., *An Introduction to Composite Materials*, 1996, Cambridge, Cambridge University Press.
163. Warrior N.A., Turner T.A., Patel C., Kirupanantham G. and Nicholls T.K., The University of Nottingham, *Advanced Structural Preforming (ASP) - Final project report*, 2012

Appendix A

Publications arising from this work

1. Warrior N. A., Patel C., Turner T. A., *Advances in Discontinuous Composites*, SAMPE Europe 32nd International Conference SEICO 11, 2011, Paris, France.

2. Patel C., Turner T. A., Warrior N. A., *A computational model for discontinuous carbon fibre preforming processes*, Computational Materials Science, (In preparation).

3. Patel C., Turner T. A., Warrior N. A., *Characterisation and modelling of airflow & fibre retention effects during suction-based preforming methods*, Applied Composite Materials, (In preparation).

Appendix B

Deposition head characteristics

Deposition head characteristic data resulting from the study in Section 4.2 is presented in Tables B-1 to B-4. The data is used to define a virtual spray cone in order to explicitly position a chopped segment on the deposition plane in the process model developed in Chapter 7.

Table B-1: Spray cone characteristics for 3 K tow segments. The mean fibre location, standard deviation of segments from the mean position and the projection angle define the spray cone geometry.

Fibre length (mm)	Fibre Speed (m/s)	TCP height (mm)	Mean fibre location (mm)		Standard deviation (mm)		Projection angle (degrees)	
			x'	*y'*	*x'*	*y'*	*x'*	*y'*
10	1	100	-9.69	-7.69	12.40	12.90	1.06	5.82
		300	-30.74	-3.59	30.47	29.67		
	2	100	-21.28	-9.56	14.92	13.21	2.12	10.57
		300	-55.13	-9.12	26.33	23.17		
	3	100	-22.92	-10.55	17.37	14.36	1.92	15.07
		300	-82.13	-7.64	34.02	27.96		
30	1	100	-7.71	3.91	25.33	19.31	0.26	12.07
		300	-68.69	-2.80	39.04	33.57		
	2	100	-19.67	-7.61	19.80	10.43	1.31	15.74
		300	-87.38	-5.09	26.98	21.56		
	3	100	1.99	-11.40	36.35	14.83	0.86	13.70
		300	-81.91	-1.18	36.98	35.58		
90	1	100	7.36	2.34	51.04	21.63	2.40	3.95
		300	-25.45	-12.00	54.12	26.27		
	2	100	-11.44	2.75	44.52	23.47	0.63	10.85
		300	-60.09	-6.81	63.88	29.74		
	3	100	21.67	2.24	40.76	26.30	1.60	12.38
		300	-80.36	-19.11	78.45	44.94		

Table B-2: Spray cone characteristics for 6 K tow segments. The mean fibre location, standard deviation of segments from the mean position and the projection angle define the spray cone geometry.

Fibre length (mm)	Fibre Speed (m/s)	TCP height (mm)	Mean fibre location (mm)		Standard deviation (mm)		Projection angle (degrees)	
			x'	*y'*	*x'*	*y'*	*x'*	*y'*
10	1	100	-11.49	-5.34	16.57	10.94	0.81	6.87
		300	-36.33	-2.93	31.51	27.15		
	2	100	-17.82	-9.41	22.99	15.40	2.50	9.58
		300	-50.32	-11.45	36.67	24.56		
	3	100	-14.42	-13.41	28.58	22.67	3.54	10.44
		300	-56.62	-16.12	41.33	24.92		
30	1	100	-6.22	-1.41	10.84	14.42	3.96	5.43
		300	-29.61	-22.61	44.74	36.04		
	2	100	-9.87	-7.12	24.95	8.97	1.94	12.48
		300	-70.50	-8.89	33.19	26.93		
	3	100	-5.50	-9.14	21.44	13.44	1.25	14.30
		300	-83.12	-4.21	40.74	25.74		
90	1	100	9.22	-0.60	35.13	14.51	0.65	8.80
		300	-54.69	-3.60	57.33	14.61		
	2	100	-30.98	-9.61	63.93	30.90	1.71	9.79
		300	-47.18	-6.75	65.05	34.54		
	3	100	-2.50	-4.16	45.73	27.06	0.60	6.49
		300	-37.09	-2.13	58.32	25.29		

Table B-3: Spray cone characteristics for 12 K tow segments. The mean fibre location, standard deviation of segments from the mean position and the projection angle define the spray cone geometry.

Fibre length (mm)	Fibre Speed (m/s)	TCP height (mm)	Mean fibre location (mm)		Standard deviation (mm)		Projection angle (degrees)	
			x'	*y'*	*x'*	*y'*	*x'*	*y'*
10	1	100	-22.39	-5.33	26.57	12.67	2.01	10.39
		300	-53.63	-9.91	35.92	26.87		
	2	100	-24.03	-8.33	25.49	21.03	2.75	14.73
		300	-79.60	-13.22	34.54	31.80		
	3	100	-32.78	-8.89	34.63	23.78	2.94	17.59
		300	-94.77	-14.18	49.31	34.18		
30	1	100	-8.64	-6.43	13.94	14.36	5.60	12.84
		300	-73.11	-30.52	32.46	35.16		
	2	100	-14.16	-5.92	21.42	8.91	2.32	18.91
		300	-109.44	-11.53	38.73	34.08		
	3	100	-6.33	-10.34	24.25	10.74	1.03	14.27
		300	-82.68	-2.54	48.01	44.51		
90	1	100	-10.67	-10.56	51.10	16.45	0.59	10.84
		300	-60.28	0.08	34.53	19.55		
	2	100	-3.84	-6.91	38.80	28.19	1.61	6.09
		300	-34.30	-7.07	66.53	29.39		
	3	100	-30.57	-2.23	61.63	36.92	3.48	4.52
		300	-16.14	-19.51	69.79	33.70		

Table B-4: Spray cone characteristics for 24 K tow segments. The mean fibre location, standard deviation of segments from the mean position and the projection angle define the spray cone geometry.

Fibre length (mm)	Fibre Speed (m/s)	TCP height (mm)	Mean fibre location (mm)		Standard deviation (mm)		Projection angle (degrees)	
			x'	*y'*	*x'*	*y'*	*x'*	*y'*
10	1	100	-6.03	-6.60	14.11	10.50	1.58	6.64
		300	-36.82	-6.99	35.04	20.94		
	2	100	-5.15	-8.51	20.08	13.29	2.97	2.08
		300	-10.40	-14.48	39.51	21.66		
	3	100	-2.45	-14.83	22.99	16.72	3.09	6.20
		300	-35.38	-13.06	41.29	23.11		
30	1	100	-7.04	-8.12	17.58	10.67	6.05	2.87
		300	19.07	-32.61	28.17	36.07		
	2	100	-6.66	-7.19	15.86	15.08	4.19	5.30
		300	-28.68	-22.00	32.53	33.94		
	3	100	-6.67	-7.95	25.48	18.41	2.53	6.94
		300	-38.37	-12.06	37.58	34.14		
90	1	100	28.38	-14.83	18.07	12.64	4.32	1.46
		300	-17.96	-13.06	41.31	20.00		
	2	100	14.56	0.76	55.99	33.09	1.89	4.87
		300	-33.24	-11.26	51.58	35.24		
	3	100	5.63	-4.52	36.30	22.28	3.68	6.42
		300	-39.37	-19.91	66.86	38.82		

Fibre orientation distributions

Table B-5: Fibre orientation distribution for deposition using 3 K tow. Fibre orientation is taken relative to the x' axis of the deposition head.

Fibre length (mm)	Speed (m/s)	TCP height (mm)	Uniform distribution	Normal distribution	Mean (degrees)	Standard deviation (degrees)
10	1	100	•	-	-	-
		300	•	-	-	-
	2	100	•	-	-	-
		300	•	-	-	-
	3	100	•	-	-	-
		300	•	-	-	-
30	1	100	•	-	-	-
		300	•	-	-	-
	2	100	-	•	5.17	36.65
		300	-	•	0.61	43.63
	3	100	-	•	-2.29	40.96
		300	-	•	0.61	43.63
90	1	100	-	•	5.79	37.37
		300	-	•	8.33	39.38
	2	100	-	•	6.95	38.96
		300	-	•	3.06	42.09
	3	100	-	•	-3.21	41.00
		300	-	•	-4.77	39.15

Table B-6: Fibre orientation distribution for deposition using 6 K tow. Fibre orientation is taken relative to the x' axis of the deposition head.

Fibre length (mm)	Speed (m/s)	TCP height (mm)	Uniform distribution	Normal distribution	Mean (degrees)	Standard deviation (degrees)
10	1	100	•	-	-	-
		300	•	-	-	-
	2	100	•	-	-	-
		300	•	-	-	-
	3	100	•	-	-	-
		300	•	-	-	-
30	1	100	•	-	-	-
		300	•	-	-	-
	2	100	-	•	5.98	33.80
		300	-	•	-2.83	43.17
	3	100	-	•	-12.12	34.44
		300	-	•	-0.48	41.10
90	1	100	-	•	2.65	37.26
		300	-	•	1.75	35.87
	2	100	-	•	-2.06	37.46
		300	-	•	5.57	39.06
	3	100	-	•	5.26	33.24
		300	-	•	-4.47	37.20

Table B-7: Fibre orientation distribution for deposition using 12 K tow. Fibre orientation is taken relative to the x' axis of the deposition head.

Fibre length (mm)	Speed (m/s)	TCP height (mm)	Uniform distribution	Normal distribution	Mean (degrees)	Standard deviation (degrees)
10	1	100	•	-	-	-
		300	•	-	-	-
	2	100	•	-	-	-
		300	•	-	-	-
	3	100	•	-	-	-
		300	•	-	-	-
30	1	100	•	-	-	-
		300	•	-	-	-
	2	100	-	•	2.29	33.27
		300	-	•	-5.50	39.58
	3	100	-	•	3.54	32.73
		300	-	•	2.97	43.56
90	1	100	-	•	-7.35	33.08
		300	-	•	6.75	35.06
	2	100	-	•	7.86	27.73
		300	-	•	8.25	39.33
	3	100	-	•	9.10	42.71
		300	-	•	4.19	43.40

Table B-8: Fibre orientation distribution for deposition using 24 K tow. Fibre orientation is taken relative to the x' axis of the deposition head.

Fibre length (mm)	Speed (m/s)	TCP height (mm)	Uniform distribution	Normal distribution	Mean (degrees)	Standard deviation (degrees)
10	1	100	•	-	-	-
		300	•	-	-	-
	2	100	•	-	-	-
		300	•	-	-	-
	3	100	•	-	-	-
		300	•	-	-	-
30	1	100	•	-	-	-
		300	•	-	-	-
	2	100	•	-		
		300	•	-		
	3	100	•	-		
		300	•	-		
90	1	100	-	•	-8.71	24.62
		300	-	•	-11.77	27.64
	2	100	-	•	-0.56	37.00
		300	-	•	0.83	33.45
	3	100	-	•	4.14	34.01
		300	-	•	-2.35	41.32

Appendix C

Fan resistance curve coefficients

Table C-1 and C-2 list the quartic and squared terms which characterise the resistance curves for each material tested. The curves are based on the relationship between superficial air velocity and pressure drop across the medium taken at 10 fan speed set points.

Table C-1: Quartic and squared term coefficients derived from fitted resistance curves taken for dry fabric and mat materials.

Material Type / Composition	Areal density (gsm)	Quartic term	Squared term	Required retention pressure (Pa)
Non-crimp UD - 300gsm,	300	37.45	524.59	2.94
	600	824.88	1605.40	
	900	4386.90	3878.80	
	1200	1826.40	8597.80	
Non-crimp UD - 450gsm,	450	5471.5	2288.1	4.41
	900	13341	12084	
	1350	-7910	29886	
	1800	-168208	59484	
Non-crimp UD – 200gsm	200	1.49	106.98	1.96
	400	247.43	137.91	
	600	1333.50	598.27	
	800	5991.50	2686.10	
	1000	12157.00	6965.40	
	1200	3966.20	17768.00	
Unifilo CoFRM ~375gsm	391	0.0759	32.546	1.51
	795	0.14	57.97	
	1165	0.22	89.52	
	1547	0.16	130.04	
	2368	0.17	202.37	
	3144	0.27	276.39	
	3940	0.42	355.53	
	4676	0.13	432.06	
	6264	0.04	595.84	
	7782	0.09	759.85	
	9326	0.10	1027.5	

Table C-2: Quartic and squared term coefficients derived from fitted resistance curves taken for discontinuous fibre architectures. Consolidated preforms and free fibre stacks were tested.

Material Type / Composition	Areal density (gsm)	Quartic term	Squared term	Required retention pressure (Pa)
24k DCFP UoN preform	939.0	5970.2	1759.6	9.21
	1951.2	43989	16701	
3k DCFP UoN preform	471.0986	160.57	331.28	4.62
	1009.042	1396.6	2868.9	
	1508.789	3858.4	3884.9	
	2040.366	3487.5	10213	
DCFP Sotira preform	1266.87	-1485	5670.6	12.42
	2597.41	-20521	18945	
	3947.04	-63683	33560	
24k DCFP - unconsolidated	67.23	0.0095	10.577	0.66
	134.45	0.0347	23.44	
	201.68	0.2162	60.214	
	268.91	0.2683	120.35	
	336.14	1.1298	209.72	
	403.36	3.2269	407.84	
	470.59	2.2234	754.25	
	537.82	0.2074	1243.8	
	605.04	27.897	2011.9	
	672.27	249.67	3293.5	
	739.50	-1033.3	5647	
	873.95	-1298.7	6940.6	
	1142.86	-7426	15748	
3k DCFP - unconsolidated	84.03	0.0763	27.242	0.82
	168.07	1.9091	90.978	
	252.10	26.646	157.848	
	336.14	102.92	212.91	
	420.17	227.28	240.23	
	504.20	394.82	346.52	
	672.27	618.33	605.83	
	840.34	1643.7	656.04	
Glass roving - unconsolidated	32.09	0.0017	6.0637	0.31
	64.17	0.0053	9.797	
	96.26	0.0106	14.057	
	128.34	0.0186	21.837	
	256.69	0.4043	56.908	
	385.03	2.974	106.62	
	513.37	13.568	140.65	
	641.71	21.391	263.13	
	962.57	93.712	347.84	
	1283.43	235.58	999.26	